

Large Area Forest Stem Volume Mapping Using Synergy of Spaceborne Interferometric Radar and Optical Remote Sensing: A Case Study of Northeast China

Dissertation

Zur Erlangung des akademischen Grades doctor rerum naturalium
(Dr. rer. nat.)

vorgelegt dem Rat der Chemisch-Geowissenschaftlichen Fakultät der Friedrich-
Schiller-Universität Jena

von Dipl. geogr. Oliver Cartus
geboren am 27. Juli 1976 in Trier

Gutachter:

1. Prof. Dr. Christiane Schmullius, Friedrich-Schiller-Universität Jena
2. Dr. Thuy Le Toan, Centre d'Etudes Spatiales de la Biosphère (CESBIO)

Disputation: 3. Februar 2010

Lass dir an meiner Gnade genügen;
denn meine Kraft ist in den Schwachen mächtig.

2. Korinther, Kapitel 12, Vers 9

Abstract

More than a decade of investigations on the use of the interferometric ERS-1/2 tandem coherence for forest applications have increased the understanding of the behaviour of C-band repeat-pass coherence over forested terrain. It has been shown that under optimal imaging conditions, ERS-1/2 tandem coherence can be used for forest stem volume retrieval with accuracies in the range of ground surveys (Santoro et al. 2002). Large-area applications of ERS-1/2 tandem coherence are rare though. One of the main limitations concerning large-area exploitation of the existing ERS-1/2 tandem archives for forest stem volume retrieval is related to the considerable dependence of repeat-pass coherence upon the meteorological (rain, temperature, wind speed) and environmental (soil moisture variations, snow metamorphism) acquisition conditions. Conventional retrieval algorithms require accurate forest inventory data for a dense grid of forest sites to tune models that relate coherence to stem volume to the local conditions. Accurate forest inventory data is, however, a rare commodity that is often not freely available.

In this thesis, a fully automated algorithm was developed, based on a synergetic use of the MODIS Vegetation Continuous Field product (Hansen et al., 2002), that allowed the training of the Interferometric Water Cloud Model IWCM (Askne et al., 1997) without further need for forest inventory data. The algorithm was developed using forest inventory data for five test sites in Central Siberia and three test sites in Northeast China for which a multi-temporal and multi-baseline ERS-1/2 tandem dataset was available. With the new algorithm it was possible to train the IWCM on a frame-by-frame basis and thus to account for the spatial and temporal variability of the meteorological and environmental acquisition conditions.

Limitations concerning the exploitation of the existing ERS-1/2 tandem archives were related to the influence of topography on the interferometric coherence measurements, forest structural diversity and the early saturation of coherence with increasing forest stem volume in case of tandem pairs that were acquired under unstable imaging conditions. When rain or freeze/thaw occurred in the timeframe of the tandem acquisitions, only a few low stem volume classes could be distinguished with sufficient accuracy.

The new algorithm was applied to a multi-seasonal ERS-1/2 tandem dataset covering Northeast China that was acquired between 1995 and 1998 with baselines up to 400 m. Because of the early saturation of coherence in case of unstable imaging conditions, only a few low stem volume classes could be classified. Due to the lack of reliable ground data for Northeast China, the produced map could not be validated. A first assessment of the accuracy of the approach for the Central Siberian test sites, however, indicated its potential for large-area forest mapping, at least for forest/non-forest discrimination..

Zusammenfassung

Der beschleunigte ökonomische Wandel der letzten Jahrzehnte und das immense Bevölkerungswachstum haben den Holzbedarf Chinas in die Höhe schnellen lassen. Die Konsequenz dieser Entwicklung war eine übermäßige Abholzung der chinesischen Wälder. Besonders deutlich sind die Folgen der Abholzung in der Manchurei, der wichtigsten Waldregion im Nordosten Chinas, zu erkennen. Die Waldfläche hat erheblich abgenommen und der durchschnittliche Holzvorrat pro Fläche bewegt sich auf sehr niedrigem Niveau (Li et al., 2004; Liu, 2005). Der chinesische Holzbedarf kann nicht mehr aus den eigenen Waldbeständen gedeckt werden, weshalb große Mengen an Holz importiert werden müssen. Weitere Konsequenzen der Abholzung sind verstärkte Erosion, Desertifikation sowie Überschwemmungen. Erst spät stellte sich die Politik den ökonomischen und ökologischen Folgen der übermäßigen Abholzung der Wälder. Dem Rückgang der Waldressourcen wurde versucht durch großangelegte Aufforstungsmaßnahmen entgegenzuwirken. Der Erfolg dieser Aufforstungsmaßnahmen war jedoch bescheiden. Die Wachstumsraten der aufgeforsteten Wälder liegen bis heute deutlich unter den erwarteten Wachstumsraten. Gründe hierfür sind vor allem in der Beschränkung auf wenige schnell wachsende Baumarten zu finden, die besonders anfällig für Krankheiten und Insektenbefall sind (Thomas et al., 2007).

Insgesamt sind die Waldressourcen Chinas nur unzureichend erfasst. Existierende Erhebungen der Waldfläche und des Holzvorrats widersprechen sich deutlich (Bull & Nilsson, 2004). Eine Möglichkeit, Informationen über die Veränderungen und den Zustand der Wälder Chinas zu erlangen ist die Fernerkundung. Im Gegensatz zur gängigen Forstinventur, die zeitaufwendig und kostspielig ist, können mithilfe von Fernerkundungssensoren in kurzen Zeitabständen Wälder großflächig kartiert werden. Eine Technik, die immer wieder diskutiert, bislang aber kaum großflächig eingesetzt wurde, ist die der Radarinterferometrie. Obwohl ursprünglich entwickelt für die Erstellung Digitaler Geländemodelle (Graham, 1974; Goldstein & Zebker, 1987), stellt die Radarinterferometrie eine interessante Technik für die Waldkartierung dar. Die Radarinterferometrie basiert auf der kohärenten arbeitsweise von sogenannten Syntetischen Apertur Radarsystemen (SAR), die Mikrowellen im Wellenlängenbereich von 1 mm bis 1 m senkrecht zur Bewegungsrichtung der Plattform, d.h. des Flugzeugs oder Satelliten, aussenden und das auf der Erdoberfläche reflektierte Signal empfangen. Die Phase des empfangenen Signals ist eine Funktion des Abstands des Sensors zum reflektierenden Objekt. Die Intensität des empfangenen Signals gibt Auskunft über die geometrischen und dielektrischen Eigenschaften des reflektierenden Objekts. Mithilfe zweier Phasemessungen aus leicht unterschiedlichen Perspektiven ist es möglich, Interferogramme zu erstellen. Interferogramme ermöglichen die Berechnung Digitaler Geländemodelle. Die interferometrische Technik erfuhr einen bedeutenden Entwicklungsschub mit dem Start der ersten europäischen SAR Missionen ERS-1 und ERS-2. Der ERS-1 Satellit mit einem SAR Sensor an Bord, der mit Mirowellen von ~5 cm Wellenlänge (dem sogenannten C-Band) arbeitete, wurde 1991 in die Erdumlaufbahn gebracht. Ein zweiter baugleicher Sensor folgte 1995 mit dem ERS-2 Satelliten. Von 1995 bis 2000 erfassten beide Sensoren den selben Erdausschnitt mit einem Tag Zeitabstand (im sogenannten Tandemmodus). Die Tandem Mission endete mit dem Ausfall von ERS-1 im Jahr 2000. Die Nutzbarkeit von Interferogrammen für die Berechnung Digitaler Geländemodelle setzt voraus, dass sich die Aufnahmebedingungen auf der Erdoberfläche zwischen den beiden SAR Messungen, die zur Berechnung des Interferogramms verwendet werden, nicht oder nur geringfügig

ändern. Ein Maß für die Stabilität der Aufnahmebedingungen, und somit für die Qualität der topographischen Information in einem Interferogramm, ist die interferometrische Kohärenz. Eine bedeutende Erkenntnis für die Anwendung der Radarinterferometrie zur Kartierung der Erdoberfläche war, dass die Kohärenz für SAR Messungen, die mit einem gewissen zeitlichen Abstand aufgenommen wurden, vom Landoberflächentyp abhängt (Wegmüller & Werner, 1995; Dammert et al., 1999; Strozzi et al., 2000; Weydahl, 2000; Engdahl & Hyypä, 2003; Srivastava et al., 2001, 2006). Insbesondere dichte Wälder zeigen in Kohärenzbildern für ERS-1/2 Bildpaare eine niedrige Kohärenz wohingegen vegetationsfreie Flächen in der Regel eine deutlich höhere Kohärenz aufweisen. Die niedrigere Kohärenz über dichten Wäldern erklärt sich im Wesentlichen aus den ständigen windbedingten Bewegungen der Äste in den oberen Schichten der Baumkronen, welche im Wellenlängenbereich von 5 cm für den Grossteil der Rückstreuung des Radarsignals zum Sensor verantwortlich sind (Chauhan et al., 1991). Die Bewegungen bedeuten eine ständige Veränderung der Rückstreugeometrie (Zebker & Villasenor, 1992; Narayanan et al., 1992, 1994). Zusätzlich senkt die Volumendekorrelation das Kohärenzniveau über Wald. Dieser Effekt hängt vom räumlichen Abstand der Sensoren, der sogenannten Basislinie, bei der Messung über demselben Erdausschnitt ab. Es gilt, je größer die Basislinie, desto mehr trägt Volumendekorrelation zum Kohärenzkontrast zwischen vegetationsfreien und dicht bewaldeten Gebieten bei. Solange die Aufnahmebedingungen am Boden stabil sind – Veränderungen werden hier vor allem durch Bodenfeuchtevariationen, Regen und Änderungen in den Schneeeigenschaften bewirkt – zeigen Kohärenzbilder einen deutlichen Kontrast zwischen Wald und vegetationsfreien Flächen. Für die Kohärenz eines Bildpunktes bedeutet dies, dass die Kohärenz abnimmt, je dichter der Wald ist, da mit zunehmender Waldbedeckung größere Anteile der Rückstreuung zum Sensor von den Baumkronen und geringere Anteile von der Bodenoberfläche kommen. Untersuchungen konnten zeigen, dass der Rückgang der ERS-1/2 Tandem Kohärenz mit der Dichte des Waldes zur Kartierung biophysikalischer Forstparameter genutzt werden kann (Hyypä et al., 2000; Manninen et al., 2000; Koskinen et al., 2001; Fransson et al., 2001; Santoro et al., 2002, 2005, 2007; Askne et al., 2003; Pulliainen et al., 2003; Wagner et al., 2003; Engdahl et al., 2004; Askne & Santoro, 2005; Drezet & Quegan, 2006, 2007). Besonders erfolgreich waren dabei Ansätze, die die ERS-1/2 Tandem Kohärenz zur Bestimmung des Stammvolumens borealer Wälder nutzten. Hier wurden mitunter Genauigkeiten im Bereich von Vorort-Messungen erreicht (Santoro et al., 2002).

Obwohl das Verständnis des Zusammenhangs von Kohärenz und biophysikalischen Forstparametern seit dem Beginn der ERS-1/2 Tandem Mission stetig zugenommen hat und Modelle entwickelt wurden (Askne et al., 1997; Koskinen et al., 2001; Treuhaft et al., 1996; Papathanassiou & Cloude, 2001), die es erlauben die Kohärenz mit biophysikalischen Forstparametern und den jeweiligen Aufnahmebedingungen in Verbindung zu setzen, sind grossflächige Anwendungen dieser Technik bisher selten. Eine wesentliche Ursache hierfür ist, dass die Kohärenz sowohl über Wald als auch über vegetationsfreien Flächen stark von den Aufnahmebedingungen (z.B. Temperatur, Windgeschwindigkeit, Niederschlag, Bodenfeuchtevariationen, Schneeeigenschaften) abhängt und sich diese Abhängigkeiten nicht einfach vorhersagen lassen, z.B. mittels meteorologischen Messungen im Zeitraum der Radarmessungen (Drezet & Quegan, 2006). Die Folge ist, dass Modelle, die die Kohärenz zu den biophysikalischen Forstparametern in Verbindung setzen, an die jeweiligen Aufnahmebedingungen angepasst werden müssen. Hierzu sind Forstinventurdaten nötig. Diese sind jedoch schwer zugänglich und häufig nur für kleinere Testgebiete verfügbar.

Das ERS-1/2 Datenarchiv der Europäischen Raumfahrtagentur ESA umfasst eine große Menge an Daten, die von großem Interesse für die Erstellung großflächiger Karten der Wälder für die neunziger Jahre sind. Von besonderem Interesse, insbesondere im Kontext des globalen Klimawandels, sind dabei das Stammvolumen und die Biomasse der Wälder, da im Holz der Bäume erhebliche Mengen an Kohlenstoff gespeichert sind. Um die ERS Daten für die Forstkartierung nutzbar zu machen, sind jedoch neue Ansätze vonnöten, die es erlauben, Modelle, die die Kohärenz mit den biophysikalischen Forstparametern in Verbindung setzen, unabhängig von Forstinventurdaten an die lokalen Aufnahmebedingungen anzupassen. Die Entwicklung einer solchen Methodik, am Beispiel Nordostchinas, war das Hauptziel der hier vorgestellten Arbeit. Ein ERS-1/2 Datensatz bestehend aus 223 ERS-1/2 Tandembildpaaren stand hierzu zur Verfügung. Die Tandempaare wurden zwischen 1995 und 1998 in allen Jahreszeiten über Nordostchina aufgenommen. Für die Algorithmenentwicklung standen jedoch nur begrenzt Forstinventurdaten für drei kleinere Testgebiete zur Verfügung weshalb ein weiterer multisaisonaler ERS-1/2 Datensatz für mehrere Testgebiete in Zentralsibirien, bestehend aus acht Tandempaaren, hinzugezogen wurde. Für diese Testgebiete konnte auf eine umfassende Forstinventurdatenbank zurückgegriffen werden.

Der Vergleich der Kohärenzwerte mit den Stammvolumenangaben in den Sibirischen Inventurdaten zeigte deutlich die Abhängigkeit der ERS-1/2 Tandem Kohärenz von den vorherrschenden Aufnahmebedingungen. Ein exponentieller Rückgang der Kohärenz mit zunehmendem Stammvolumen konnte für jedes der Tandempaare beobachtet werden. Deutliche Unterschiede im Zusammenhang von Kohärenz und Stammvolumen zeigten sich insbesondere zwischen den Tandempaaren, die im Winter unter gefrorenen Bedingungen aufgenommen wurden, und denen, die im Frühjahr und Herbst unter ungefrorenen Bedingungen aufgenommen wurden. Die Winterszenen waren durch eine hohe Kohärenz über vegetationsfreien Flächen, einen ausgeprägten Kontrast zwischen dichtem Wald und vegetationsfreien Flächen und eine hohe Korrelation von Kohärenz und Stammvolumen gekennzeichnet. Die Kohärenz zeigte eine deutliche Abhängigkeit vom Stammvolumen bis zu Stammvolumina von mindestens $200 \text{ m}^3/\text{ha}$. Die Kohärenz über vegetationsfreien Flächen zeigte leichte Unterschiede zwischen den Tandempaaren aufgrund unterschiedlicher Schneeeigenschaften. Die Kohärenz über dichtem Wald hing von den Windgeschwindigkeiten und der Länge der Basislinie ab. Die Kohärenz im Fall der Tandempaare, die im Frühjahr und Herbst unter ungefrorenen Bedingungen aufgenommen wurden, zeigte deutlich niedrigere Werte über vegetationsfreien Flächen und eine frühe Sättigung mit zunehmendem Stammvolumen bei etwa $100 \text{ m}^3/\text{ha}$. Dies war eine Konsequenz der insgesamt deutlich instabileren Aufnahmebedingungen. Der Aufnahme mehrerer der fünf Tandempaare gingen Regenfälle voraus, welche das Kohärenzniveau über vegetationsfreien sowie dicht bewaldeten Flächen absenkten. Lediglich eines der fünf Kohärenzbilder, die unter ungefrorenen Bedingungen aufgenommen wurden, zeigte eine hohe Kohärenz über vegetationsfreien Flächen und keine Sättigung mit zunehmendem Stammvolumen unterhalb von $200 \text{ m}^3/\text{ha}$.

Im Fall der drei chinesischen Testgebiete waren lediglich Tandempaare verfügbar, die unter gefrorenen Bedingungen aufgenommen wurden. Im Gegensatz zu den Tandempaaren für die sibirischen Testgebiete konnte fast keine Korrelation von Stammvolumen und Kohärenz festgestellt werden. Eine geringe Genauigkeit der Inventurdaten dürfte der Hauptgrund für die niedrige Korrelation gewesen sein. Ein weiterer Grund für die niedrige Korrelation könnte jedoch die Struktur der Wälder Nordostchinas gewesen sein. Im Fall der sibirischen Testgebiete wurde beobachtet, dass die Korrelation von

Stammvolumen und Kohärenz für Bestände mit niedrigem Bestockungsgrad niedriger ausfiel als für Bestände mit hohem Bestockungsgrad (Santoro et al., 2007). Der Bestockungsgrad bezeichnet das Verhältnis von gemessener und einer erwarteten ‚optimalen‘ Bestandsgrundfläche (Pretzsch, 2002). Bestände mit niedrigem Bestockungsgrad sind bei gegebenem Stammvolumen durch eine niedrigere Baumdichte und eine heterogenere Bestandsstruktur gekennzeichnet. Angaben über den Bestockungsgrad waren lediglich für die sibirischen Testgebiete verfügbar. Mittels allometrischer Betrachtungen konnte jedoch für die chinesischen Testgebiete gezeigt werden, dass die Wälder Nordostchinas infolge der übermäßigen Abholzung im Schnitt einen niedrigeren Bestockungsgrad aufweisen als die Wälder in den sibirischen Testgebieten, sodass die niedrige Korrelation von Kohärenz und Stammvolumen, zumindest teilweise, auch darauf zurückzuführen sein könnte.

Insgesamt bestätigte der Vergleich von Kohärenz und Stammvolumen für die Testgebiete die Erwartung, dass ein Algorithmus, der auf die großflächige Bestimmung des Stammvolumens mittels ERS-1/2 Tandem Kohärenz abzielt, die Abhängigkeit der Kohärenz von den Aufnahmebedingungen berücksichtigen muss. Wie bereits erwähnt, existieren mehrere Modelle, die es erlauben die Kohärenz als Funktion des Stammvolumens zu modellieren. Ein semiempirisches Modell, das erfolgreich für die Bestimmung des Stammvolumens borealer Wälder mittels ERS-1/2 Tandem Kohärenz getestet wurde, ist das ‘Interferometric Water Cloud Modell’ IWCM (Askne et al., 1997). Das Modell beruht auf der ‘Radiative Transfer’ Theorie und modelliert die Kohärenz über Wald als Summe der Kohärenzbeiträge von Waldboden und Baumkrone. Die von der Basislinie und Baumhöhe abhängige Volumendekorrelation wird ebenfalls berücksichtigt. Die Beiträge der Kohärenz des Waldbodens und der Baumkrone zur gemessenen Kohärenz werden durch die Transmissivität der Baumkronen bestimmt. Die Transmissivität kann laut Pulliainen et al. (1994) als Funktion des Stammvolumens modelliert werden und hängt im Wesentlichen von den Lücken in der Baumkrone, durch die das Radarsignal ungehindert zum Boden vordringen kann, ab (Askne et al., 1995). Eine relativ kleine Rolle spielt hingegen die Transmissivität der Bäume, da das kurzwellige C-Band Signal kaum in Baumkronen eindringen kann. Das IWCM umfasst fünf zu bestimmende Parameter. Diese Parameter werden üblicherweise mittels Regression für Testgebiete mit vorhandenen Stammvolumenangaben bestimmt. Zwei der Parameter, γ_{gr} und γ_{veg} , kennzeichnen die Kohärenz des Waldbodens und der komplett geschlossenen Baumkrone. Die Parameter σ_{gr}^0 und σ_{veg}^0 geben die Rückstreuintensität von Waldboden und Baumkrone an und der Transmissivitätskoeffizient β wird benötigt, um die Transmissivität mit dem Stammvolumen in Verbindung zu setzen.

Für die Bestimmung der Parameter wurde der Zusammenhang von Kohärenz und den Kronenbedeckungsangaben im optischen Fernerkundungsprodukt ‘MODIS Vegetation Continuous Field’ VCF (Hansen et al., 2003) analysiert. VCF liefert globale Schätzungen der Kronenbedeckung mit einer Pixelgröße von 500x500 m². Zum Zeitpunkt der Untersuchung stand VCF nur für das Jahr 2001 zur Verfügung. Mittlerweile (Jahr 2009) ist VCF für die Jahre 2000 bis 2005 verfügbar. Trotz der unterschiedlichen Pixelgröße (die geokodierten ERS Daten hatten eine Pixelgröße von 50x50 m²) zeigte der Vergleich von Kohärenz und den Kronenbedeckungsangaben in VCF eine deutliche Korrelation. Der beobachtete enge Zusammenhang von ERS-1/2 Tandem Kohärenz und VCF deutete an, dass es mithilfe des VCF Produkts möglich sein sollte, die räumliche und zeitliche Variabilität der Kohärenz zu beschreiben, d.h. die unbekannt Parameter des IWCM zu bestimmen. Grundgedanke der synergetischen

Nutzung des VCF Produkts war, mittels einfacher Schwellwerte für den VCF Kronenbedeckungsgrad in den ERS-1/2 Tandem Kohärenz- und Intensitätsbildern offene und dicht bewaldete Gebiete zu identifizieren und mittels einfacher statistischer Maße der Zentraltendenz (der Modus erwies sich als optimal) die Parameter γ_{gr} , γ_{veg} , σ_{gr}^0 und σ_{veg}^0 abzuleiten.

Bezüglich der Schätzung der Parameter γ_{gr} und σ_{gr}^0 war die grundlegende Annahme der VCF-basierten Parameterschätzung, dass es möglich ist von den über offenem Gelände gemessenen Kohärenzen und Intensitäten auf die Kohärenz und Intensität zu schließen, die über Waldboden gemessen würde (wäre dieser nicht von Bäumen verdeckt). Im Fall der Parameter γ_{veg} und σ_{veg}^0 war die Grundannahme, dass es möglich ist von den über dichtem Wald gemessenen Kohärenzen und Intensitäten auf die Kohärenz- und Rückstreuungseigenschaften von komplett undurchlässigen Baumkronen zu schließen. Die über (laut VCF) dichtem Wald gemessenen Kohärenzen und Rückstreuintensitäten spiegeln eine unvollständige Kronenbedeckung wieder, d.h. um die Parameter γ_{veg} und σ_{veg}^0 bestimmen zu können, müssen die Boden- und Volumendekorrelationsanteile in den Kohärenz- und Intensitätsmessungen über (laut VCF) dichtem Wald bestimmt werden. Der Vergleich der Stammvolumenangaben aus der Sibirischen Forstinventur und den VCF Kronenbedeckungsangaben zeigte, dass Wälder mit maximalem Kronenschluss in der VCF Karte - der Maximalwert in Sibirien und Nordostchina lag bei etwa 80 % - ein Stammvolumen von mindestens 200 m³/ha aufweisen. Eine Sensitivitätsanalyse mittels IWCM zeigte, dass für Stammvolumenbereiche über 200 m³/ha nur geringe Änderungen in den Boden- und Volumendekorrelationsanteilen zu erwarten sind. Lediglich im Fall sehr langer Basislinien über 200 m können nennenswerte Variationen der Volumendekorrelation auftreten. Aufgrund der geringen zu erwartenden Änderungen der Boden- und Volumendekorrelationsanteile für Stammvolumina über 200 m³/ha im Fall von Tandempaaaren, die mit Basislinien < 200 m aufgenommen wurden, konnten die Parameter γ_{veg} und σ_{veg}^0 bestimmt werden, indem angenommen wurde, dass die über Wäldern mit maximalem Kronenschluss (laut VCF) gemessenen Kohärenzen und Intensitäten ein Stammvolumen von mindestens 250 m³/ha widerspiegeln. Lediglich für Tandempaare, die mit langen Basislinien deutlich über 200 m aufgenommen wurden, könnten Angaben über die Stammvolumenverteilung in Wäldern mit maximalem Kronenschluss in den VCF-Karten vonnöten sein, um die Modellparameter bestimmen zu können. Da keines der Testgebiete von einem Tandempaar abgedeckt wurde, dass mit langer Basislinie aufgenommen wurde, war eine Überprüfung der Bestimmungsgenauigkeit von γ_{veg} für Tandempaare, die mit langen Basislinien aufgenommen wurden, nicht möglich.

Der Transmissivitätskoeffizient β konnte nicht mittels VCF bestimmt werden. Die Bestimmung des Parameters mithilfe der sibirischen ERS-1/2 Tandem- und Inventurdaten zeigte jedoch, dass der Zusammenhang von Stammvolumen und Transmissivität des Waldes gegenüber den Radarsignalen im Fall stabiler Aufnahmebedingungen mit hoher Waldbodenkohärenz nur geringe Variationen zwischen den Tandempaaren und den verschiedenen Testgebieten aufwies. Im Fall instabiler Aufnahmebedingungen mit niedriger Waldbodenkohärenz führte die Bestimmung von β allerdings zu physikalisch bedeutungslosen Ergebnissen. Die starke Streuung der Kohärenz gegenüber dem Stammvolumen (wahrscheinlich durch kleinräumige Variationen in den Aufnahmebedingungen) und das insgesamt niedrigere Kohärenzniveau, welches eine größere Unsicherheit in der Kohärenzschätzung nach sich zieht, könnten die Gründe hierfür gewesen sein. Ein rein empirisches Modell (Wagner et al., 2003) konnte im Fall instabiler Aufnahmebedingungen besser an den

Kohärenz-Stammvolumen Trend angepasst werden als das IWCM. Dieses empirische Modell wies eine ähnliche Grundstruktur auf wie das IWCM. Es berücksichtigte jedoch nicht die möglichen Volumendekorrelationseffekte. Ein fester Wert für den Parameter des empirischen Modells, der (rein mathematisch) dem Transmissivitätskoeffizienten des IWCM entspricht, erlaubte eine, wenn auch grobe, Charakterisierung des generellen Trends der Kohärenz als Funktion des Stammvolumens.

Die Gültigkeit der Grundannahmen des VCF-basierten Modelltrainings wurde für die Testgebiete in Sibirien überprüft. Als Referenz dienten die Modellparameter, die mithilfe der Stammvolumenangaben in den Inventurdaten geschätzt wurden. Zuerst wurde das VCF-basierte Training auf Bild-Basis getestet, d.h. die Parameter wurden einmal für jedes Tandempaar (entspricht einer Fläche von $100 \times 100 \text{ km}^2$) bestimmt. Der Vergleich der VCF- mit den Inventurdaten-basierten Modellparameterschätzungen ergab ein zwiespältig Bild. Eine hohe Übereinstimmung der geschätzten Parameter wurde für Tandempaare erreicht, die unter gefrorenen Bedingungen aufgenommen wurden. Deutliche Unterschiede zwischen den Schätzungen für γ_{gr} und σ_{gr}^0 mittels VCF und den Inventurdaten mussten vor allem für die Tandempaare, die bei instabilen Aufnahmebedingungen aufgenommen wurden, festgestellt werden. Die VCF- und Inventurdaten-basierten Schätzungen für γ_{veg} und σ_{veg}^0 zeigten hingegen eine deutlich bessere Übereinstimmung. Die Übereinstimmung für alle Parameter konnte verbessert werden, indem die VCF-basierte Modellparameterschätzung auf das Gebiet der Testgebiete beschränkt wurde. Dies zeigte, dass räumliche Variationen der Aufnahmebedingungen innerhalb eines Kohärenz- bzw. Intensitätsbildes eine erhebliche Rolle spielten. Diese räumlichen Variationen waren am deutlichsten erkennbar für Tandempaare, die unter ungefrorenen Bedingungen aufgenommen wurden. Doch auch unter gefrorenen Bedingungen konnten leichte räumliche Variationen festgestellt werden. Die insgesamt gute Anpassung der Modelle an die Messungen über den Testgebieten bestätigte weitestgehend die Grundannahmen des VCF-basierten Modelltrainings. Lediglich im Fall des Parameters σ_{gr}^0 schien die Annahme, dass es möglich ist von den Intensitätsmessungen über vegetationsfreien Flächen auf die Waldbodenintensität zu schließen, nicht immer erfüllt zu sein. Unter ungefrorenen Bedingungen wurde σ_{gr}^0 in mehreren Fällen deutlich überschätzt. Dies deutete auf ein höheres Bodenfeuchteniveau über vegetationsfreien Flächen im Vergleich zu Waldboden hin. Da dies vor allem unter feuchten Bedingungen nach Regenfällen zu beobachten war, könnte eine Erklärung hierfür sein, dass Evapotranspiration und Interzeption systematische Bodenfeuchteunterschiede zwischen Waldboden und vegetationsfreien Flächen verursacht haben.

Ein weiteres Kapitel beschäftigte sich mit dem Einfluss der Topographie auf die ERS-1/2 Tandem Kohärenz. Es ist bekannt, dass topographische Effekte in Kohärenzbildern die Information über die Waldbedeckung erheblich stören können (Castel et al., 2000). Der topographiebedingte Kohärenzverlust hat mehrere Ursachen. Ein Grund liegt in der Frequenzverschiebung, die die Radarsignale mit der Reflektion an der Erdoberfläche erfahren. Da diese Frequenzverschiebung vom Einfallswinkel der Radarwellen abhängt, erfahren die Radarmessungen aus leicht unterschiedlichen Perspektiven, d.h. mit einer gewissen Basislinie, eine unterschiedliche Frequenzverschiebung (Gatelli et al., 1994). Diese relative Frequenzverschiebung hängt nicht nur von der Basislinie, sondern auch von der lokalen Hangneigung ab. Die nicht übereinstimmenden Anteile der Frequenzbänder beider für die Generierung des Interferogramms genutzten SAR Bilder führen zu einem Verlust an Kohärenz. Eine die Bandbreite der Signale überschreitende relative Frequenzverschiebung führt zu einem kompletten Verlust der Kohärenz.

Solange die relative Frequenzverschiebung die Bandbreite der Signale nicht überschreitet, kann die Kohärenz durch eine Entfernung der nicht übereinstimmenden Anteile der Frequenzbänder wiederhergestellt werden. Dieser sogenannte ‚commonband filter‘ (Gatelli et al., 1994) muss jedoch ohne exakte Informationen über die lokale Topographie eine Frequenzverschiebung annehmen, die der über flachem Untergrund entspricht. Über Gebirge führt dies dazu, dass nicht übereinstimmende Anteile der Frequenzbänder in den Daten verbleiben und somit die Kohärenz nicht vollständig wiederhergestellt wird. Dieser Effekt zeigte sich deutlich in den ERS-1/2 Tandem Kohärenzbildern, die über den Gebirgsregionen Nordostchinas aufgenommen wurden. Besonders stark fiel der Verlust der Kohärenz über Hängen aus, die zum Sensor hin geneigt waren. Auf sensorabgewandeten Hängen blieb die Kohärenz hingegen bis zu Basislinien von etwa 100 m weitestgehend erhalten. Für alle Hänge steiler als 5 bis 10° (abhängig von der Basislinie) nahm der topographiebedingte Verlust der Kohärenz mit der Länge der Basislinie zu. Weitere topographiebedingte Kohärenzverluste konnten auf die unvollständige Kompensation des topographischen Phasenanteils im Interferogramm vor der Kohärenzschätzung zurückgeführt werden. Prinzipiell zeigten vegetationsfreie und bewaldete Flächen sehr ähnliche topographische Effekte in der Kohärenz, d.h. auch über Wald ist der Kohärenzverlust durch nicht übereinstimmende Anteile der Frequenzbänder nach dem ‚common band filtering‘ der wichtigste Effekt. Weitere topographiebedingte Effekte im Zusammenhang von Kohärenz und Stammvolumen könnten mit der Abhängigkeit des Kronenbedeckungsgrads oder der Volumendekorrelation vom Einfallswinkel des Radarsignals zusammenhängen. Diese konnten jedoch mangels akkurater Forstinventurdaten für Wälder in den Gebirgen Nordostchinas nicht untersucht werden. Die Konsequenz topographiebedingter Kohärenzverluste ist, dass über steilen Hängen, abhängig von der Länge der Basislinie und der Ausrichtung der Hänge, eine Stammvolumenbestimmung nicht möglich ist. Im Fall der ERS-1/2 Tandemdaten für Nordostchina war dies für fast ein Drittel der abgedeckten Gesamtfläche von ungefähr 1,5 Mio. km² der Fall.

Anhand des ERS-1/2 Tandemdatensatzes für Nordostchina wurde eine Forstkarte erstellt. Dazu wurde für jedes der 223 Kohärenzbilder das VCF-basierte Modelltraining durchgeführt. Das mittels VCF trainierte Modell wurde invertiert, um aus der Kohärenz das Stammvolumen zu berechnen. Da etwa ein Drittel der 223 Tandempaare unter instabilen Wetter- und Umweltbedingungen aufgenommen wurde, konnten Stammvolumenklassen über 100 m³/ha nicht zuverlässig unterschieden werden. Deshalb wurden die geschätzten Stammvolumina in die Klassen 0-20, 20-50, 50-80 und >80 m³/ha zusammengefasst. Die Klassifikationsgenauigkeit konnte lediglich für die sibirischen Testgebiete bestimmt werden. Die Genauigkeitsanalyse zeigte hohe Übereinstimmungen mit den Inventurdaten für die Klassen 0-20 und >80 m³/ha, solange keine räumlichen Variationen der Aufnahmebedingungen innerhalb der Kohärenzbilder auftraten; diese traten vor allem in Kohärenzszenen auf, die unter feuchten Bedingungen aufgenommen wurden. Die Übereinstimmung der Klassen 20-50 und 50-80 m³/ha mit den Inventurdaten war hingegen immer gering. Diese niedrige Übereinstimmung für die mittleren Stammvolumenklassen war teilweise eine Konsequenz ungenauer Stammvolumenangaben in den Inventurdaten. Die Übereinstimmung der produzierten Stammvolumenkarten mit den Inventurangaben verbesserte sich deutlich mit der Berücksichtigung der Möglichkeit ungenauer Stammvolumenangaben aus der Inventur. Unter Berücksichtigung fehlerhafter Inventurdaten ergaben sich für die Tandempaare, die unter ungefrorenen Bedingungen aufgenommen wurden, Kappa-Koeffizienten der Übereinstimmung von mindestens 0,5 und für Tandempaare, die unter gefrorenen Bedingungen aufgenommen wurden, von mindestens 0,7. Es zeigte sich jedoch auch, dass

für Bestände mit niedrigem Bestockungsgrad deutlich niedrigere Genauigkeiten erreicht wurden.

Der Nutzen der produzierten Forstkarte Nordostchinas ist mangels Validierung unklar. Die Ergebnisse für die Testgebiete in Zentralsibirien deuteten an, dass die Karte derzeit besser als Indikator für dichte und spärliche Bewaldung interpretiert werden sollte. Mit dem VCF-basierten Modelltraining wurde jedoch eine Methodik entwickelt, die auch für andere Radardatentypen, insbesondere der L-Band SAR- und InSAR-Daten des PALSAR Sensors an Bord des japanischen Advanced Land Observing Satellites ALOS oder der C-band SAR- und InSAR-Daten des nächsten europäischen Radarsatelliten SENTINEL-1, von hohem Nutzen sein könnte.

Table of contents

ZUSAMMENFASSUNG	III
LIST OF ACRONYMS AND SYMBOLS	XV
CHAPTER 1 - INTRODUCTION	1
1.1 FORESTS IN NORTHEAST CHINA: ECOLOGICAL AND SOCIOECONOMIC CONTEXT	1
1.2 FOREST STEM VOLUME RETRIEVAL BY MEANS OF ERS-1/2 TANDEM COHERENCE.....	3
1.3 SCOPE OF THE THESIS.....	6
1.4 OUTLINE OF THE THESIS	8
CHAPTER 2 - SAR AND INSAR REMOTE SENSING.....	9
2.1 BASICS OF RADAR REMOTE SENSING	9
2.1.1 <i>The radar signal</i>	9
2.1.2 <i>Radar cross section</i>	12
2.1.3 <i>Speckle</i>	13
2.1.4 <i>Radar scattering from forested terrain</i>	15
2.1.5 <i>Stem volume and biomass mapping with C-band SAR intensity</i>	22
2.2 SAR INTERFEROMETRY.....	23
2.2.1 <i>Interferogram and interferometric phase</i>	24
2.2.2 <i>Coherence</i>	26
2.2.3 <i>Coherence over land surfaces</i>	29
2.2.4 <i>Stem volume and biomass retrieval by means of C-band repeat-pass coherence</i>	32
CHAPTER 3 - STUDY AREA, GROUND AND SATELLITE DATA	35
3.1 CHINESE TEST SITES	35
3.1.1 <i>Northeast China</i>	35
3.1.2 <i>Test sites in Northeast China</i>	36
3.1.2.1 <i>Daxinganling</i>	37
3.1.2.2 <i>Xiaoxinganling</i>	38
3.1.2.3 <i>Changbai</i>	38
3.2 CENTRAL SIBERIAN TEST SITES	39
3.2.1 <i>Bolshe-Murtinsky</i>	40
3.2.2 <i>Chunsky</i>	41
3.2.3 <i>Primorsky</i>	41
3.3 FOREST STRUCTURAL CONSIDERATIONS	42
3.4 SATELLITE DATA	49
3.4.1 <i>ERS-1/2 tandem data</i>	49
3.4.2 <i>Additional Earth Observation data</i>	51
3.5 METEOROLOGICAL DATA	52
CHAPTER 4 - SAR & INSAR MEASUREMENTS AT THE TEST SITES.....	57
4.1 SIBERIAN TEST SITES	57
4.2 CHINESE TEST SITES	63
4.3 SUMMARY	66
CHAPTER 5 - COHERENCE MODELING AND MODEL TRAINING.....	68
5.1 MODELING OF ERS-1/2 TANDEM COHERENCE AS FUNCTION OF STEM VOLUME	68
5.2 MODEL TRAINING.....	72
5.2.1 <i>Inventory data-based model training</i>	72
5.2.2 <i>The SIBERIA model training approach</i>	73
5.2.3 <i>VCF-based model training</i>	74
5.2.3.1 <i>Relationship between ERS-1/2 tandem coherence and VCF tree cover</i>	75

5.2.3.2 <i>Exploiting VCF for model training</i>	78
5.2.3.3 <i>Parameter estimation with VCF</i>	79
5.2.3.4 <i>Forest transmissivity</i>	81
5.2.3.5 <i>Derivation of γ_{veg}, γ_{∞} and σ_{veg}^{θ}</i>	87
5.3 SUMMARY	90
CHAPTER 6 - TOPOGRAPHIC EFFECTS IN SAR AND INSAR IMAGERY	92
6.1 TOPOGRAPHIC EFFECTS IN ERS INTENSITY	92
6.2 TOPOGRAPHIC EFFECTS IN ERS-1/2 TANDEM COHERENCE.....	95
6.3 IMPLICATIONS WITH RESPECT TO A VCF-BASED MODEL TRAINING	100
CHAPTER 7 - MODEL TRAINING RESULTS	101
7.1 SIBERIA MODEL TRAINING APPROACH.....	101
7.2 VCF-BASED MODEL TRAINING FOR THE ERS-1/2 TANDEM DATA OF SIBERIA.....	103
7.2.1 <i>VCF-based model training on a frame-by-frame-basis</i>	103
7.2.2 <i>Regionalized VCF-based model training</i>	109
7.3 VCF-BASED MODEL TRAINING FOR THE ERS-1/2 TANDEM DATA OF NORTHEAST CHINA.....	114
7.4 SUMMARY	120
CHAPTER 8 - LARGE-AREA FOREST STEM VOLUME MAPPING	123
8.1 STEM VOLUME RETRIEVAL	123
8.2 FOREST STEM VOLUME MAPPING.....	124
8.3 CREATION OF A FOREST STEM VOLUME MAP FOR NORTHEAST CHINA	131
CHAPTER 9 - CONCLUSIONS.....	134
9.1 SUMMARY AND DISCUSSION	134
9.2 OUTLOOK.....	138
REFERENCES.....	141
APPENDIX A.....	158

List of Acronyms and Symbols

AVHRR	Advanced Very High Resolution Radiometer
CAF	Chinese Academy of Forestry
DEM	Digital Elevation Model
DWD	Deutscher Wetterdienst
ERS	European Remote Sensing Satellite
ESA	European Space Agency
FAO	and Agriculture Organization of the United Nations
FID	Forest Inventory Data
FIP	Forest Inventory and Planning
GAMMA RS	GAMMA Remote Sensing Research and Consulting AG
HH	Transmission and reception of radar signals in horizontal polarization
HV	Transmission in horizontal and reception in vertical polarization
InSAR	Interferometric Synthetic Aperture Radar
IPCC	Intergovernmental Panel on Climate Change
IWCM	Interferometric Water Cloud Model
JERS	Japanese Earth Resources Satellite
LiDAR	Light Detecting and Ranging
MODIS	Moderate Resolution Imaging Spectroradiometer
MOST	Ministry of Science and Technology, China
MPI	Local Forest Management Planning Inventory
NFI	National Forest Inventory
NSIDC	National Snow and Ice Data Center
SAR	Synthetic Aperture Radar
SIBERIA	SAR Imaging for Boreal Ecology and Radar Interferometry Applications
SIR	Shuttle Imaging Radar
SRTM	Shuttle Radar Topography Mission
UTC	Coordinated Universal Time
VCF	Vegetation Continuous Field product
VV	Transmission and reception of radar signals in vertical polarization
VH	Transmission in vertical and reception in horizontal polarization
WCM	Water Cloud Model
WMO	World Meteorological Organization
A	Amplitude
B_n	Normal baseline
B_p	Parallel baseline
C_A	Pixel area normalization factor
CI	Confidence interval
D	Tree density
DBH	Diameter at breast height
ENL	Equivalent Number of Looks
G	Antenna gain
I	Intensity
L	Independent Number of Looks
L_A	Antenna size (in azimuth)
ML	Maximum Likelihood
N	Number, counts
NDVI	Normalized Difference Vegetation Index
NDWI	Normalized Difference Water Index

P_t	Transmitted power
P_r	Received power
R	Slant range distance
R^2	Coefficient of determination
RCS	Radar Cross Section
RMS	Root Mean Square
RMSE	Root Mean Square Error
RS	Relative stocking
SD	Standard error
SDI	Stand Density Index
SWE	Snow Water Equivalent
T_{tree}	Tow-way tree transmissivity
T_{for}	Forest transmissivity
V	Stem volume in m^3/ha
V_{eq}	Equivalent stem volume of dense forest, delineated by means of MODIS Vegetation Continuous Field tree cover
W	Signal bandwidth
d_s	Depth of a snow layer
f	Frequency
f_0	Carrier frequency
f_z	tree stem form factor
$g(t)$	Chirp function
h	Tree height
h_a	Height of ambiguity
h_i	Signal path length through the canopy
h_{sd}	Standard deviation of surface height variation
k	Wave number
$p(t)$	Pulse function
p_0	Overall accuracy (percentage of correctly classified polygons)
p_e	Expected chance agreement
r	Pearson correlation coefficient
u	Complex SAR image
α	two-way tree signal attenuation
α_s	local slope
β	forest transmissivity coefficient
β^0	Radar brightness
γ	Complex interferometric coherence
$ \gamma $	Coherence
$\left \gamma_{ML} \right $	Maximum Likelihood estimate of coherence
γ_0	Coherence of open ground
γ_∞	Coherence of dense forest canopies
γ_{for}	Forest coherence
γ_{gr}	IWCM parameter for forest floor coherence
γ_{veg}	IWCM parameter for coherence over forest with opaque canopy
γ_{VCF}	Dense forest coherence estimated by means of MODIS Vegetation Continuous Field tree cover
Δf	Frequency shift
$\Delta \rho$	Atmospheric path delay difference

$\Delta\eta$	Coherent movements
$\Delta\phi$	InSAR phase
$\Delta\Phi$	InSAR phase difference between two points
Δz	Height difference
ΔR	Slant range difference
δ	Penetration depth
ε	White noise process
ε_r	Relative dielectric permittivity
ε_c	Dielectric permittivity
ε_0	Dielectric permittivity of free space
η	Area fill factor
θ	Incidence angle
θ_i	Local incidence angle
ψ	Projection angle
κ	Kappa coefficient
κ_w	Weighted kappa coefficient
λ	Wavelength
σ	Radar Cross Section
σ^0	Backscatter coefficient (sigma nought)
σ^0_{for}	Forest backscatter coefficient
σ^0_{gr}	WCM parameter for ground backscatter
σ^0_{veg}	WCM parameter for intensity over forest with zero transmissivity
σ^0_{VCF}	Dense forest intensity estimated by means of MODIS Vegetation Continuous Field tree cover
σ_v	Volumetric backscatter coefficient
σ_{ve}	Volumetric backscatter coefficient for temporally stable scatterers
σ_ε	Standard deviation of a Gaussian white noise process ε
σ_ϕ	Uncertainty in phase estimation
σ_γ	Standard error of coherence estimation
ϕ	SAR phase
ϕ_{scatter}	SAR phase component due to a set of distributed scatterers in a pixel
ϕ_t	Topographic InSAR phase
Φ	InSAR phase
Φ_{snow}	Interferometric phase shift due to snow
Ψ	Projection angle
Ψ_a	Beamwidth
Ψ_{eff}	Effective Beamwidth
ω	InSAR geometry coefficient

Chapter 1 - Introduction

1.1 Forests in Northeast China: Ecological and socioeconomic context

The forests of Northeast China represent, together with those in the Southwest, the main wood supply for China, being important for the economic development of a highly wood demanding industry as well as for the livelihood of the Chinese people, e.g. as fuel-wood. The rapid development of the Chinese population and industry has increased in the last decades the pressure on forest land in China. According to the 'Food and Agriculture Organization' Forest Resource Assessment (FAO, 2001), China ranks fifth in the world considering forest area and seventh when considering stem volume. Massive logging and expansion of agricultural areas to forest or arid grassland areas have changed the Chinese landscape and the quality of its natural environment tremendously. Desertification (Yang et al., 2007), erosion, a higher intensity of forest fires because of an active suppression of fire over several decades (Chang et al., 2008) as well as a loss of biodiversity are some of the prominent consequences of this development.

The immoderate exploitation of Northeast China's forest resources was first promoted with the construction of the Russian railway at the end of the 19th century and the Japanese takeover of Manchuria, i.e. the Northeastern provinces, in the early 20th century and reached its peak during the 'Great Leap Forward (1958-1960)' when the government boosted intense logging, mainly for the provision of fuel for backyard steel furnaces (Chen et al., 2007), and the conversion of forest, marshland, grassland and fallow land to farmland. The consequences of this policy were most pronounced in China's Northeast, which represents the 'grain base' of China (Gao et al., 2006) as the main producer of soybean and wheat.

As recently as in the 1980s the Chinese government tried to counteract the emerging environmental consequences of this policy, introducing a number of programs which aimed at increasing the wood supply from Chinese forests as well as to mitigate the ecological consequences of the immoderate forest exploitation. This comprised a change in the agricultural management, departing from a purely quantitative paradigm (Gao et al., 2006), and a huge plantation program which since 1980 has made China the country with the largest plantation area worldwide. With the 'Natural Forest Protection Program', introduced in 1998, the logging of natural forest was mostly forbidden in order to allow for regeneration. Plantations of fast growing tree species are now designated to cover the Chinese wood demand. Even though increases in forest area (FAO, 2006; Zhao & Zhou, 2005) have been reported since the beginning of the protection and plantation activities, the condition of the Chinese forests, in particular in the Northeast, is still considered alarming in both ecological and economic perspective.

Currently, the forest resources in China are not considered adequate to meet the need of the Chinese people and industry (Bull & Nilsson, 2004; Li et al., 2004). A consequence is the increasing need for imported wood, mainly from Russia (Lu, 2004; Nemilostiv & Reymer, 2007). The current state of the Chinese forests was summarized in Li et al. (2004) as follows:

- 1) Insufficient total volume: Even though China hosts the fifth largest forest area of the world, the average growing stock of 78 m³/ha is low (Li et al., 2004; Liu,

2005); everything below 100 m³/ha is usually considered unproductive (Bull & Nilsson, 2004).

- 2) Natural forests are of low quality with 70 % of the forest area being young or middle age forest. The proportion of mature and over-mature forest still declines (Yin, 1998; Li et al., 2006) because of extensive illegal logging (Xu et al., 2003 as quoted in Bull & Nilsson, 2004). The residual mature and over-mature forest will likely be restricted to remote areas soon.
- 3) The growth rates of the plantations of about 3-3.5 m³/ha/year fall by far below the expected growth rates of 8-18 m³/ha/year (Bull & Nilsson, 2004). These low growth rates trace back to the planting of a few single species (mainly fast growing species like larch, pine and to a lesser extent also poplar and birch), which are susceptible to diseases, and bad seedling quality with low survival rate (Liu, 2005). According to model simulations, the planting of slower growing hardwood species would reduce these problems and result in a higher productivity (Thomas et al., 2007). Other modeling results suggest active thinning as effective way to improve yield and to lower the susceptibility to diseases (Lei et al., 2007). Currently, the management status of most plantations is low (Li et al., 2004) and the planned 6.39 million hectares, not only in the Northeast, of new plantations for the period between 2001 and 2010 comprise mostly conventional fast growing species (Thomas et al., 2007).

The loss of mature and over-mature forests on one side and the badly growing plantations on the other side lead to predictions that a large fraction of forest enterprises will have to cease production of timber in the foreseeable future (Rozelle et al., 1997 as quoted in Bull & Nilsson, 2004). The statistics about forest area, growing stock and forest types published in different official reports or scientific studies differ considerably though. These differences were pointed out in Bull & Nilsson (2004). When considering the reported discrepancies in forest statistics, it is obvious that there is a need for repeated and consistent measurements in order to provide decision makers an appropriate decisional base. Not to forget, China has signed the Kyoto Protocol on August 30th 2002. Even though not one of the Annex-I countries, China can participate in Clean Development Mechanisms projects, for which, if related to afforestation and reforestation, transparent forest resource assessments are crucial (Chen et al., 2007).

Most of the described developments are valid for the Chinese forests in general. Some specific characteristics of the forests in the Northeast, however, have been of interest in particular. Northeast China represents a transitional zone between the temperate and the boreal zone and hosts all the major forest types of Northeast Asia. The climate changes latitudinally from warm temperate to cool temperate and the forests change from deciduous broadleaf forest, needle-leaf and broadleaf mixed forest (abbr. NBMF) to boreal forest. The climax vegetation is mixed broadleaved Korean pine forest for latitudes below 50° and Dahurian larch forest above 50° North (Chen & Li, 2003; Qian et al., 2003), which only dominates under extreme continental climate conditions with very cold winters (Krestov, 2003). A significant climatic control of the structure of these forests has been reported in Wang et al. (2006a, 2006b) and a substantial effect of climate change on the Northeast Chinese forests has been predicted (Ni, 2002; Chen, 2002). Since Northeast China has experienced the largest increase in temperature in China over the last decades and also a drier and warmer future climate has been predicted (Ding & Dai, 1994 as quoted in Tan et al., 2007), the development of

Northeast China's forests are of high interest for vegetation modelers. The forests represent a showcase scenario for forest development under the premises of global climate change and anthropogenic disturbance (Chen et al., 2003; Wang et al., 2006; Xiaodong & Shugart, 2005; Leng et al., 2008). The models predict, for instance, a significant loss of the potential growing area for Dahurian larch (Leng et al., 2008) and a change in species composition in the mixed broadleaf Korean pine forests (Chen et al., 2003).

Thus, the forests of Northeast China represent a vulnerable ecosystem, highly threatened by recent climatic and socioeconomic developments. The existing information about the region is not sufficient and, as the disagreeing statistics show, the National Forest Inventory or the Local Forest Management Planning Inventory, the main inventory levels in China (Pang et al., 2005), can hardly fill this gap. The need for information about quantity and quality of forests is obvious and remote sensing as an alternative information source, capable of delivering large area information on a regular basis, an obvious choice.

1.2 Forest stem volume retrieval by means of ERS-1/2 Tandem coherence

One of the most desired forest parameters, in particular in the context of Global Climate Change, is forest biomass as forests store large amounts of carbon in their biomass (Houghton, 2005). National forest inventories usually do not include biomass, which is defined as the fraction of dry organic matter in trees. Therefore, forest biomass assessments utilize the stem volume measurements for a high number of forest sample plots, i.e. circles of several meters diameter for which foresters have measured the main tree parameters. The definition of forest stem volume differs from country to country and ranges from total volume of all tree stems per hectare including bark to different utilization levels of stem volume excluding bark, stump, stem top and very thin trees (Wulder et al., 2008). The knowledge about stem volume allows estimating the total forest biomass (above- and belowground) through forest type and forest age specific conversion factors (IPCC, 2006). The results of a forest biomass assessment for China that utilized the National Forest Inventory (NFI) stem volume measurements and volume-to-biomass conversion factors have been published in Fang et al. (2001).

A biomass assessment based on forest inventory data is time consuming, costly and only feasible for countries with an established forest inventory system. The different stem volume definitions between the countries or even between provinces further complicate a consistent biomass assessment. In contrast, remote sensing provides repeated measurements in short intervals for almost every place on the Earth. Wall-to-wall mapping of forests and forest biophysical parameters in Northeast China has yet been conducted with medium resolution optical remote sensing data, i.e. with the data of the Advanced Very High Resolution Radiometer AVHRR or SPOT-4 VEGETATION missions with 1 km resolution (Xiao et al., 2002; Tan et al., 2007). Based on a multitemporal analysis of spectral band ratios like the widely exploited Normalized Difference Vegetation Index (abbr. NDVI) or the Normalized Difference Water Index (abbr. NDWI), forest types, percentage of forest cover and biomass were classified. No accuracy assessment was reported for the biomass map yet. When validated, this product may be of interest for regional- to country-level biomass reporting. Wall-to-wall biomass maps in a scale of interest for local forest management authorities do not exist.

A remote sensing data type that has the potential to close this gap is spaceborne active radar. Radar is the abbreviation for 'RADio Detection And Ranging' and denotes active sensors that transmit and receive electromagnetic waves with wavelengths in the microwave range of ~1 mm to 1 m. Modern so-called Synthetic Aperture Radars (abbr. SAR) allow the mapping of the Earth's surface from space with resolutions in the range of few meters to 100 m, dependent on the mode of acquisition. The intensity of the radar echo that is received at the sensor, after travelling through the atmosphere and being scattered back on the ground, contains information about the geometry (size, shape, orientation) and dielectric properties of the illuminated object and can be used to map the Earth's land cover as well as the ocean surface. The phase of the echo is related to the distance between the sensor and the backscattering object and has led to applications in the field of topographic measurement. When having acquisitions from two identical SAR sensors that illuminated the same spot on the Earth from slightly different perspectives, the two images can be combined to compute a so-called interferogram. Interferograms allow the generation of Digital Elevation Models (DEM). The first publications about interferometric SAR measurements (abbr. InSAR) were released in the 1970s and 80s (Graham, 1974; Goldstein & Zebker, 1987). After a rather decelerated start of this technique, the first spaceborne radar mission of the European Space Agency (ESA), the 'European Remote Sensing Satellites' ERS-1 (launched in 1991) and ERS-2 (launched in 1995), pushed the development of interferometric techniques for the mapping of topography as well as displacements or mass movements with the newer techniques of Differential Interferometry and Persistent Scatterers, which can be applied when more than two acquisitions are available (Feretti et al., 2007). Between 1995 and 2000, both satellites flew in an interferometric constellation with one-day time lag between the ERS-1 and ERS-2 overpasses. The radar instruments onboard the satellites were identical and transmitted and received microwaves with a wavelength of 5.67 cm. This wavelength is referred to as the C-band.

Although SAR interferometry was initially intended for topographic mapping, it represents an interesting tool for forest mapping (see review in Balzter et al., 2001). One type of application is the determination of tree height by means of the interferogram as forests appear as topographic features in the interferograms (e.g. Kellndorfer et al., 2004; Balzter et al., 2007). Another type of application utilizes the interferometric coherence, which is a measure for the stability of the backscattering conditions/geometry between the images used to form the interferogram. The quality of the topographic information in the interferogram is a function of coherence. High coherence means good and low coherence means weak topographic information in the interferogram. Interferometric C-band repeat-pass coherence (repeat-pass means that the images were acquired with a certain time lag) was observed to decrease with increasing forest cover which in turn means that the quality of the topographic information in the interferograms is lower over densely forested areas. This decrease in coherence can be exploited to map forest stem volume or biomass (Askne et al., 1995, 1996, 1997; Koskinen et al., 2001; Santoro et al., 2002, 2007; Gaveau et al., 2003; Pulliainen et al., 2003; Wagner et al., 2003; Engdahl et al., 2004; Askne & Santoro, 2005a, 2007).

Stem volume retrieval by means of ERS-1/2 tandem coherence has been discussed mainly for the forests in the boreal zone (Hyypä et al., 2000; Manninen et al., 2000; Koskinen et al., 2001; Fransson et al., 2001; Santoro et al., 2002, 2007; Askne et al., 2003; Pulliainen et al., 2003; Engdahl et al., 2004; Askne & Santoro, 2005, 2007a, 2007b). For managed boreal forest in Scandinavia, stem volume retrieval by means of ERS-1/2 tandem coherence has been found to be possible with accuracies in the range

of the accuracy of ground surveys (Santoro et al., 2002), in particular when having a multitemporal stack of images and combining the single image retrieval results. The retrieval accuracy possible with ERS-1/2 tandem coherence exceeds that of SAR intensity measurements with wavelengths between 3 and 23 cm; i.e. the wavelengths that were available from spaceborne SAR missions yet (Hyypä et al., 2000; Askne et al., 2003). A large number of publications have shown that SAR intensity measurements in these wavelengths are somewhat correlated to forest stem volume and biomass but a considerable response of the measurements to, for instance, soil moisture variations (Pulliainen et al., 1994; Rignot et al., 1994; Wang et al., 1995) and an early signal saturation with respect to increasing forest stem volume or biomass present severe limitations (Le Toan et al. 1992; Kasischke et al. 1994; Dobson et al. 1995b; Kasischke et al., 1995; Imhoff, 1995; Harrel et al., 1995; Pulliainen et al., 1994, 1996, 1999; Fransson & Israelsson, 1999; Kurvonen et al., 1999; Quegan et al., 2000; Santoro et al., 2006). With SAR instruments using wavelengths between 3 and 23 cm, biomass levels above 50 to 100 t/ha can hardly be distinguished. A spaceborne SAR instrument with a long wavelength of ~70 cm, which would not experience such early saturation (Le Toan et al., 1992; Rignot et al., 1995; Ranson et al., 1994, 1997; Saatchi et al., 2007), may be launched in the next decade in the frame of ESA's Earth Explorer Missions (Bensi et al., 2007) but yet 23 cm is the maximum wavelength that is available from spaceborne SAR missions.

Saturation of ERS-1/2 tandem coherence generally occurs at higher stem volumes or biomass levels and the biophysical forest information in coherence is generally less distorted by, for instance, soil moisture effects compared to short wavelength SAR intensity measurements (Askne et al., 2003). However, saturation of coherence is a complex phenomenon that depends on the meteorological conditions in the period of the sensor overpasses and the orbital constellation of the interferometric acquisitions, i.e. the spatial distance between both sensors when acquiring over a certain area.

This brings us to a common demur against the use of interferometric coherence. The forest biophysical information in repeat-pass coherence traces back to the higher temporal stability of the backscatter from the forest floor compared to that from the forest canopies for which the scattering geometry can change within very short periods due to wind induced movements of the branches (Narayanan et al., 1992, 1994). Considerable differences in coherence for both, forest floor and canopy, arise between interferometric image pairs that were acquired in different seasons (e.g. under frozen or unfrozen conditions), under wet or dry conditions, at different wind speeds or with different baselines (Castel et al., 2000; Koskinen et al., 2001; Askne et al., 2003, Pulliainen et al., 2003; Drezet & Quegan, 2006). This variation needs to be captured by an algorithm that aims at mapping forest biophysical parameters with coherence.

Because of this variability, the mapping of forest biophysical parameters with ERS-1/2 tandem coherence has postulated so far the availability of accurate ground data, i.e. forest inventory data, to train empirical (Hyypä et al., 2000; Wagner et al., 2003; Fransson et al., 2001) or semi-empirical models (Askne et al., 1997, 2003; Koskinen et al., 2001; Pulliainen et al., 2003; Santoro et al., 2002, 2005, 2007) that relate coherence to stem volume, tree height (Hagberg et al., 1995; Dammert & Askne, 1998; Papathanassiou & Cloude, 2001; Santoro et al., 2005a) or forest age (Drezet & Quegan, 2006, 2007). Strong limitation to exploiting these approaches is represented by the need for dense grids of reliable forest inventory datasets. Inventory data is a rare commodity and even if it exists often not freely available. Furthermore, it generally delivers a

punctual view, which means that the model training results cannot be transferred automatically to areas where no inventory data is available.

A first approach to overcome this problem was the so-called SIBERIA algorithm (Schmullius et al., 2000; Balzter et al., 2002; Wagner et al., 2003). Within the SIBERIA project, the abbreviation for ‘SAR Imaging for Boreal Ecology and Radar Interferometry Applications’, a fully automated classification approach was developed, which derived the required unknown parameters of a simple empirical model, relating coherence to stem volume, from the coherence histogram; note that in SIBERIA also the intensity measurements of the Japanese Earth Resource Satellite JERS-1 were used (mainly for the classification of water surfaces) but this was not of interest in the context of this thesis as JERS data was not available for Northeast China. The approach was used to map four forest stem volume classes (0-20, 20-50, 50-80 and >80 m³/ha) over an area of almost 1 Million km² in Central Siberia. However, the method was developed for ERS-1/2 tandem coherence data acquired only in fall. Hence, it is questionable if the same approach works for ERS-1/2 tandem data that has been acquired in other seasons. Furthermore, the dominance of dense forest in the area covered by the ERS image was mandatory and the empirical model basis comprised a number of simplifications that prevented a straightforward transfer of the approach to other forest areas or multi-seasonal ERS-1/2 tandem datasets.

1.3 Scope of the thesis

It is still considered of high interest to exploit the existing archives of the ERS-1/2 tandem mission for the production of forest resource maps for the mid 1990s in order to obtain reference information for future forest resource assessments. The overall goal of this thesis was therefore to investigate, for the showcase scenario of Northeast China, the possibility to map forest stem volume over large areas with ERS-1/2 tandem coherence data independently of the availability of reference information in form of forest inventory data. For Northeast China, the available multi-seasonal ERS-1/2 tandem dataset comprised 223 tandem pairs, providing an almost complete coverage of Chinas Northeast. For the algorithm development, ground reference information was given for three test sites in the main forest areas of Northeast China. As the amount of ground reference data for China was limited, the investigation considered as well several well-known test sites in Central Siberia for which a multi-seasonal ERS-1/2 tandem dataset and an extensive forest inventory database was available.

A promising information source, that may provide the information required to capture the temporal and spatial variability of coherence over forested terrain, is the MODIS Vegetation Continuous Field product VCF (DeFries et al., 2000; Hansen et al., 2002a, 2002b, 2003, 2005). VCF is available since 2003 and provides global estimates of percent tree canopy cover at 500 m pixel size. VCF represents a new approach in characterizing global land cover by means of medium resolution optical remote sensing data, which allows frequent mapping of the Earth’s surface at a global scale. Yet, traditional global mapping approaches classified the satellite images into a discrete number of classes, diminishing a lot of the gradual information about the land cover that was in the imagery. Also the parameter that is focused on in this thesis, i.e. forest stem volume, represents a continuous parameter that is known to correlate to some extent with tree canopy cover (Van Laar & Akca, 2007). The global availability of information

about forest tree cover thus opens up new possibilities for a synergistic use of the main pillars of Earth Observation, i.e. optical and radar remote sensing.

One type of synergy between radar and optical remote sensing, for which spectral reflectances in different wavelengths provide information about forest stem volume or biomass at least for young stands with open canopy structure (Franklin, 1986; Spanner et al., 1990; Trotter et al., 1997; Reese et al., 2002; Foody et al., 2003; Magnusson & Fransson, 2004; Mäkelä & Pekkärinen, 2004; Houghton et al., 2007), would be to use the measurements from both sensors for stem volume retrieval and to combine the estimates. This was, for instance, tested in Magnussen & Fransson (2004). In this study, however, only coherence was intended for stem volume retrieval. The role of the optical remote sensing product was to ‘replace’ forest inventory data.

Although the work presented in this thesis focused on a particular radar data type, the interferometric measurements of the ERS-1/2 tandem mission, the issue of variability in the measured signals with the prevailing imaging conditions is as well relevant for other SAR data types, e.g. intensity measurements in different wavelengths or polarizations, so that the investigations carried out in this thesis may as well indicate solutions for the use of the data of recent or upcoming SAR missions.

In the context of the overall goal of the thesis, several questions had to be analyzed:

- 1) Feasibility of an automated training of models that relate coherence to stem volume:
 - Identification of the mechanisms causing spatial and temporal variations in the interferometric coherence measurements over forested terrain.
 - Analysis of the feasibility of the only yet existing approach for an automated model training which relies solely on coherence histogram statistics (Schmullius et al., 2000; Balzter et al., 2002; Wagner et al., 2003).
 - Investigation on the relationship between ERS-1/2 tandem coherence and VCF tree cover and the possibility to capture the spatial and temporal variability of ERS-1/2 tandem coherence with the aid of VCF.

- 2) Forest structure:

The forest structure at a given stem volume or biomass can differ significantly; e.g. in terms of tree species, age composition or stand density. It has been shown that forest structural diversity has an effect on the accuracy of the retrieval of forest biophysical parameters by means of SAR and InSAR methods (Dobson et al., 1995a; Ferrazzoli & Guerriero, 1995; Harrel et al., 1997; Kasischke et al., 1997; Castel et al., 2002; Treuhaft & Siqueira, 2004; Santoro et al., 2007; Saatchi et al., 2007; Askne & Santoro, 2007b). Hence, the structural properties of the Northeast Chinese and Central Siberian forests had to be taken into account.

3) Topographic effects:

Topography is known to affect interferometric coherence measurements. While for intensity various studies have addressed the issue of topographic distortions in the measurements (e.g. Teillet et al., 1985; Ulaby et al., 1986; Holecz, 1993; Van Zyl et al., 1993; Ulander, 1996; Luckman, 1998; Castel et al., 2001a; Leclerc et al., 2001; Sun et al., 2002; Loew & Mauser, 2006), only few studies have considered the limitations in the use of coherence for forest mapping because of topographic effects, interfering the desired forest biophysical information (Stebler et al., 1996; Castel et al., 2000; Lee & Liu, 2001; Santoro et al., 2007c). In case of the only yet existing large-area forest map derived from ERS-1/2 tandem coherence, i.e. the forest stem volume map produced in the SIBERIA project (Wagner et al. 2003), a rather coarse masking procedure, mostly based on information about local topography from a global DEM with 1 km pixel size, was applied to ‘roughly’ exclude areas where coherence was affected by topography. Meanwhile, global DEMs (<60° N) with a pixel size of 90 m have become available, which should allow a more precise identification of topographic effects in coherence.

1.4 Outline of the thesis

In Chapter 2, the theory of SAR- and InSAR remote sensing will be outlined. The chapter focuses on aspects relevant for the understanding of the measurements over forested terrain. Chapter 3 introduces the ground reference and satellite database that was available for the work presented in this thesis. This comprises a description of the SAR data, including SAR data processing, VCF, the meteorological data as well as the forest inventory data. Chapter 4 focuses on the exploratory analysis of the factors influencing the measurements respectively the relationship between ERS-1/2 tandem coherence and forest stem volume (accuracy of reference data, weather, forest structure, topography) at the Siberian and Northeast Chinese test sites. Chapter 5 describes the development of a new procedure for the training of empirical or semi-empirical models, relating coherence to stem volume, with the aid of VCF. Chapter 6 focuses on topographic effects in coherence and intensity imagery. The automated model training approaches are then tested in Chapter 7 for the ERS-1/2 tandem data covering the test sites. In Chapter 8, a scheme for large-area mapping of forest stem volume will be outlined and applied for the showcase scenario of Northeast China.

Chapter 2 - SAR and InSAR Remote Sensing

In this chapter, a brief description of radar remote sensing theory will be given. This comprises the data acquisition as well as the main mechanisms determining the interaction of radar waves with the Earth's surface. In Chapter 2.2, the theoretical background of radar interferometry will be outlined. The descriptions in this chapter are focused on aspects, necessary for the understanding of radar and interferometric radar measurements over forested terrain, and refer mostly to C-band measurements with 5 cm wavelength as this was the wavelength of the SAR data considered in this study.

2.1 Basics of radar remote sensing

2.1.1 The radar signal

Imaging radar antennas are mounted on moving platforms like airplanes or satellites. In case of a monostatic setup, i.e. the same antenna transmits and receives a signal of a certain frequency f respectively wavelength λ , linked through the speed of light c with $c = \lambda f$ ($c \sim 2.998 \times 10^8$ m/s). These frequencies have been grouped into so-called bands. The common bands are the P- (0.3-1.0 GHz), L- (1.0-2.0 GHz), S- (2.0-4.0 GHz), C- (4.0-8.0 GHz) and X- bands (8.0-12.5 GHz). Sensors in operation transmit signals in either horizontal (H) or vertical (V) linear polarization. The same is true for the reception of the signal, leading to four possible combinations of transmission and reception: horizontally transmitted and horizontally (HH) or vertically (HV) received respectively vertically transmitted and vertically (VV) or horizontally received (VH).

Electromagnetic waves comprise an electric and a magnetic field moving mutually along the same path and oscillating perpendicular to each other. The polarization of an electromagnetic wave, propagating in direction z , can be described with the electric field vectors E_X , E_Y and E_Z (e.g. Rees, 2001):

$$\begin{aligned} E_X &= E_{0X} \cos(\omega t - kz - \phi_X) \\ E_Y &= E_{0Y} \cos(\omega t - kz - \phi_Y) \\ E_Z &= 0 \end{aligned} \tag{2.1}$$

where ϕ_X and ϕ_Y determine the oscillation of the electric field vector with amplitudes E_{0X} and E_{0Y} in the perpendicular X- and Y-directions. The coefficient ω denotes the angular frequency, defined as $2\pi f$, and k the wave number, defined as $2\pi/\lambda$. The phase difference in X- and Y-direction, $\phi_X - \phi_Y$, determines the polarization state of the wave. For a phase difference of 0, π and $-\pi$, the wave is linearly polarized, i.e. the electric field vector does not oscillate around the propagation axis of the wave. For a difference of $\pm \pi/2$ and constant amplitudes $E_{0X} = E_{0Y}$, the wave is circularly polarized. In case of different amplitudes of E_X and E_Y and phase differences of $\pm \pi/2$, the wave is elliptically polarized. In case of the radar measurements analyzed in this thesis, only the linear polarized fraction of the electric field amplitudes will be of interest since the sensors considered transmitted and received signals in only one polarization (VV).

A radar antenna mounted on a satellite, space- or aircraft sends out the signal to its side and perpendicular to the flight direction with a certain pulse repetition frequency (PRF)

and pulse length τ . With a pulse length of $37 \mu\text{s}$, the antennas mounted on the ERS satellites produce a pulse of $\sim 11 \text{ km}$ length. The terrain illuminated by one pulse is called the footprint; the width of this footprint in the direction perpendicular to the platform motion is referred to as swath. The flight direction of the platform is known as the ‘azimuth’ and the direction perpendicular to the flight path is referred to as ‘range’. The forward motion of the platform causes a continuous illumination of the ground in azimuth direction.

Table 2.1. Characteristics of the ERS-1 and ERS-2 SAR missions (cf. Kramer, 2002)

	ERS-1 & ERS-2
Duration	ERS-1: July 1991 – March 2000, ERS-2: April 1995 -
Wavelength	0.0567 m
Polarization	VV
Incidence angle	23° (image center)
Bandwidth	15.5 MHz
Pulse length	$37.1 \mu\text{s}$
PRF	1680 Hz
Antenna Size	10 x 1 m (azimuth x elevation)
Swath width	100 km
Altitude	785 km

A single pulse can be described as a function of time t with carrier frequency f_0 and the complex envelope $g(t)$ (Bamler & Hartl, 1998):

$$p_t(t) = g(t) \cdot e^{i2\pi f_0 t} \quad (2.2)$$

In order to achieve a high transmitting power, the signal is linearly frequency modulated using a ‘chirp’ function $g(t)$. The pulse comprises frequencies between $f_0 - W/2$ and $f_0 + W/2$ with W denoting the bandwidth. After travelling to the ground, interacting with the surface and being scattered back to the sensor, the pulse is received after a time delay of $2R/c$, with R representing the distance to the backscattering object:

$$p_r\left(t - \frac{2R}{c}\right) = g\left(t - \frac{2R}{c}\right) \cdot e^{i2\pi f_0 \cdot \left(t - \frac{2R}{c}\right)} \quad (2.3)$$

For spaceborne radar sensors flying at high altitude, the received pulse does not correspond to the last pulse send. In case of the ERS sensors, nine consecutive pulses are transmitted in the meantime before a pulse is received. Every pulse is then coherently demodulated by removing the carrier frequency from the transmitted signal, leaving the phase component dependent on R :

$$\phi(R) = -\frac{4 \cdot \pi}{\lambda} R \quad (2.4)$$

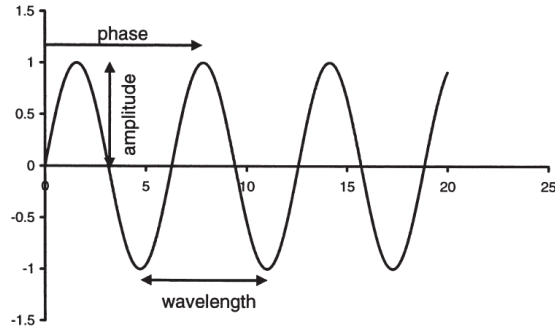


Figure 2.1. Amplitude, wavelength and phase of a radar signal (Courtesy of Balzter, 2001).

The resolution of radar measurements has to be considered separately in the two dimensions of the imaging geometry, which is called the Range-Doppler geometry with geometric characteristics to be discussed later in this section. The resolution in the propagation direction of the transmitted signal, the so-called slant-range, is related to the bandwidth W ; the wider the bandwidth, the higher the resolution. Again exemplified for ERS, the resolution, r_{sr} , is 9.7 m as the relation to W is:

$$r_{sr} = \frac{c}{2 \cdot W} \quad (2.5)$$

The resolution in slant-range does not equal the resolution on the ground. In case of flat terrain, the slant-range resolution is related to the ground-range resolution, r_{gr} , through:

$$r_{gr} = \frac{r_{sr}}{\sin(\theta)} \quad (2.6)$$

The ground-range resolution depends on the incidence angle, θ , which increases from near to far range, i.e. the areas closest respectively furthest from the sensor. Thus, the resolution improves from near to far range.

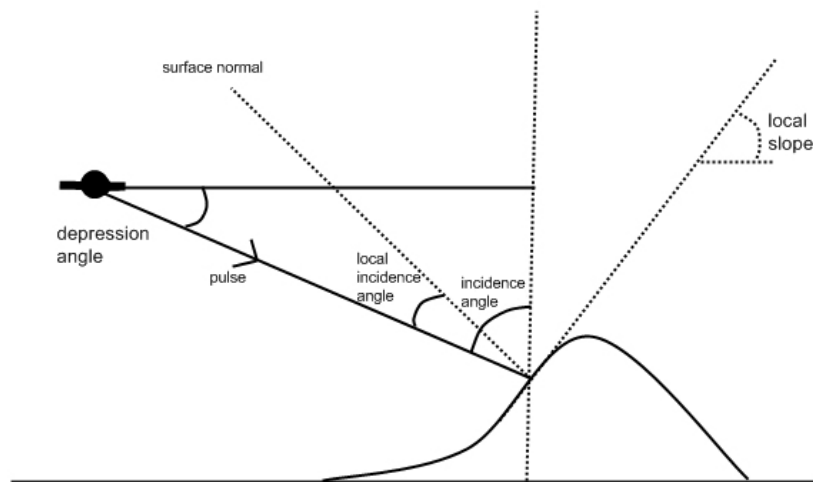


Figure 2.2. Radar imaging geometry.

In case of a so-called Real Aperture Radar, the azimuth resolution, i.e. in the direction of the platform motion, depends on the wavelength and the size of the antenna used. The pulse spreads out from the antenna with an angle ψ_a of:

$$\psi_a[\text{radians}] = \frac{\lambda}{L_A} \quad (2.7)$$

with L_A being the antenna size in azimuth direction. For a distance R of ~ 850 km, i.e. the approximate slant-range distance of sensor and ground for ERS, the beam reaches a width of ~ 5 km in azimuth direction before reaching the ground. Thus, a received pulse contains the returned echoes from each object in a strip of this length. As the possibility to elongate the antenna is limited, Real Aperture Radar data from spaceborne platforms are useless. However, each target on the ground is illuminated repeatedly. The ERS footprint moves only 4 m between two consecutive pulses. Each time a new pulse reaches a target on the ground, the relative position of the sensor with respect to the target has changed, which is why the echo of a target in each pulse experiences a different Doppler frequency shift. The Doppler history of a target in the pulses provides an additional coordinate for target discrimination (Curlander & McDonough, 1991). When considering the Doppler history of a target, it is possible to synthesize an aperture with an effective beamwidth ψ_{eff} of:

$$\psi_{eff} = \frac{L_A}{2 \cdot R} \quad (2.8)$$

The azimuth resolution of a SAR is independent of range distance and wavelength as: $\psi_{eff} R = L_A / 2$. SAR data is generally delivered in a complex format of the form $u = \text{Re}(u) + i \text{Im}(u)$, with the quadrature $\text{Re}(u)$ and in-phase $\text{Im}(u)$ component containing amplitude, A , and intensity, I , information:

$$A = \sqrt{\text{Re}(u)^2 + \text{Im}(u)^2} \quad I = A^2 \quad (2.9)$$

as well as the phase, ϕ , information:

$$\phi = \arctan \left[\frac{\text{Im}(u)}{\text{Re}(u)} \right] \quad (2.10)$$

This brief discussion does by far not reflect the complexity of SAR image formation but is considered sufficient for the understanding of the work presented in this thesis. For further details, the reader is referred to Elachi et al. (1988), Curlander & McDonough (1991), Olmstedt (1993), Bamler & Schättler (1993), Oliver & Quegan (1998), Henderson & Lewis (1998).

2.1.2 Radar cross section

The power P_r a radar antenna receives from an illuminated target on the ground is described by the radar equation:

$$P_r = \frac{P_t G_t A_e}{(4 \cdot \pi \cdot R^2)^2} \sigma \quad (2.11)$$

P_r depends on the transmitted power P_t , the distance between antenna and scatterer R , the gain G_t and effective area A_e of the antenna and the target radar cross section σ , RCS. Besides σ , all parameters are defined by the sensor and the imaging geometry. The radar cross section depends on the geometric and dielectric properties of the target. In practice, a resolution cell much larger than the wavelength of the signal will contain a large number of scattering objects, all contributing to the signal received by the antenna. Therefore, the backscatter coefficient σ^0 [m^2/m^2], defined as radar cross section per unit area (Ulaby et al., 1986), has to be used. σ^0 is often reported in logarithmic scale in order to emphasize the lower range of the σ^0 spectrum, which comprises most of the land surface related information:

$$\sigma^0[dB] = 10 \cdot \log_{10}(\sigma^0) \quad (2.12)$$

The side-looking imaging principle of SAR measurements introduces radiometric distortions in the imagery as the ground area, contributing to the backscatter from a resolution cell, changes from near to far range (see Equation (2.6)) and depends on the topography. In order to determine σ^0 from the radar brightness β^0 , i.e. the backscatter received at the antenna from a resolution cell, information about the local relief is required (Ulander, 1996; Luckman, 1998; Castel et al., 2001a; Laur et al., 2004; Loew & Mauser, 2007). The radiometric distortions are accompanied by geometric distortions in the radar images. These effects are related to the fact that in SAR images the pixels are arranged according to the pulse delay time, i.e. the slant-range distance between sensor and target, and the Doppler history. These two parameters specify the SAR image plane. Altitudinal differences on the ground alter the sensor to target distance and the Doppler history so that the arrangement of the pixels in the SAR image does not reflect their ‘true’ arrangement on the ground in a two-dimensional map projection. DEMs are required to reconstruct the location of a pixel on the ground. When visually interpreting SAR images, they present rather irritating geometric effects over mountainous terrain, known as ‘layover’, ‘foreshortening’ and ‘shadowing’. In case of layover, when the slope exceeds the radar look angle, the echo from the mountain top is received before the echo from the mountain base, which is why mountains appear to lean towards the sensor in the radar images. For less steep slopes, still facing the sensor, the slopes appear as narrow and bright stripes as the slant-range distances are shortened. This effect is referred to as foreshortening. In case of slopes tilted away from the sensor, the images show widened and darker areas. When slopes are steeper than $90^\circ - \theta$ and tilted away from the sensor, the so-called shadowing occurs as no signal is received at the antenna then.

2.1.3 Speckle

The radar imaging process is coherent which means that amplitude and phase are measured. For each resolution cell, the phase measured at the antenna comprises a systematic contribution related to the slant-range distance plus, in case of distributed scatterers that are much smaller than the resolution cell, a contribution attributed to the elementary scatterers in the resolution cell. Therefore, Equation (2.4) has to be extended

for an additional phase term $\phi_{scatter}$ that is related to the total phase for the set of distributed scatterers within the resolution cell:

$$\phi(R) = -\frac{4 \cdot \pi}{\lambda} R + \phi_{scatter} \quad (2.13)$$

When coherently summing up amplitude and phase of each elementary scatterer in a resolution cell, interference occurs. An arbitrary number of realizations of interference between the echoes from the elementary scatterers is the reason why homogenous areas show a kind of ‘salt and pepper effect’ in an intensity image. This effect is called speckle. It appears as completely random noise in a phase image.

The probability density function (abbr. pdf) of intensity I over a uniformly distributed target follows a negative exponential distribution (Bamler & Hartl, 1998; Oliver & Quegan, 1998):

$$pdf(I) = \frac{1}{\sigma^0} \exp\left\{-\frac{I}{\sigma^0}\right\} \quad (2.14)$$

with expected mean \bar{I} :

$$\bar{I} = \frac{1}{\sigma^0} \int_0^{\infty} I e^{-\frac{I}{\sigma^0}} dI = \sigma^0 \quad (2.15)$$

In contrast, the phase is distributed uniformly between $-\pi$ and π . Even though speckle appears as noise in an intensity image, it is not random. It is a consequence of local surface characteristics and shows, under certain premises, a comparable form of appearance for repeated measurements (cf. SAR Interferometry section).

The easiest way to reduce speckle is averaging or ‘multilooking’ over neighboring intensity pixels. When averaging over N pixels, the resulting image is called N -look intensity and the resolution is reduced by factor N . A more effective way of multilooking can be applied before image formation when dividing the azimuthal spectral band into N bands, i.e. N images are produced, and incoherently summing up the power of the N images (Bruniquel & Lopes, 1997; Moreira, 1991). As long as no strong single scatterer dominates the backscatter from a resolution cell, the distribution of multilook intensity over homogenous terrain can be described with the Gamma pdf (Holecz, 1993; Bruniquel & Lopes, 1997):

$$pdf(I) = \frac{1}{\Gamma(L)} \left(\frac{L}{\sigma^0}\right)^L I^{L-1} e^{-\frac{LI}{\sigma^0}} \quad (2.16)$$

with gamma function $\Gamma(\cdot)$ and the order parameter in form of the number of independent looks L . The maximum likelihood estimate of σ^0 is simply the average over all pixels in a sample window. If spatial autocorrelation is present, the spatial average is no longer the Maximum Likelihood estimate of σ^0 but still represents an unbiased estimator (Oliver & Quegan, 1998). Special filters have been developed which aim at the reduction of speckle without eliminating spatial context information in the intensity images, e.g. edges or strong single scatterers (e.g. Lee et al., 1981; Frost et al., 1982;

Lopes et al., 1993). These filters always cause a loss of spatial resolution. The loss of resolution can be reduced when a multi-channel SAR dataset is available, i.e. a set of images acquired at different times or even images from different SAR sensors (Bruniquel & Lopes, 1997; Quegan & Yu, 2001). The performance of speckle filtering is generally quantified by means of the Equivalent Number of Looks (ENL), which can be estimated with the ratio of the squared average intensity to the variance of intensity in a homogeneous area without texture. Filtering results in a higher ENL. In general, the ENL is lower than the nominal number of looks, i.e. the number of pixels used to reconstruct σ^0 .

2.1.4 Radar scattering from forested terrain

When electromagnetic waves have propagated through the atmosphere and interact with the Earth's surface, three main processes need to be distinguished: absorption, reflection/scattering and transmission. The relevance of each mechanism depends on the dielectric properties, size, shape and orientation of the objects the signal interacts with as well as the frequency, polarization and incidence angle of the signal. A fundamental property of the material, the wave is interacting with, is the relative dielectric permittivity or constant, ε_r (e.g. Rees, 2001):

$$\varepsilon_r = \frac{\varepsilon_c}{\varepsilon_0} = \varepsilon_r' - j\varepsilon_r'' \quad (2.17)$$

with ε_c being the dielectric permittivity of the material and ε_0 of free space. The relative dielectric permittivity determines the ratio of transmitted and reflected power when media boundaries in the travel path of the wave occur as well as the amount of absorbed power within a medium (mainly determined by ε_r''). It depends on the frequency of the electromagnetic wave with the real part ε_r' being larger than 1 and the imaginary part ε_r'' larger than 0 for all media but free space. In theory, also the magnetic permeability would have to be considered. For most materials, making up the Earth's surface, the magnetic permeability can be assumed equal which is why in general only dielectric effects need to be considered.

One of the most important elements on the Earth's surface is water. The dipole character of water allows a high degree of polarization when an electric field with a frequency in the microwave range is present. The response of water molecules to alternating electric fields is, however, much reduced when water freezes. As the dielectric constant for other relevant materials, e.g. organic matter in vegetation or the mineral components of soils, is much lower, the free water content and aggregation state drive the dielectric properties of these materials (Ulaby et al., 1986). In case of trees, the sapwood beneath the bark represents the area with the highest dielectric constant within a tree (Salas et al., 1994). The moisture content of the sapwood is influenced by the water availability in the soil. For instance, a reduced water availability because of draught is followed by a reduced moisture content of the water conducting sapwood, or as reported in Moghaddam & Saatchi (1999), an increased water availability because of snowmelt in spring results in an increased canopy moisture content that can last throughout most of the growing season. Significant alterations of dielectric properties of trees can arise because of variations in sap chemistry (McDonald et al., 2002). The dielectric properties are also related to the diurnal cycles of tree activity. Photosynthetic activity and transpiration during the day lower the water content and the water uptake

from the soil at night increases it. Variations of the dielectric properties in a range of hours are possible (Way et al., 1991; McDonald et al., 1991; Pulliainen et al., 1994; Salas et al., 1994). Freezing of the sapwood, which occurs at temperatures below -5 to -7° C (Lin, 1967 as quoted in Koskinen et al., 2001), causes a much reduced dielectric constant.

In radar remote sensing of forests, three types of scattering have to be distinguished:

- 1 Surface scattering
- 2 Volume scattering
- 3 Double bounce (trunk-ground or canopy-ground interaction)

All three mechanisms together contribute to the radar backscatter from forested terrain, from now on referred to as σ_{for}^0 :

$$\sigma_{for}^0 = \sigma_{surface}^0 + \sigma_{double-bounce}^0 + \sigma_{volume}^0 \quad (2.18)$$

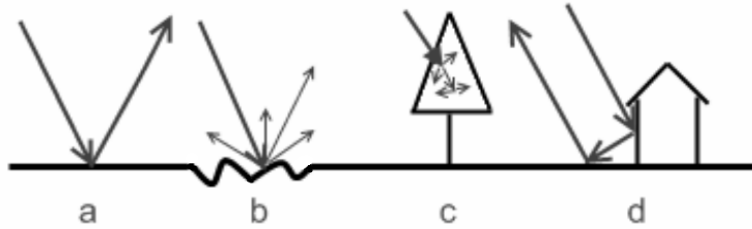


Figure 2.3. Scattering mechanisms: a – smooth surface reflection, b – rough surface scattering, c – volume scattering, d – double bounce.

Surface scattering takes place at the boundary of two media with different dielectric properties. In case of plane boundaries, reflection can be described with the Fresnel Law. The Fresnel Law determines the fraction of radiation, i.e. fraction of electric field amplitude, that is reflected at the surface or transmitted into the medium. Reflection and transmission depend on incidence angle and polarization of the wave as well as the dielectric properties of the two media forming the boundary. For plain surfaces, only reflection into the direction away from the sensor occurs, i.e. a side-looking monostatic sensor configuration would not receive any returning power. In most cases, the media boundaries, like the air-soil or air-water interface, are not flat which is why roughness effects need to be considered. With increasing roughness, the specular reflection amplitude, often referred to as the ‘coherent’ component, decreases and a diffuse scattering component, accordingly referred to as the ‘incoherent’ component, increases which means that the signals are increasingly scattered in all directions, approaching the ideal case of Lambertian scattering (Ulaby et al., 1986). The angular (i.e. incidence angle) dependence of backscatter meanwhile decreases with increasing roughness. In case of smooth surfaces, a sensor would only receive a backscattered signal in case of close to normal incidence angles whereas with increasing roughness, the dependence of the power scattered back to the sensor on the incidence angle decreases. The roughness of the surface needs to be considered with respect to the wavelength of the signal. A surface might appear rough at a certain wavelength but still smooth at a longer wavelength. This finding has motivated the definition of roughness criteria, which

indicate if a surface can be considered smooth with respect to a certain wavelength. A simple measure is the so-called Fraunhofer criterion (cf. Ulaby et al., 1986; Rees, 2001):

$$h_{sd} < \frac{\lambda}{32 \cdot \cos(\theta)} \quad (2.19)$$

The criterion states that a surface can be considered smooth when the standard deviation of surface height variation, h_{sd} , does not exceed $\lambda/32$ for steep incidence angles. For less steep incidence angles, higher standard deviations of surface height variations can still be considered smooth.

The dielectric properties of soils, which are mainly determined by its volumetric moisture content, control the magnitude of the Fresnel reflection at the surface and the penetration of the signal into the soil. The penetration depth of C-band signals is generally in the range of millimeters (wet soil) to few centimeters (frozen soil) (Wegmüller, 1990), unless the soil is extremely dry like in loose sandy desert soils (Schaber et al., 1986). The mostly low penetration of radar signals makes roughness and moisture the main parameters determining soil backscatter with only minor effects of so-called volume scattering.

Volume scattering is of particular importance in case of radar backscatter from vegetation, snow or ice. It represents the effect of multiple scattering within an inhomogeneous medium characterized by dielectric discontinuities. The strength of the backscatter from a volume is determined by the magnitude and density of the dielectric discontinuities within the volume (Ulaby et al., 1986). Multiple scattering in a volume of ‘arbitrarily’ oriented elementary scatterers takes place in a wide range of directions, which is why the angular dependence of the measurement is reduced compared to the surface scattering case. A tree crown represents such an inhomogeneous medium, consisting mainly of air and the tree constituents in form of leaves, needles, twigs, branches and the stem. Size and orientation with respect to wavelength and polarization of the radar signal as well as the dielectric properties are the fundamental properties of the tree constituents that have an influence on volume scattering. Volume scattering can only be observed when the surface of the volume allows the signal to penetrate into the medium. In case of forests, surface scattering effects at the boundary of the atmosphere and the tree canopy can be considered negligible (Ulaby et al., 1986).

Different approaches for the modeling of volume scattering from forest canopies have been developed. One common type of model treats the canopy as a layered volume with simple shapes like discs or cylinders representing needles, leaves, branches or the stem. Size, distribution and orientation of these scattering elements are approximated based on observations made for a particular tree species (e.g. Bosisio & Dechambre, 2004; Castel et al., 2001b). Volume scattering is then modeled by coherently summing the scattered fields from the elementary scatterers following electromagnetic wave theory (e.g. Chauhan et al., 1991; Saatchi & McDonald, 1997) or by incoherently summing the scattered energies according to radiative transfer theory (e.g. Ulaby et al., 1990; Karam et al., 1992). As these models require a high number of input parameters, they have mostly been used for backscatter simulation purposes. Another type of model, suited for inversion and thus for forest parameter retrieval, is the so-called Water-Cloud-Model (abbr. WCM) (Attema & Ulaby, 1978). The WCM treats a forest canopy as infinite horizontal layer of homogeneously distributed water droplets and considers the flow of energy through the volume. The particles, i.e. water droplets held in place by the

organic framework of the trees, are characterized by a radar cross section σ and an attenuation cross section κ_e . The attenuation cross section accounts for the loss of energy of the signal when propagating through the volume because of absorption or scattering into a direction away from the sensor. The energy of the radar signal is assumed to decay exponentially with the distance the signal has covered within the volume. Attenuation is accounted for in both directions, i.e. for the signal travelling into the medium as well as for the fraction of the signal scattered back within the medium. When incoherently summing up the scattering and attenuation cross section of each infinitesimal thin layer along the propagation direction z , the total backscatter coefficient σ_v^0 for a volume of thickness h is obtained:

$$\sigma_v^0 = \int_0^h N \sigma e^{-2N\kappa_e(h-z)/\cos\theta} dz = \int_0^h \sigma_v \cdot e^{-\alpha \cdot (h-z)} dz = \sigma_{veg}^0 (1 - T_{tree}) \quad (2.20)$$

where σ_v denotes the volumetric backscattering coefficient defined as radar cross section per unit volume and N the number of scattering particles per unit volume. σ_{veg}^0 is the idealized backscatter coefficient of a layer with zero two-way transmissivity, T_{tree} , which specifies the fraction of energy penetrating the volume:

$$T_{tree} = e^{-2N\kappa_e h / \cos\theta} = e^{-\alpha h} \quad (2.21)$$

The coefficient α [Np/m] expresses the two-way attenuation per meter. The penetration depth, δ , of the signal is defined as the depth where the signal power is reduced to ~37 % (i.e. $100/e$) (Ulaby et al., 1986), and can be calculated with α^{-1} respectively:

$$\delta = \left(2 \cdot \ln 10 \frac{\alpha [dB]}{10} \right)^{-1} \quad (2.22)$$

when α is given in dB/m. In case of a simple structured one-layered forest canopy (typical for boreal and temperate forests), it is convenient to consider the tree height as the depth of the volume. The radar cross sections of the scatterers in the canopy depend on the size and orientation of the scatterers as well as their dielectric properties. The main backscattering elements of the canopy are those with a size comparable or larger than the wavelength of the signal and an orientation similar to the polarization of the signal. Elements smaller than the wavelength of the signal mainly contribute to signal attenuation and less to backscatter. For short wavelengths like the X-band ($\lambda \sim 3$ cm), the needles, leaves and twigs at the upper margin of the canopy cause the main backscatter. At C-band, the twigs and branches cause the main backscatter with still significant contributions from needles and leaves. For further increasing wavelengths, the large components of a tree become important scattering agents, i.e. primary branches and the stem (Ulaby et al., 1990; Chauhan et al., 1991; Le Toan et al., 1992; Fung, 1994; Wang et al., 1995a). As the relevance of leaves decreases with increasing wavelength, the differences in forest backscatter between leaf-on and leaf-off periods reduce with increasing wavelength (Fleischmann et al., 1996; Bosisio & Dechambre, 2004; Guglielmetti et al., 2007). Meanwhile, the penetration depth of the signal increases with increasing wavelength. In case of C-band, measurements and model simulations indicated typical penetration depths of only few meters (cf. Leckie & Ranson, 1998).

A non-zero tree canopy transmissivity gives rise to a scattering effect known as double bounce. This effect is of particular importance when observing urban areas but is also relevant in forests when the signal penetrates the canopy and reaches stem and ground. In order to obtain double bounce, two surfaces larger than the wavelength of the signal need to be arranged perpendicular to each other. In this case, the incoming wave is reflected at both surfaces and directed back to the sensor so that a strong signal is received at the sensor. This precondition is fulfilled for the angle between stems and the ground as long as tree stems grow approximately vertical and on flat ground (Van Zyl, 1993; Israelsson & Askne, 1994). Minor double bounce may also arise from canopy-ground interactions.

Table 2.2. Important forest and radar sensor characteristics influencing radar backscatter from forested terrain (as summarized in Askne et al., 1997).

Geometrical Properties	Temporal Properties	Dielectric Properties	Radar Properties
Shape Size Density Orientation Roughness Areal coverage	Water content of trees and soil Freeze / thaw Snow cover	ϵ_r of branches, stems, soil etc Attenuation	Frequency Polarization Incidence angle

Table 2.2 summarizes the most important target, environmental and sensor properties that need to be considered when interpreting radar intensity data acquired over forested terrain. In order to understand the variability of backscatter with varying environmental conditions, the contributions of the three scattering mechanisms to the backscatter measured need to be distinguished.

C-band backscatter over forested terrain is predominantly volume scattering (Chauhan et al., 1991; Pulliainen et al., 1994; Karam et al., 1995; Wang et al., 1995b). It is influenced by canopy moisture variations and the phenological state of the trees and reveals diurnal and seasonal patterns. In addition, short-term responses to meteorological events like rainfall are possible. McDonald et al. (1991) observed diurnal variations of backscatter up to 3 dB in C-band for young walnut trees growing in a semi-arid environment. Lower diurnal variations of less than 1 dB have been reported in Dobson et al. (1991a) for loblolly pine forest growing in a more humid environment and in Rignot et al. (1994) for Alaskan boreal forest. Model simulations and measurements reported in Pulliainen et al. (1994) indicated a maximum diurnal variability of C-VV backscatter of about 1.8 dB under typical summer conditions in Finland. The largest diurnal variations in volume backscatter can be expected in times of “high transpirative demands” (Dobson et al., 1995b), for instance during dry seasons when large diurnal variations in plant water potential arise. The interpretation of forest backscatter variations is complicated by variations in tree water chemistry (McDonald et al., 2002), tree species specific differences in the variability of tree water content (Pulliainen et al., 1994) or the general water conductance ability of trees which has been found to decrease with tree age (Pothier et al., 1989). Differences between the leaf-off and leaf-on periods of deciduous forest should occur as well as in C-band leaves act mostly as attenuators, lowering the backscatter. However, the differences related to the foliage dynamics have been observed to be rather weak (in a sub-dB range) compared to other environmental effects (Ahern et al., 1993; Proisy et al., 2000; Kasischke et al., 2007; Lang et al., 2008). Besides diurnal variations, responses of C-band backscatter

from forest to short-term events like rainfall have been observed. Increases in C-band backscatter from wet forest canopies shortly after rainfall of up to 3 dB have been reported in Dobson et al. (1991b) or Bergen et al. (1997). The seasonal variations in canopy backscatter are generally most pronounced for forests in the boreal zone (Ahern et al., 1993; Rignot & Way, 1994; Rignot et al., 1994; Askne et al., 2003). Here, a very low backscatter from forest is reached under frozen conditions due to the much lower dielectric constant of the tree water when the trees are frozen. Differences in backscatter between the frozen and unfrozen state of the canopies in the range of 2 to 6 dB have been reported for C-band (Rignot & Way, 1994; Pulliainen et al., 1999; Ranson & Sun, 2000; Kasischke et al., 2007). The largest changes can be observed during the thawing periods in spring when the scatterers in the canopy defrost and snowmelt causes a high water availability in the soils. The frequency of freeze/thaw events can be very different in different parts of a tree canopy (Mayr et al., 2006). The branches at the upper margin of the canopy, which are most relevant for C-band backscatter, can be exposed to more frequent freeze/thaw cycles than the larger branches below. Backscatter variations over forest because of frequent freeze/thaw transitions have been reported in Rignot et al. (1994). Rignot et al. observed differences in ERS-1 backscatter over Alaskan boreal forest between day- and nighttime passes of 2 dB in late fall because of diurnal freeze/thaw transitions of the relevant scatterers in the canopy. Compared to boreal forests, C-band backscatter from temperate forests in Europe has been observed to undergo a considerably lower variability throughout the seasons (Fellah et al., 1997; Quegan et al., 2000; Proisy et al., 2000).

The crown architecture differs between the tree species and forest types and thus has an effect on SAR intensity measurements. Several studies have discussed the use of SAR for tree species and forest type discrimination. Tree species and forest type classification have been found to be hardly possible with sufficient accuracy when having acquisitions in only one frequency and polarization. For ERS intensity, Proisy et al. (2000) and Quegan et al. (2000) reported differences of only 1 to 1.5 dB throughout all seasons between deciduous and coniferous species in temperate broadleaf and mixed forests in France and Great Britain. Rignot et al. (1994) found ERS-1 backscatter to vary less than 2 dB between different boreal forest tree species in Alaska. The highest potential for tree species discrimination can be assigned to multi-frequency and multi-polarization data (Ranson & Sun, 1994a, 2000; Ranson et al., 2001a). In Ranson et al. (2001a), for instance, six principle components of several band ratios of SIR-C C- and L-band multi-polarization data were used to classify forests in the Sayani mountains in Siberia with a minimum accuracy of 73 % for the class 'young deciduous forest' and at least 82 % for the classes 'old deciduous forest', 'young conifers' and 'old conifers'. In Dobson et al. (1995b), a discrimination of pine, spruce and broadleaf forests in Michigan was found not to reach sufficient accuracy when using either ERS C-VV or JERS L-HH intensity images. A Maximum Likelihood classification achieved accuracies of 63.5 and 65.9 %, respectively. Combined, however, an accuracy of 93.7 % was achieved. A classification accuracy of 75 % for ERS and 98 % for JERS was achieved when not differentiating between tree species but between biophysical properties (short and tall trees), indicating that the biophysical forest parameters (like stem volume, biomass, height, etc.) are an important, if not the dominant, information in SAR imagery. However, accounting for forest structural differences in terms of species or forest types when aiming at forest biophysical parameter retrieval may improve the retrieval accuracy (Dobson et al., 1995a; Castel et al., 2002).

If the signal attenuation in the forest canopy is low enough to allow the signal to penetrate the canopy or if there are gaps in the canopy, scattering from the forest floor contributes to the backscatter measured. Modeling results in Wang et al. (1995) for HH, VV and HV-polarized C-band backscatter from sparse pine forest and incidence angles between 20 and 60° indicated that forest floor roughness and moisture, litter depth and litter moisture content are almost equally important in explaining the variability of C-band backscatter from forest floor. In VV and HH polarization, the sensitivity was highest for steep incidence angles with a maximum simulated variability of about 5 dB at 20° and 3 dB at 30° incidence angle. HV was mostly insensitive to changes in forest floor conditions at all incidence angles. In Pulliainen et al. (1994) model simulations predicted a variation of ERS C-VV forest floor backscatter up to 5 dB due to soil moisture variations typical for moraine lands in Finland. Large changes of forest floor backscatter can be observed when freezing occurs. Pulliainen et al. (1996) and Borgeaud & Wegmüller (1996), for instance, reported a drop of 2 to 4 dB in ERS C-band backscatter when soils froze. SIR-C C-HH, C-HV and C-VV measurements acquired over recent clear cuts were found to exhibit an even larger difference of up to ~9, 13 and 6 dB, respectively, between frozen and unfrozen conditions in Ranson & Sun (2000).

A very variable composition of backscatter contributions can be observed for snow covered soil with surface and volume effects occurring dependent on snow metamorphism. Snow represents a volume of densely distributed dielectric discontinuities as it is mainly composed of ice crystals, air and liquid water in case of wet snow. Snow properties like grain size, snow density, liquid water content, surface roughness, stratification and snow depth can vary considerably and they all have an effect on the radar backscatter. In the frequency domain of C-band, dry snow, i.e. no liquid water is present, can be considered almost transparent and the penetration depth is in the range of tens of meters (Mätzler et al., 1995). The dielectric constant, which is directly related to snow density and wetness (Nagler et al., 2004), remains low as long as there is no liquid water incorporated in the snow layer. In case of recently fallen dry snow, backscatter is mainly governed by the snow-soil interface. For older snow layers, significant backscatter may arise from ice lenses, pipes and grain clusters (Mätzler et al., 1997; Shi et al., 1997). Volume scattering in ERS C-band backscatter has been found to arise when dry snow ages and vertical temperature gradients between the cold air and a relatively warm snow/ground interface promote the development of coarse skeletal ice crystals. Rignot et al. (1994) observed that volume scattering from coarse skeletal ice crystals increased C-band backscatter for about 1 to 2 dB. Further snow related effects in C-band backscatter are the refraction at the air-snow boundary because of different dielectric permittivities of snow and air (Guneriussen et al., 2001) and the shift in wavenumber (Shi & Dozier, 2000a, 2000b), causing a steeper incidence angle and a reduced wavelength of the wave incident upon the snow-soil boundary, respectively. This means that the backscatter from the snow/soil interface should be increased because the soil surface appears rougher to the radar. On the other side, the reduced dielectric contrast between snow and soil causes a lower backscatter. In spite of these effects of dry snow on backscatter, the discrimination of dry snow and bare soil has been found to be hardly possible (e.g. Shi & Dozier, 1997; Koskinen et al., 1997) in C-band. In case of wet snow, i.e. when melting has caused the accumulation of liquid water in the snowpack, the penetration depth decreases and the backscatter contributions from the snow volume and the snow surface gain importance (Guneriussen, 1997). C-band backscatter was observed to decrease with increasing liquid water content due to signal attenuation in the snow layer. This change in backscatter could be used to map

snow parameters like wet snow areal extent and liquid water content (Shi & Dozier, 1995; Koskinen et al., 1997, 1999). Different weights of surface and volume contributions, which depend on the snow surface roughness, incidence angle, snow stratification and metamorphism, significantly affect the performance of retrieval algorithms (Magagi & Bernier, 2003). Problems in C-band arise in particular for steep incidence angles when considerable backscatter may arise from rough snow surfaces imposed on the volume contributions (Strozzi et al., 1999).

A consequence of the diurnal, seasonal and short-term changes in backscatter is a varying contrast between forest floor and canopy backscatter. The intensity contrast is known to hardly exceed 2 to 3 dB in case of co-polarized C-band intensity with a maximum being reached under frozen conditions when the signal penetrates deeper into the canopy and the backscatter from the forest floor becomes very low. In case of unfrozen and in particular under wet soil conditions, the contrast between forest floor and canopy backscatter is often low; for very wet conditions forest floor backscatter can even be higher than backscatter from dense forest canopies (Ahern et al., 1993; Pulliainen et al., 1994; Rignot et al., 1994; Rignot & Way, 1994; Harrell et al., 1995; Pulliainen et al., 1996; Proisy et al., 2000; Ranson & Sun, 2000).

2.1.5 Stem volume and biomass mapping with C-band SAR intensity

Many studies have shown the potential of SAR intensity data for mapping forest biophysical properties like stem volume, aboveground biomass, crown biomass, tree height or age (Le Toan et al., 1992; Kasischke et al., 1994; Dobson et al., 1995b; Imhoff, 1995; Kasischke et al., 1995; Harrel et al., 1995; Pulliainen et al., 1994, 1996, 1999; Ranson & Sun, 1997; Ranson et al., 1997; Fransson & Israelsson, 1999; Kurvonen et al., 1999; Quegan et al., 2000; Ranson et al., 2001b; Balzter et al., 2002; Santoro et al., 2006; Saatchi et al. 2007). The link between SAR backscatter measurements and forest biophysical properties is a consequence of an increasing number of tree constituents causing backscatter and signal attenuation when forests grow and a meanwhile decreasing backscatter contribution from the forest floor. The size, orientation and dielectric properties of the tree constituents with respect to a certain radar wavelength and polarization determine if they function as attenuator or scatterer, which is why differences in the sensitivity of radar intensity to biophysical forest parameters arise dependent on the radar sensor specifications. As several biophysical properties like tree height, diameter, density, stem volume, biomass or crown cover are correlated (cf. Chapter 3.3), correlation between these properties and radar intensity measurements can be observed. The highest correlations between backscatter and forest biophysical properties can usually be observed for simple structured homogeneous forests, which is to a certain degree a consequence of higher correlations between different biophysical properties, in particular between stem volume/biomass and the crown dimensions (Zeide, 1985; Ranson et al., 1997; Mougine et al., 1999; Castel et al., 2001b; Van Laar & Akca, 2007). The main properties of a radar, determining the suitability of a certain radar system for the mapping of forest biophysical properties are the dynamic range, i.e. the intensity contrast between forest and underlying floor, and the saturation level for which further growth of a forest does not result in any change in backscatter. Both, dynamic range and saturation level have been found to be a function of radar wavelength and polarization. The dynamic range generally increases with wavelength, which means from X-, C- and L- to P-band, and with polarization in the order VV, HH and HV (Le Toan et al., 1992). As volume scattering in the canopy is less

sensitive to incidence angle variations compared to soil backscatter, larger incidence angles result in a higher dynamic range as well. Still, environmental effects, as described in the last section, can alter the dynamic range significantly.

Saturation of intensity with respect to forest biophysical properties occurs when the transmissivity of the crown layer becomes negligible. Saturation has been reported to be a function of the wavelength; the longer the wavelength the later saturation occurs. As most studies focused on the retrieval of forest stem volume and biomass by means SAR measurements, saturation levels were usually reported in terms of a stem volume [m^3/ha] or biomass [t/ha] level up to which changes in intensity could be observed. In Proisy et al. (2000), a biomass saturation level of 50 t/ha for deciduous and 80 t/ha for coniferous forest in Central France was reported for ERS C-band measurements. Kasischke et al. (1994) and Harrel et al. (1995) found ERS-1 C-band to be sensitive to biomass changes up to 60 t/ha for Alaskan boreal forests. Imhoff (1995) reported saturation levels of 20 t/ha in case of C-band measurements over Hawaiian evergreen broadleaf forest and loblolly pine forests. Concerning forest stem volume, Fransson & Israelsson (1999) observed ERS-1 C-band to saturate at 60 m^3/ha for Swedish boreal forests. In contrast, Santoro et al. (2007b) were able to map Siberian boreal forest stem volume with no sign of saturation up to stem volumes of 400 m^3/ha using a multitemporal retrieval approach based on multitemporal stacks of ENVISAT ASAR Wide Swath C-VV intensity data. Similar results were obtained in Pulliainen et al. (1996) and Kurvonen et al. (1999) with multitemporal stacks of ERS data acquired over Finnish boreal forest sites. These studies indicated that C-band measurements might contain more information about boreal forest stem volume than has been reported in the studies mentioned before. However, when having only one or very few acquisitions, spatial variations in forest floor conditions - in terms of soil moisture, snow cover, litter depth - generally cause responses in backscatter in the range of or even larger than the intensity contrast between forest canopy and forest floor, strongly interfering the forest biophysical information (Rignot et al., 1994; Pulliainen et al., 1994, 1996, 1999; Wang et al., 1995; Hallikainen et al., 1998; Drezet & Quegan, 2006). A multitemporal consistency analysis, i.e. when correlating the standwise intensity measurements for different images, revealed a rather inconsistent behavior of ERS intensity measured over boreal forest with a mostly low correlation between standwise intensity measurements for even short repeat intervals (Askne et al., 2003). This observation stressed that effects like soil moisture variations have a large impact on C-band measurements over forest, interfering the forest biophysical information. In general, those environmental conditions can be considered the optimal acquisition conditions where soil moisture variations are minimized, for instance when the soils are frozen or very dry (Harrel et al., 1995, 1997; Pulliainen et al., 1996; Kurvonen et al., 1999). The advantage of multitemporal retrieval algorithms is that they are able to average out the variability in intensity related to the forest floor conditions.

2.2 SAR Interferometry

In Section 2.1.3, it was mentioned that the phase information in a single SAR acquisition is of no practical use because of 'random' phase effects in a resolution cell. This situation changes for an interferometric SAR constellation, when two radar antennas observe a target from slightly different positions in space. In an interferometric constellation the spatial distance between the two SAR antennas when acquiring over the same area is called interferometric baseline. The baseline can be split in two

components, a component in the line of sight B_p and perpendicular to the line of sight B_n (Figure 2.4). They are referred to as parallel and perpendicular baseline. If the two images forming an interferometric pair are acquired at the same time, we speak of ‘single-pass’ interferometry. An example for single-pass interferometry is the so-called Shuttle Radar Topography Mission SRTM (Rabus et al., 2003). Contrary, we speak of ‘repeat-pass’ interferometry when the images are acquired with a certain time lag. This time lag is often referred to as the temporal baseline. Since in this thesis, solely ERS-1/2 tandem data with 1-day time lag between the acquisitions are considered, only repeat-pass interferometry will be addressed in the following sections.

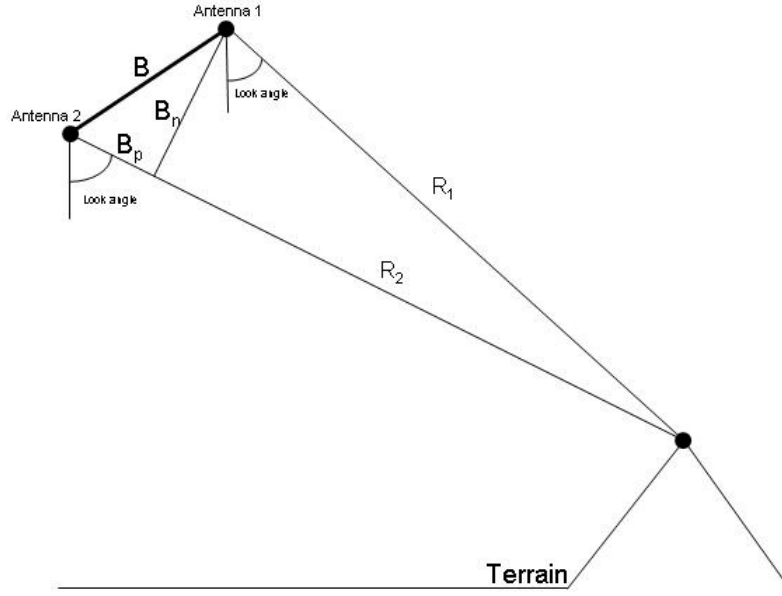


Figure 2.4. Geometry of interferometric SAR measurements.

2.2.1 Interferogram and interferometric phase

Two SAR images are needed to compute the so-called interferogram, which is obtained with the product of the first complex SAR image and the complex conjugate of the second SAR image. For the amplitude components of the SAR images this means simply a multiplication of both amplitudes. For the phase components, the product of one complex image with the complex conjugate of the other image results in the phase difference Φ , i.e. the interferometric phase:

$$\Phi = \phi_1 - \phi_2 = \frac{4 \cdot \pi}{\lambda} B_p + (\phi_{scatter,1} - \phi_{scatter,2}) \quad (2.23)$$

which is related to the difference in the slant-range distances, B_p , as well as to the differences in the target phase contributions. The interferometric phase difference between two pixels can be decomposed into following contributions:

$$\Delta\Phi = \frac{4\pi B_n}{\lambda R \tan(\theta)} \Delta R + \frac{4\pi B_n}{\lambda R \sin(\theta)} \Delta z + \frac{4\pi}{\lambda} \Delta \eta + \frac{4\pi}{\lambda} \Delta \rho + \Phi_{noise} + n \cdot 2\pi \quad (2.24)$$

The first term is related to the variation of the slant range difference, ΔR , within the interferogram. It is a systematic effect, which can be removed when accurate data about the orbital acquisition geometry is available. In an interferogram over completely flat terrain, the resulting interferometric phase variations appear as iso-phase lines, called ‘fringes’, in along-track direction, i.e. parallel to the flight direction. The removal of this systematic effect is called ‘flat-earth-removal’. The second term is related to the height difference, Δz , between two pixels and can be used to calculate Digital Elevation Models. In a ‘flattened’ interferogram (see example in Figure 2.5), i.e. flat earth-removal has been carried out, a complete phase cycle $[0-2\pi]$ corresponds to an altitude difference h_a of:

$$h_a = \frac{\lambda R \sin(\theta)}{2B_n} \approx \frac{9400}{B_n} \rightarrow ERS - 1/2 \quad (2.25)$$

This altitude is called the ambiguity height. Larger altitude differences cause phase ambiguities because it is measured between 0 and 2π . If the altitudinal variation in the area covered by the interferogram exceeds the ambiguity height, ‘phase unwrapping’, i.e. adding the correct integer multiple n of 2π to the flattened interferogram, needs to be done to resolve the ambiguity of phase and to calculate absolute height differences (last term in Equation 2.24). The third term in Equation (2.24) only applies if coherent movements, $\Delta\eta$, of all scatterers in a resolution cell along the line of sight occur between the acquisitions. This can be caused by earthquakes, subsidence, volcanic activity or other mass movement events. The fourth term accounts for differences in the atmospheric path delay between both acquisitions. Temporal and spatial variations in the electron density of the ionosphere as well as variations of the water vapor concentration in the troposphere can cause atmospheric artifacts in interferograms (e.g. Goldstein, 1995; Hanssen et al, 1999). The noise contribution is related to changes in speckle. It becomes relevant when changes at the Earth’s surface between the acquisitions occur that alter the scattering geometry. In addition, some other effects have to be addressed in this context (see Chapter 2.2.2).

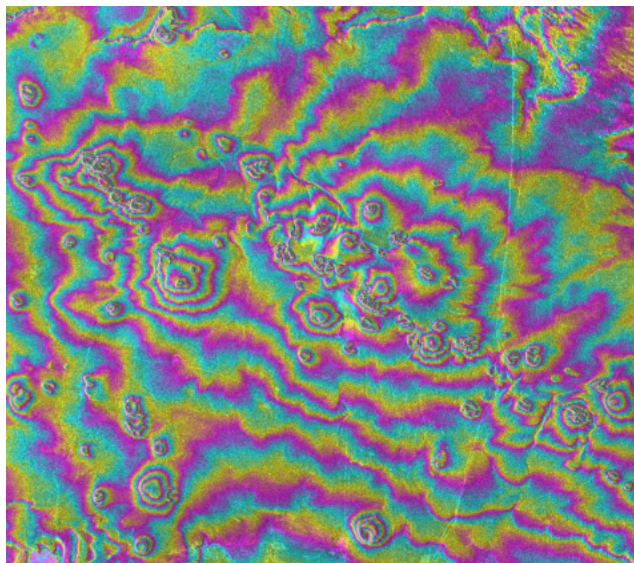


Figure 2.5. Flattened interferogram showing an area in Inner Mongolia, China, with several small volcanoes. The ERS-1/2 tandem pair was acquired with a perpendicular baseline of 236 m. One color cycle represents altitudinal differences of ~ 40 m.

2.2.2 Coherence

The interferometric phase measurement is governed by several factors, which have systematic character - imaging geometry and topography - or appear in form of noise or offsets superimposed on the systematic flat-earth and topography-induced fringes. A measure for the noise in an interferogram is the interferometric coherence; or in other words, the visibility of fringes in an interferogram is a function of coherence. The complex interferometric coherence is defined as (Born & Wolf, 1980):

$$\gamma = \frac{E\{u_1 \cdot u_2^*\}}{\sqrt{E\{|u_1|^2\} \cdot E\{|u_2|^2\}}} \quad (2.26)$$

where u_1 denotes the first complex SAR image, u_2^* the complex conjugate of the second SAR image and $E\{\}$ the expectation value operator. The argument of γ represents the expectation value of interferometric phase and the magnitude the normalized correlation of both acquisitions. In practice, the magnitude of complex coherence as well as the interferometric phase have to be estimated using a sampled average over N pixels; usually a rectangular window centered on the particular pixel, i . The Maximum Likelihood estimate of the magnitude of complex coherence can be obtained with (Dammert, 1996):

$$|\bar{\gamma}_{ML}| = \frac{\left| \sum_{i=1}^N u_{1,i} \cdot u_{2,i}^* \cdot e^{-j\phi_i} \right|}{\sqrt{\sum_{i=1}^N |u_{1,i}|^2 \sum_{i=1}^N |u_{2,i}|^2}} \quad (2.27)$$

It is common to refer to the magnitude of the complex coherence simply as the ‘coherence’. Coherence takes values between 0 and 1, i.e. complete decorrelation with fully developed noise and perfect correlation, respectively. If possible, the estimator should account for topography-induced phase variations, ϕ_i , in the interferogram as these fringes are not noise but would lower coherence as well when not compensating for in the coherence estimation window. If no information about topography, e.g. in form of a digital elevation model, is available, assumptions about topography induced phase variations within the coherence estimation window have to be made (Dammert, 1996), e.g. with linear, quadratic or other functions of phase variation. Alternatively, phase slope estimates can be derived from the interferogram itself, which, however, are prone to errors over steep mountainous terrain as phase noise over steep terrain will be significant. Residual phase variations because of uncompensated topographic phase in the coherence estimation window cause a loss of coherence according to (Dammert, 1996; Askne et al., 1997):

$$|\gamma_{topo}| = e^{-\frac{1}{2} \left(\frac{4\pi B_n}{\lambda R \sin(\theta)} \sigma_h \right)^2} \quad (2.28)$$

when assuming Gaussian distributed root mean square height variations, σ_h . This effect gains importance with increasing perpendicular baseline.

The Maximum Likelihood estimate of coherence is biased. The lower the true coherence $|\gamma|$, the more the estimated coherence represents an overestimate. The

standard error of coherence estimation, σ_γ , can be approximated with (Hagberg et al., 1995; Touzi et al., 1999):

$$\sigma_\gamma = \frac{1 - |\gamma|^2}{\sqrt{2L}} \quad (2.29)$$

where L represents the number of independent samples used for the estimation. The number of independent samples can be estimated roughly with the number, N , of pixels actually used for the estimation (Dammert, 1999 as quoted in Santoro, 2003):

$$L = 1 + \frac{N - 1}{2} \quad (2.30)$$

If surface types in a coherence image are present that are known to cause complete decorrelation (e.g. non-frozen water surfaces), L can alternatively be estimated based on the average observed coherence over these surfaces (Oliver & Quegan, 1998). The lower the coherence, the more pixels need to be included in the coherence estimation to achieve a desired accuracy. As coherence needs to be estimated over a window of a certain size, it is clear that the spatial resolution of coherence will be lower than the resolution of the SAR images.

Likewise, the standard error of the interferometric phase estimate, σ_ϕ , can be expressed as function of coherence (Rodriguez & Martin, 1992):

$$\sigma_\phi = \frac{1}{\sqrt{2L}} \frac{\sqrt{1 - |\gamma|^2}}{|\gamma|} \quad (2.31)$$

This approximation is reasonable for $L > 4$ (Rosen et al., 2000). According to this expression, the uncertainty in the phase estimate decreases with increasing coherence.

The degree of noise in an interferogram traces back to a number of factors (Zebker & Villasenor, 1992):

$$|\gamma| = |\gamma_{\text{processing}}| \cdot |\gamma_{\text{azimuth}}| \cdot |\gamma_{\text{noise}}| \cdot |\gamma_{\text{spatial}}| \cdot |\gamma_{\text{temporal}}| \quad (2.32)$$

Implying that modern SAR processors are able to preserve coherence, $|\gamma_{\text{processing}}|$ can be neglected, i.e. it can be set to unity. $|\gamma_{\text{noise}}|$ is only relevant for land surfaces generating very low backscatter, e.g. deserts or smooth water surfaces. As for the ERS sensor configuration with steep incidence angle backscatter from most land surfaces is high, this decorrelation source can usually be neglected. $|\gamma_{\text{azimuth}}|$ accounts for decorrelation because of non-perfectly parallel flight tracks respectively azimuth orientations of the two antennas, causing a shift in the azimuth spectra of the SAR images. In case of the ERS-1/2 tandem configuration, this shift was generally small so that band-pass filtering techniques could compensate for this effect (Schwäbisch & Geudtner, 1995).

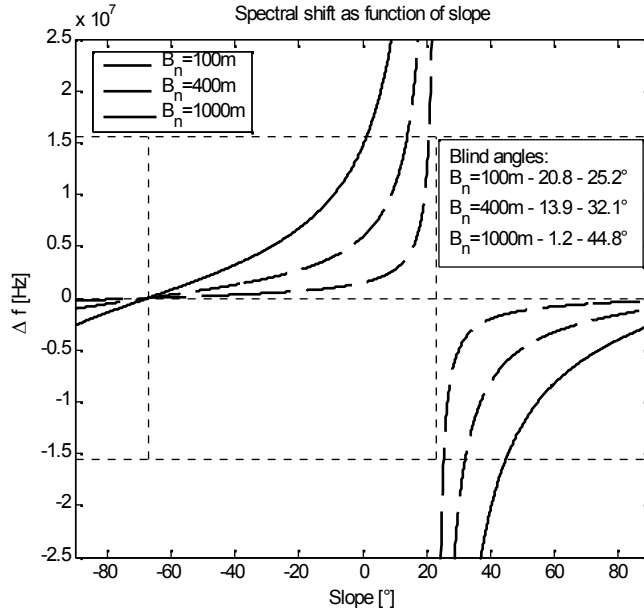


Figure 2.6. Relative spectral shift as function of local slope for perpendicular baselines up to 400 m; exemplified for the ERS-1/2 configuration. Positive slope values indicate surfaces tilted towards the sensor. The dashed horizontal lines denote the bandwidth W .

Spatial decorrelation summarizes two decorrelation effects, which are related to the length of the baseline, one denoted as $|\gamma_{\text{slant-range}}|$ and the other as $|\gamma_{\text{volume}}|$:

$$|\gamma_{\text{spatial}}| = |\gamma_{\text{slant-range}}| |\gamma_{\text{volume}}| \quad (2.33)$$

When distributed multiple elementary scatterers within the resolution cell are confined to a plane (i.e. the surface scattering case), the difference in incidence angle between both acquisitions causes a relative shift in frequency, Δf , between both backscattered signals (Gatelli et al., 1994):

$$\Delta f = -\frac{cB_n}{\lambda R} \cot(\theta - \alpha_s) \quad (2.34)$$

This relative frequency shift depends on the length of the perpendicular baseline and the local slope, α_s . The resulting non-common fractions of the range signal spectra cause a decrease of coherence, reaching zero coherence when the spectral shift exceeds the bandwidth W of the signal. Hence, coherence over flat terrain will be completely lost when the baseline exceeds a certain length, called the critical baseline. In case of ERS, the critical baseline is ~ 1100 m. Local slope alters the relative frequency shift between both signals and therefore the slant-range decorrelation (see Figure 2.6). The strongest decorrelation occurs for slopes facing the radar. With increasing baseline, the blind angles, i.e. slopes where total decorrelation occurs, expand. The effect of the wavenumbershift can be reduced with common band filtering (Gatelli et al., 1994).

When elementary scatterers in a resolution cell are not confined to a plane but distributed in vertical direction and total backscatter is a superimposition of backscatter contributions from different heights, z , which correspond to the interferometric phase of $2\pi z/h_a$ (Krieger et al., 2007), another baseline dependent decorrelation factor arises,

referred to as volume decorrelation. Volume decorrelation can be formulated as the Fourier transform of the height distribution, z' , of the temporally stable backscatter with σ_{ve} being the effective backscatter coefficient for temporally stable scatterers (Askne et al., 1997):

$$\gamma_{volume} = \frac{\int_0^h \sigma_{ve}(z') e^{-j\left(\frac{4\pi \cdot B_n}{R \cdot \lambda \cdot \sin(\theta)} z'\right)} dz'}{\int_0^h \sigma_{ve}(z') dz'} \quad (2.35)$$

The vertical backscatter distribution must be known respectively approximated in order to describe volume decorrelation effects (Askne et al., 1997; Gaveau, 2002; Hajnsek et al., 2008). It has to be noted that the division of spatial decorrelation into separate slant-range and volume decorrelation terms is only valid under the assumption that the stable part of volume backscatter is solely a function of the height above the surface plane.

Temporal decorrelation traces back to changes at the Earth's surface between both acquisitions. This includes movements of the scatterers as well as changes in the dielectric properties. When assuming Gaussian motion statistics, coherence decays exponentially with increasing rms movements of the elementary scatterers in a resolution cell in horizontal, σ_y , and vertical, σ_z , direction (Zebker & Villasenor, 1992):

$$|\gamma_{movements}| = e^{-\frac{1}{2} \left(\frac{4\pi}{\lambda} (\sigma_y^2 \sin^2 \theta + \sigma_z^2 \cos^2 \theta) \right)^2} \quad (2.36)$$

According to Equation (2.36), temporal decorrelation gains importance with decreasing wavelength. In case of C-band repeat-pass coherence, total decorrelation should occur with ~ 3 cm rms motions (Zebker & Villasenor, 1992; Floury et al., 1997). The sensitivity to either horizontal or vertical movements changes with the incidence angle.

2.2.3 Coherence over land surfaces

The time scales of temporal decorrelation as well as the magnitude of volume decorrelation effects depend on the land cover type, which is why repeat-pass coherence has been found suited for the mapping of different types of land cover including forest land (Wegmüller & Werner, 1995; Dammert et al., 1999; Strozzi et al., 2000; Weydahl, 2000; Engdahl & Hyyppä, 2003; Srivastava et al., 2001, 2006; Santoro et al., 2007a). SAR intensity measurements over forest can be considered a sum of a forest floor and a vegetation contribution. This also applies in case of decorrelation, which is why the different decorrelation mechanisms relevant for the forest canopy and the ground surface have to be considered.

Over bare surfaces, high coherence is usually observed for long temporal baselines. Rocks or dry soils do not change for long periods and coherence remains high (Zebker & Villasenor, 1992; Weydahl, 2001). If no soil moisture is involved, sand erosion and accumulation can lower coherence, as reported in Liu et al. (2001) for ERS repeat-pass measurements with 35 days repeat cycle over an Algerian desert area. Outside of the arid zones, Luo et al. (2001) identified heterogeneous soil moisture variations in resolution cells characterized by rough soil as source of temporal decorrelation in C-

band. Homogeneous soil moisture changes between the acquisitions do not result in significant decorrelation even if the differences in intensity are large (Hagberg et al., 1995; Borgeaud & Wegmüller, 1996; Sarabandi & Wilson, 2000; Luo et al., 2001; Srivastava & Jayaraman, 2001). As observed in Smith et al. (1996), coherence loss in C-band because of heterogeneous soil moisture variations tends to be a monotonic function of the temporal baseline. Smith et al. observed that coherence over open fields decreased from 0.8 to 0.5 for temporal baselines between 3 and 15 days. Similar observations were reported in Srivastava & Jayaraman (2001). Freezing of the soil in the period between the acquisitions was as well found not to affect C-band repeat-pass coherence as strong as intensity. In Borgeaud & Wegmüller (1996) and Wegmüller & Werner (1995), high coherence for ERS-1 measurements with a three-day repeat interval (acquired during the so-called ERS-1 ICE-Phase) was observed when soil freeze occurred between the acquisitions and intensity dropped for more than 4 dB. In contrast, changes in roughness, e.g. because of tillage, between the observations cause strong decorrelation (Moeremans & Dautrebande, 2000; Blaes & Defourny, 2003). Strong decorrelation can as well be assigned to rain events in the period of the acquisitions. In Drezet & Quegan (2006) a Pearson correlation of -0.79 between ERS-1/2 tandem coherence of forest floor and the maximum daily rain rate in 10 days prior to the satellite measurements was reported. In Askne & Santoro (2005), a Pearson correlation of forest floor coherence (ERS-1/2 tandem) and the mean rain rate in six days prior to the acquisitions of -0.81 was found. Rain between the acquisitions results in ground coherence to drop even below 0.2 as shown in Koskinen et al. (2001), Santoro et al. (2002) and Pulliainen et al. (2003) for ERS-1/2 tandem coherence over Scandinavian boreal forest sites.

Water surfaces are generally prone to complete decorrelation in even the shortest time scales because of constant surface movements. Exceptions arise for frozen water surfaces for which Weydahl (2001) reported an ERS-1/2 tandem coherence of 0.31 to 0.39. Built-up areas represent the type of land cover that usually exhibits the highest coherence for very long repeat intervals in the range of months or even years (Usai & Klees, 1999; Strozzi et al., 1999; Weydahl, 2001). Built-up areas, however, introduce a sub-pixel topography that cannot be compensated for when estimating coherence, which is why coherence decreases dependent on baseline length and causes built-up areas not to exhibit values as high as for stable open fields in case of short repeat intervals (Wegmüller & Werner, 1995).

High coherence over open ground is usually observed in case of frozen or stable dry conditions when the fluctuations of free soil water are minimized. When a snow cover is present, decorrelation can occur because of wind induced erosion and accumulation of snow or snowfall (Guneriusen et al., 2001; Rott et al., 2003; Li & Sturm, 2002). Interferometric phase shifts, Φ_{snow} , because of a dry snow layer of depth d_s with permittivity ε' (which depends on snow density) can be calculated according to Guneriusen et al. (2001):

$$\Phi_{snow} = -\frac{4\pi}{\lambda} d_s \left(\cos \theta - \sqrt{\varepsilon' - \sin^2 \theta} \right) \quad (2.37)$$

when accounting for refraction and the different propagation constants in snow and air. Volume scattering effects in C-band can usually be neglected unless the snow cover reaches a depth of tens of meters and/or ice lenses, pipes or grain clusters develop within the snowpack (Rignot et al., 1994; Mätzler et al., 1997; Hoen & Zebker., 2000).

When wind induced erosion or accumulation - snowfall can have the same effect - between the acquisitions occur, the interferometric phase shift due to the snow pack can be significantly altered at the sub-pixel scale and decorrelation occurs. Simulations, carried out by Rott et al. (2003), indicated relevant temporal decorrelation in C-band for snowfall events typical for the Alps. Finally, the melt of snow has been found to cause strong decorrelation in ERS-1/2 tandem coherence (Strozzi et al., 1999; Guneriussen et al., 2001, Pulliainen et al., 2003; Engdahl et al., 2004), as it is accompanied by large scattering geometry and permittivity changes.

Forests are subject to temporal and volume decorrelation. ERS-1/2 tandem coherence measured over dense forest typically varies between 0.1 and 0.5. The relevance of volume decorrelation in C-band has been reported to be of minor importance compared to temporal decorrelation for baselines up to ~300 m (Askne & Smith, 1996; Gaveau, 2002; Drezet & Quegan, 2006). Model simulations in Askne & Santoro (2005), carried out for a Scandinavian boreal forest with a maximum stem volume of ~550 m³/ha, predicted volume decorrelation factors of 0.48 in case of perpendicular baselines up to 220 m, showing that even when temporal decorrelation dominates, volume effects can have a significant impact on ERS-1/2 tandem coherence.

Temporal decorrelation over forest is mainly caused by movements of the scatterers. Wind speed can be considered the most critical parameter, determining temporal decorrelation over forest. Observations, confirming this expectation, have been reported in Proisy et al. (1999), Askne et al. (2003) and Drezet & Quegan (2006) where a decrease of dense forest coherence up to a wind speed of ~4 m/s was found for ERS-1/2 tandem data acquired over Swedish boreal and French and British temperate forest, respectively. The time scales of decorrelation because of wind are very short (Narayanan et al., 1992, 1994). Significant temporal decorrelation has been observed for temporal baselines as short as 28 minutes in Santoro et al. (2007a) for ERS-ENVISAT coherence. As wind represents a spatially heterogeneous force, unfavorable effects (at least with respect to forest mapping applications) are possible. Castel et al. (2000) observed wind directional effects in ERS-1/2 tandem coherence over mature pine forest in France. The coherence of forest was observed to be a function of the wind exposition of forests located on hilly terrain.

The highest coherence over forest has been reported for winter frozen conditions (Koskinen et al., 2001; Pulliainen et al., 2003; Santoro et al., 2007) when an increased transmissivity of the frozen canopy causes the main backscatter to come from the larger and stiffer branches. As soon as rain, freeze/thaw or snow melt is involved, coherence drops to a low level (Drezet & Quegan, 2006; Koskinen et al., 2001, Pulliainen et al., 2003; Santoro et al., 2007; Askne et al., 2003, Engdahl et al., 2004). Drezet & Quegan (2006) observed that ERS-1/2 tandem coherence over dense temperate forest never exceeded 0.2 when rain at one of the acquisition days exceeded 3 mm. An example for the impact of freeze/thaw has been illustrated in Santoro et al. (2007) for Siberian boreal forest. Forest stands located on slopes exposed to the East showed lower coherence than those located on slopes tilted towards the West in an ERS-1/2 tandem coherence image acquired in late October when day and night temperatures oscillated around 0° C. The observation was considered a result of unequal sun illumination in the morning hours, when the tandem pair was acquired. Stands on east-facing slopes were likely to be thawed whereas the stands located on the west-facing slopes were probably still frozen because of the sub-zero temperatures in the night before.

The coherence contrast between open areas and dense forest varies with the meteorological and environmental imaging conditions and with the length of the perpendicular baseline. The best contrast can be expected for very stable ground conditions, i.e. when no heterogeneous soil moisture or snow related variations occur, and windy conditions lowering coherence over dense forests. With respect to forest mapping applications, these conditions are often referred to as the ‘optimal’ conditions (Koskinen et al., 2001; Santoro et al., 2002, 2007; Pulliainen et al., 2003; Engdahl et al., 2004). Perpendicular baselines of at least 100 m (in case of C-band) further increase the contrast because of additional volume decorrelation in the forest canopy (Askne & Santoro, 2005, 2007; Santoro et al., 2007). Short repeat intervals are suited best for forest mapping applications as the risk of strong decorrelation at the forest floor due to rain, freeze/thaw, snowmelt, soil moisture variations, etc. is lower. Although this assumption is generally reasonable, exceptions may arise when, for instance, temporally oscillating meteorological conditions (e.g. diurnal freeze/thaw cycles under hibernal conditions) cause more or less equal conditions in repeated intervals.

Coherence over forest can be expected to depend on tree species as the differing crown architectures of the species should cause differences in the sensitivity to wind induced movements of the scatterers. Törmä (1999), for instance, classified pine and spruce with reasonable accuracy using ERS-1/2 tandem coherence. Koskinen et al. (2001) observed higher coherence over deciduous forest than over coniferous forest in ERS-1/2 tandem coherence from winter. Castel et al. (2000) reported higher ERS-1/2 tandem coherence over coniferous forest than over deciduous forest stands in Southern France for two acquisitions from summer. In winter, the opposite observation was made. These observations suggested that in the leaf-off period in winter, deciduous species exhibit lower sensitivity to wind-induced motions than coniferous species whereas in summer the leaves are likely to introduce a higher sensitivity to wind induced motions than the needles of conifers. All these studies, however, did not consider the possibility that the forest types distinguished may have represented different stem volume ranges.

2.2.4 Stem volume and biomass retrieval by means of C-band repeat-pass coherence

C-band repeat-pass coherence measurements, mainly those of the ERS-1/2 tandem mission, have been reported to be strongly correlated to boreal and temperate forest stem volume (Hyypä et al., 2000; Manninen et al., 2000; Koskinen et al., 2001; Fransson et al., 2001; Santoro et al., 2002, 2007; Askne et al., 2003; Pulliainen et al., 2003; Wagner et al., 2003; Engdahl et al., 2004; Askne & Santoro, 2005) and biomass (Luckman et al., 2000; Castel et al., 2000). Coherence has been found to decrease exponentially with increasing forest stem volume; in some cases the relationship can appear rather linear though (Fransson et al., 2001). Comparable to C-band intensity measurements, the relationship is driven by the coherence contrast between the temporally stable forest floor and the unstable forest canopy backscatter contributions in the measurements. With increasing forest cover, the contribution from the highly coherent forest floor decreases and the contribution from the less coherent forest canopy increases. In addition, the tree height and baseline dependent volume decorrelation and InSAR geometry affect the relationship. Thus, coherence is sensitive to canopy closure, which is correlated to the diameter and density of the trees (Zeide et al., 1985; Van Laar & Akca, 2007; Hirata et al., 2009), and through volume decorrelation and InSAR geometry to the tree height. This explains the high correlation to stem volume as

coherence reflects the horizontal (diameter, density) and vertical dimension (tree height) of forest growth.

The multitemporal consistency of ERS-1/2 tandem coherence measurements over boreal forest has been observed to be superior to that of ERS intensity measurements (Askne et al., 2003; Santoro et al., 2004; Askne & Santoro, 2005) as long as no strong decorrelation of the ground contribution in the signals because of rain or snowmelt occurred. Multitemporal consistency analysis, i.e. when correlating the coherence in one image to the coherence in another image, helps to evaluate if measurements are consistent with respect to the forest biophysical information or noisy due to, for instance, soil moisture or other environmental effects. These results indicated that coherence is less prone to stem volume independent variations than intensity.

It has been shown that boreal forest stem volume retrieval by means of ERS-1/2 tandem coherence can reach accuracies in the range of ground surveys (Santoro et al., 2002), i.e. $\sim 15\%$ relative error. The contrast of forest floor and dense forest coherence has been reported to be an indicator for the suitability of an ERS-1/2 tandem coherence image for stem volume retrieval (Engdahl et al., 2004). As described in the last section, a maximum contrast can be observed in case of stable frozen ground and windy conditions, lowering coherence over forest – these conditions are from now on referred to as the ‘optimal’ conditions - and perpendicular baselines in the range of 100 to 250 m, further increasing the contrast due to the baseline dependent volume decorrelation. For a test site in Finland, ERS-1/2 tandem coherence, acquired under stable frozen conditions, was found to be sensitive to stem volume changes up to the maximum stem volume in the test region of $540\text{ m}^3/\text{ha}$ (Pulliainen et al., 2003). Consistent stem volume estimates, however, were reported feasible for stem volumes up to only $200\text{ m}^3/\text{ha}$ in Santoro et al. (2002) when comparing pixel-wise stem volume estimates from ERS-1/2 tandem coherence, acquired under optimal conditions, and stem volume measurements from Swedish National Forest Inventory plots. This was considered a consequence of the increasing uncertainty in the coherence estimation, the lower the coherence gets (see Equation (2.29)), and a reduced sensitivity of coherence to stem volume changes at higher stem volumes. The saturation level of coherence can drop to low stem volume levels, often around $100\text{ m}^3/\text{ha}$, in case of unstable imaging conditions, for instance because of rainfall before the acquisitions respectively the emerging heterogeneous soil moisture variations afterwards. Still, such conditions have been found to allow consistent mapping of at least a few low stem volume classes (Wagner et al., 2003; Gaveau et al., 2003; Tansey et al., 2004). Rainfall or snowmelt between the acquisitions, however, cause strong decorrelation, diminishing most of the forest related information in the coherence images (Santoro et al., 2002; Pulliainen et al., 2003). In the tropical regions, where such adverse imaging conditions occur frequently, the stem volume or biomass mapping capabilities of ERS-1/2 tandem coherence are much reduced (Rignot, 1996). Still, some forest related information could be derived from ERS-1/2 tandem coherence acquired over tropical forest (Ribbes et al., 1997; Tansey et al., 2004).

The effect of forest structural diversity on the accuracy of forest stem volume retrieval by means of ERS-1/2 tandem coherence has been discussed in Santoro et al. (2007) with respect to the forest structural parameter relative stocking. Siberian boreal forests with high relative stocking were found to allow higher stem volume retrieval accuracy than stands with low relative stocking. It was argued that forest stands with higher relative stocking represented a more homogeneous and managed type of forest. The definition

and a more detailed discussion of this parameter will follow in Chapter 3.3. Yet, the highest accuracy of stem volume retrieval by means of ERS-1/2 tandem coherence was achieved for tandem pairs that were acquired under stable weather conditions with high ground coherence over a very homogeneous and managed type of boreal forest in Sweden (Santoro et al., 2002; Askne et al., 2003). The results achieved at other test sites in Sweden and Finland were generally worse (Pulliainen et al., 2003; Askne & Santoro et al., 2005, 2007a, 2007b), even when having ERS-1/2 tandem pairs that were acquired in winter. The lower accuracy could, at least partially, be assigned to a higher forest structural diversity at these test sites. In Askne & Santoro (2007a), it was shown that stem volume retrieval at one of those test sites in Finland improved when only considering large homogeneous stands with high stem volume proportions of pine and spruce.

Chapter 3 - Study area, ground and satellite data

In this chapter, the study area and the available ground reference and earth observation data are presented. In Chapters 3.1 and 3.2, the main properties of test sites in Northeast China and Central Siberia are summarized, followed by a discussion of structural differences between the forests in the two regions in Chapter 3.3. In Chapter 3.4, the available satellite and weather data are described.

3.1 Chinese test sites

3.1.1 Northeast China

Northeast China comprises the provinces of Heilongjiang, Jilin, Liaoning and the eastern part of the autonomous Inner Mongolian provinces. Dongbei, that is how the Northeast is called in China, covers an area of ~ 1.5 million km² and is located between the North Korean border in the Southeast, the Russian border in the North and the Mongolian border in the West. In geographic coordinates, Northeast China ranges from 38 to 53° North and from 115 to 135° East. Three major mountain ranges, surrounding the Northeast China Plain, a large synclorium filled with Quaternary sediments and altitudes between 200 and 300 m, characterize the landscape: namely the Greater Hinggan (*chin.* Daxinganling), Lesser Hinggan (*chin.* Xiaoxinganling) and Changbai (*chin.* Changbaishan) Mountains (Figure 3.1), which reach maximum elevations of 1400 m, 1160 m and 2691 m, respectively (Kostak et al., 2003).

The three mountain ranges represent the main wood supply for China and the large fertile Northeast China Plain is referred to as the grain base of China. Soybean and sugar beet are the main crop types grown. The arid grasslands of Inner Mongolia west of the plain and the Sanjiang Plain in the Northeast represent the border area to Mongolia and Russia respectively. According to Burger & Zhao (1988 as quoted in Qian et al., 2003) 38.4 % of Northeast China is covered with forest but changes have occurred since 1988. In most of the forest areas, deep dark brown forest soils can be found which developed on basaltic and granitic bedrock and which show an Ah horizon containing a high percentage of organic matter. In the Daxinganling area brown coniferous forest soils with eluvial Ae and iron-enriched B-horizons can be found. Large fractions of the Northeast China Plain are characterized by black chernozem and chestnut soils (Qian et al., 2003). In the Southwest of the Plain, close to the sandy Inner Mongolian grasslands, large areas of sand can be found.

The monsoon climate of Northeast China exhibits steep latitudinal and longitudinal gradients and changes latitudinally from warm to cool temperate and longitudinally from humid to semiarid (Wang et al., 2006). The mean annual temperatures are below zero in the northernmost regions along the Amur River and around 10° in the southern regions close to the Yellow Sea (Box & Choi, 2003). Annual precipitation decreases longitudinally from 900 mm in the East to 200 mm in Inner Mongolia (Chao, 1994). The topography has a strong influence on the rain distribution. The highest rain rates are measured at the high altitudes of the Changbai Mountains. In winter, the climate is strongly continental with dry cold northwesterly winds coming from Mongolia and the continental Russian Far East. In summer, the wind comes from the Yellow Sea, causing most of the annual precipitation to fall in this season.

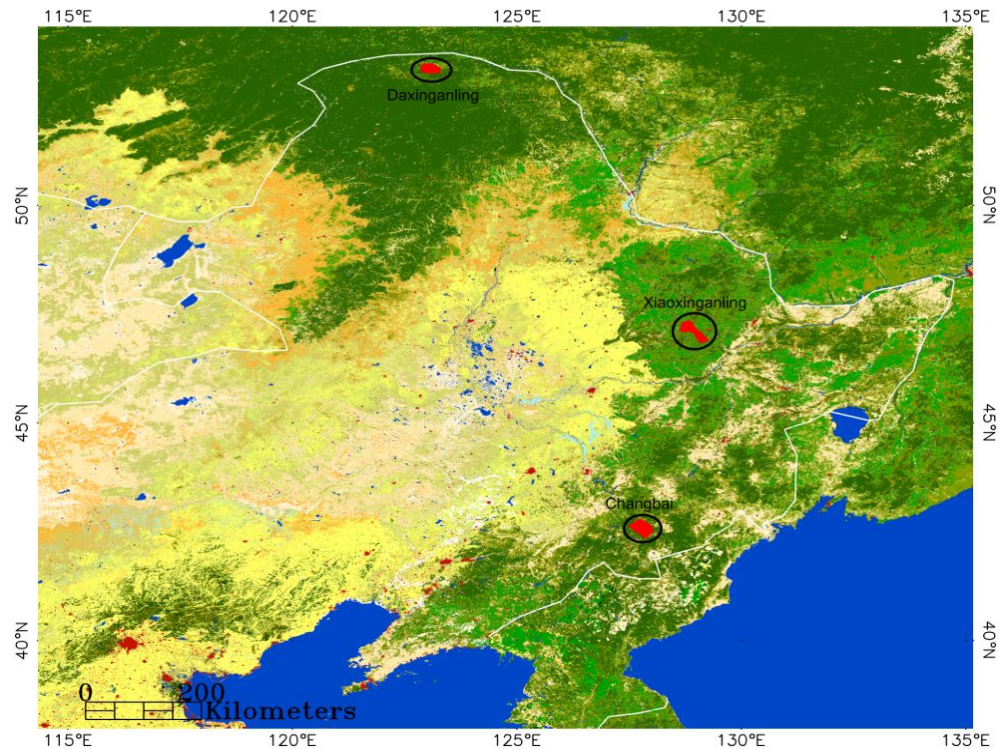


Figure 3.1. Location of the test sites in Northeast China. The map shows the latest global land cover product, the MERIS GLOBCOVER map, with 300 m pixel size (Bicheron et al., 2008).

3.1.2 Test sites in Northeast China

The Chinese Academy of Forestry, Beijing, has made available forest inventory data for three test sites located in the most important forest ranges in Northeast China: the Tuqiang forest compartment in the Daxinganling area, the Dailing forest compartment in the Xiaoxinganling area and the Lushuihe forest compartment in the Changbai Mountains. For all three test sites, forest maps have been selected and digitized. The data were collected in the framework of the Local Forest Management Planning Inventory (Pang et al., 2003, 2005), which is completed every 10 years for each Forest Enterprise.

The smallest unit in the forest maps is the forest stand sub-compartment, which is also the smallest operational unit in China's forest management. In a sub-compartment soil, relief and tree conditions are uniform and each forest stand sub-compartment experiences uniform management. The boundaries are mostly inferred from air photos and topographic maps. The attributes of each sub-compartment are obtained by field measurements taken at sample plots in each sub-compartment. For all three test sites, stem volume of all standing trees in m^3/ha without open grown trees (old trees in young stands) and average tree height in meters were provided. The accuracy of these measurements is unknown as well as the date of the latest update. The polygon based maps were rasterized and edge-eroded within a 50 m wide buffer zone along the stand edges in order to minimize the effect of mis-registrations between inventory and satellite data and to account for the spatial estimation principle of coherence which results in uncertainties when estimating over boundaries. The average size of the rasterized polygons has been reported in Table 3.1.

3.1.2.1 Daxinganling

The Changqing forest farm in the Tuqiang forest compartment is located at the southern banks of the Heilongjiang River in Heilongjiang province (53°8' N, 123°4' E). The area is located in the northern Daxinganling and is characterized by gentle hills and relatively smooth topography. Slopes are on average below 5° (the standard deviation is 3°). Elevations range from 338 m to 768 m. The soils are mainly brown coniferous forest soils (Chao, 1994; Qian et al., 2003). The climate is extremely continental with long dry winters without much snow. The region represents the coldest area of China. The mean annual temperature is below 0° C and the mean temperature in January is below -30° C (Qian et al., 2004). Summers are short with about 100 frost-free days. The annual precipitation is about 360 to 500 mm and occurs almost completely in the warm months. Forests are dominated by larch (*Larix Gmelii*) and represent the southern extension of the boreal zone. The major broad-leaved species is birch (*Betula Platyphylla* and *Betula Dahurica*). Also pine (*Pinus Sylvestris* var. *Mongolia*), oak (*Quercus Mongolica*) and poplar (*Populus Davidiana*) can be found in the test site. An altitudinal zonation is not present since the topography is mostly gentle. The area has been widely affected by a catastrophic forest fire in May 1987 (Wang et al., 2006). 2.31 x 10⁵ ha and 70% of the forests in the area of the Tuqiang Forest compartment were destroyed. In order to avoid forest diseases, all burnt trees were removed shortly after the fire. Figure 3.2 shows the area in the year 2005. Young regrowing stands of birch and larch dominate the scenery. Because of the fire, the maximum stem volume in the test site is low (125 m³/ha).

For a second test site, located close to the Changqing forest farm in the Tuqiang forest compartment, the Chinese Academy of Forestry provided tables of diameter at breast height (dbh), height and stem volume without any georeference information which is why a comparison of coherence with the forest parameters given in the inventory data was not possible but the inventory data extended for the diameter information could be used to reconstruct forest structural properties (see Chapter 3.3). The forest at this test site was similar to the forest at the Changqing forest farm and was strongly affected by the fire in 1987. The maximum stem volume here was 200 m³/ha.



Figure 3.2. Young regrowing birch and larch at Daxinganling (left) and Mixed-Broadleaf-Korean-Pine forests at Xiaoxinganling (right).

3.1.2.2 Xiaoxinganling

The second test site is located in the Xiaoxinganling mountain range in the Liangshui Natural Reserve, Heilongjiang (47°10' N, 128°53' E). The altitude in the area ranges from 200 to 1200 m and the average slope is 10° (standard deviation is 5°). Annual precipitation is in the range of 600 to 800 mm, which mostly falls in July and August. The mean annual air temperature is 2.8 °C (-31° in January and 32.8° in July) (Wang, 2006; Chao, 1994). The frost-free period is one month longer than at Daxinganling. The reserve comprises primary forests of mixed-broadleaf-Korean-pine (*Pinus Korianensis*) accompanied by more than a dozen hardwood species like maple (*Acer Manchuricum*) or oak (*Quercus Mongolica*) as well as secondary forest in all development stages of larch (*Larix Dahurica*), fir (*Picea Abies*) or spruce (*Picea Korianensis*) or plantations of pine, larch and spruce (Qian et al., 2003). The area belongs to the northern extension of the temperate mixed forest region. An altitudinal zonation of forest types can be found for the mountain peaks in Xiaoxinganling. Above 800 m, the proportion of fir and spruce increases and that of pine and broadleaf species decreases. The stem volume is mostly below 200 m³/ha, indicating a low productivity of the stands in the area. The test site has been the base for forest research since the 1950s and is a reserve since 1997.

3.1.2.3 Changbai

The third test site is located in the Changbai mountain range near the Chinese-North-Korean border (42°60' N, 128°10' E) in Jilin province. The study site belongs to the Changbai Mountain Natural Reserve. It was established in 1960 and therefore has a longer history of protection than the other two test sites. The climate is warmer than at Xiaoxinganling with annual average temperatures of 5° C. Precipitation at the montane forest belt below 1100 m is the same as for Xiaoxinganling. With increasing altitude, the annual average temperature decreases and the precipitation increases up to 1300 mm for the highest peaks of the Changbai Mountain (which are not located in the test site). In the Changbai Mountain range, forests show a distinct altitudinal zonation (Qian et al., 2003). Below ~ 1100 m, Korean pine is the major tree species accompanied by a large number of hardwood species. Compared to the Xiaoxinganling mountain range, the composition of the hardwood species is more diverse with, for instance, 13 different maple types occurring (Qian et al., 2003). Above ~ 1100 m altitude spruce and fir are the dominant species with a declining occurrence of pine. Only few broadleaf species like birch (*Betula Costata*) grow in this altitude. Above this altitudinal zone a sub-alpine dwarf-belt can be found with almost exclusively birch (*Betula Ermanii*) growing here. This belt is not represented in the test site. Stem volume reaches 500 m³/ha but the majority of stands has less than 400 m³/ha. The average slope in the area is 10° (standard deviation is 7.5°).

Table 3.1. Forest properties at the test sites in Northeast China.

	Daxinganling	Xiaoxinganling	Changbai
Area [km ²]	606	221	311
Number of stands	1339	2170	2523
Mean & Max. stand size [ha] (after edge-erosion)	10 / 68	7.1 / 62	3.5 / 34
Stem volume [m ³ /ha] (mean / min-max)	20 / 1-125	126 / 1-548	190 / 1-502
Tree height [m] (mean / min-max)	7 / 0-21	13 / 0-46	17 / 0-30

3.2 Central Siberian test sites

As for the large area of Northeast China only three test sites were available that were furthermore covered by only three ERS-1/2 tandem pairs (cf. Chapter 3.4), *in situ* measurements for several test sites located in the Siberian forest territories of Chunksky (57° 45' N, 96° 43' E), Bolshe-Murtinsky (57° 5' N, 92° 55' E) and Primorsky (55°46' N, 102°30') were considered as well. Each of the forest territories comprised four to five forest compartments with a size between 200 and 400 km². These compartments are named according to their location within the forest territory, e.g. Chunksky North or Bolshe-Murtinsky Northeast. Out of the 13 forest compartments at Primorsky, Bolshe-Murtinsky and Chunksky, five have been selected because of the quality of the inventory data for these compartments. These compartments are Bolshe-Murtinsky Northeast, Bolshe-Murtinsky Northwest, Chunksky East, Chunksky North and Primorsky East according to their location within the forest territories (see Figure 3.3). From now on, they are referred to as Bolshe NE, Bolshe NW, Chunksky N, Chunksky E and Primorsky E. Much experience with these sites has been gathered in several studies preceding this one (Schmullius et al., 2000; Wagner et al., 2003; Eriksson et al., 2003; Santoro et al., 2007), witnessing the quality of the inventory data for these test sites. The test sites are located in the southern taiga within the administrative territories of Irkutsk and Krasnoyarsk. The climate is extremely continental with annual snow cover periods of eight months and growing periods in the short and moist summers as short as ~90 days. The temperatures during the cold and dry winters reach -50° C. Forest cover is generally in the range of 60-70% and reaches an all Russian maximum in the Irkutsk territory with 81% (Shvidenko et al., 2007). Mature and over-mature forests in this region are mainly composed of coniferous species like pine (*Pinus Sylvestris*), larch (*Larix Dahurica*), fir (*Abies Sibirica*), spruce (*Picea Sibirica*) and cedar (*Pinus Sibirica*). Younger forests are dominated by birch (*Betula Pendula*) and aspen (*Populus Tremula*), which grow first after disturbance. In natural forest succession, these pioneer birch and aspen forests are replaced by coniferous species after 60 to 100 years.

The forest inventory data available was collected in the framework of the Russian Forest Inventory and Planning (FIP), which is completed every 10 to 20 years for each forest enterprise. The ground data consisted of digital forest stand boundary maps in which each polygon represented the primary inventory unit of the Russian inventory. The borders of these polygons were derived from aerial photographs and reflected forest stands of comparable relative stocking, site index, species composition, age, etc. The forest attributes were measured on the ground by an ocular field inventory at sample plots. These attributes comprised information about stem volume per hectare of all living trees with a diameter at breast height > 6 cm including bark (for young stands also stems with diameter at breast height <6 cm are included), age of the dominant species in the stand, quadratic mean diameter at breast height (dbh) and average height for all dominant species, species composition and relative stocking. Quadratic mean diameter is calculated from stem density per hectare and basal area B_a , i.e. the product of the average cross-sectional area at breast height and stem density per hectare, with $dbh = \sqrt{4B_a/\pi N}$ (West, 2004). Species composition is given in steps of 10 % of total stem volume. In case of dbh and height, the measurements for the dominant species were converted to the mean stand height and dbh using a weighted average of the single species. Age is not given for the dominant species in a stand but the one with the highest economic value. Cedar has the highest value, followed by pine. The lowest value is assigned to deciduous species (Schmullius et al., 2001). Relative stocking relates the basal area of a stand to an 'optimal' basal area. The definition of the

optimum depends on the development stage of the forest, the site quality and the forest type. It is given in steps of 10 % from 0 to 100 %. The parameter relative stocking will further be discussed in Chapter 3.3.

The accuracy of the forest inventory data is not known. Legally the accuracy of the stem volume estimates should be between 12 and 20 % (confidential probability 0.95). A confidence interval as wide as $\pm 20 \text{ m}^3/\text{ha}$ has been considered possible though (Balzter et al., 2002), in particular for stands that are difficult to access. In order to minimize the influence of mis-registrations between satellite data and FI data, the FI data was rasterized to the pixel size of the ERS data ($50 \times 50 \text{ m}^2$) and all pixels at the edge of a forest stand were removed. The buffer zone was 50 m wide.

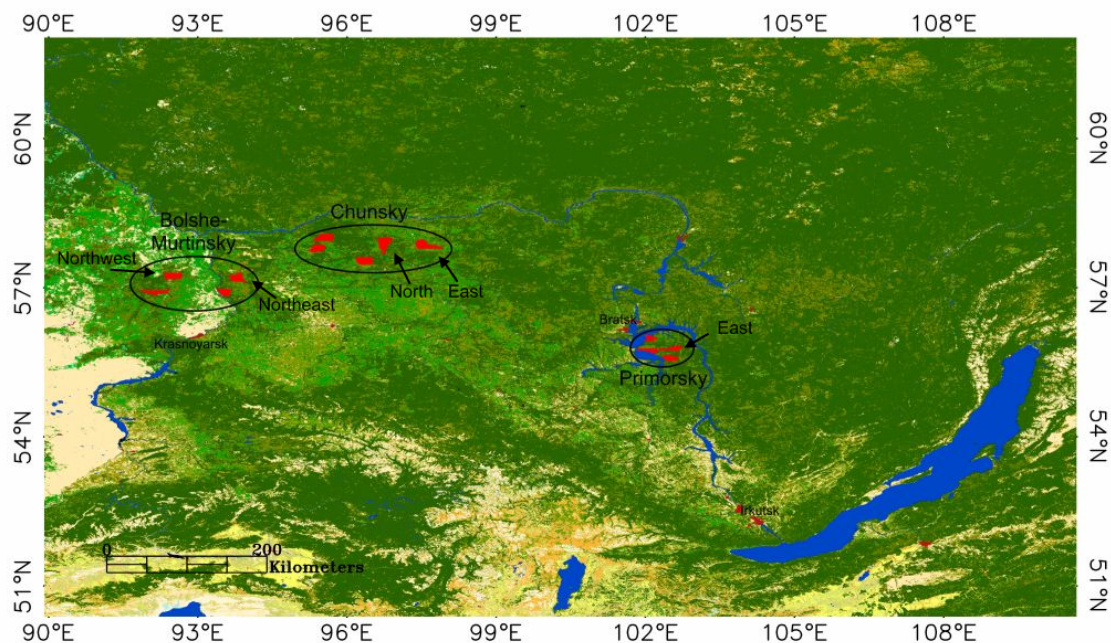


Figure 3.3. Location of the Siberian forest compartments considered for this study. The map shows the latest global land cover product, the MERIS GLOBCOVER map, with 300 m pixel size (Bicheron et al., 2008).

3.2.1 Bolshe-Murtinsky

The Bolshe-Murtinsky forest territory ($57^{\circ} 5' \text{ N}$, $92^{\circ} 55' \text{ E}$) is located along the banks of the Yenisei River. The two forest compartments considered, Bolshe NE and Bolshe NW, comprise 1251 and 1604 stands with an average size of 25 and 17 ha, respectively. Bolshe NE is located east of the Yenisei River and is characterized by hilly terrain. Steep slopes can be found along the eastern banks of the Yenisei River. Altitudes on this side of the river increase to more than 300 m above sea level and fall again to a level of 200 m in the easternmost parts of the test site Bolshe NE. The forests, which are growing on peaty forest floor, are dominated by naturally growing uneven-aged stands, hardly influenced from harvest or other anthropogenic disturbance and thus show a heterogeneous structure. Recent clear-cuts can be found in the compartment though. The main tree species are fir, spruce, birch and aspen with only small percentages of pine, larch and cedar at Bolshe NE. Bolshe NW is located west of the Yenisei River in the Central Siberian flood plain. Topography is mostly gentle with heights varying between 220 and 260 m. Forests in these compartments have been intensively harvested

for several decades and are dominated by even-aged and more homogeneous forest stands regrowing after clear-cutting. Compared to Bolshe NE, the northwestern forest compartment has a higher percentage of cedar and a lower percentage of aspen. Amongst the five forest compartments selected for this study, Bolshe NE and NW have the highest average stem volume of 162 and 214 m³/ha, respectively.

3.2.2 Chunsky

The Chunsky forest territory (57° 45' N, 96° 43' E) is located south of the Angara River. The two forest compartments considered for this study, Chunsky N and E, comprise 1284 and 1113 stands with average sizes of about 30 ha, which is larger than the average stand size at the other compartments. The topography is mostly flat in the northern part of Chunsky N with altitudes ranging from 300 to 400 m. In the southern part of Chunsky N, steeper slopes can be found along stream valleys crossing the area mainly from North to South. Topography at Chunsky E is mostly gentle with altitudes ranging from 200 to 250 m. Only few peaks reach altitudes up to 350 m. Chunsky N and E are characterized by a similar tree species composition. In contrast to the Bolshe-Murtinsky compartments, the percentage of larch and pine is much higher whereas fir and cedar are almost not present. The existence of forestry infrastructure in form of roads and railroads close to the forest compartments indicates active exploitation of the forests at the forest compartments.

3.2.3 Primorsky

The Primorsky forest territory (55° 46' N, 102° 14' E) is located at the southern banks of the Bratskove Reservoir. The easternmost forest compartment, Primorsky E, comprises 1490 stands with an average stand size of 20 ha. The topography at Primorsky E is rather gentle with a few steep slopes along two riverbeds crossing the area mainly from North to South. Altitude ranges from 440 m above sea level in the stream valleys to 600 m at the peaks between the stream valleys and at hills in the westernmost part of the test site. The compartment is located close to the city of Bratsk and is characterized by a grid of roads indicating an extensive logging of the forests. The tree species composition is very similar to that at the Chunsky test sites.

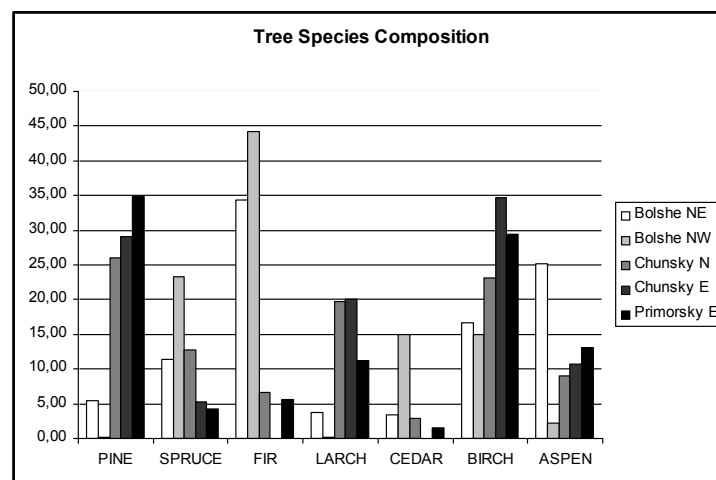


Figure 3.4. Tree species composition (in percent of total stem volume) at the Siberian test sites.

Table 3.2. Forest attributes at the selected Siberian test sites for all stands in the inventory data respectively for all stands that were used for the analysis, i.e. with a stand size of >2 ha, stem volume >0 m³/ha and an average slope per stand of $<10^\circ$ (for an explanation see Chapter 4.1).

	Chunsky East (last FI update 1998)						Chunsky North (last FI update 1998)					
	All (1113 stands)			Used (470 stands)			All (1284 stands)			Used (591 stands)		
	Mean	Max.	SD	Mean	Max.	SD	Mean	Max.	SD	Mean	Max.	SD
Volume [m ³ /ha]	126	420	118	130	420	115	136	430	110	142	390	104
Height [m]	13	27	10	15	28	9	14	28	10	16	28	9
Stand size [ha]	34	550	50	27	452	39	30	450	38	24	378	32
RS [%]	52	100	26	58	100	18	51	100	23	58	100	14

	Bolshe Northeast (last FI update 1998)						Bolshe Northwest (last FI update 1998)					
	All (1604 stands)			Used (499 stands)			All (1251 stands)			Used (450 stands)		
	Mean	Max.	SD	Mean	Max.	SD	Mean	Max.	SD	Mean	Max.	SD
Volume [m ³ /ha]	162	450	109	161	380	101	214	470	120	231	470	106
Height [m]	17	32	9	19	32	8	18	28	8	19	28	8
Stand size [ha]	17	250	21	12	200	15	24	220	25	18	135	19
RS [%]	55	100	23	60	100	15	61	100	23	65	100	15

	Primorsky East (last FI update 1996)					
	All (1490 stands)			Used (381 stands)		
	Mean	Max.	SD	Mean	Max.	SD
Volume [m ³ /ha]	148	500	109	159	500	108
Height [m]	13	29	9	14	29	8
Stand size [ha]	20	264	24	30	240	21
RS [%]	61	100	25	68	100	16

3.3 Forest structural considerations

As described in Chapter 1.1, the condition of the forests in Northeast China is far from optimal. Large forest areas are characterized by low stem volume, a lack of mature and over-mature forests and growth rates of planted forests far below the predicted rates (Bull & Nilsson, 2004; Li et al., 2004). In contrast, the largest fraction of the forests in Central Siberia is in the mature and overmature stages of forest development (Shvidenko et al., 2007). It can be expected that forest structure in both areas differs and that the differences should have had an influence on the ERS measurements and the possible stem volume retrieval accuracy when considering results of previous studies (Santoro et al., 2007; Askne & Santoro, 2007a). In general, forest biophysical parameter retrieval can be expected to perform best for the more homogeneous and managed types of forests.

In Santoro et al. (2007), it was shown that stem volume retrieval by means of ERS-1/2 tandem coherence at the Chunksy and Bolshe test sites improved significantly when only considering stands with high relative stocking. As relative stocking was found to have a major effect on the accuracy of stem volume retrieval by means of satellite measurements, it was of interest if the structural deficits of the forests in Northeast China reflected in an overall lower relative stocking. Information about relative stocking was only given for the Siberian but not the Chinese test sites. Stem volume and height were the only forest parameters that were available for all test sites. Santoro et al. (2007) showed that different relations between tree height and stem volume existed for Central Siberian boreal forest stands with low and high relative stocking, respectively. The results indicated that it should be possible to distinguish forests with different relative stocking by means of the stem volume to height relation regardless of the species composition and site quality. Thus, the scope of the analysis presented in this section was to reconstruct the relation between tree height, stem volume and relative stocking in order to:

- provide more insight into the structural differences between the Siberian and Northeast Chinese forests.
- evaluate if an identification of stands with low and high relative stocking is possible for the Northeast Chinese forests based on the relations between height and stem volume (the two forest parameters available for all test sites) in order to be able to discuss the effect of forest structural diversity on the satellite measurements.

Furthermore, the relationship between stem volume and height was of particular interest for the modeling part of this study (see Chapter 5).

The investigation presented in this section considered so-called allometric relations between plant growth dimensions, e.g. stem volume and height. Allometry, in a very simple definition, relates easy to measure plant parameters like diameter of a tree stem to the other dimensions of the plant and is therefore of high importance in forestry as measurements of parameters like biomass or stem volume are laborious. Biomass estimation, for instance, requires destructive methods, which means that the trees have to be felled. Other parameters like dbh are very easy to measure and a link between dbh and biomass facilitates the estimation of biomass tremendously. The ecophysiological interpretation of allometric relations is very complex and beyond the scope of this thesis. Size relations of plants are basically a function of the available growth energy and the plants strategy in allocating this energy to different plant components in a competing situation for energy in form of sunlight, water or nutrients. For a fundamental description of allometry, the reader is referred to Niklas (1994) or Enquist & Niklas (2001).

As a first step, the allometric interrelations between density, dbh, height and stem volume at the Siberian test sites were analyzed with respect to tree species and relative stocking. Stem density, D [ha^{-1}], i.e. one of the main growth dimensions of forest, was not given in the inventory data but could be estimated with the following equation (Pretzsch, 2002; West, 2004):

$$D = \frac{4 \cdot V}{\pi \cdot dbh^2 \cdot h \cdot f_z} \quad (3.1)$$

where V denotes stem volume [m^3/ha], h the tree height [m] and f_z the dimensionless shape factor. The only parameter in Equation (3.1) that was not given was the shape factor, f_z . The shape factor converts a cylinder of volume $dbh^2 \cdot h/4$ to the volume of a real stem. In actual fact, f_z changes with the growth of a stem. Still, Baker & Luckman (1999) found for Scots Pine and Norway Spruce that a factor of 0.5 represented a good approximation unless the trees were very young. In Israelsson et al. (1994), a shape factor of 0.45 was found to be a good approximation for temperate forests in the Netherlands dominated by poplar, ash, oak, maple, willow and beech. According to Franz et al. (1973 as quoted in Pretzsch, 2002), the shape factor can be estimated based on tree height and dbh. This has been tested for a number of tree species using the dbh and height measurements at the Chunsky North test site. Only stands where a single species exceeded 80 % in the species composition were considered. The obtained shape factors have been illustrated in Figure 3.5 for larch, pine, spruce and a generalized expression for deciduous softwood species. The shape factors increased with increasing diameter and height of the trees. For heights below ~ 15 m and a dbh below 10 cm, the shape factors were almost identical for all species. For larger heights, respectively diameters, the shape factors varied between 0.4 and 0.5. It has to be noted that, when inferring from single trees on stand relations, the standwise distribution of dbh and tree height needs to be known. However, this information was not given in the inventory data. That is why, it was decided to use the relation obtained for pine (ignoring possible effects of dbh/height frequency distributions) for the following analysis as it should represent a good compromise for most species.

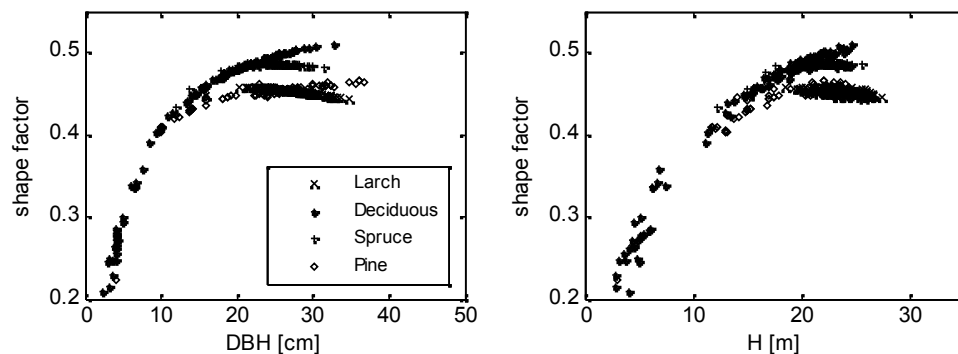


Figure 3.5. Shape factor as function of dbh (left) and tree height (right) according to Franz et al. (1973 as quoted in Pretzsch, 2002).

Figure 3.6 illustrates the relations between different forest properties at the Siberian test sites. Plot (a) shows that the stem volume reached much higher levels in case of fully stocked stands. Low relative stocking stands hardly exceeded a stem volume of $200 \text{ m}^3/\text{ha}$. It has to be kept in mind that the age information in the inventory only referred to the economically most valuable tree species in a stand so that age relations should be interpreted with caution. As has already been shown in Santoro et al. (2007), the tree heights for low relative stocking stands (e) were higher for a given stem volume than for fully stocked stands (b). The allometric relation was expressed as a simple exponential function (cf. Askne et al., 1997; Mette et al., 2004). For stands with high relative stocking the observed relation was very close to the relation reported for fully stocked Scandinavian boreal forests (Askne et al., 1997). The allometric relationship between tree height and dbh, however, did not differ for low (f) or high (c) relative stocking.

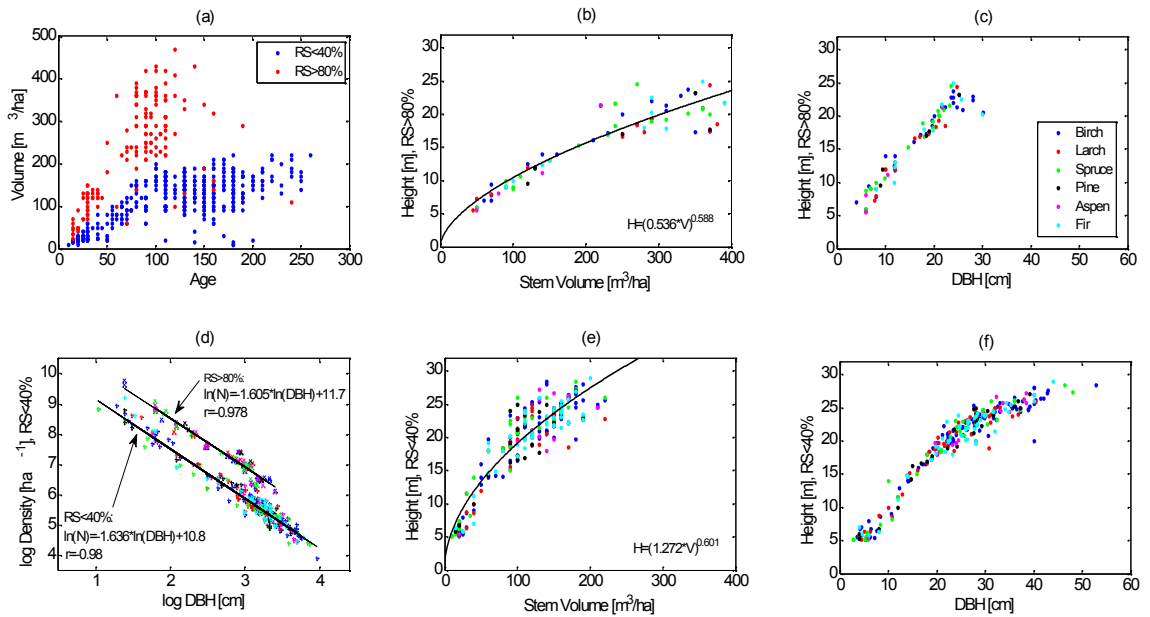


Figure 3.6. Relationship between stand age and stem volume (a), stem volume and height (b & e), dbh and height (c & f) and dbh and density (d) for low (<40%) and high (>80%) relative stocking, RS, at Chunksy, Bolshe and Primorsky.

Tree species-specific alterations of the relations were not significant, neither in the dbh-height nor the stem volume-height relation; note that the specified species is the dominant species in a stand (>50 % of total stem volume). This observation was somewhat surprising as the dbh-height relation is commonly known to depend on species, site quality and climatic conditions (Pretzsch, 2002; Wang et al., 2006). The observations suggested that it was mainly the density that drove the volume differences between low and high relative stocking stands for a given tree height (respectively dbh) and that species and site quality specific alterations were of minor importance. When comparing dbh and estimated density in the logarithmic scale in plot (d), this assumption was confirmed. For both, high and low relative stocking, the logarithm of density decreased linearly with increasing logarithm of dbh. The density of low relative stocking stands was consistently lower than for fully stocked stands even though for both an increased spread around the linear trend could be observed for the higher dbh classes. This increased spread may have been related to what has been reported in Zeide (1985). Zeide observed a deviation from the linear trend between the logarithm of density and dbh for mature and over-mature stands due to a reduced ability of old forests to close gaps in the canopy that occurred because of fallen trees.

The linear decrease of density with increasing dbh in log-log scale for close to fully stocked stands was in good agreement with the so-called Reineke rule (Reineke, 1933). According to the Reineke rule, the stand density, D , of fully stocked naturally growing forests decreases with increasing stand average quadratic diameter at breast height and both can be related to each other with the stand density index SDI (Pretzsch, 2002):

$$SDI = D \left(\frac{25}{dbh} \right)^{-1.605} \quad (3.2)$$

The SDI relates the observed stand density to the density that can be expected for a stand with a mean quadratic dbh of 25 cm. The exponent -1.605 was considered a

universal constant for all plant communities growing under maximum crowding conditions, i.e. when growth is limited by the availability of resources. Although Pretzsch (2006) showed that the exponent depends on tree species and Zeide (1985) found the exponent to vary with forest age, the SDI still represents a widely applied tool in forestry.

Based on Equation (3.2), the SDI has been estimated for the Siberian and the Daxinganling (the one for which also dbh was given) test sites. The calculated SDI was on average ~ 715 with a standard deviation of ~ 140 for high relative stocking ($>80\%$) forest stands at the Siberian test sites; when considering single species, the average SDI varied between 697 (Cedar) and 852 (Pine). Lower SDIs were found for low relative stocking stands ($RS \leq 40\%$) with an average of ~ 240 and a standard deviation of 60. In the histograms in Figure 3.7, it can be seen that the SDI tended towards lower values at Daxinganling. This can be considered a sign of a stocking deficit. The maximum observed SDI was approximately the same for both, the Siberian test sites as well as the Daxinganling site (~ 1000), and in good agreement with values reported for fully stocked stands in Europe (Sterba, 1991 as quoted in Pretzsch, 2002).

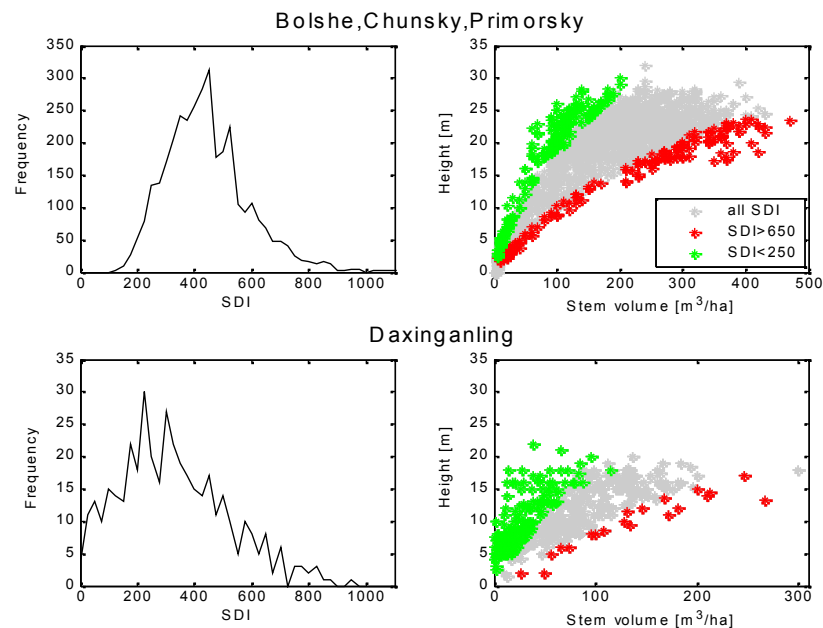


Figure 3.7. Histograms of SDI (left column) and stem volume measurements versus corresponding tree height for all stands (grey), $SDI < 250$ (green) and $SDI > 650$ (red).

When considering the stem volume-height relationship for stands with low respectively high SDI (Figure 3.7, right), the same relations as for stands with high and low relative stocking were found. The stands with high SDI showed almost the same trend for the tree height as function of stem volume at both sites, i.e. Siberia and Daxinganling. Stands with high SDI reflected the lower bound of the total range of tree heights for a given stem volume. This was confirmed when plotting the fitted curves for the stem volume and tree height relationship at the Daxinganling test site together with the measured stem volumes and heights at the other Chinese test sites (Figure 3.8). The high relative stocking curves described the lower bound of the trend of height as function of stem volume. Significant deviations were only noticed for the Xiaoxinganling test site where a number of stands under-ran the anticipated height of

high relative stocking stands. This would correspond to extremely dense but low forest. The reason for this observation was not clear. As at Xiaoxinganling several experimental plantations were established, these stands may have represented sample areas for testing different planting densities so that they may not have represented natural growth conditions.

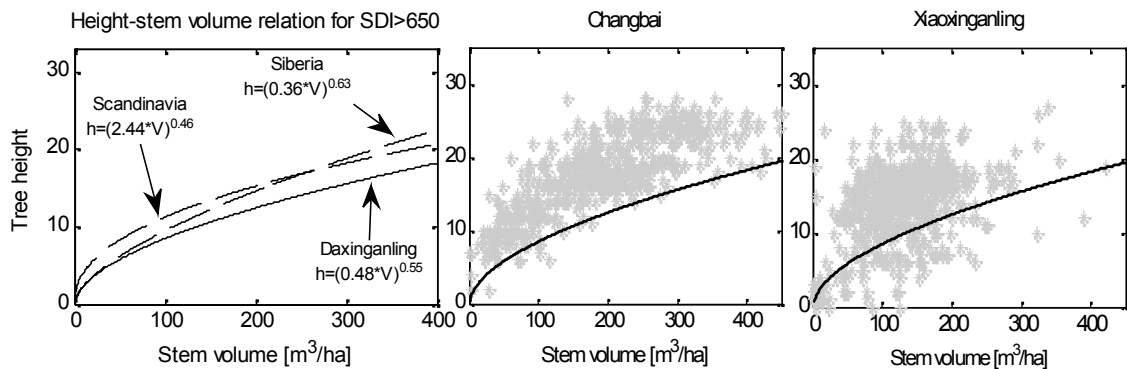


Figure 3.8. Left – relation between stem volume and height for fully-stocked stands (SDI>650) at the Siberian and the Daxinganling test sites. Also a relation obtained for Scandinavian boreal forest has been included (Askne et al., 1997). Middle and Right - Stem volume and height measurements at the Chinese test sites and the allometric relation observed for stands with high SDI at Daxinganling.

Shortcomings in the estimation of density and SDI were related to stand heterogeneity and the underlying frequency distributions of height and dbh within a stand. Diameter and height were calculated as a weighted average over the dominant species in a stand. In order to better account for stand heterogeneity, the SDI was calculated in an alternative way. In Stage (1968 as quoted in Woodall et al., 2003), the summation method was found better suited for SDI estimation in heterogeneous uneven-aged stands. In the summation method, the SDI is calculated for each dbh group in a stand separately and then all single SDIs are summed up. This approach could be tested as in the Siberian inventory data the species composition was given in percent of the total volume and dbh and height were given for each species (assuming that at least each species represented a single dbh class). When calculating the SDI according to the summation method, differences between the summation method and the calculation for the stand-wise averaged parameters were found to be low with an average difference of 8 % (Pearson correlation was 0.83). Part of the difference could be assigned to the coarse species composition variable in the inventory data, which was only given in steps of 10% and affected the density estimation. The highest differences of up to 30 % were observed for heterogeneous stands with species representing very different dbh classes. Still, when using the new SDI estimates to identify the height-stem volume relation for fully stocked stands (SDI>650), the same allometric trend was indicated as for the initial SDI estimates (in Figure 3.8).

The ‘Reineke’ line in Figure 3.6 (d) describes the temporal development of forest in case of fully stocked stands. In case of under-stocked stands, the stand density does not follow the line indicated for low relative stocking stands in Figure 3.6 (d). An approach that transfers the self-thinning theory to under-stocked stands has been developed in Tang et al. (1994, 1995). The model developed based on Equation (3.2) but was enhanced for stands with stocking deficits. The model, from now on referred to as the

Tang model, is not further explained here as it only serves illustrational purposes. In Tang et al. (1995), the model was trained for larch forests in the Changbai Mountains. The outcome of this model training is shown in Figure 3.9 (left) together with the dbh and density measurements for Daxinganling. In case of fully stocked stands, the modeled dbh-density relationship well described the upper bound of the observed range of densities at a given dbh. In case of an initial stocking deficit, the Tang model predicted a constant density with increasing dbh until the maximum possible stocking was approached. According to the model, a stand always develops towards 100 % relative stocking. Based on the dbh-density relationship obtained by Tang et al., an allometric relation between stem volume and height has been calculated. For this, Equation (3.1) was used, integrating the density-dbh relation from the Tang model for different ‘typical’ initial stocking deficits and replacing dbh with an allometric expression for dbh and height that was reported in Wang et al. (2006) for larch forests in Daxinganling. In Figure 3.9 (right), it can be seen that for fully-stocked stands the curve, describing the height as function of stem volume, well described the lower bound of observed heights for a given stem volume. The heights in case of an initial stocking deficit were higher but approached the ‘full-stocking line’ with increasing stem volume. The stocking deficits used did not explain the full range of height deviation from the full-stocking case so that even larger stocking deficits at the Daxinganling test site were likely, maybe because of the fire in 1987 or ongoing illegal logging.

In conclusion, it can be stated that the identification of fully stocked stands according to their height at a certain stem volume should be feasible for the Northeast Chinese forests. The Reineke rule allowed a reasonable description of the density development of fully stocked Siberian as well as Northeast Chinese boreal forests. A very similar allometric relation between stem volume and height was found for stands with an SDI above 650 at the Siberian and the Daxinganling test sites. Species-specific effects, site quality and climatic differences seemed to be of minor relevance in this context. The estimated SDI values as well as the simulations with the Tang model furthermore confirmed for the Daxinganling test site the expectation that larger fractions of the forests were under-stocked.

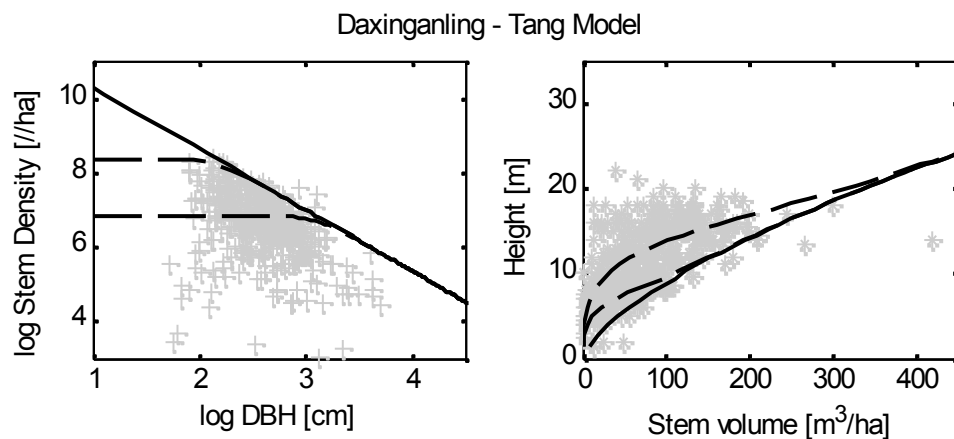


Figure 3.9. Left - Stand density as function of dbh (model and measurements). The solid line refers to fully stocked stands and the thick dashed and dash-dotted lines to stands with different initial stocking deficits. Right – Modeled and observed stem volume-height relation for different initial stocking deficits.

3.4 Satellite data

3.4.1 ERS-1/2 tandem data

The SAR data used for this study was acquired during the ERS-1/2 tandem mission when the ERS-1 and ERS-2 C-Band SAR systems flew with one day time lag over the same area. For Northeast China, a dataset of 223 image pairs was available. This dataset was collected in the frame of two ERS-1/2 mission periods. 2/3rd of the tandem pairs were acquired during the first ERS-1/2 global coverage campaign in 1995-1996. The 1997-1998 dataset was acquired in the frame of the SIBERIA project, i.e. between September and October 1997 and in June 1998. Only tandem pairs with a perpendicular baseline below 400 m were selected (see Appendix A). Because of the restriction to baselines below 400 m, the coverage over Northeast China was not complete with some gaps occurring mainly in non-forested areas. All images were acquired along descending orbits. The ERS tandem dataset covering the Siberian test sites consisted of eight tandem pairs. Three tandem pairs were acquired during winter 1995/96, four during fall 1997 and one in May 1998. The perpendicular baselines were between 65 and 313 m. Table 3.3 lists which image covered which test sites.

Interferometric processing started with the co-registration of the tandem pairs in Single Look Complex (SLC) format by cross-correlating a high number of image chips in the images and estimating the offset fields (Curlander & McDonough, 1991; Wegmüller et al., 2001) to reproject one of both into the geometry of the other image. The standard deviation of co-registration offsets was always below 0.2 pixels which means that the coherence loss due to co-registration errors was < 5%; note that coherence decreases with *sinc* ($\pi * \Delta px$) (Ferretti et al., 2007) where Δpx denotes the offset in terms of the fraction of the pixel size. Further processing steps were multilooking (1x5 for the Siberian data and 2x10 for the Chinese data), range (Gatelli et al., 1994) and azimuth (Schwäbisch & Geudtner, 1995) common band filtering and computation of coherence using an adaptive window size between 3x3 and 9x9 pixels for high and low coherent areas, respectively. The adaptivity of coherence estimation was achieved by first calculating coherence with a fixed window size. Then a second computation was carried out, adapting the window sizes to the initial coherence estimates (Wegmüller et al., 1998). In addition, the image texture, calculated from ERS intensity, was integrated in the coherence estimation. Texture was used to keep the estimation window small over areas with high texture. Phase slope information from the ERS-1/2 tandem interferogram, which was filtered before, was included in the computation of coherence in order to account for topography-induced phase variations. The intensity images were calibrated to σ^0 , including a compensation for the variation of the pixel area from near to far range assuming flat terrain.

The coherence and the intensity images were terrain corrected and geocoded to 50 x 50 m² pixel size in case of the Chinese and to 25 x 25 m² in case of the Siberian dataset utilizing the ‘Shuttle Radar Topography Mission’ SRTM-3 DEM with 90 m pixel size. The SRTM-3 DEM has a vertical accuracy of ± 16 m at the 90 % confidence interval (Rabus et al., 2003). Geocoding started with the generation of an initial look-up table. The look-up table indicated for a pixel in the DEM in map coordinates the corresponding position in the SAR image in range-Doppler geometry based on the available information about the satellite orbit, the SAR imaging geometry and the local terrain height. Uncertainties in the orbit data, the SAR imaging geometry or the geolocation of the DEM may result in geocoding errors. Hence, the initial look-up table

was refined by means of an automated procedure, crosscorrelating a high number of image chips in the intensity image and a simulated SAR image (Wegmüller, 1999). The simulated SAR image was derived from the DEM and basically simulated the radiometric effects of topography in intensity images (see Chapter 6.1). For the crosscorrelation with the SAR intensity image, the simulated image was reprojected into the SAR geometry using the initial transformation look-up table. With the refined transfer function from the crosscorrelation, the look-up table was updated and used for reprojecting the ERS image products in SAR geometry into the map geometry. The required resampling of the images was done using the nearest-neighbor technique. The selected projection of the geocoded products was the Albers Conical Equal Area projection. As the geocoding procedure with a simulated SAR intensity image requires topographic features, the accuracy of the geocoding was lowest for mostly flat areas; e.g. Inner Mongolia and the Northeast China Plain. Offsets of 1-2 pixels were observed between overlapping tracks in these areas. In the mountainous areas, the geolocational accuracy was at the sub-pixel level. As a by-product of the geocoding, local incidence and aspect angle maps, pixel area normalization maps (see Chapter 6.1) and layover/shadow masks were produced.

Actually, the Chinese and Siberian ERS-1/2 tandem datasets were processed for different studies, which explains the different multilooking and pixel sizes of the geocoded products. In order to work with a more uniform and comparable dataset, the geocoded Siberian images were further 2 x 2 multilooked to a pixel size of 50 x 50 m². The ENL of all geocoded intensity images was now in the range of 9 to 10. The average coherence over unfrozen water surfaces was consistently around 0.05 for the images covering Northeast China, indicating a low bias in coherence. The coherence images covering the Siberian test sites revealed a higher average coherence over water surfaces and appeared in general noisier which is why they were median filtered using a moving window of 5 by 5 pixels. Visual inspection of the filtered coherence images revealed a much reduced noise at a slight loss of spatial resolution.

To illustrate the characteristics of Northeast China, Figure 3.10 shows the RGB color composite of ERS-1/2 tandem coherence, ERS-1 intensity and ERS-1/2 intensity difference for all 223 image frames mosaiced together (Santoro et al., 2005a). The red channel corresponds to ERS-1/2 tandem coherence, the green channel to ERS-1 intensity and the blue channel to the ERS-1/2 intensity ratio. The forested areas appear in green, the Inner Mongolian grasslands in red and the agricultural areas of the Northeast China Plain in yellow. This means high backscatter and low coherence over forested terrain, high coherence and low backscatter over the arid grassland areas in Inner Mongolia and high backscatter as well as high coherence over the agricultural areas. Water surfaces appear blue or green because of low coherence and either high or low backscatter. High intensities above -5 dB were observed for frozen rivers or lakes where backscatter occurred at the rough ice-water interface. One of the biggest issues concerning the use of SAR/InSAR methods for land mapping applications is clearly visible in the mosaic. As the tracks were acquired in different seasons and under varying environmental and meteorological conditions, coherence and intensity varied considerably between the different tracks, causing abrupt color variations between neighboring data strips in the mosaic.

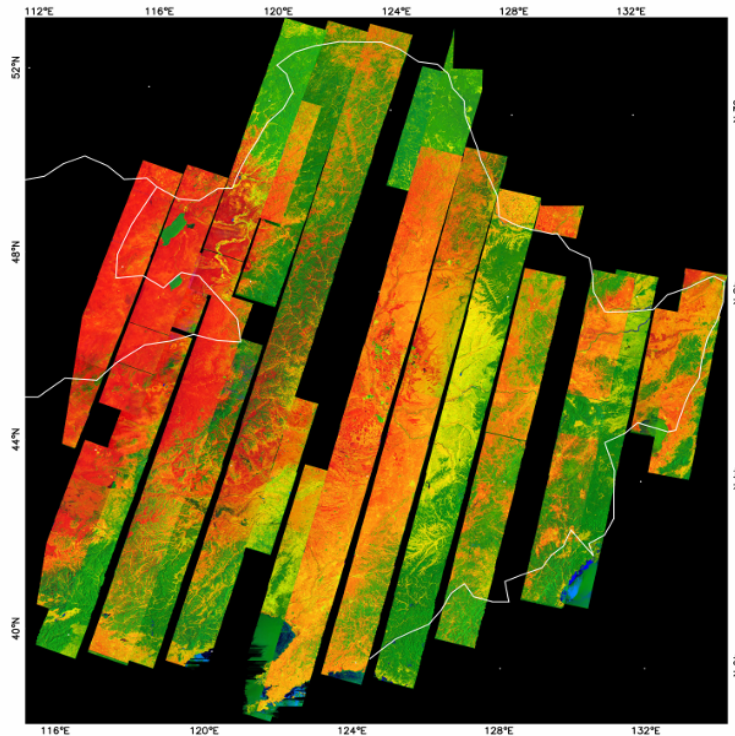


Figure 3.10. RGB color composite of ERS-1/2 tandem coherence, ERS-1 intensity and ERS-1/2 intensity difference for Northeast China. Red corresponds to ERS-1/2 tandem coherence, green to ERS-1 intensity and blue to ERS-1/2 intensity difference. 223 tandem image pairs were used for the creation of the mosaic (Santoro et al., 2005b).

3.4.2 Additional Earth Observation data

The work presented in this thesis aimed at the synergistic use of interferometric SAR data and optical remote sensing products in form of the Vegetation Continuous Fields VCF product of the Moderate Resolution Imaging Spectroradiometer MODIS (Hansen et al., 2002a, 2002b, 2003, 2005). The MODIS VCF product, which is available since 2003, provides global sub-pixel estimates of tree canopy cover at 500 m pixel size. Tree canopy cover refers to the fraction of skylight obstructed by canopies of trees that are at least 5 m high (Hansen et al., 2003); note that canopy cover differs from crown cover which is often used for forest inventory purposes and which is usually inferred from aerial photography. Crown cover represents the percentage of ground that is covered by the canopy not considering gaps within individual crowns and overlaps. Hansen et al. (2003) indicated that a canopy cover of approximately 80 % in VCF, the actual percentage depends on the forest type, should correspond to 100 % crown cover.

The utilized MOD44 version was produced with 2001 MODIS data by calculating 68 metrics like maximum annual NDVI or channel-based measures for annual minimum, maximum and mean of the spectral information including all seven MODIS land reflectance bands. AVHRR band 4 brightness temperature data from 1995/96 was used for global climate stratification and served the calculation of the multi-temporal spectral metrics only for the warmest months of the year (Hansen et al., 2002a). MODIS brightness temperature products were not operational by the time of the production of the first MODIS VCF version. The metrics were used as input to a regression tree classifier. Landsat optical remote sensing images for more than 250 globally distributed

sites were used as reference data (to train the regression tree classifier) by assigning each pixel herein to four coarse tree cover classes (0%, 25%, 50% and 80%) and aggregating those pixels to the 500 m pixel size of MODIS.

Yet, the VCF product is only partially validated. The accuracy has been assessed in Hansen et al. (2003) by means of finer resolution optical remote sensing products (IKONOS, Landsat) for forest sites located in Colorado, USA, and in Hansen et al. (2005) for Zambian forest sites. The assessment showed that the accuracy increased when aggregating the tree cover map to coarser pixel sizes as for Colorado the coefficient of determination, R^2 , improved from 0.81 at 500 m pixel size to 0.89 at 1 km pixel size and to 0.94 at 2 km pixel size. Similar improvements were observed for Zambia. In White et al. (2005), the VCF accuracy was assessed using inventory plot data for a test site in Arizona, USA. VCF was found to systematically underestimate tree cover (White et al., 2005).

The ERS coherence mosaic in Figure 3.10 was resampled to the 500 m pixel size of the VCF product to check for co-registration offsets. Visual inspection revealed a good agreement and no further adjustment was considered necessary. Finally, water body masks were produced by rasterizing the SRTM Water Body Mask in GIS vector format (Anonymous, 2003). The SRTM Water Body Mask depicts all water surfaces exceeding the width of 90 m. The mask was used to exclude water surfaces for all following investigations. A classification of water surfaces by means of ERS coherence and intensity was not possible as signatures varied in a wide range between the acquisitions.

3.5 Meteorological data

One or more daily measurements of temperature, wind speed, precipitation and snow depth were available for several weather stations of the World Meteorological Organization (WMO); four stations were located near the Bolshe, two stations near the Chunksky and two near the Primorsky test sites. Although the distances between the test sites and the stations were large (up to 150 km), no relevant differences between the measurements at the different stations were noticed (cf. Eriksson, 2004; Santoro et al. 2007). Wind speeds and temperatures measured at 6:00 UTC (Universal Time Coordinated), i.e. ~1.5 hours after image acquisition, are given in Table 3.3 in form of the mean values for several weather stations.

For Northeast China, measurements from 43 WMO stations (Figure 3.11), provided by Deutscher Wetterdienst (DWD), included four daily measurements of temperature, wind speed and precipitation for the complete period of the ERS-1/2 tandem acquisitions. The ERS measurements were acquired at ~3:00 UTC, i.e. in the middle of a 6-hour interval of meteorological measurements, which is why the temperature measurements from 0:00 and 6:00 UTC were averaged (local time was UTC+8h). In case of the wind speed measurements, this did not necessarily make sense as wind can be spatially and temporally highly variable. The wind speeds reported in Table 3.3 correspond to the maximum and minimum wind speeds measured in the period of the acquisitions, i.e. the measurements before and after the ERS-1 and ERS-2 overpasses were considered. For the test site at Xiaoxinganling the station with id 50774 at Yichun (47°43' N, 128°54' E, 230m altitude) and for Changbai the station with id 54186 at Dunhua (43°22' N, 128°12' E, 520m altitude) were located closest (< 50 km) to the test sites. In addition, the second closest weather stations were considered (id 54273 for Changbai and id 50756 for

Xiaoxinganling). All stations reported comparable temperatures. The reported wind speeds, however, differed considerably, indicating that the wind speeds given in Table 3.3 should be interpreted with caution as wind appeared to be highly variable, especially in the mountainous terrain of the test sites. For the Daxinganling test site, no weather station in the DWD dataset was located nearby. The Chinese Academy of Forestry, however, provided daily measurements for the two weeks prior to the ERS acquisitions from the WMO station 50136 at Mohe (7-21 December 1995) which is located approximately 35 km away from the test site (not included in Figure 3.11).

The weather data for Northeast China was examined for the main weather characteristics in the period of the ERS acquisitions. Figure 3.12 illustrates temperatures and precipitation measured at six representative weather stations located all over Northeast China and in different altitudes. Temperatures were generally very low in winter. In the Daxinganling region, -40°C were approached in January (station 50434). Winter temperatures revealed a clear latitudinal but no longitudinal gradient. This gradient is exemplified in Figure 3.13 in form of the daily maximum temperature (averaged per month and weather station) plotted against the latitude of the particular weather station. The duration of stable frozen conditions varied with latitude as well, lasting longest in the Daxinganling area and shortest in the areas close to the Yellow Sea coast (e.g. station 54337) where in all months freeze/thaw events were possible. Besides areas close to the coast, thawing events did not occur for a rather long period from December to beginning of March. In addition, precipitation (in form of snow) was hardly registered throughout the overall dry winter. With the beginning of thaw in March and April, the number and intensity of rain events increased. According to long year statistics (Chao, 1994), longitudinal gradients of precipitation exist in Northeast China. However, no significant longitudinal gradients were observed in the precipitation data from winter 1995/96 nor from fall 1997. However, the lowest amount of rain in the period of the satellite observations was registered at a weather station in Inner Mongolia (station 50603). The weather data from fall 1997 indicated mostly unstable conditions with frequent rain events and a constant decrease in temperature with daily oscillations around 0°C , i.e. frequent freeze/thaw events, in September in the northern latitudes (e.g. station 50434) and end of October in the areas close to the Yellow Sea (station 54337).

Information about snow cover was not given in the WMO data. Coarse information about snow cover extent could be obtained from the archives of the National Snow and Ice Data Center (NSIDC). The “Northern Hemisphere EASE-Grid Weekly Snow Cover and Sea Ice Extent” product (Armstrong & Brodzik, 2005) provides weekly estimates of snow cover extent at 25 km pixel size based on manual interpretation of the Advanced Very High Resolution Radiometer (AVHRR) visible bands. The maps reported the presence of snow for most of Northeast China until the beginning of February when snow started to melt in the areas close to the coast. In the following weeks, the southern border of the snow covered area moved northward until in May the complete area of Northeast China was snow-free. Snow cover maps showing the snow cover for eight dates between December 1995 and May 1996 have been illustrated in Figure 3.14. However, these maps did not provide information about the snow wetness, which, with respect to C-band measurements, would have been more important to know than the pure snow cover extent.

Table 3.3. Meteorological conditions at the acquisition of the ERS-1/2 tandem data available for the Siberian and Chinese test sites (for the Siberian test sites see also Eriksson (2004) or Santoro et al. (2007)). T_1 , T_2 , WS_1 and WS_2 denote the temperatures and wind speeds measured at the time of the ERS-1 and ERS-2 overpasses, respectively. SD stands for snow depth.

Acquisition date	Area	B_n	Weather conditions
29.12.1995 30.12.1995	Chunsky N	171 m	$T_1 \approx -10^\circ\text{C}$, $T_2 \approx -23^\circ\text{C}$, $WS_1 \approx 6\text{ m/s}$, $WS_2 \approx 0\text{ m/s}$, SD: 18 cm, Refreezing
1.1.1996 2.1.1996	Bolshe NE	144 m	$T \approx -20^\circ\text{C}$, $WS_1 \approx 5\text{-}6\text{ m/s}$, $WS_2 \approx 1\text{-}3\text{ m/s}$, SD: 16 cm, Snowfall, Refreezing
14.1.1996 15.0.1996	Chunsky N & E	65 m	$T_1 \approx -18^\circ\text{C}$, $T_2 \approx -23^\circ\text{C}$, $WS < 2\text{ m/s}$, SD: 27 cm
22.9.1997 23.9.1997	Bolshe NE	260 m	$T_1 \approx 16^\circ\text{C}$, $T_2 \approx 19^\circ\text{C}$, $WS < 2\text{ m/s}$, Rainfall on 21 st
25.9.1997 26.9.1997	Bolshe NE & NW	233 m	$T_1 \approx 20^\circ\text{C}$, $T_2 \approx 13^\circ\text{C}$, $WS < 2\text{ m/s}$, Rainfall on 21 st
27.10.1997 28.10.1997	Bolshe NE	158 m	$T \approx 2^\circ\text{C}$ ($\pm 0^\circ\text{C}$ between passes), $WS < 1\text{ m/s}$, Rainfall one week before
28.05.1998 29.05.1998	Bolshe NE & NW	313 m	$T_1 \approx 26^\circ\text{C}$, $T_2 \approx 19^\circ\text{C}$, $WS < 3\text{ m/s}$, Rainfall one week before
9.10.1997 19.10.1997	Primorsky E	183 m	$T_1 \approx 10^\circ\text{C}$, $T_2 \approx 10^\circ\text{C}$, WS not available
20.12.1995 21.12.1995	Daxinganling	191 m	$T_1 \approx -21^\circ\text{C}$, $T_2 \approx -15^\circ\text{C}$, $WS \approx 0\text{-}2\text{ m/s}$
9.1.1996 10.1.1996	Xiaoxinganling	75 m	$T_1 \approx -16^\circ\text{C}$, $T_2 \approx -10^\circ\text{C}$, $WS \approx 0\text{-}3\text{ m/s}$
9.1.1996 10.1.1996	Changbai	89 m	$T_1 \approx -16^\circ\text{C}$, $T_2 \approx -15^\circ\text{C}$, $WS \approx 0\text{-}3\text{ m/s}$

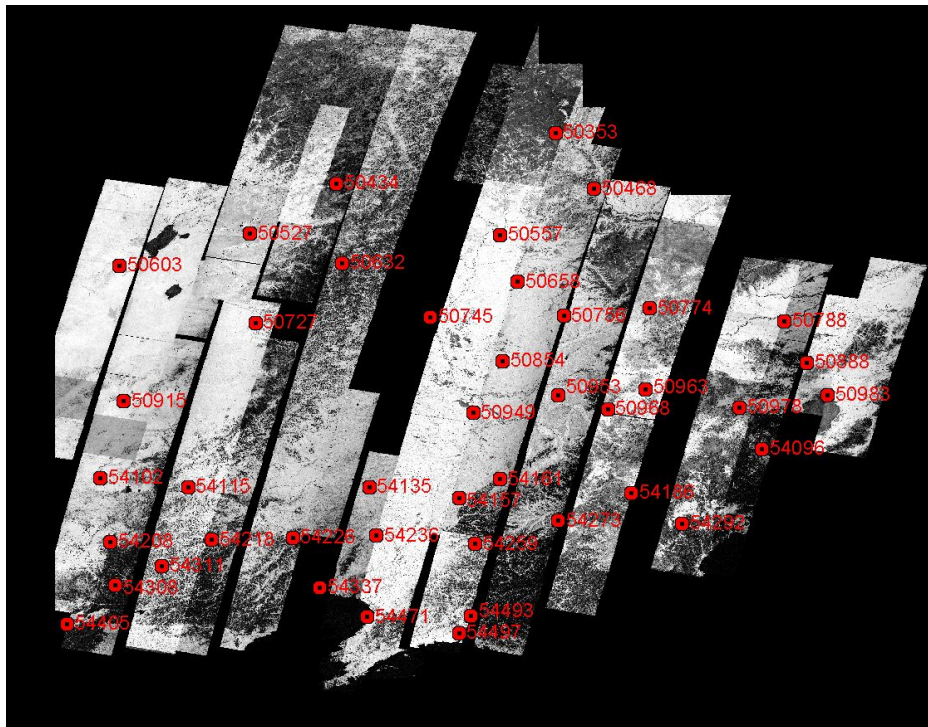


Figure 3.11. WMO weather stations in Northeast China for which measurements were available. The image shows the ERS-1/2 tandem mosaic of Northeast China.

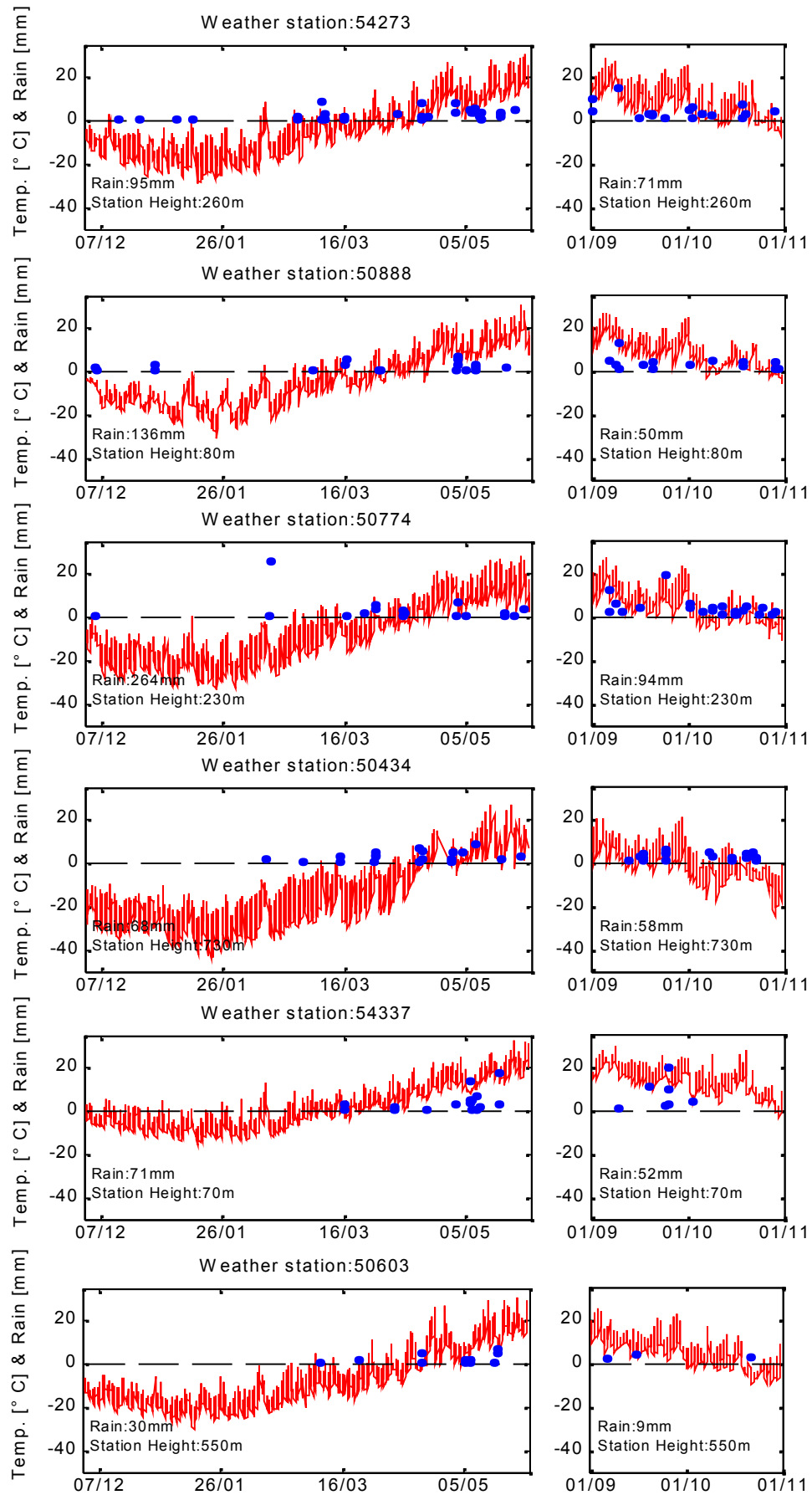


Figure 3.12. Temperature (red lines) and precipitation (blue dots) measured at six weather stations located in different areas of Northeast China. Left: winter 1995/96, right: fall 1997.

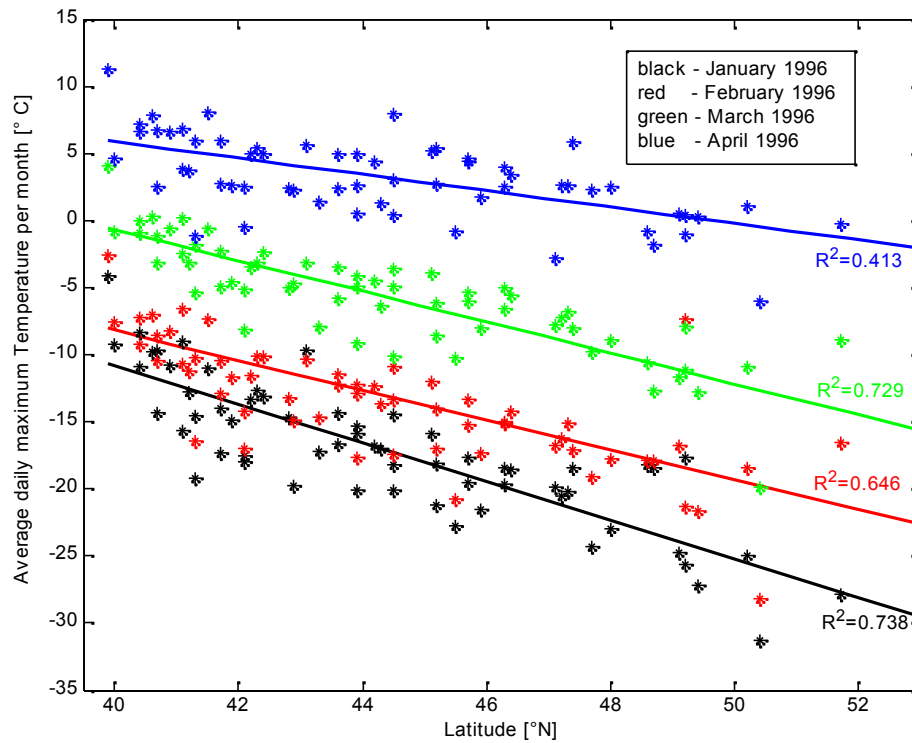


Figure 3.13. Average daily maximum temperature per month versus latitude of the weather station.

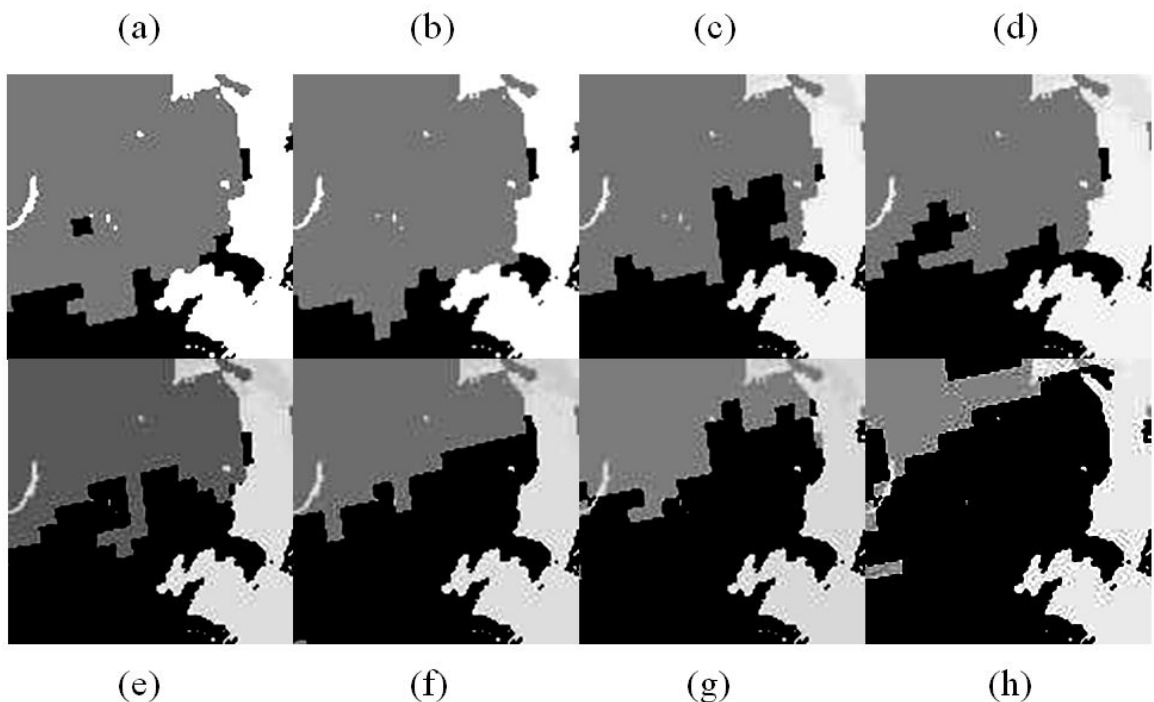


Figure 3.14. NSIDC snow cover maps for eight weeks in the time frame of the ERS acquisitions over Northeast China: a) 21 Dec. 1995 b) 18 Jan. 1996 c) 08 Feb. 1996 d) 28 Feb. 1996 e) 21 Mar. 1996 f) 28 Mar. 1996 g) 18 Apr. 1996 h) 09 May 1996. The grey areas show the snow covered ground.

Chapter 4 - SAR & InSAR measurements at the test sites

In this chapter, the results of the exploratory analysis of the relationship between the standwise ERS-1/2 tandem coherence/intensity measurements and the *in situ* stem volume measurements at the Siberian and Chinese test sites will be described. The discussion addresses the variability of the ERS measurements with the prevailing meteorological and environmental imaging conditions, the relationship between stem volume and coherence as well as the effects of forest structural diversity. First, the observations at the Siberian test sites will be described. A detailed analysis has already been carried out in Santoro et al. (2004, 2007) and Eriksson (2004) which explains why Chapter 4.1 is mainly a recapitulation of their observations. In Chapter 4.2, the observations at the Chinese test sites will be discussed.

4.1 Siberian test sites

The relationship between stem volume and coherence has been illustrated in Figure 4.1 for six ERS-1/2 tandem coherence images. In all cases, the standwise averaged coherence decreased with increasing stem volume; nonetheless considerable differences between the acquisitions were observed. All images acquired in winter as well as the image from 9-10 October 1997 showed no saturation of coherence with respect to stem volume up to at least ~ 200 m³/ha. The least tendency to saturate could be observed in case of the image from 14-15 January 1996 that was acquired with a short baseline of 65 m over Chunsy N & E. For all other images, acquired in fall or spring over the test sites Bolshe NE and NW, saturation was reached at about 100 m³/ha, regardless of the baseline length. For stem volumes above the saturation level coherence ‘clumped’ at low values. The tendency of ERS-1/2 tandem coherence to clump at low values at even intermediate stem volumes in the range of 100 to 200 m³/ha was observed in several publications and can be considered a typical sign of unstable imaging conditions (e.g. Koskinen et al., 2001; Santoro et al., 2002; Pulliainen et al., 2003; Santoro et al., 2007). An explanation for this saturation behavior has not been found yet.

Even though the decrease of coherence with increasing stem volume was apparent in all coherence images and at all test sites, the plots revealed a considerable spread of coherence along the main trend almost independent of stem volume. These variations could have been due to:

- Topographic distortions
- Errors in the inventory data
- Forest structural diversity
- Spatial variability of environmental and meteorological conditions

A detailed discussion of topographic effects in the intensity and coherence images will follow in Chapter 6. For the following analysis, stands with an average slope of more than 10° were not considered. A maximum slope threshold of 10° was found to reliably exclude affected stands (Santoro et al., 2007). As the topography at the Siberian test sites was mostly gentle, only few stands were affected.

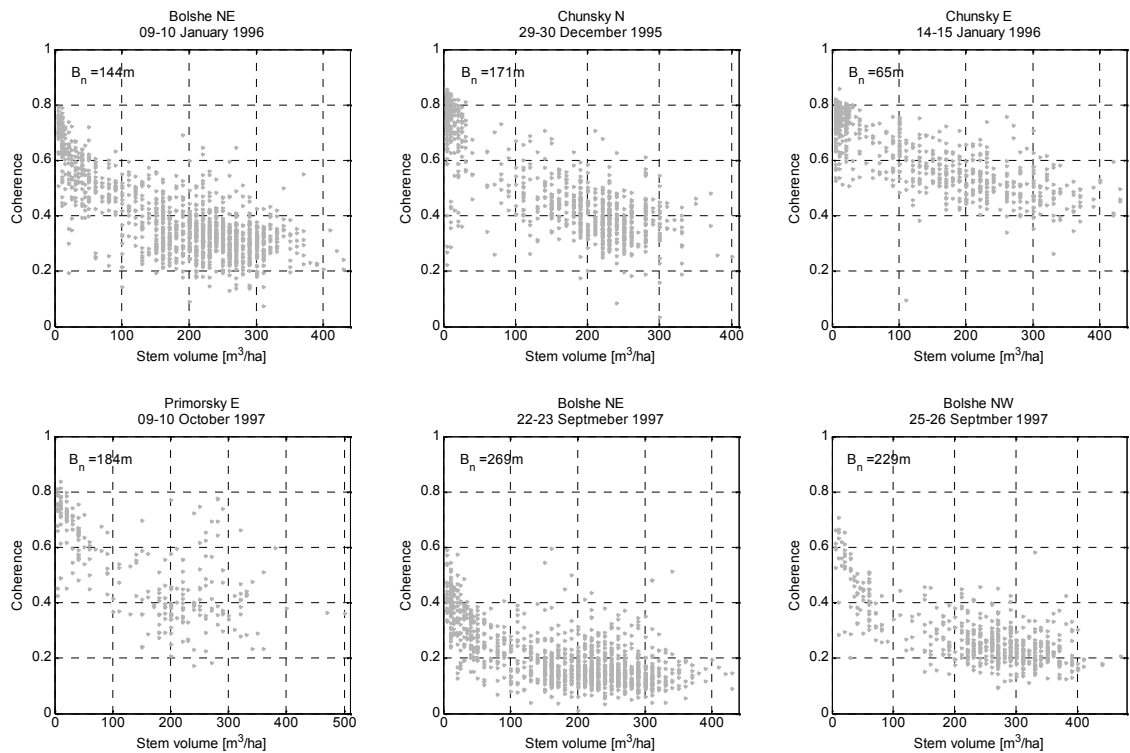


Figure 4.1. ERS-1/2 tandem coherence versus stem volume for three tandem pairs acquired in winter and three tandem pairs acquired in fall at the Central Siberian test sites.

Errors in the inventory data, either in the location of the polygons or the measured forest attributes, would affect the inventory data-based training of models as well as the inventory data-based accuracy assessment (see Chapter 8.2). Hence, errors in the inventory data should be identified and removed from the dataset as far as possible. In order to minimize the effect of mis-registrations between the ERS imagery and the *in situ* data as well as the effect of noise in the coherence measurements, very small stands should be excluded (Fransson et al., 2001; Hyypä & Hyypä, 2001; Santoro et al., 2007; Askne & Santoro, 2005). Santoro et al. (2007) showed for the same dataset that was used for this study that the exclusion of small stands resulted in an increase (in absolute values) in Pearson correlation between stem volume and coherence. The largest increase in correlation was observed when excluding stands smaller than 2 ha. When further excluding stands with sizes larger than 2 ha, improvements could still be noticed but were mostly less pronounced. For the following investigations, a threshold of 2 ha for the minimum stand size was used. Furthermore, some stands were excluded after visual inspection of the data when the borders of the inventory polygons clearly mismatched with visible stand borders in the coherence imagery. High uncertainty was associated with stands with 0 m³/ha stem volume - a volume of 0 m³/ha contradicts the requirements of the Russian forest inventory manuals (cf. Santoro et al., 2007) - or stands that were not labeled as forest in the inventory data (e.g. clear-cuts, burnt areas, unproductive land) which is why they were not considered in the analysis. When screening the forest parameters in the inventory data for erroneous measurements, obvious discrepancies with the satellite data were found. For some stands, the inventory data indicated high stem volume although the coherence was very high. This was most likely the consequence of a failed update of the inventory data after logging has been done. Extreme outliers in the stem volume-coherence relationship were discarded by identifying all stands with a coherence more than two standard deviations of all

standwise coherence measurements above or below the main trend, which was identified by means of a simple regression model that was fitted to the data:

$$\Gamma = a \cdot e^{-cV} + b \cdot (1 - e^{-cV}) \quad (4.1)$$

The parameters a , b and c represent regression parameters and V the stem volume. In Askne et al. (2003) it has been reported that for boreal forest stands of 2 to 14 ha size, the standard error of coherence in a homogeneous forest should be in a range of 0.03 to 0.07. A much larger standard error indicates very heterogeneous forest cover (e.g. partial clear-cut) for which the inventory data was probably erroneous. That is why, stands with a standard error of more than 0.1 were excluded as well.

C-band measurements over forested terrain are the sum of contributions from the forest floor and the canopy. In order to identify the coherence properties of the forest floor and dense forest canopies and to relate them to the meteorological imaging conditions, the simple exponential model in Equation (4.1) was fitted to the standwise coherence measurements. The regression parameter a gave an estimate for the ground coherence and the modeled coherence $\Gamma(V_{max})$ at the maximum stem volume in the inventory data was interpreted as the dense forest coherence. The same was done for the intensity measurements. The results have been illustrated in Figure 4.2.

In case of frozen conditions, the coherence over open ground was in the range of 0.7 to 0.8. Both measurements at the Chunksky test sites (29-30 December 1995 and 14-15 January 1996) revealed a ground coherence of 0.8 whereas the image acquired under subzero temperatures over Bolshe NE (1-2 January 1996) showed a ground coherence of 0.7. This reduced ground coherence was most likely caused by snow cover changes as the image was acquired under refreezing conditions with snowfall occurring, probably accompanied by changes in the snow depth and maybe the snow metamorphism. High ground coherence above 0.8 was also observed for the coherence image from 9-10 October 1997 at Primorsky E. This tandem pair was acquired during a period of rain-free and unfrozen conditions so that heterogeneous soil moisture variations as possible decorrelation source were obviously minimized. For all images acquired in fall or spring over the Bolshe NE and NW test sites, the ground coherence was considerably lower and did not exceed a level of 0.7; in case of the Bolshe NE test site, even 0.5 was hardly exceeded. This was most likely a consequence of rain few days prior to the sensor overpasses respectively the emerging heterogeneous variations of soil moisture after the rain events. In case of the image from 27-28 October 1997, also freeze/thaw effects were involved in addition to rainfall that occurred one week before. In case of the images from 25-26 September 1997 and 28-29 May 1998 there was a clear difference between the ground coherence that was observed at the test sites Bolshe NE and Bolshe NW. In both images, the ground coherence was about 0.15 to 0.2 higher at Bolshe NW. In Santoro et al. (2007), this difference was assumed to be a consequence of differences in heterogeneous soil moisture variations after rainfall as the test sites were characterized by different soil types. Bolshe NE is located east of the Yenisei where peat soils dominate whereas Bolshe NW is located west of the Yenisei where soils are mostly sandy. For the tandem pair from 25-26 September, rain was registered 3 days before the ERS-1 overpass. The sandy soils were probably more dried up at the time of the sensor overpasses than the peat soils, which may still have been in the drying process, accompanied by heterogeneous soil moisture variations lowering coherence. In case of the May acquisition, there was rain one week prior to the sensor overpasses. In addition, the image was acquired after a period of snowmelt resulting in

high soil moisture so that differences in the response of sandy and peaty soils to rain or snow melt induced wetting may as well explain the differences in forest floor coherence between Bolshe NE and Bolshe NW.

Over dense forests, the coherence in the images from fall and spring was mostly in the range of 0.15 to 0.25 and showed no dependence upon the wind speed or the baseline length. This range of coherence values can be considered a typical sign of unstable imaging conditions due to rain or freeze/thaw transitions in the timeframe of or closely before the sensor overpasses (Pulliainen et al., 2003; Drezet & Quegan, 2006). The only exception amongst the acquisitions from fall was observed for the coherence image acquired under more stable conditions and with a baseline of 183 m over Primorsky E; note that for this image no information about wind speed was available. In this case, coherence over dense forest was almost 0.4 which was in the range observed for the winter acquisitions when coherence was between 0.3 and 0.45. In case of the coherence image from 14-15 January 1996 covering Chunsky N and E, the coherence over dense forest was about 0.4 to 0.45 as the canopy was frozen, the baseline was short (65 m), i.e. volume decorrelation was negligible, and the wind speed was moderate (< 2 m/s). In case of the coherence images from 1-2 January 1996 and 29-30 December 1995, stronger winds coincided with baselines above 100 m, both lowering the coherence measured over dense forest to about 0.3.

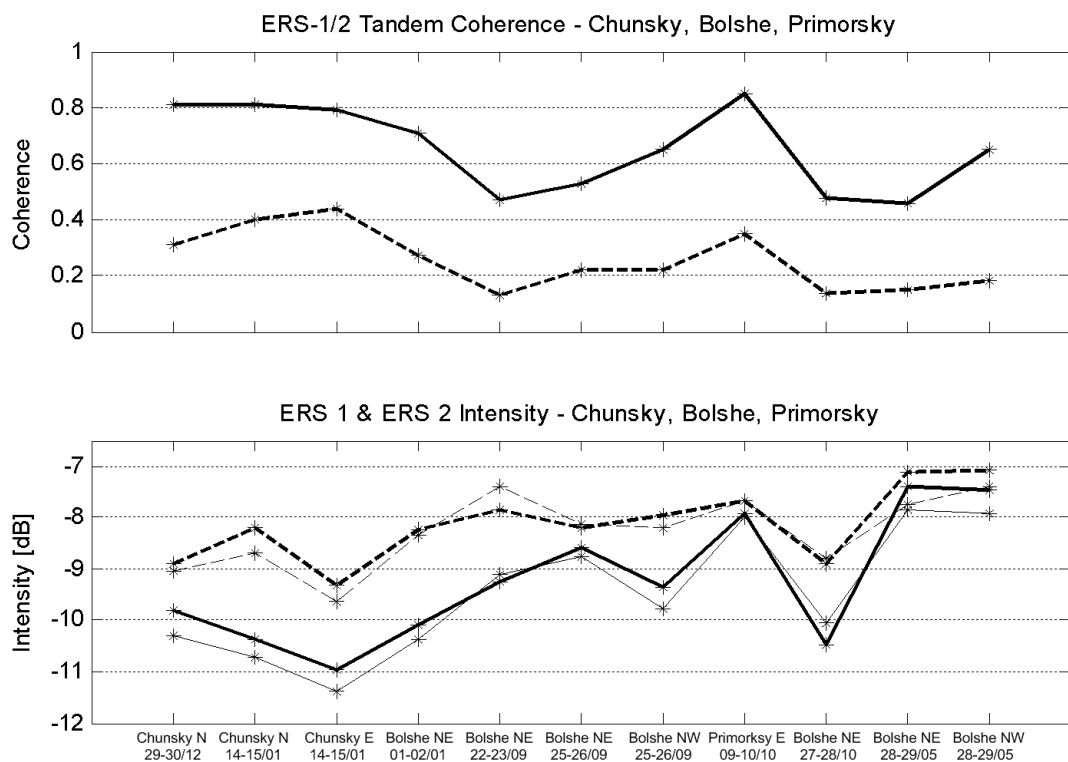


Figure 4.2. Coherence and ERS-1 (thick lines) and ERS-2 (thin lines) intensity over open ground (solid line) and dense forest (dashed line).

Forest floor as well as dense forest intensity were lowest under frozen conditions. When the forest floor was frozen and covered with snow, the intensity was in the range of -9.5 to -11.5 dB. Backscatter from dense forest varied between -8 and -10 dB. In case of the ERS-1 and ERS-2 intensity images from 14-15 January 1996, differences in dense

forest and forest floor intensity of about 1 dB between the test sites Chunksy E and N could be observed, indicating spatial variations of the imaging conditions within the images. The variations of intensity in winter may have been caused by different properties of the snow cover on the ground or on the branches (in Siberia the mostly dry snow is usually blown off the branches quickly) or incomplete freezing of the canopy; the images from 1-2 January 1996, for instance, were acquired under refreezing conditions. In case of unfrozen conditions, forest floor intensity varied between -7.5 and -10 dB. Dense forest backscatter was rather stable between -7 and -8 dB. For the ERS-1/2 tandem intensity images from 27-28 October 1997, acquired in a period with diurnal oscillations of temperatures around 0° C, the backscatter from forest floor and dense forest was comparable to that observed when the conditions were constantly frozen. In case of the ERS-1 and ERS-2 intensity images from 25-26 September 1995, lower backscatter from the forest floor was observed at the test site Bolshe NW which seemed to confirm the assumption (in context of the interpretation of coherence) that the sandy soils at this test site were more dried up after rainfall that occurred 3 days before. The ground backscatter in the acquisitions from 9-10 October 1997 over Primorsky E was -8 dB and as high as the backscatter from dense forest, indicating wet soil. The highest intensity over dense forest (-7 dB) was observed for the images that were acquired in May. This should have been due to an increased tree activity in spring with high water availability resulting from snowmelt (Moghaddam & Saatchi, 1999; Kasischke et al., 2007). The ground backscatter was as well high with about -8 to -7.5 dB due to the wet soil after snowmelt. Furthermore, it has been noticed that the consistency of the standwise intensity measurements in terms of Pearson correlation between the tandem ERS-1 and ERS-2 intensity images was lowest for the May acquisition over Bolshe NE and NW. The Pearson correlation coefficient was about 0.6 in this case whereas it was above 0.8 for all other tandem intensity images, indicating that the tandem pair from May was affected by changing imaging conditions.

Despite the considerable effects of meteorological (frozen/unfrozen temperatures, wind speed, rain) and environmental (soil moisture variations, snow properties) imaging conditions on the overall level of coherence measured over forest floor, the multitemporal consistency of coherence was high. When correlating the standwise coherence measurements for different pairs of coherence images, the Pearson correlation coefficient was, with only one exception, above 0.8 (Figure 4.3), witnessing the robustness of the forest biophysical information in coherence. In general, the lowest correlations were observed when one of the coherence images was the one from 27-28 May 1998. In contrast, when correlating the standwise ERS-1 intensity measurements for different acquisition dates, the correlations varied in a much wider range. While for the winter intensity measurements over Chunksy N, the correlation was high with about 0.8, much lower correlations between 0 and 0.7 were observed when at least one of the two intensity images was acquired in fall or spring.

A higher Pearson correlation between stem volume and ERS-1/2 tandem coherence was observed in Santoro et al. (2007) for large stands with high relative stocking. Figure 4.4 (left) illustrates this for the coherence image from 29-30 December 1995 and the test site Chunksy N. In Chapter 3.3, it was shown that stands with high relative stocking are characterized by a higher density of trees for a given stem volume and probably show a more regular canopy structure. The increase in correlation was observed up to relative stocking thresholds of ~ 80%. When applying higher thresholds, correlation often decreased again as then the stem volume distribution was considerably altered. In case of Chunksy N, for instance, mainly stands with low stem volume <100 m³/ha were then

left in the dataset. Most images in the Siberian dataset showed a higher correlation when considering only large stands with high relative stocking. However, for some of the images, in particular those acquired under unstable imaging conditions over Bolshe NE, the correlation between stem volume and coherence as function of relative stocking revealed an irregular behavior with no consistent improvements in correlation (Figure 4.4, right).

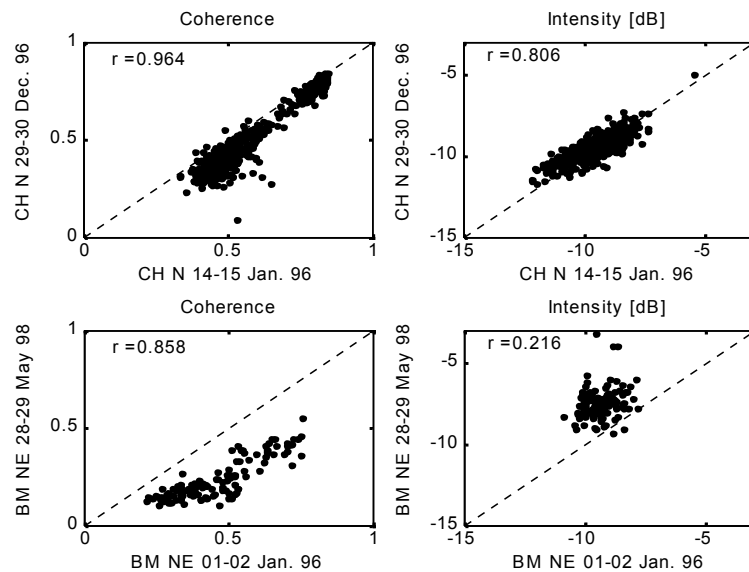


Figure 4.3. Multitemporal consistency of the standwise ERS-1/2 tandem coherence and ERS-1 intensity measurements.

Concerning the overall trend of coherence as function of stem volume, no significant differences between the tree species could be observed. However, a slightly higher correlation between stem volume and coherence could be observed for stands dominated by coniferous species compared to stands dominated by broadleaf species. One example has been illustrated in Figure 4.5 where both, stands with low and high proportions of conifers, covered a comparable range of stem volumes. All acquisitions from winter covering the test sites Chunksy N, Chunksy E and Bolshe NE showed a slightly better correlation when going from stands with less than 20 % to stands with more than 80 % stem volume fractions of conifers. This increase could be observed independent of the relative stocking range considered. For the acquisitions from spring and fall, no increase in correlation was noticed.

In case of the ERS-1 and ERS-2 intensity measurements, the correlation hardly improved with increasing relative stocking because of the low sensitivity of intensity to stem volume. The spread around the mostly ‘flat’ trend, however, was found to decrease with increasing relative stocking. The standard deviation of all standwise intensity measurements, for instance, decreased for about 10 to 25% when excluding all stands with a relative stocking lower than 50 %. No tree species related effects were noticed. The main trend of the standwise intensity measurements with respect to stem volume as well as the spread around the trend were similar for stands dominated by coniferous and broadleaf species, respectively.

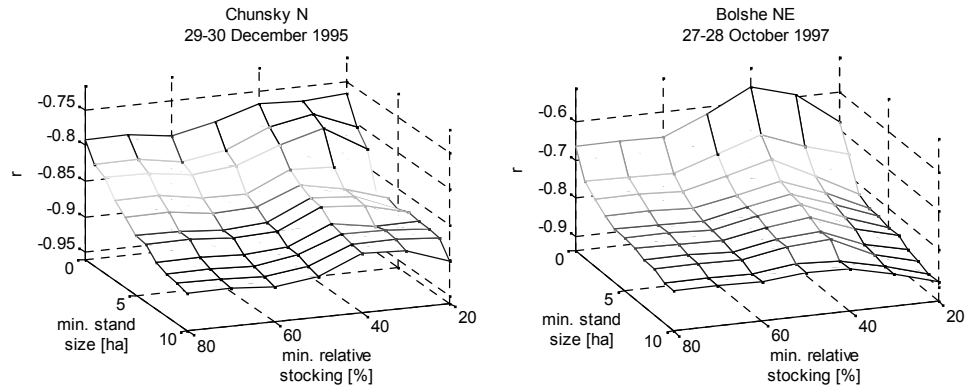


Figure 4.4. Pearson correlation r of coherence and stem volume for different thresholds of minimum stand size and relative stocking.

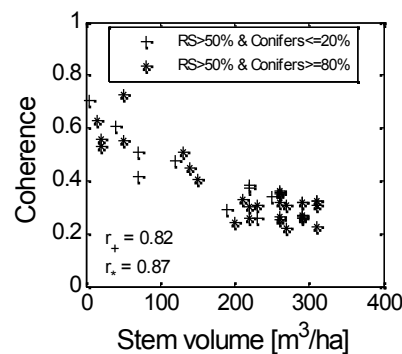


Figure 4.5. Coherence versus stem volume (Bolshe NE 01-02 January 1996) for stands of at least 50 % relative stocking and either less than 20 or more than 80 % conifers (in terms of stem volume fractions).

4.2 Chinese test sites

In contrast to the Siberian data, a decrease of coherence with increasing stem volume was hardly noticeable for the coherence images covering the Chinese test sites. A large spread of the standwise averaged coherence measurements independent of stem volume had to be noticed. This spread was much more pronounced than for the Siberian test sites and the Pearson correlation coefficients of coherence and stem volume were in the range of -0.1 to -0.2. The possibilities to analyze the causes for the spread were limited as the dataset comprised only tables of standwise stem volume, height, size of the edge-eroded stands (in number of pixels), average slope and the corresponding average coherence and intensity. A systematic screening of the inventory data for stand locational errors or a failed inventory update, as it was done for the Siberian test sites, was not possible. Solely stands with a stem volume of 0 m³/ha and a standard deviation of coherence >0.1 were removed from the dataset for the same reasons as in case of the Siberian test sites. The exclusion of these stands, however, had almost no effect on the correlation between stem volume and coherence.

The test sites in the Xiaoxinganling and Changbai Mountains were characterized by steep topography with average slopes of about 10° and altitudes ranging from 500 to 1200 m in the Xiaoxinganling test area and from 750 to 1350 in the Changbai test area. At the Daxinganling test site the topography was mostly gentle with altitudes ranging

from 500 to 750 m. For the analysis of the impact of topographic effects on coherence, only the average slope for each stand was available. The effect of topography-induced decorrelation was first addressed by calculating the Pearson correlation between stem volume and coherence repeatedly, applying different thresholds for the maximum slope. There was no positive effect in terms of a higher correlation in case of two of the test sites when successively excluding the stands located on the steepest slopes. Only in case of the coherence image covering the Changbai test site, the correlation improved to -0.4 when excluding all stands located on slopes steeper than 10° . In case of the Daxinganling test site, it was noticed that the coherence measurements at stands located on slopes steeper than 10° represented the lower margin of the coherence trend as function of stem volume. The exclusion of these stands had, however, almost no effect on the correlation between stem volume and coherence as only few stands were located on slopes steeper than 10° . In case of the coherence images acquired with short baselines < 100 m over the mountainous Xiaoxinganling and Changbai test sites, only some of the stands with an average slope of more than 10° represented the lower margin of the trend with respect to stem volume; some stands revealed a coherence in line or even at the upper margin of the main trend although they were located on slopes steeper than 10° . The reason for this was related to the differences in wavenumbershift for slopes tilted towards or away from the sensor (Gatelli et al., 1994); a detailed explanation of this effect will follow in Chapter 6 where the topography-induced coherence loss will be analyzed with the aid of the SRTM-3 DEM. For the analysis presented in this section, all stands with an average slope of more than 10° were excluded, regardless of their orientation with respect to the sensor as for the test sites no information about the exposition of the slopes was available. At all three test sites, a further exclusion of stands located on even less steep slopes would have affected a large number of stands which showed no clear sign of topography-induced decorrelation.

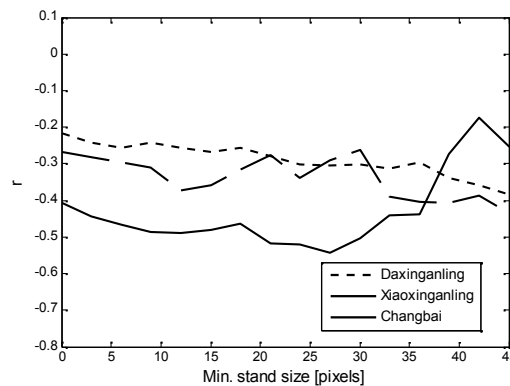


Figure 4.6. Pearson correlation r of coherence and stem volume for different thresholds of minimum stand size in pixels (4 pixels = 1 ha).

The influence of stand size on the correlation of stem volume and coherence has been analyzed for all three test sites. For the Daxinganling test site, the correlation constantly improved from -0.2 to -0.4 when raising the threshold for the minimum stand size to 45 pixels (~ 11 ha). For the other two test sites, the correlation improved slightly when excluding the smallest stands but did not show a consistent improvement in case of thresholds > 12 pixels (3 ha). It was noticed that the selection of a threshold had a great impact on the number of stands and the distribution of stem volumes. The average stand size at the Chinese test sites was much smaller than at the Siberian test sites. When

excluding all stands smaller than 2 ha, the number of stands reduced to 334 (Daxinganling), 308 (Xiaoxinganling) and 532 (Changbai) and the range and distribution of stem volumes was kept. Higher thresholds would have caused a massive reduction of stands in the low ($<100 \text{ m}^3/\text{ha}$) and the high stem volume ranges ($>250 \text{ m}^3/\text{ha}$).

When fitting the model in Equation (4.1) to the coherence measurements at stands larger than 2 ha and with an average slope of less than 10° (see Figure 4.7), the estimated ground coherence for the tandem pairs from 9-10 January 1996 covering Xiaoxinganling and Changbai was ~ 0.6 and the coherence of dense forests was 0.4. A dense forest coherence of 0.4 indicates stable frozen imaging conditions with moderate wind speeds and minor volume decorrelation effects; note that the baselines were $< 100 \text{ m}$. The very low temperatures measured at the nearest weather stations as well as the low ERS-1 intensity measured over dense forest (-10 dB) and open ground (-11 to -12 dB) confirmed this expectation. Considering the constantly frozen temperatures, the ground coherence of 0.6 appeared to be low though. The reason for this was not clear. At Daxinganling, the maximum stem volume was only $120 \text{ m}^3/\text{ha}$ so that no statement was possible concerning the dense forest coherence in the coherence image from 20-21 December 1995. The ground coherence was also 0.6 but the massive spread of coherence between 0.4 and 0.8 for even the lowest stem volumes (Figure 4.7) caused the estimation of the ground coherence to be very uncertain.

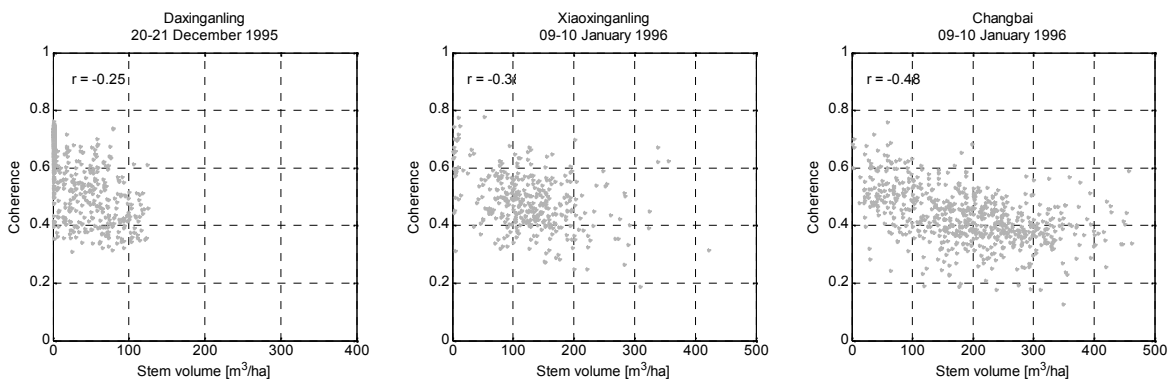


Figure 4.7. Coherence versus stem volume for all stands at the Chinese test sites with slope $< 10^\circ$, stem volume $> 0 \text{ m}^3/\text{ha}$ and stand size $> 2 \text{ ha}$.

Based on the considerations in Chapter 3.3, stands assumed to be fully or close to fully stocked were isolated by means of their stem volume to height relation. The correlation of stem volume and coherence was calculated including only those stands for which the tree height was in a defined range above or below the tree height defined by the allometric stem volume-height relationship valid for the forests at Daxinganling with high SDI > 650 . When narrowing this height range, an improvement of the correlation between stem volume and coherence was noticed (Figure 4.8). The most pronounced improvement was observed for Daxinganling whereas for the other test sites the improvement was moderate. The highest correlation was achieved when allowing for a maximum deviation of $\pm 1 \text{ m}$ from the reference allometric stem volume-height relation but then the number of stands was massively reduced, e.g. only three stands at Daxinganling.

On the one side, the observations seemed to confirm the higher suitability of fully stocked stands for stem volume retrieval. On the other side, it had to be noticed that the correlation between coherence and stem volume was still much lower than for the ERS-1/2 tandem coherence images covering the Siberian test sites (see Figure 4.4).

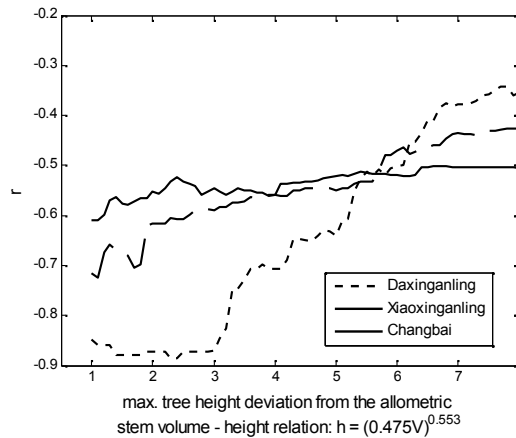


Figure 4.8. Pearson correlation r of stem volume and coherence when isolating stands for which tree height deviates less than ± 1 to 8 m from the allometric relation, obtained in Chapter 3.3 for stands with high SDI.

Table 4.1. ERS-1/2 tandem coherence and ERS-1 intensity of open ground and dense forest for the ERS-1/2 tandem pairs covering the Chinese test sites.

Test site	Acq. Dates	γ_0	γ_{dense}	σ_0^0 [dB]	σ_{dense}^0 [dB]
Daxinganling	20-21 Dec. 95	0.59	-	-12.0	-
Xiaoxinganling	9-10 Jan. 96	0.61	0.40	-11.8	-10.1
Changbai	9-10 Jan. 96	0.60	0.41	-11.3	-10.3

4.3 Summary

In this chapter, the relationship between stem volume and coherence was analyzed and the factors were discussed that influenced the relationship between stem volume and coherence. The investigation considered the effect of the weather conditions, topography, properties of the reference data and forest structure.

While the coherence decrease with increasing forest stem volume was apparent and temporally consistent in the coherence images covering the Siberian test sites, the variability of the overall coherence, as well as intensity, level with meteorological and environmental acquisition conditions was large. Even within-frame variations of coherence and intensity properties were noticed when comparing the signatures for different test sites covered by one image. Although there were some seasonal patterns in both, the coherence and intensity signatures measured over open ground and dense forest (e.g. higher forest floor coherence in winter than in the other seasons), the use of any kind of generalized statistics for forest stem volume retrieval can clearly be ruled out. Rainfall, freeze/thaw transitions or differing wind speeds have a considerable short-term influence on the measurements. A prediction of the coherence properties with the

aid of meteorological measurements cannot be considered feasible (cf. Drezet & Quegan, 2006) as coherence not only depends on the weather conditions, i.e. temperature or wind speed, but also on environmental effects related to soil moisture or the snow properties.

The saturation of coherence with increasing stem volume depended on the imaging conditions. In case of stable frozen imaging conditions and perpendicular baselines between 65 and 171 m, no saturation could be observed for stem volumes up to at least 200 m³/ha whereas saturation was reached at about 100 m³/ha for all tandem pairs that were acquired in fall or spring over the Bolshe test sites regardless of baseline length; note that the shortest baseline was 158 m. Still, in case of the image from 9-10 October 1997, no saturation up to 200 m³/ha stem volume was found, showing that also under unfrozen conditions ERS-1/2 tandem coherence can be sensitive to differences in forest stem volume above 100 m³/ha.

Forest structural differences in terms of relative stocking and tree species composition had an effect on the relationship between coherence and stem volume. The highest correlation between stem volume and coherence was found for coniferous forest stands with high relative stocking. The higher correlation for fully-stocked stands was most likely caused by a more regular and homogeneous forest canopy structure.

The subsumption of the observations at the Chinese test sites was difficult. At first sight, the results suggested that coherence was less suited for stem volume retrieval in case of the Northeast Chinese forests. A limiting factor may have been that a higher structural diversity of the forests caused a lower correlation between stem volume and coherence. In Chapter 3.3, it was shown for the Daxinganling test site that, compared to the Siberian test sites, a higher proportion of forest stands grew in an understocked state (lower average SDI) which could explain the lower correlation between stem volume and coherence. But even when considering only those stands with a high SDI, i.e. those stands that should exhibit a more regular canopy structure, the correlation between coherence and stem volume was much lower than for the coherence images acquired over the Siberian test sites under comparable weather conditions. The unknown quality and/or timeliness of the ground data is considered a crucial issue though. As the inventory data was not available in form of digital stand boundary maps, no screening for locational errors or a failed inventory update was possible. In addition, the average stand size was rather small so that the possibility to focus the analysis on large stands, for which the effects of stand locational errors and noise in coherence should have been reduced, was limited.

Chapter 5 - Coherence modeling and model training

This chapter addresses the modeling of coherence as function of stem volume and explores different approaches to train the models, i.e. to determine the unknown model coefficients.

The chapter starts with a description of the two models used for this study, both relating coherence to stem volume. Yet, there exists only one approach that aims at the automated training of an empirical model without further need for forest inventory measurements. This so-called SIBERIA training algorithm will be described in Chapter 5.2. In the following sections, the possibility to capture the spatial and temporal variability of ERS-1/2 tandem coherence over forested terrain and to determine the unknown parameters of a semiempirical model with the aid of the MODIS Vegetation Continuous Field tree cover product will be discussed.

5.1 Modeling of ERS-1/2 tandem coherence as function of stem volume

The modeling of coherence as function of forest biophysical parameters, in particular stem volume, was yet done with simple empirical linear or exponential models (e.g. Hyypä et al., 2000; Manninen et al., 2000; Fransson et al., 2001; Wagner et al., 2003) or semi-empirical models where model parameters have physical relevance and can be related to forest structural properties as well as the environmental and meteorological imaging conditions (Treuhaft et al., 1996; Askne et al., 1997; Koskinen et al., 2001; Papathanassiou & Cloude, 2001).

For the production of the first large-area forest stem volume map of Central Siberia with ERS-1/2 tandem coherence, a simple exponential model was utilized (Wagner et al., 2003):

$$\gamma(V) = \gamma_{\infty} + (\gamma_0 - \gamma_{\infty}) \cdot e^{-V_{\gamma} \cdot V} \quad (5.1)$$

The model in Equation (5.1) describes the relationship between coherence and stem volume as an exponential decrease of coherence with increasing stem volume. γ_0 represents the coherence for a stem volume of 0 m³/ha and γ_{∞} the saturated coherence of dense forest. V_{γ} gives the rate of coherence decrease with increasing stem volume.

The most widely tested and mature semi-empirical model is the Interferometric Water Cloud Model 'IWCM' (Askne et al, 1997, 2003; Santoro et al, 2002). In contrast to the empirical model in Equation (5.1), the IWCM accounts for volume decorrelation and InSAR geometry effects as well as differences in the backscatter contributions coming from the forest floor and the canopy. It was successfully tested for ERS-1/2 tandem coherence measurements at various boreal forest sites in Scandinavia and Siberia (Santoro et al., 2002, 2007; Askne et al., 2003; Askne & Santoro, 2005, 2007). As the objective of this study was not (at least primarily) to improve or refine the understanding of the existing models but to integrate the existing knowledge into a fully-automated model training procedure, the extensive experience that has been gathered with the IWCM in previous studies was the reason why it was chosen as modeling basis.

The concept of the IWCM bases on a Water-Cloud-type-of model for intensity measurements that was introduced in Askne et al. (1995). Herein, intensity is related to stem volume based on observations in Pulliainen et al. (1994). Pulliainen et al. found an exponential relationship between the two-way forest transmissivity, T_{for} , and the stem volume, V , for profiling X- and C-band scatterometer measurements over a boreal forest site in southern Finland:

$$T_{for} = e^{-\beta V} \quad (5.2)$$

with β being an empirical coefficient that was considered to be a function of the canopy moisture content. The backscatter measured over forest, σ_{for}^0 , could thus be expressed as an incoherent sum of a canopy and a forest floor contribution, both weighted by the forest transmissivity:

$$\sigma_{for}^0 = \sigma_{gr}^0 T_{for} + \sigma_{veg}^0 (1 - T_{for}) \quad (5.3)$$

where σ_{gr}^0 and σ_{veg}^0 represent the forest floor and canopy backscatter. Several authors reported a significant impact of gaps in the canopy on the penetration of C- and X-band signals into a forest canopy (Hagberg et al., 1995; Askne et al., 1997; Martinez et al., 2000; Izzawati et al., 2006). It was observed that backscatter occurred in depths lower than could have been expected for a homogeneous canopy layer with typical signal attenuation characteristics. Martinez et al. (2000) and Izzawati et al. (2006) interpreted this to be a consequence of decreasing canopy diameters with tree height, which means that at the margin of a tree a (vertical) signal would reach the lower branches without being attenuated before. Askne et al. (1995) concluded that the forest transmissivity is determined by two separate terms, the two-way transmissivity of trees and the gaps in the canopy. The effect of gaps was described with the area-fill factor, η , which represents the fraction of ground covered by the forest canopy in the perspective of the sensor. Thus, forest backscatter can be understood as the sum of three contributions (see Figure 5.1):

- 1 Volume scattering in the crown
- 2 Ground backscatter attenuated by the canopy
- 3 Direct backscatter from the ground

The incoherent sum of these three contributions then becomes:

$$\sigma_{for}^0 = \eta [\sigma_{veg}^0 (1 - T_{tree}) + \sigma_{gr}^0 T_{tree}] + (1 - \eta) \sigma_{gr}^0 \quad (5.4)$$

with the two-way tree transmissivity, T_{tree} , expressed according to Equation (2.21). Equation (5.4) can be re-arranged so that it corresponds to the model in Equation (5.3) when formulating the forest transmissivity as follows:

$$T_{for} = (1 - \eta) + \eta T_{tree} = e^{-\beta V} \quad (5.5)$$

This forest transmissivity concept accounts for vertical discontinuities in the canopy in form of a temporally variable signal attenuation and horizontal discontinuities in form of gaps. Because of the strong signal attenuation in the canopy in case of C-band, the forest transmissivity should mainly be determined by the gaps in the canopy. When considering the tree transmissivity negligible, Equation (5.5) can be simplified to:

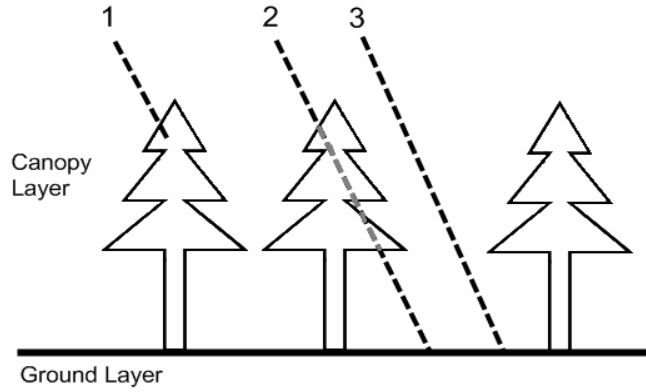


Figure 5.1. The main scattering mechanisms over forest in case of C-band: 1) volume scattering in the crown, 2) ground backscatter attenuated by the canopy, 3) ground backscatter not attenuated by the canopy.

$$T_{for} = (1 - \eta) \quad (5.6)$$

Evidence for a correlation between area-fill factor and forest transmissivity, at least for a homogeneous managed type of boreal forest, has been provided in Askne et al. (1999). Askne et al. compared area-fill estimates from digital photographs with transmissivity estimates by means of scatterometer measurements. Though quite noisy, the measurements confirmed the assumed linear trend. Modeling results with ERS-1/2 tandem coherence acquired over managed Scandinavian forest (accompanied by ground measurements of area-fill) in Santoro et al. (2002) and Siberian boreal forest in Santoro et al. (2007) indicated that in case of C-band, β should vary in a rather narrow range between 0.003 and 0.007 ha/m³ with the lowest value possible under frozen conditions when signal attenuation in the canopy is weak(er). Comparable values were reported in Pulliainen et al. (1994) for C-band scatterometer and in Kurvonen et al. (1999) for ERS intensity measurements over Finnish boreal forest sites. The relationship between stem volume and forest transmissivity, T_{for} , according to Equation (5.2) has been illustrated in Figure 5.2. The figure shows that for a lower β , the decay of transmissivity with increasing stem volume is less steep.

Accordingly, the IWCM in Equation (5.7) describes the complex forest coherence, γ_{for} , as the sum of a ground and a canopy contribution weighted by the forest transmissivity:

$$\gamma_{for} = \gamma_{gr} \frac{\sigma_{gr}^0}{\sigma_{for}^0} e^{-\beta V} + \gamma_{veg} \frac{\sigma_{veg}^0}{\sigma_{for}^0} (1 - e^{-\beta V}) \left[\frac{\alpha}{(\alpha - j\omega)} \frac{(e^{-j\omega h} - e^{-ah})}{(1 - e^{-ah})} \right] \quad (5.7)$$

$$\omega = \frac{4\pi B_n}{\lambda R \sin \theta} \quad (5.8)$$

In the model, the backscatter from the forest floor, σ_{gr}^0 , and canopy, σ_{veg}^0 , with respect to the total forest backscatter, σ_{for}^0 , are weighted by the temporal coherence of the forest floor, γ_{gr} , and the canopy, γ_{veg} , respectively. γ_{veg} represents the temporal coherence of an ideally opaque canopy and is assumed to be the same at all heights within the canopy. σ_{for}^0 is modeled as function of stem volume according to Equation (5.3).

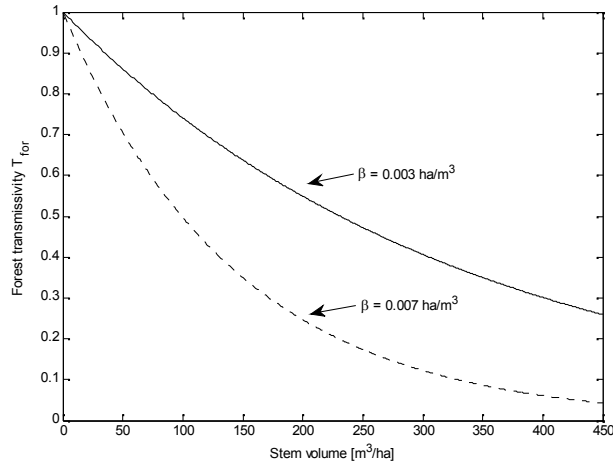


Figure 5.2. Forest transmissivity as function of stem volume according to Equation (5.2) for β of 0.003 and 0.007 ha/m^3 .

σ_{gr}^0 and σ_{veg}^0 are assumed to be equal for both acquisitions that are used for the calculation of coherence; the sensitivity of the model to changes in backscatter between the ERS-1 and ERS-2 acquisitions has been shown to be weak (Santoro, 2003). The term in square brackets in Equation (5.3) accounts for the volume decorrelation and InSAR geometry effects, with the coefficient ω denoting the InSAR geometry (Equation (5.8)). The volume decorrelation expression in the square brackets can be derived from Equation (2.35) when assuming that the strength of volume backscatter decreases exponentially with the distance the signal has covered within the canopy. Volume decorrelation depends on the length of the perpendicular baseline, the depth of the canopy layer (assumed to equal tree height) and the two-way signal attenuation, α . IWCM modeling results for ERS-1/2 tandem coherence acquired over boreal forest revealed a low sensitivity of the model to the exact value of α (Santoro et al., 2002; Santoro, 2003). This was considered a consequence of the strong attenuation of the C-band signal in the tree canopy. Thus, most studies that utilized the IWCM for the modeling of ERS-1/2 tandem coherence used a constant value for α of 2 dB/m (Santoro et al., 2002, 2005; Askne et al., 2003; Askne & Santoro, 2005). A sensitivity analysis in Santoro et al. (2007), based on the same data that was used for this study, indicated somewhat more realistic modeling results when setting α to 1 dB/m in case of frozen conditions.

In order to reduce the number of unknowns in the model, the tree height is usually expressed as function of stem volume (Askne et al., 1997; Santoro et al., 2002, 2007). In Chapter 3.3, it was shown that a simple equation of the form $h=(a*V)^b$ can be used to describe the allometric relationship between stem volume and height. According to the allometric relations obtained for several Scandinavian boreal forest test sites (Askne et al., 1997; Santoro et al., 1999), which were very similar to the allometric relation obtained in Chapter 3.3 for high relative stocking stands at the Siberian test sites, it can be presumed that these Scandinavian test sites were dominated by close-to-fully stocked stands (Figure 3.8). The impact of the different allometric relations for fully stocked stands on the modeling of coherence with the IWCM has been analyzed in Santoro et al. (2007). It was concluded that the differences in the allometric expressions were of minor importance. For stands with low relative stocking, no analysis has been carried out yet.

The modeled coherence in Equation (5.7) is a complex number. The amplitude represents the forest coherence. The phase of γ_{for} represents the interferometric phase as seen by the radar over forest. The phase, related to height through ω , lies between the ground level and the canopy scattering level and depends on the signal attenuation and the canopy gap structure. With increasing canopy closure, the effective height of the interferometric phase approaches the interferometric tree height level, which is the real tree height minus the penetration depth (Floury et al., 1997). In case of ERS-1/2 tandem data, the phase noise due to the temporal instability of backscatter from the tree canopies as well as atmospheric effects strongly limit the use of the interferometric phase for tree height estimation (Santoro et al., 2005).

Basically, the IWCM predicts an exponential decrease of coherence with increasing stem volume until the forest transmissivity becomes negligible. The volume decorrelation and InSAR geometry effects, however, cause additional decorrelation and introduce an oscillation of coherence, i.e. an increase with increasing stem volume, when the tree height exceeds half the ambiguity height. The stem volume, V_{min} , for which coherence reaches a minimum, can be approximated with following expression (Santoro, 2003):

$$V_{min} = \frac{1}{a} b \sqrt{\frac{\lambda R \sin \theta}{4B_n}} \quad (5.9)$$

where a and b are the coefficients of the allometric tree height to stem volume relation. When setting a and b to 2.44 and 0.46 (see Chapter 3.3), Equation (5.9) predicts an oscillation in the range of stem volumes that can be found in the boreal zone, i.e. up to $\sim 500 \text{ m}^3/\text{ha}$, only when the baseline exceeds $\sim 180 \text{ m}$. In case of a baseline of 300 m , the minimum coherence is reached for a stem volume of $\sim 165 \text{ m}^3/\text{ha}$.

Finally, it has to be mentioned that the IWCM in Equation (5.7) reduces to the simple model in (5.1) when $\sigma_{gr}^0 = \sigma_{veg}^0 = \sigma_{for}^0$ and $B_n = 0 \text{ m}$. In all other cases, γ_∞ and V_γ have to be considered as mere regression parameters with very limited physical meaning.

5.2 Model training

When setting the signal attenuation α to 1 dB/m in case of frozen and 2 dB/m in case of unfrozen conditions and replacing the unknown tree height with an allometric equation, formulating height as function of stem volume, five parameters in Equation (5.7) remain unknown: γ_{gr} , γ_{veg} , σ_{gr}^0 , σ_{veg}^0 and β . In the empirical model in Equation (5.1), there are three unknowns: γ_0 , γ_∞ and V_γ . The determination of the unknown model parameters requires up-to-date ground reference data for a dense set of test sites in order to capture the temporal and spatial variability of coherence. The following sections in this chapter will consider the possibility to determine the unknown model parameters without using inventory data. Still, the inventory data driven training of the models in Equation (5.1) and (5.7) will serve as reference for the following analysis.

5.2.1 Inventory data-based model training

The regression procedure that has been suggested for the inventory data-based training of the IWCM (Santoro et al., 2002) is carried out iteratively and aims at a minimization

of the sum of the squared residuals between measured, $\gamma_{measured}$, and modeled, $|\gamma|_{model}$, coherence as function of stem volume (the index i denotes the stand):

$$\sum_{i=1}^N \left[\gamma_{measured,i} - |\gamma|_{model,i} \left(\gamma_{gr}, \gamma_{veg}, \beta, \sigma_{gr}^0, \sigma_{veg}^0 \right) \right]^2 = \min \quad (5.10)$$

In a first step, $\sigma_{gr}^0 = \sigma_{veg}^0 = \sigma_{for}^0$ is assumed. The three unknowns γ_{gr} , γ_{veg} and β are determined by fitting the IWCM in Equation (5.7) to the coherence measurements (averaged for each stand) at the test sites. With the value obtained for β , σ_{gr}^0 and σ_{veg}^0 are estimated by fitting the model in Equation (5.3) to the intensity measurements at the test sites:

$$\sum_{i=1}^N \left[\sigma_{measured,i}^0 - \sigma_{model,i}^0 \left(\sigma_{gr}^0, \sigma_{veg}^0, \beta \right) \right]^2 = \min \quad (5.11)$$

These values for σ_{gr}^0 and σ_{veg}^0 are then used for a refinement of γ_{gr} , γ_{veg} and β by fitting the IWCM to the coherence measurements at the test sites again. The last two steps are repeated until the parameters converge (generally two to three iterations).

In case of the simple empirical model in Equation (5.1) with three unknowns, least-squares regression was done in a single step:

$$\sum_{i=1}^N \left[\gamma_{measured,i} - \gamma_{model,i} \left(\gamma_0, \gamma_\infty, V_\gamma \right) \right]^2 = \min \quad (5.12)$$

5.2.2 The SIBERIA model training approach

In the SIBERIA project a method was developed that allowed the fully-automated training of the empirical model in Equation (5.1) for an ERS-1/2 tandem dataset covering a 1 Million km² large area in Central Siberia on a frame-by-frame basis (Wagner et al. 2003), i.e. training was done for each coherence image covering an area of 100 x 100 km² separately. It was found that γ_∞ could be calculated from the coherence histogram as there was a high correlation between γ_∞ , obtained when fitting the model in Equation (5.1) to the measurements at several Central Siberian test sites (including those used for this study), and the coherence value where the typical ‘forest peak’ in the coherence histograms at low coherence values reached 75 % of its maximum ‘height’ on the left flank (see Figure 5.3). This histogram parameter is from now on referred to as γ_{75} . With γ_∞ being adaptive, the parameter for forest floor coherence γ_0 could be derived as γ_0 was, at least to some extent, linearly related to γ_∞ ($R^2 = 0.54$). The parameter V_γ varied in a wide range when fitting the model to the measurements at the test sites. Still, it was decided to use a fixed value for V_γ for the automated model training; the mean of all obtained values for V_γ (0.0082 ha/m³). As the sum of squared residuals between modeled and measured coherence differed only for a few percent when fitting the model in Equation (5.1) to the measurements at the test sites using this fixed value for V_γ and when including V_γ as unknown parameter in the regression, respectively, the decision for a fixed V_γ was considered reasonable.

Once being trained on an ERS frame, Equation (5.13) could be used for the discrimination of stem volume classes:

$$\gamma(V) = \gamma_{75} + (0.33 + 0.581 \cdot \gamma_{75}) \cdot e^{-0.0082 \cdot V} \quad (5.13)$$

As the only unknown in Equation (5.13), γ_{75} , could be calculated from the coherence histogram, the approach was fully-automated. However, the feasibility of the approach can be expected to experience narrow constraints. It has been developed for ERS-1/2 tandem coherence data that was acquired solely in fall and with a narrow range of baselines around 200 m. A first test of the model training approach with ERS-1/2 tandem pairs acquired under stable frozen winter conditions showed that the forest peak in the histograms reached higher values than for any of the ERS-1/2 tandem pairs from fall that were used for SIBERIA-1 (Eriksson et al., 2002). Further constraints of the approach are that volume decorrelation effects are not considered in the empirical model and that the training procedure relied upon the dominance of dense forest in each image. Otherwise the characteristic ‘forest peak’ at low coherence values in the histogram would not appear.

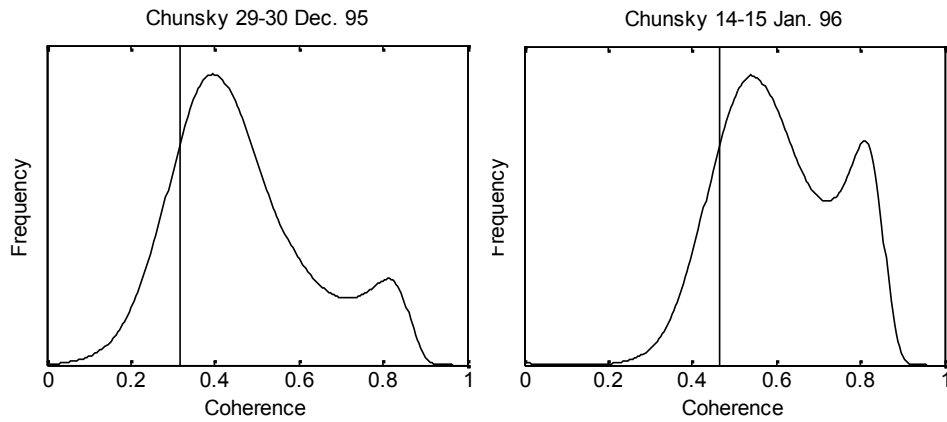


Figure 5.3. Histograms of ERS-1/2 tandem coherence acquired over the Chunsky test sites. The vertical lines represent the coefficient γ_{75} in Equation (5.13). Coherence histograms generally show two peaks over forested areas. The peak at lower coherence values corresponds to forest, the peak at higher coherence values to open areas.

It has to be mentioned that the SIBERIA algorithm also used L-band intensity measurements of the Japanese Earth Resource Satellite JERS-1. The L-band intensity data mainly served the identification of water surfaces and less the discrimination of forest stem volume classes. As JERS data was not available for Northeast China, the JERS intensity related part of the algorithm has not been considered in this study.

5.2.3 VCF-based model training

In the following sections, it is investigated if the VCF tree cover product can be exploited for the determination of the unknown coefficients in the IWCM.

5.2.3.1 Relationship between ERS-1/2 tandem coherence and VCF tree cover

To compare the VCF tree cover map with the ERS imagery, VCF was resampled to the pixel size and projection of the geocoded ERS-1/2 images utilizing the nearest neighbor resampling method. The upscaling of the original VCF data to the pixel size of the ERS imagery was done by creating the corresponding number of equal valued $50 \times 50 \text{ m}^2$ pixels out of one $500 \times 500 \text{ m}^2$ VCF pixel. In this way, it was possible to carry out a pixel-by-pixel comparison of the ERS and VCF data without tampering the VCF tree cover information by any kind of interpolation. To avoid the inclusion of coherence measurements that were affected by topography, all pixels located on slopes steeper than 10° were masked. In addition, the surrounding pixels up to 200 m away from the pixels located on steep slopes were masked; for an explanation see Chapter 6. Water surfaces were masked with the SRTM water body map.

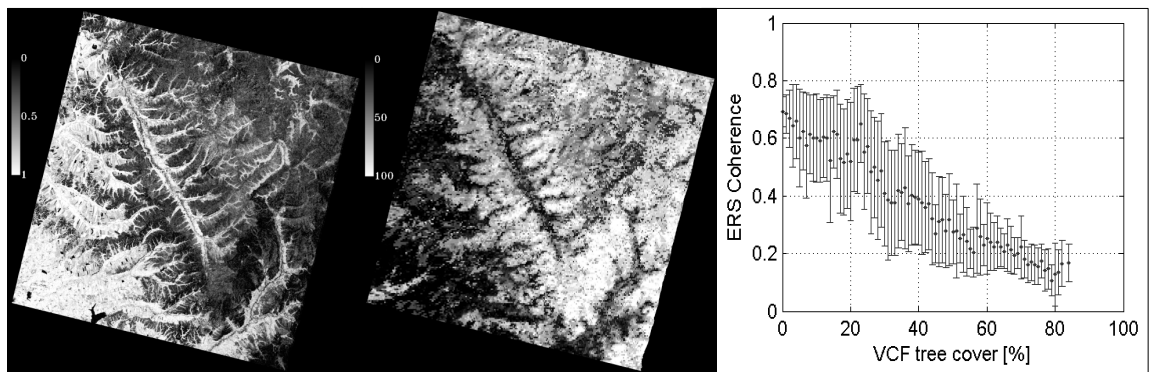


Figure 5.4. ERS-1/2 tandem coherence (left) and VCF tree cover (middle) for a forested area in the Xiaoxinganling. The coherence image was acquired 3-4 October 1997 with a perpendicular baseline of 291 m. The right plot shows the decrease of the average coherence with increasing VCF tree cover \pm one standard deviation of coherence.

When visually comparing the ERS-1/2 tandem coherence images and the MODIS VCF product, it was obvious that they contained a very similar type of information. One example has been illustrated in Figure 5.4. The similarity between the ERS coherence image and the VCF map became even more evident when calculating the average coherence for each VCF tree cover level. In the example shown in Figure 5.4 (right), coherence decreased almost linearly with increasing VCF tree cover up to the highest tree cover of $\sim 80\%$; a tree cover level that is hardly exceeded in the boreal zone. The coherence decrease was accompanied by a considerable spread, shown in Figure 5.4 with the errorbars denoting the standard deviation of coherence.

To clarify the link between coherence and VCF tree cover, coherence histograms were computed for different VCF tree cover classes. First, following classes were considered: 0 – 100%, 0 – 10%, 11 – 40%, 41 – 75% and $>75\%$. Figure 5.5 shows the histograms for two ERS-1/2 tandem coherence images that were acquired with comparable baselines and under similar weather conditions, i.e. frozen temperatures and snow cover on the ground. The examples were chosen as they represented extremes in the relationship between VCF tree cover and ERS-1/2 tandem coherence and provided a good insight into the relationship. For the following discussion, they are referred to as:

- Scenario 1 – which represents a largely exploited forest area in the northwestern Xiaoxinganling region with a mostly open canopy structure and only few mature forests left. The northwestern Xiaoxinganling region was reported to be an area of extensive selective logging in Achard et al. (2006).
- Scenario 2 – which represents an area in the Chunsky forest territory where mature and over-mature forests dominate and where logging is usually carried out in form of large clear cuts.

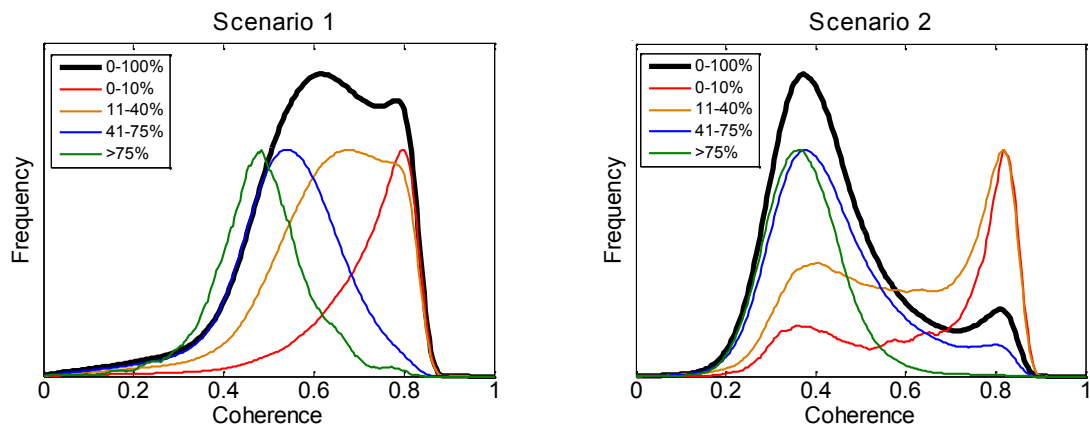


Figure 5.5. Coherence histograms for four VCF tree cover classes. Both coherence images were acquired under frozen conditions. Scenario 1: coherence from 30-31 December 1995, Xiaoxinganling ($B_n = 202$ m); Scenario 2: coherence from 29-30 December 1995, Chunsky ($B_n = 171$ m). The histograms for the four VCF classes have been rescaled to a common peak height for better interpretability.

In both examples (and all other images tested), the coherence histograms for the highest and the lowest VCF tree cover classes represented the margins of the total coherence range in the images, suggesting that the areas delineated corresponded to sparse forest and dense forest cover, respectively. However, in case of the red coherence histogram in the scenario 2 example a clear second peak at low coherence values could be seen. These low coherence values were either caused by strong decorrelation over some of the open areas (e.g. roughness or moisture changes between the tandem acquisitions) or by dense forests that were erroneously classified as areas with low tree cover in the VCF map. As the temperatures during acquisition were deeply frozen, the latter was the more likely explanation. In the red coherence histogram for scenario 1 there was no second peak at low coherence values but the histogram was clearly tailed towards lower coherence values. Similar observations were made for a large number of coherence images in the Siberian and Northeast Chinese ERS-1/2 tandem dataset. When considering that the ERS and MODIS images were acquired with about five years time lag, logging or fire disturbance in these five years were most likely responsible for the discrepancies between VCF and the ERS imagery. For the high tree cover areas, no comparable observations were made. They generally showed a Gaussian type of coherence distribution.

The coherence histograms for the intermediate 11-40 % and 41-75 % tree cover classes revealed very different relations in both examples. In the scenario 1 case, the coherence measurements appeared as unimodal distributions whereas the coherence distributions in scenario 2 were clearly bimodal, i.e. one part of the corresponding coherence pixels

showed high coherence, indicating no or sparse forest cover, and the other part showed low coherence, indicating dense forest. In the scenario 1 case, the coherence histogram successively shifted towards lower coherence values with increasing VCF tree cover when computing the coherence histograms for different intermediate VCF tree cover ranges. In scenario 2, the location of the two coherence peaks did not change when considering different intermediate VCF tree cover levels. With increasing tree cover, however, the number of pixels at the high coherence peak decreased, i.e. the height of the peak decreased, and the number of pixels at the low coherence peak increased, i.e. the height of the peak increased.

To explain the differences between both scenarios, let us start with what is shown in Figure 5.6. The figure shows the area of two $500 \times 500 \text{ m}^2$ VCF pixels. The grey lines show the extent of the pixels in the ERS-1/2 tandem coherence images. The circles represent tree crowns. For both 500 m pixels, the tree cover should be in an intermediate range; for the sake of simplicity let us assume it was 50 % for both VCF pixels. The two examples show that a VCF tree cover of 50 % at 500 m can mean a different tree cover in the scale of the ERS imagery:

- 1) In case of a homogeneous distribution of trees, tree cover will be comparable in both scales, i.e. the 50 m pixel size of coherence as well as the 500 m pixel size of VCF. Coherence will thus be in an intermediate range as it reflects intermediate tree cover as well. The image in Figure 5.6 (right) illustrates this scenario.
- 2) 50 % tree cover in the scale of VCF can mean that 50 % of the pixel area is covered with dense and 50 % with sparse or no forest. Coherence pixels located within the VCF pixel show either high coherence over open areas or low coherence over dense forest. Figure 5.6 (left) illustrates this a case.

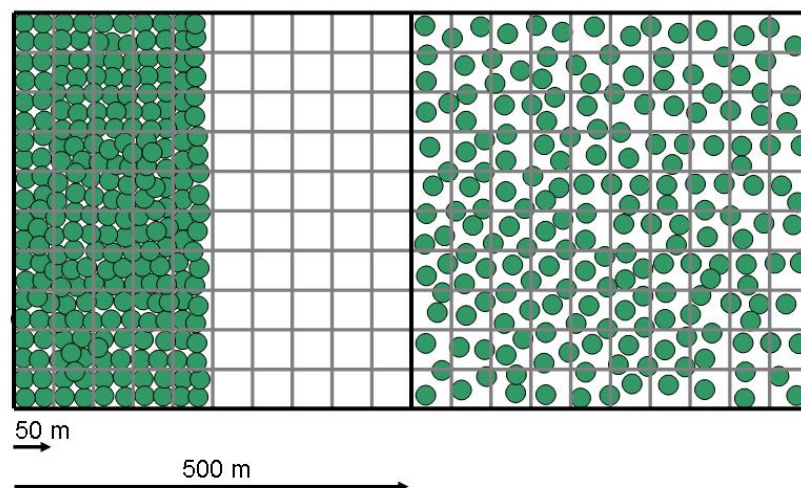


Figure 5.6. Schematic representation of two $500 \times 500 \text{ m}^2$ VCF pixels. The extent of the corresponding $50 \times 50 \text{ m}^2$ ERS pixels is shown with the grey lines. The green circles denote tree crowns. Both $500 \times 500 \text{ m}^2$ pixels represent intermediate tree cover. At the scale of the $50 \times 50 \text{ m}^2$ pixels this can mean 1) dense forest or open ground (left) or 2) intermediate tree cover as well (right).

The scale, i.e. pixel size, dependence of tree cover could clearly be identified when computing the mean and the mode values of coherence as function of VCF tree cover (Figure 5.7). Mode and mean of coherence were calculated for VCF tree cover ranges of 5 % width. Concerning the mode of coherence, the two scenarios revealed different relations between coherence and VCF tree cover whereas the average coherence showed a very similar behavior in both cases. In the scenario 1 case, the mode and the mean value of coherence decreased with increasing VCF tree cover (Figure 5.7, left). The standard deviation of coherence was the same for all VCF tree cover levels with about 0.08. A constant standard deviation of 0.08 indicates rather homogeneous forest cover at all VCF tree cover levels (cf. Askne et al., 2003).

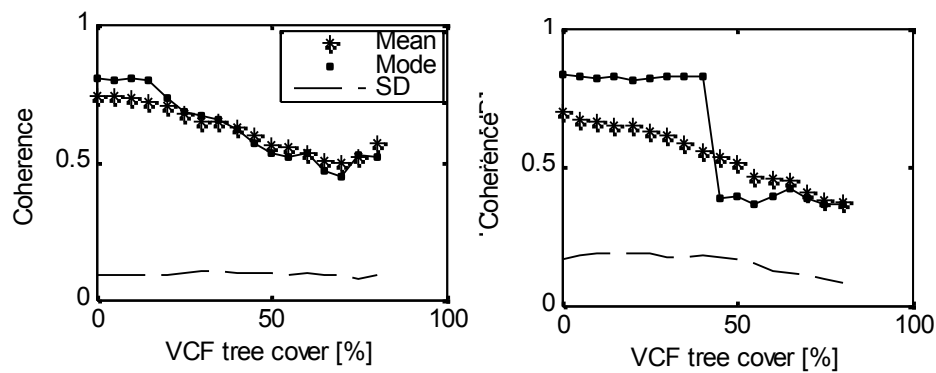


Figure 5.7. Mean, mode and standard deviation (SD) of coherence as function of VCF tree cover (5 % tree cover intervals) for scenario 1 (left) and 2 (right).

In the second scenario, only the average coherence decreased constantly whereas the mode did not show any response to increasing VCF tree cover up to about 45 % and then switched to a low coherence level, remaining constant up to the highest tree cover levels again. This was a consequence of the bimodal distribution of coherence for the intermediate VCF tree cover classes. In case of a tree cover up to ~45 %, the peak at higher coherence values was ‘higher’, which means that it comprised more pixels than the peak at low coherence values. For a tree cover of more than 45 %, the opposite case commenced, i.e. there were more dense forests with low coherence than unforested areas with high coherence in the area of the VCF pixels. Furthermore, the standard deviation of coherence at the intermediate tree cover levels was clearly higher in the scenario 2 case (maximum of 0.2), being as well a consequence of the bimodal distribution of coherence in scenario 2. For the highest tree cover levels, the standard deviation of coherence in the scenario 1 and scenario 2 images equaled, which most likely meant that a closed forest cover was reached in both scenarios. Thus, the pixel size dependent effects in tree cover were no longer relevant in case of the highest tree cover levels. The ERS-1 intensity images have been explored for comparable relations with VCF tree cover but the typical low intensity contrast between open areas and dense forests did not allow any equivalent conclusions.

5.2.3.2 Exploiting VCF for model training

The close relationship between coherence and VCF suggested that it should be possible to identify areas with no and dense forest cover in the coherence images with the aid of

VCF, respectively. A determination of the unknown IWCM parameters γ_{gr} , γ_{veg} , σ_{gr}^0 and σ_{veg}^0 with the aid of VCF should be possible when following preconditions are fulfilled:

1) It is possible to infer from the coherence and intensity in areas with low VCF tree cover on the forest floor coherence and intensity:

Forest floor beneath a canopy is characterized by a more or less variable soil surface roughness, soil moisture and litter/understorey cover. Strictly speaking, areas with low tree cover according to VCF are not forest floor. Low tree cover can mean many land cover types like barren ground, grassland, cropland, wetland or any type of artificial surface. The main question is thus if or when it is possible to infer from the coherence and intensity observed over these land cover types on the coherence and intensity that would be measured over forest floor (if there were no trees covering the forest floor).

2) It is possible to infer from the coherence and intensity measured over forest with high VCF tree cover on the parameters γ_{veg} and σ_{veg}^0 :

The IWCM parameters γ_{veg} and σ_{veg}^0 refer to the temporal coherence and intensity of ideally opaque forest canopies, i.e. forest with infinite stem volume. In contrast, the coherence and intensity measured over forest with high VCF tree cover reflect a finite stem volume range. In order to infer from the coherence and intensity that is measured over forest with high VCF tree cover on the IWCM parameters, the residual ground contributions and volume decorrelation effects (in case of coherence) have to be compensated for. For the compensation, it had to be clarified 1) which range of stem volume corresponds to a high tree cover in the VCF maps and 2) how much the ground and volume decorrelation contributions differ within this range of stem volumes.

In the next two sections, following questions are addressed first before discussing these fundamental issues (in the last section in this chapter and in chapter 7):

1. How to estimate the IWCM parameters from the coherence and intensity images with the aid of VCF?
2. How to determine the forest transmissivity parameter β , which cannot be estimated with the aid of VCF?

5.2.3.3 Parameter estimation with VCF

The VCF-based model training aims at estimating the unknown IWCM model parameters from the coherence and intensity measurements in areas where VCF indicates high and low tree cover, respectively. One of the open questions was which statistical measure of central tendency of the coherence and intensity measurements should be used for the estimation of the model parameters. The mean of the coherence and intensity pixels in areas with low or high VCF tree cover would have been the most plausible choice as the mean represents the statistically correct way to estimate coherence as well as σ^0 (in linear scale) over a number of pixels covering the same land cover type (Oliver & Quegan, 1998). However, the mean was observed to be rather sensitive to the timeliness of VCF. In the last section, it was shown that the coherence distributions in areas with low VCF tree cover were often strongly tailed towards lower coherence values or even showed a second peak at a low coherence, probably because of logging or forest fires in the years between the acquisition of the ERS and the

MODIS imagery. Hence, when estimating the ground coherence level with the mean of all pixels located in areas with low VCF tree cover, the estimate should be too low. In order to become less sensitive to these kinds of distortions, the mode (the peak in the histograms) of the distributions was considered for the IWCM parameter estimation. Basically, the mode would only represent a good estimator if the underlying pdf of the measurements over uniform terrain was normal. However, neither coherence nor intensity are normally distributed (Oliver & Quegan, 1998; Smith et al., 2001). Figure 5.8 illustrates this for intensity. The two distributions shown refer to Gamma distributed speckle according to Equation (2.16) for an ENL of 9, i.e. the ENL of the intensity data that was used for this study, and σ^θ values of -10.2 and -7.1 dB. The figure shows that the mode values were 0.5 dB lower than σ^θ .

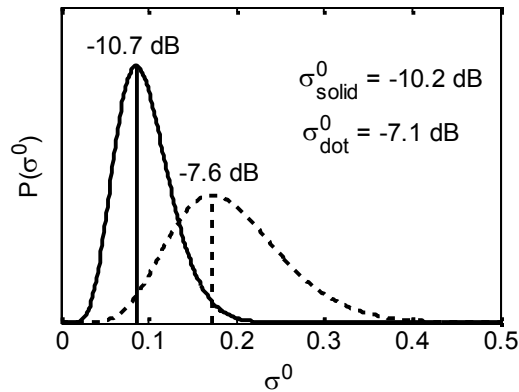


Figure 5.8. Gamma distributed speckle for an expected mean intensity of -10.2 and -7.1 dB. The vertical lines denote the peaks of the distributions.

In order to check for systematic differences, the mean and the mode values of the coherence and intensity measurements over dense forest areas with a stem volume of at least 300 m³/ha in the inventory data were computed for all images covering the Siberian test sites. The comparison of the mean and the mode values showed that the differences were negligible (<0.02 in coherence and < 0.3 dB in intensity). Thus, the mode of the coherence and intensity measurements should represent an adequate statistical measure to estimate the model parameters.

From now on, the peaks of the coherence and intensity distributions in areas with low VCF tree cover will be referred to as γ_{gr} and σ^θ_{gr} as they are assumed to have the same meaning as the IWCM parameters. The IWCM model parameters γ_{veg} and σ^θ_{veg} refer to ideally opaque forest canopies whereas the coherence and intensity measured over areas with high VCF tree cover reflect a finite stem volume range. That is why, the mode of the coherence and intensity measurements in areas with high tree cover will from now on be referred to as γ_{VCF} and σ^θ_{VCF} .

When estimating the mode of the coherence and intensity measurements in areas with low and high VCF tree cover, it was observed that a certain number of coherence and intensity measurements was needed for the estimation of γ_{gr} , σ^θ_{gr} , γ_{VCF} and σ^θ_{VCF} . When including too few measurements, the coherence and intensity histograms became very noisy, not allowing a reasonable determination of the mode. Figure 5.9 illustrates such a case. Non-noisy coherence and intensity histograms with a clear peak were generally achieved when at least one to two percent of the VCF pixels in the area of an ERS frame

were considered for the generation of the histograms. This means that, when defining an ERS frame as the basic unit for which model training is carried out, reliable estimates of the peaks of the coherence and intensity distributions should be possible when at least two percent of the area covered by an ERS-1/2 tandem pair have low and high tree cover in the VCF map, respectively. In other words, the 2nd percentile of VCF tree cover needs to be at a low and the 98th percentile at a high tree cover value to identify open and dense forest areas in the ERS imagery.

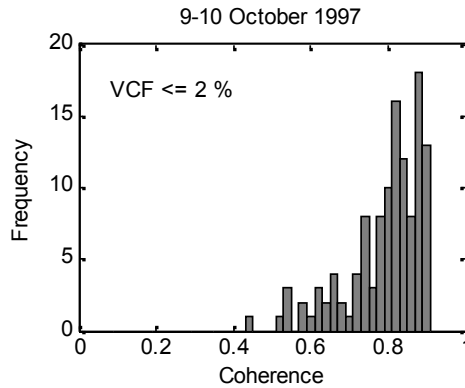


Figure 5.9. Histogram of coherence measurements in areas with low VCF tree cover when using too few pixels for the determination of γ_{gr} .

5.2.3.4 Forest transmissivity

The forest transmissivity parameter β could not be determined by means of VCF. In order to fully parameterize the IWCM, β was first determined by fitting the IWCM to the ERS-1/2 tandem coherence and intensity measurements at the Siberian test sites following the procedure described in section 5.2.1. The two-way signal attenuation was set to 1 dB/m for images acquired under frozen conditions and 2 dB for the rest. Tree height was expressed as function of stem volume with $h=(2.44*V)^{0.46}$, i.e. the expression valid for stands with high relative stocking (see Chapter 3.3). The goal was to evaluate if, with respect to the automated model training by means of VCF, it was possible to use either a fixed value for β or if β could be related to one of the other model parameters. According to the forest transmissivity concept in Askne et al. (1995), temporally stable gaps should mainly drive the forest transmissivity with only minor effects due to a variable two-way tree transmissivity, i.e. the use of a fixed value for β , at least for a given type of forest, may be reasonable. If there were significant temporal alterations in forest transmissivity because of variations in the signal attenuation in the canopy, it may be possible to relate the transmissivity coefficient β to σ_{veg}^0 as the two-way signal attenuation and volume backscatter from forest are closely related to the dielectric properties of the forest canopy, i.e. the moisture content and the aggregation state. Such a relationship between forest transmissivity and σ_{veg}^0 has, for instance, been presumed in the Water-Cloud-based model that was introduced in Pulliainen et al. (1994).

The estimation of β by means of regression was reported to be rather sensitive to the selection of stands used for model training (Askne & Santoro, 2005). That is why, in an additional step, the stands selected for model training were varied by randomly selecting 50 % of the stands in stem volume intervals of 50 m³/ha. The model training was repeated 50 times, each time with a new selection of stands. The 5th- and 95th-percentiles of the estimated values for β have been included in Table 5.1. For

comparison, also the corresponding parameter V_γ in the model in Equation (5.1) was estimated by fitting the model to the measurements at the test sites.

The estimates for β covered a wide span, exceeding in some cases by far the range of values with any physical meaning in the forest transmissivity sense (see Table 5.1); note that a realistic range for boreal forest should be somewhere in the range of 0.003 and 0.007 ha/m³ (Pulliainen et al., 1994; Kurvonen et al., 1999; Santoro et al., 2002, 2005, 2007). A rather narrow range of values for β between 0.0055 and 0.0073 ha/m³ was obtained for all images for which saturation of coherence did not occur up to at least 200 m³/ha stem volume, i.e. all winter images but also the image from 9-10 October 1997 acquired over Primorsky E. These values were in good agreement with those reported in Santoro et al. (2002, 2005, 2007), Pulliainen et al. (1994) and Kurvonen et al. (1999). The narrow range of β estimates for the repeated model training with quasi random stand selection showed that the sensitivity to the selection of stands was low. Except in one case, the estimates for V_γ were higher than β and varied in a larger range for the images acquired under stable conditions (0.0058-0.0111 ha/m³). This should have been a consequence of the disregard of volume decorrelation effects and the assumption of equal forest canopy and forest floor intensity in the empirical model.

Table 5.1. Inventory data-based estimates of the IWCM forest transmissivity coefficient β and the corresponding parameter in the model in Equation (5.1), V_γ . The 95 % confidence intervals (abbr. CI) are provided as well.

Date	Test site	IWCM		SIBERIA
		β and 95% confidence bounds	5 - 95% percentiles of β – random training sample selection	V_γ – CI 95% [ha/m ³]
29-30 Dec. 95	Chunsky N	0.0057 +/-0.0010	0.0036-0.0064	0.0086 +/-0.0020
14-15 Jan. 96	Chunsky N	0.0055 +/-0.0012	0.0046-0.0066	0.0082 +/-0.0017
14-15 Jan. 96	Chunsky E	0.0060 +/-0.0020	0.0053-0.0067	0.0058 +/-0.0019
1-2 Jan. 96	Bolshe NE	0.0073 +/-0.0013	0.0062-0.0079	0.0111 +/-0.0021
22-23 Sep. 97	Bolshe NE	0.0076 +/-0.0012	0.0054-0.0088	0.0149 +/-0.0025
25-26 Sep. 97	Bolshe NE	0.0221 +/-0.0078	0.0083-0.0240	0.0239 +/-0.0087
27-28 Oct. 97	Bolshe NE	0.0087 +/-0.0013	0.0078-0.010	0.0118 +/-0.0022
9-10 Oct. 97	Primorsky E	0.0067 +/-0.0016	0.0052-0.0078	0.0106 +/-0.0037
28-29 May 98	Bolshe NE	0.0029 +/-0.0010	0.0021-0.0032	0.0195 +/-0.0071
25-26 Sep. 97	Bolshe NW	0.0151 +/-0.0032	0.0024-0.0169	0.0140 +/-0.0032
28-29 May 98	Bolshe NW	0.0279 +/-0.0054	0.0211-0.0292	0.0396 +/-0.0065

In case of the images that were acquired under unstable imaging conditions, i.e. when saturation of coherence occurred at about 100 m³/ha, the regression resulted in a wide span of values for β . Also the repeated model training with quasi random training sample selection revealed in some cases very wide intervals between the 5th- and 95th-percentiles of the β estimates; note that the estimation of the other four IWCM parameters was hardly affected by the random training sample selection. This wide spread of the estimates for β in case of the images that were acquired under unstable imaging conditions, exceeding by far the range of values with a physical meaning, may have been a consequence of :

- the spread of the measurements because of strong standwise variations in the imaging conditions.
- the overall lower coherence level with an increased noise respectively uncertainty in the coherence estimation (see Equation (2.29)).

both interfering the forest transmissivity-stem volume relationship and the volume decorrelation effects. Even in those cases, when the estimates for β were in a range comparable to those obtained for the coherence images that were acquired under stable conditions, e.g. the estimates for the images acquired 22-23 September 1997 ($\beta = 0.0076$) and 28-29 May 1998 ($\beta = 0.0029$) over Bolshe NE, the results could not be considered physically meaningful. A β of 0.0029 ha/m^3 should only be realistic in case of frozen conditions, i.e. when the signal attenuation in the canopy drops to a very low level. Furthermore, the estimate for β for the same image at the test site Bolshe NW was 0.0279 ha/m^3 , which is far beyond any physical relevance in the forest transmissivity sense as this would mean that canopy closure was reached at extremely low stem volumes. Also the model fit for the acquisition from 22-23 September could not be considered realistic as the model predicted an oscillation of coherence at about $170 \text{ m}^3/\text{ha}$. This oscillation was not visible in the measurements (see Figure 4.1) and should not have occurred for stem volumes below $\sim 220 \text{ m}^3/\text{ha}$ (according to Equation (5.9) for a baseline of 260 m).

The predictability of β was low when correlating it to the other IWCM parameters, obtained when fitting the IWCM to the measurements at the test sites. When, for instance, relating β to σ_{veg}^0 , no statistical relationship could be found (Pearson correlation was 0.28), even when considering the parameter estimates for images acquired under frozen and unfrozen conditions separately. What could be observed was that β was fairly stable when γ_{veg} and γ_{gr} exceeded 0.25 and 0.7, respectively. A wide spread of the estimates for β arised for lower γ_{gr} and γ_{veg} values (Figure 5.10).

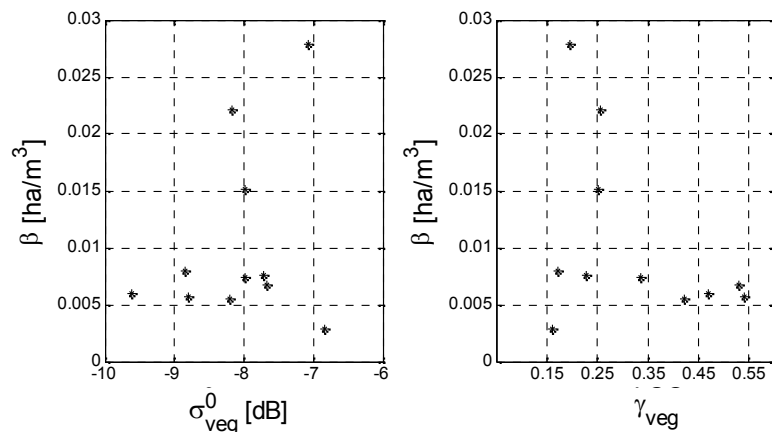


Figure 5.10. Forest transmissivity coefficient β as function of γ_{veg} and σ_{veg}^0 (determined by means of least-squares regression).

In the case of stable imaging conditions, the narrow range of β estimates indicated a rather similar relation between area-fill factor and stem volume at all test sites (presuming that the forest transmissivity is mainly a function of the gap fraction in the canopy). Still, when considering the observations in Chapter 3.3 concerning the forest structural parameter relative stocking, the canopy gap structure could be expected to

differ for stands with low and high relative stocking as they represented different densities at equal stem volume levels. Hence, it was investigated if differences in forest transmissivity between stands with low and high relative stocking could be found. First, the IWCM was fitted to the measurements at the test sites repeatedly applying different thresholds of minimum relative stocking to the standwise measurements, i.e. stands with a relative stocking below the threshold were not considered for model training. The analysis focused on the ERS-1/2 tandem pairs that were acquired under stable conditions for which the estimates for β in Table 5.1 were in good agreement with the physical meaning of the parameter. In Figure 5.11, the dependence of β on the threshold of minimum relative stocking has been illustrated for the ERS-1/2 tandem pair acquired 29-30 December 1995. It can be seen that β did not change when increasing the threshold of minimum relative stocking to 60 %; the four other model parameters did not show significant changes either. When further increasing the threshold to 70 %, the estimate changed considerably. This was clearly related to the changing stem volume distribution when setting the threshold for minimum relative stocking to more than 60 % (Figure 5.11, right). For the other ERS-1/2 tandem coherence images from winter, β hardly changed as well when increasing the threshold of minimum relative stocking. Minor changes were only observed for the coherence image from 1-2 January 1996 over Bolshe NE. In this case, β constantly decreased from 0.0073 to 0.005 ha/m³ when increasing the threshold of minimum relative stocking up to 70 %. In summary, it can be stated that the model fit, obtained when training the model with the measurements at all stands, represented also a reasonable description of the trend of coherence as function of stem volume for stands with high relative stocking.

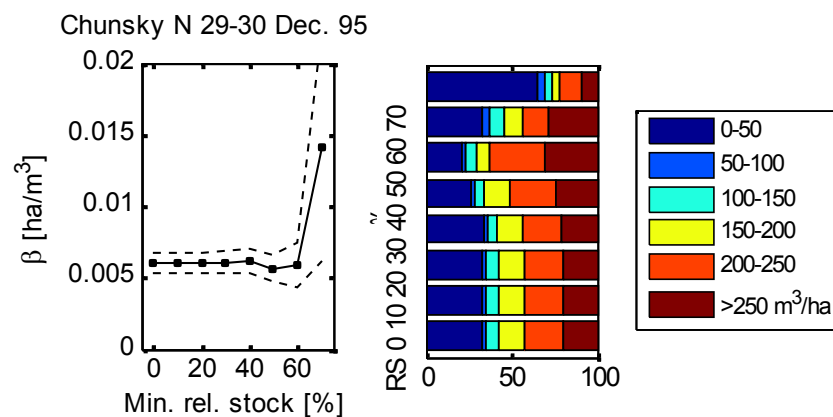


Figure 5.11. Left - Estimated forest transmissivity coefficient β for increasing thresholds of minimum relative stocking including the 95 % confidence bounds (dashed lines). Right - proportion of stem volume classes (50 m³/ha wide intervals) in percent for increasing thresholds of minimum relative stockings.

When only considering stands with low relative stocking ≤ 40 %, the model training was prone to high uncertainty as the stem volume range was reduced to a maximum volume of ~ 200 m³/ha and the spread of coherence measurements along the main trend was large. When fitting the IWCM to the measurements at stands with low relative stocking, the obtained parameters were in some cases even unphysical, e.g. negative γ_{veg} . Hence, the model training was carried out in a different way. Assuming that the IWCM parameters γ_{gr} , γ_{veg} , σ_{gr}^0 and σ_{veg}^0 did not differ for stands with high or low

relative stocking, the IWCM was calculated using the parameters obtained when training the model with the measurements at all stands (as listed in Table 7.1 in Chapter 7). For the allometric relation between stem volume and tree height now the expression valid for forests with low relative stocking was used, i.e. $h=(1.272*V)^{0.601}$. Different values for β between 0.001 and 0.008 ha/m³ were tested. As can be seen in Figure 5.12, the IWCM still allowed a reasonable description of the coherence trend as function of stem volume when comparing the modeled relationship with the measurements at stands with a maximum relative stocking of 40 %.

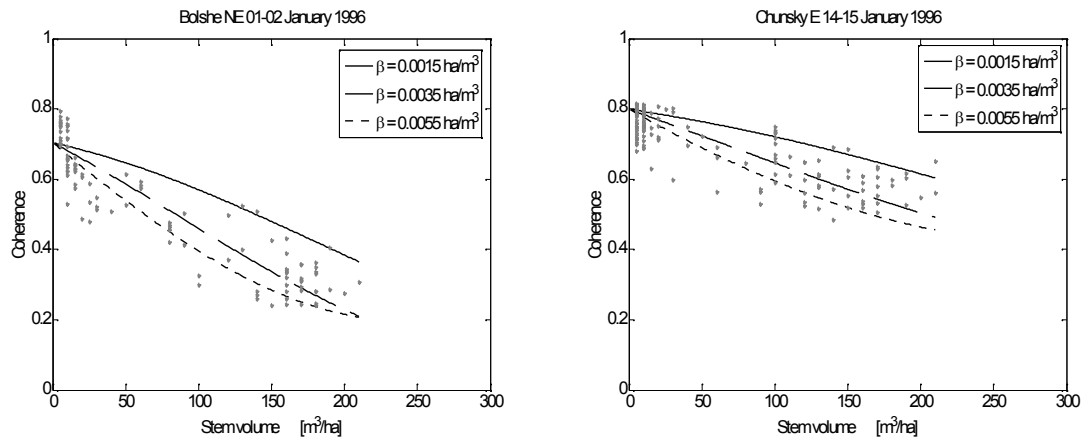


Figure 5.12. Coherence measurements and modeled coherence as function of stem volume for stands with low relative stocking $\leq 40\%$.

The rms residuals between the model fit and the measurements at stands with low relative stocking $\leq 40\%$ were minimized for β values between 0.003 and 0.0035 ha/m³ for all images that were acquired under stable conditions whereas for a β of 0.0055 ha/m³, i.e. a ‘typical’ value for high relative stocking stands, the model rather followed the lower margin of the coherence trend as function of stem volume (Figure 5.12). When relating the stem volume to the area-fill factor according to Equation (5.5), it could be seen that for a β of 0.0035 ha/m³ and the allometric height-stem volume relation valid for stands with low relative stocking, the area-fill factor at a given stem volume was clearly lower than for a β of 0.005 or 0.007 ha/m³ and the allometric stem volume-height relation valid for stands with high relative stocking (Figure 5.13). This indicated that stands with low relative stocking were characterized by a more open canopy structure at a given stem volume. When considering that the density at a given stem volume should be lower for stands with low relative stocking (see Chapter 3.3), this interpretation seemed reasonable. However, for a confirmation of this assumption, further investigations accompanied by ground measurements would be required.

The differences in the relationship between forest transmissivity and stem volume for stands with different fractions of conifers respectively broadleaved species were analyzed as well. Contrary to the observations made for stands with different relative stocking, no consistent differences were observed. The trend of coherence with increasing stem volume was generally very similar for stands with low and high stem volume fractions of conifers, respectively.

The observations indicated that an ‘optimal’ training of the IWCM would also have to account for forest structural differences. As it was not possible to distinguish forests

with different relative stocking in the coherence images, a training adaptive to forest structural differences was not feasible. It was decided to use a fixed value for β of 0.006 ha/m^3 and the allometric stem volume-height relation valid for stands with high relative stocking for the VCF-based training of the IWCM in case of images that were acquired under stable conditions. In this way, the overall trend of coherence as function of stem volume, regardless of relative stocking, appeared to be represented best.

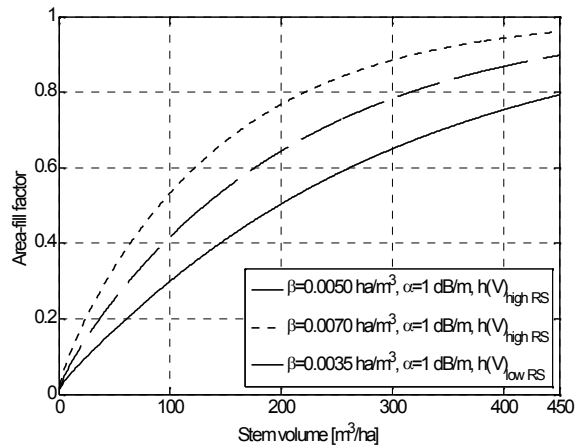


Figure 5.13. Area-fill factor as function stem volume for a) β of 0.005 and 0.007 ha/m^3 and the allometric relation between stem volume and height for stands with high relative stocking and b) β of 0.0035 ha/m^3 and the allometric relation valid for stands with low relative stocking (see Chapter 3.3).

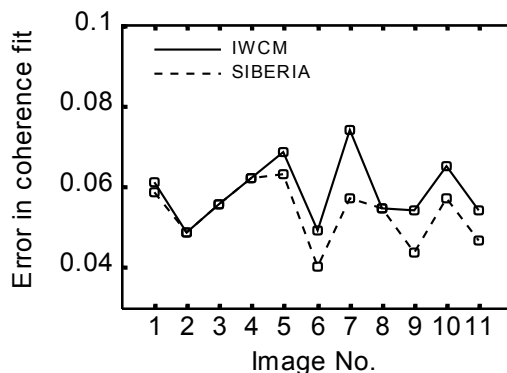


Figure 5.14. Error in the IWCM and the SIBERIA model fit to the coherence measurements at the test sites. The image numbers correspond to the order in Table 5.1.

Considering the inconsistent and unpredictable estimates for β in case of unstable imaging conditions with an overall lower coherence level, the advantage of using the IWCM instead of the simple empirical model was put into question. When computing the rms error of the model fit to the measurements for both, the empirical model and the IWCM, an even better model fit of the empirical model had to be stated for the images that were acquired under unstable imaging conditions (Figure 5.14). As there appeared to be no advantage in using the IWCM, it was analyzed if the VCF-based training of the empirical model, using a fixed value for V_{γ} , allowed a reasonable description of the trend of coherence as function of stem volume when the imaging conditions were not

stable. In order to find the best compromise, the empirical model in Equation (5.1) was fitted repeatedly to the measurements at the test sites using different values for V_γ , i.e. only γ_0 and γ_∞ were regressed. Each time the rms residuals of the model fit were calculated. Then the optimal value for V_γ was determined by selecting the one for which the sum of rms residuals at all test sites and for all acquisitions was minimized. This optimal value for V_γ was 0.015 ha/m³ (the optimal value for β would have been 0.012 ha/m³). Next, the percental difference in rms error of the two (fixed V_γ of 0.015 ha/m³) and the ‘optimal’ three parameter model fit was compared for all coherence images. The average difference was only 3.3 % and the maximum difference was 8.6 % (in case of the coherence image from 28-29 May 1998 at Bolshe NW). This suggested that a reasonable description of the trend of coherence as function of stem volume should be possible when using a fixed value for V_γ .

5.2.3.5 Derivation of γ_{veg} , γ_∞ and σ_{veg}^0

The IWCM model parameters γ_{veg} and σ_{veg}^0 refer to the temporal coherence and backscatter of ideally opaque canopies whereas γ_{VCF} and σ_{VCF}^0 reflect a finite stem volume range. Thus, γ_{VCF} and σ_{VCF}^0 have to be compensated for residual ground contributions and volume decorrelation effects to derive γ_{veg} and σ_{veg}^0 . σ_{veg}^0 can be derived from σ_{VCF}^0 when interpreting σ_{VCF}^0 as intensity that was measured over forest with a yet unknown equivalent stem volume, V_{eq} , with:

$$\sigma_{veg}^0 = \frac{\sigma_{VCF}^0 - \sigma_{gr}^0 e^{-\beta V_{eq}}}{1 - e^{-\beta V_{eq}}} \quad (5.14)$$

Because of the complex volume decorrelation term in the IWCM, an iterative procedure had to be used for the estimation of γ_{veg} , so that:

$$|\gamma(V_{eq}, \gamma_{veg})| - \gamma_{VCF} = 0 \quad (5.15)$$

$|\gamma(V_{eq}, \gamma_{veg})|$ denotes the modeled coherence at V_{eq} as function of γ_{veg} . In order to derive γ_{veg} , the IWCM was calculated using the VCF-based estimates for the model parameters γ_{gr} , σ_{gr}^0 and σ_{veg}^0 and different values for γ_{veg} , starting with $\gamma_{veg} = \gamma_{VCF}$. The value for γ_{veg} was selected for which the modeled coherence at V_{eq} and γ_{VCF} matched. When using the empirical model in Equation (5.1) instead of the IWCM, γ_∞ could be derived from γ_{VCF} with:

$$\gamma_\infty = \frac{\gamma_{VCF} - \gamma_0 e^{-V_\gamma V_{eq}}}{1 - e^{-V_\gamma V_{eq}}} \quad (5.16)$$

Thus, it had to be investigated which stem volume range corresponds to forest with high tree cover according to VCF. A comparison of the VCF tree cover map with the stem volume information in the inventory data was carried out but did not provide useful information when computing the average tree cover per polygon; basically because of the coarse pixel size of the MODIS product compared to the size of the polygons in the inventory data. That is why, the VCF map was compared to the rasterized stem volume maps from the inventory data as illustrated in Figure 5.15 (left). All pixels in the inventory stem volume maps with 50 m pixel size were averaged in the area of the corresponding VCF pixel with 500 m pixel size.

Figure 5.15 (right) shows the relationship between stem volume and VCF tree cover at the Chunksky test sites. In case of the test sites at Bolshe and Primorsky, only few VCF pixels indicated low tree cover, which is why the overall trend was less clear. Figure 5.15 (right) shows a relationship that closely resembles the relationship between the area-fill factor and stem volume used for the modeling of coherence as function of stem volume. The curves in Figure 5.15 (right) show the modeled relationship between stem volume and area-fill factor (in percent) according to Equation (5.5) for two different values of β . VCF tree cover and area-fill factor obviously denote a similar type of information. Figure 5.15 (right) also shows that forests with a VCF tree cover close to the maximum of $\sim 80\%$ should mostly have a stem volume above $200\text{ m}^3/\text{ha}$.

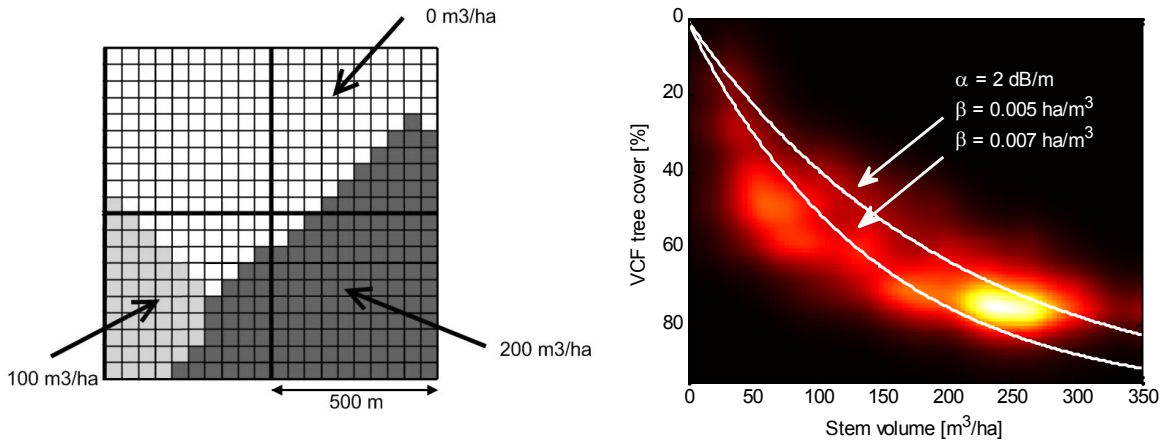


Figure 5.15. Left – Scheme for the averaging of 50 m pixels (thin lines) in the rasterized inventory data stem volume maps in the area of a VCF pixel with 500 m pixel size (thick lines). Right – Scatterplot of VCF tree cover versus stem volume at Chunksky N & E. The curves show the modeled relationship between stem volume and area-fill factor according to Equation (5.5).

A model sensitivity analysis was carried out to assess the expected relationship between $\gamma_{VCF} / \sigma_{VCF}^0$ and the model parameters and to evaluate the sensitivity of the estimation of γ_{veg} , γ_{∞} and σ_{veg}^0 on V_{eq} . For this, the VCF-based training of the models was tested for the images in the Siberian ERS-1/2 tandem dataset. The 2nd and 98th percentiles of VCF tree cover in the corresponding subsets of the VCF map for all these tandem pairs were at very low ($< 5\%$) and very high ($> 78\%$) tree cover levels, respectively. Thus, the VCF-based estimation of γ_{gr} and σ_{gr}^0 could be done by estimating the mode of the coherence and intensity measurements in areas with VCF tree cover $< 5\%$ and γ_{VCF} and σ_{VCF}^0 could be estimated with the mode of the coherence and intensity measurements in areas with a tree cover $> 78\%$, i.e. a tree cover very close to the maximum tree cover in VCF.

In case of the coherence images that were acquired under unstable conditions, i.e. when the empirical model in Equation (5.1) was used with V_{γ} set to 0.015 ha/m^3 , as well as the intensity images, for which the model in Equation (5.3) was trained using a β of 0.006 ha/m^3 , the decision for an equivalent stem volume was uncritical as the differences in the estimates for γ_{∞} and σ_{veg}^0 were generally very low. This low sensitivity was related to the fact that the models predicted a mostly saturated coherence and intensity for the range of stem volumes between 200 and $500\text{ m}^3/\text{ha}$.

In case of the ERS-1/2 tandem coherence images acquired under stable conditions, i.e. when the IWCM was used for modeling, the dependence of γ_{veg} on V_{eq} could be expected to be related to the length of the baseline. Since in the Siberian ERS-1/2 tandem dataset there was no tandem pair that was acquired under stable conditions with a baseline longer than 200 m, the sensitivity analysis was extended to three tandem pairs in the Northeast Chinese tandem dataset that were acquired under stable frozen conditions with baselines of ~ 300 m. For all three tandem pairs the VCF-based determination of the IWCM parameters could be considered successful insofar as the 2nd percentile of VCF tree cover was at a very low tree cover (<3 %) and the 98th percentile was close to 80 %. As all three coherence images revealed a very similar behavior, only one of them will be discussed in the following.

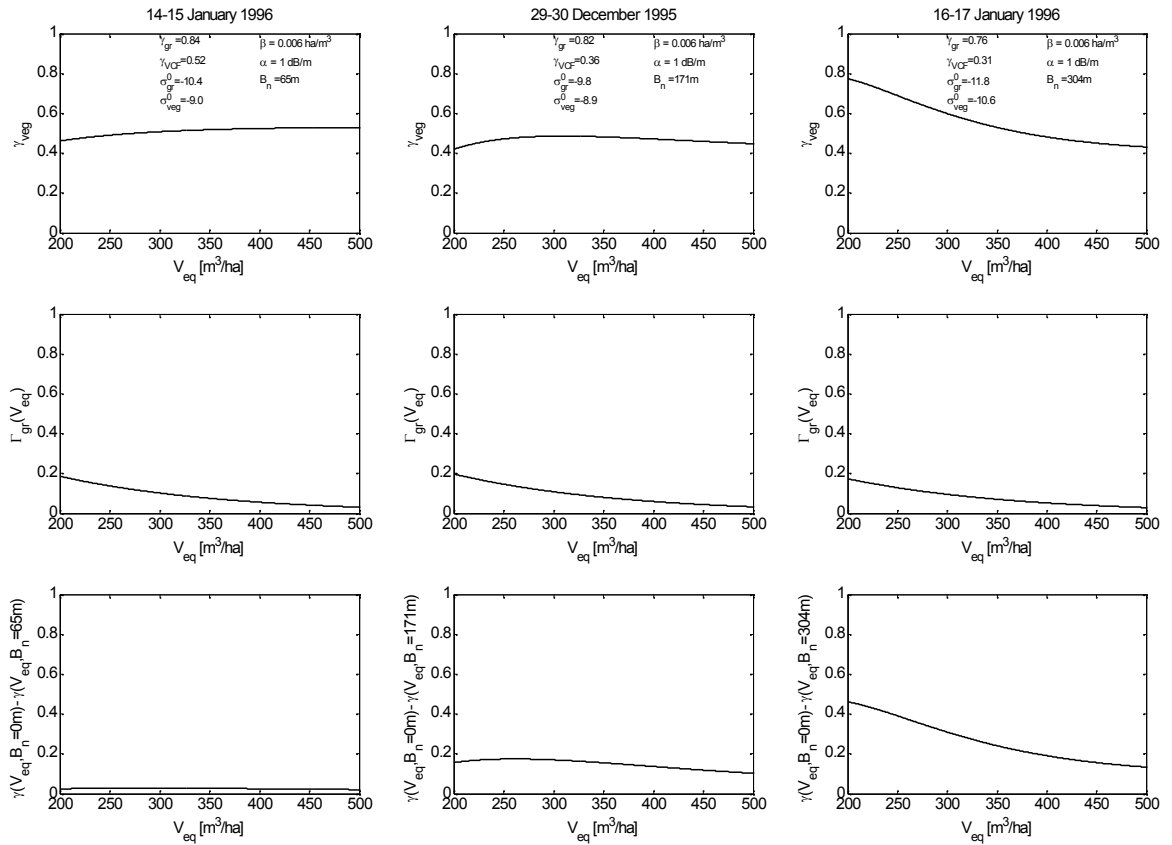


Figure 5.16. Upper row - Derivation of the IWCM parameter γ_{veg} from γ_{VCF} as function of the stem volume V_{eq} assumed to represent the forest with high tree cover in VCF. Middle row - Ground coherence contribution Γ_{gr} at the equivalent stem volume V_{eq} . Bottom row - Influence of volume decorrelation at the stem volume V_{eq} obtained by calculating the difference between the modeled forest coherence at V_{eq} when setting the baseline to 0 m and when using the real baseline, respectively.

Figure 5.16 (upper row) shows the dependence of the estimates for γ_{veg} on V_{eq} for three coherence images that were acquired under stable frozen winter conditions with baselines of 65, 171 and 304 m. The short baseline images both covered the Chunksky forest territory where stem volumes reach 400 to 450 m^3/ha . The long baseline image from 16-17 January 1996 covered the Changbai Mountain area where stem volumes reach 500 m^3/ha . The middle row in Figure 5.16 shows the ground coherence

contributions at the equivalent stem volume, $\Gamma_{gr}(V_{eq})$ (calculated with the first term in the IWCM in Equation (5.7)). The bottom row shows the expected effect of volume decorrelation, estimated by subtracting the modeled coherence at V_{eq} from the modeled coherence when setting the baseline artificially to 0 m.

The estimation of γ_{veg} hardly depended on V_{eq} in case of the images from 14-15 January 1996 and 29-30 December 1996 when V_{eq} exceeded $\sim 250 \text{ m}^3/\text{ha}$. This was due to the fact that the model predicted only minor ground coherence contributions (Figure 5.16, middle row) as well as minor differences in volume decorrelation for this range of stem volumes (Figure 5.16, bottom row). In case of the image from 16-17 January 1996, the γ_{veg} estimation showed a higher sensitivity to V_{eq} . This was a consequence of the stronger predicted volume decorrelation and InSAR geometry effects due to the long baseline of 304 m (Figure 5.16, lower right). When considering the values for γ_{veg} that have been reported in previous studies (Santoro et al., 2002; Askne & Santoro, 2005), it can be stated that a γ_{veg} much higher than 0.6, which would have been obtained in this example when setting V_{eq} to a value below $300 \text{ m}^3/\text{ha}$, was rather unlikely. In case of the other two coherence images that were acquired with long baselines in the range of 300 m, the estimates for γ_{veg} were even slightly higher.

For baselines up to 200 m, γ_{VCF} should, according to the model simulations, approximate what can be considered the saturation level of coherence which is why it is not important to identify exactly if γ_{VCF} reflects the coherence that would be measured over a forest with a stem volume of, for instance, 300 or $400 \text{ m}^3/\text{ha}$. On the other side, when volume decorrelation introduces considerable responses in coherence to increasing stem volume in the range of stem volumes corresponding to high VCF tree cover, γ_{VCF} may strongly depend on the stem volume distribution in areas with maximum tree cover as the coherence in this range of stem volumes would not be constant. This would mean that for a definition of V_{eq} , the stem volume distribution in areas with maximum VCF tree cover needs to be known. No tandem pair was available that was acquired under stable conditions and with a long baseline over one of the test sites so that the VCF-based parameter estimates could not be checked for long baseline tandem pairs. At this point, it can only be stated that, in order to achieve realistic estimates for γ_{veg} in case of the long baseline coherence images acquired over the Changbai Mountain area, an equivalent stem volume closer to the maximum stem volume occurring in Northeast China would be required.

5.3 Summary

In this chapter, two existing models, a simple empirical model and the semiempirical IWCM, have been introduced as basis for the modeling of ERS-1/2 tandem coherence as function of stem volume. Next, two automated model training procedures have been described, both aiming at capturing the variability of coherence as function of the imaging conditions on a frame-by-frame basis.

The first model training approach, which was developed for the classification of Siberian boreal forest stem volume by means of ERS-1/2 tandem coherence data from fall (Schmullius et al., 2000; Wagner et al., 2003), relies solely on the histogram statistics and comprises a number of assumptions for which the validity in case of a multi-seasonal and multi-baseline ERS-1/2 tandem dataset has to be checked.

A new model training procedure has been introduced based on the MODIS Vegetation Continuous Field tree cover product. The analysis of the relationship between ERS-1/2 tandem coherence and VCF tree cover showed that the coherence in areas with the lowest and the highest VCF tree cover represented the margins of the total coherence range, reflecting the coherence of unforested open areas and dense forest, respectively. The underlying assumptions of the VCF-based model training are that 1) it is possible to infer from the coherence and intensity measurements in areas with low VCF tree cover on the IWCM model parameters γ_{gr} and σ_{gr}^0 that describe the coherence and intensity of the forest floor, and 2) it is possible to infer from the coherence and intensity measured over forest with maximum VCF tree cover on the IWCM parameters γ_{veg} and σ_{veg}^0 , which refer to ideally opaque canopies.

Concerning the latter issue, the comparison of the VCF tree cover map with the stem volume measurements in the Russian inventory data indicated that the majority of forests with a tree cover close to the maximum of about 80 % in the VCF maps should have a stem volume of 200 m³/ha and higher. A model sensitivity analysis with the IWCM showed that in case of baselines < 200 m, the coherence in areas with maximum VCF tree cover should be close to what can be considered the saturation level of coherence as the predicted differences in the ground contributions in the coherence measurements as well as the differences in volume decorrelation for stem volumes above 200 m³/ha were low. In this case, it should be possible to infer from the coherence in areas with maximum tree cover on the IWCM parameter γ_{veg} without prior knowledge about the stem volume distribution in the area that is to be mapped. In case of longer baselines, this may no longer be the case. The estimation of σ_{veg}^0 was generally uncritical as the model predicted a mostly saturated signal for stem volumes above 200 m³/ha.

The forest transmissivity coefficient β in the IWCM could not be determined with the aid of VCF. When determining the parameter by fitting the IWCM to the measurements at the test sites, the results indicated only minor differences in forest transmissivity as function of stem volume between the test sites as long as the imaging conditions were stable. In this case, the use of a fixed β value for a VCF-based training of the IWCM could be considered reasonable. Although differences in forest transmissivity between stands with different relative stocking were found, the forest transmissivity coefficient β , as determined when orienting the model training at the high relative stocking stands (i.e. when using the allometric relation between tree height and stem volume valid for stands with high relative stocking) allowed a reasonable characterization of the overall trend of coherence as function of stem volume for stands in all relative stocking ranges. In case of unstable imaging conditions, when coherence saturated at a stem volume of ~100 m³/ha, the obtained estimates for the transmissivity coefficient β were physically meaningless. It was found that the simple empirical model could be fitted to the coherence measurements at the test sites even better which is why, with respect to the VCF-based training, the use of the empirical model with a fixed value for the corresponding parameter V_γ , appeared to be preferable in case of unstable imaging conditions. For the discrimination of stable conditions, when the use of the IWCM was justified, and unstable conditions, the IWCM parameters related to temporal ground and canopy coherence, γ_{gr} and γ_{veg} , were found to be a good indicator as for $\gamma_{gr} > 0.7$ and $\gamma_{veg} > 0.25$, the obtained estimates for β were reasonable.

Chapter 6 - Topographic effects in SAR and InSAR imagery

In this chapter, topographic effects in the ERS intensity and coherence imagery are addressed. For the identification of topographic effects, the SRTM-3 DEM with 90 m pixel size is used as topographic reference.

6.1 Topographic effects in ERS intensity

The standard procedure for the derivation of σ^0 presumes flat terrain (Laur et al., 2004). However, the intensity measured over sloped terrain is affected by the varying pixel area contributing to the backscatter measured. In case of ERS, topography was observed to alter the measured intensities for up to +/- 5 dB (Beaudoin et al, 1995). The effect of topography can be compensated for when having a DEM. An approach that aims at a correction of this effect has been presented in Ulander (1996). Here the cosine of the projection angle was found suited to describe the changes in ground scattering area over sloped terrain. Other approaches were described in Curlander & McDonough (1991) or Van Zyl et al. (1993) but these approaches only represented approximations for the projection angle-based approach (Ulander, 1996). The projection angle ψ is defined as the angle between the local surface normal and the image plane normal. An illustration of the imaging geometry over sloped terrain, including ψ , is given in Figure 6.1.

The compensation for varying ground scattering area could be done with a pixel area normalization map, C_A , derived from the SRTM-3 DEM (Wegmüller, 1999). C_A was calculated with the ratio: $\cos(\psi)/\sin(\theta)$; note that the sine of the incidence angle accounts for the fact that the compensation for the variation of the pixel area over flat terrain from near to far range was already done during calibration. According to Loew & Mauser (2006), a good normalization performance can be expected when using the SRTM-3 DEM with 90 m pixel size for pixel area normalization. Loew & Mauser observed only minor changes in the estimated pixel area (they also used ψ to estimate the pixel area) when using either the SRTM-1 DEM with 30 m pixel size, i.e. a pixel size of the order of the SAR image resolution, or a degraded version of the same DEM, resampled to 100 m pixel size, for the topographic normalization of ENVISAT ASAR C-band intensity ($\theta = 23^\circ$).

The layover/shadow masks, produced with the GAMMA software from the SRTM-3 DEM, were found to underestimate the area affected by layover (shadow is hardly observed in ERS intensity images due to the steep incidence angle) as the masked areas were surrounded by bright pixels in the intensity images. This effect has as well been reported in Loew & Mauser (2006). In Loew & Mauser, the produced layover masks were found to increasingly underestimate the area affected by layover and shadow, the lower the resolution of the DEM. To improve the layover masks, it was decided to widen the areas that were indicated as layover for three pixels in all directions. In this way, the pixels with high backscatter surrounding the identified layover areas could be excluded.

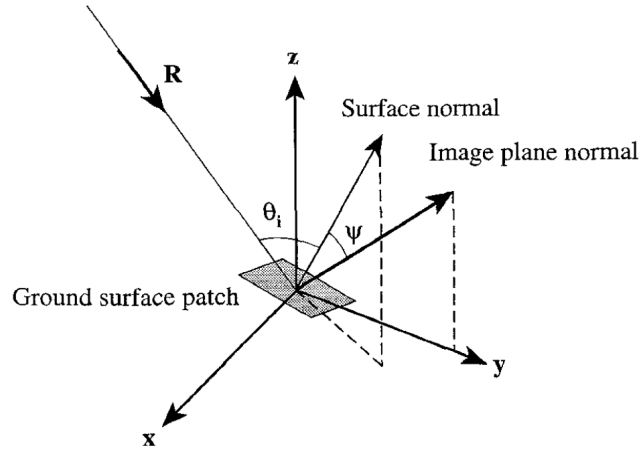


Figure 6.1. Radar imaging geometry over sloped terrain with R denoting the radar look vector, x the azimuth and y the range direction, θ_i the local incidence angle and ψ the projection angle (Courtesy of Ulander, 1996).

Topography is known to alter the backscatter dependent on the scattering mechanisms respectively land cover type. A dependence of backscatter on the local incidence angle, θ_i , can be observed for most land cover types (Ulaby et al., 1986). The local incidence angle is defined as the angle between the propagation direction vector and the local surface normal. The variation of surface and volume scattering with local incidence angle can be compensated for with a simple cosine correction of the form (Teillet et al., 1985; Ulaby et al., 1986; Holecz, 1993; Castel et al., 2001a; Leclerc et al., 2001; Sun et al., 2002):

$$\sigma^0_{cor} = \sigma^0(\theta_i) C_A \left(\frac{\cos(\theta)}{\cos(\theta_i)} \right)^n \quad (6.1)$$

The compensation for the pixel area variation with C_A has been included in Equation (6.1). The exponent n can take values between 0 and 2, approaching 2 for Lambertian scattering. For most land surface types, lower values for n have to be used to describe the dependence of backscatter on local incidence angle adequately (Ulaby et al., 1986; Abdel-Messeh & Quegan, 2000). In case of volume scattering, the exponent n in Equation (6.1) can be adjusted for each forest stand when having information about canopy height and signal attenuation. Castel et al. (2001a) developed a normalization procedure, based on the Water-Cloud-Model, that accounted for the variation of the path length, h_i , the signal has to cover within the canopy dependent on local slope and local incidence angle:

$$h_i = h \cdot \cos(\alpha_s) \cdot \sec(\theta_i) \quad (6.2)$$

The signal attenuation, κ_e , and the volumetric backscattering coefficient, σ_v , (cf. Equation (2.20)) were assumed to be independent of the incidence angle. The value for n depended on the optical depth of the canopy, defined as the product of signal attenuation and crown depth, and could take values between 0 and 1, approaching 1 for opaque canopies. At a given canopy height, a lower signal attenuation in the canopy, e.g. in case of frozen winter conditions, would require the use of a lower value for n . The n values were estimated for Austrian Pine stands in southeastern France. In case of ERS intensity data, high values for n close to 1 (on average 0.93) with only little

dispersion between young and old stands were obtained, indicating that a good topographic normalization should be possible when using a fixed value for n regardless of stand age (or height, stem volume, biomass, etc.).

When applying the normalization in Equation (6.1) with an exponent n of 1 to the ERS intensity images available for this study (after masking areas affected by layover), a good performance of the normalization procedure could be observed. Figure 6.2 shows for one example that, when averaging all intensity measurements that corresponded to a certain local incidence angle, the dependence of intensity on topography was mostly compensated for in case of open surfaces (VCF < 10 %) as well as forested terrain (VCF > 60 %). Concerning open areas, it was expected that different values for n would be required for an adequate normalization as the decrease of surface backscatter with increasing incidence angle is a function of the surface roughness (Ulaby et al., 1986). When, however, considering the average intensity over a wide range of non-forest land cover and surface roughness types (i.e. all areas with VCF < 10 %), the use of a fixed n of 1 apparently resulted in a good normalization of topographic effects (Figure 6.2, right). For dense forest areas, it was also tested if the use of an $n < 1$ for images that were acquired under frozen conditions, i.e. when the penetration depth increased, improved the topographic normalization. No improvements were noticed though.

The good performance of the topographic normalization was further confirmed when applying the topographic normalization to all intensity images in the Chinese ERS-1 dataset for which all VCF tree cover levels up to 80 % were represented in the area covered. The coefficient of variation CV, which is the ratio of the standard deviation of intensity to the mean, was calculated for each intensity image in areas with low (< 10 %) and high (> 60 %) VCF tree cover before and after topographic normalization. A lower CV indicates low texture, which is why it should also show if the topographic normalization reduces the variability of intensity due to topographic effects to a level comparable to that over flat terrain. Figure 6.3 shows for both, open areas and dense forest, that after topographic normalization, the CVs of the intensity measurements in steep areas were in a similar range as those over flat terrain; note that in case of the open areas, the flat areas show a relatively wide range of CVs as in these areas considerable texture arised from croplands or settlements.

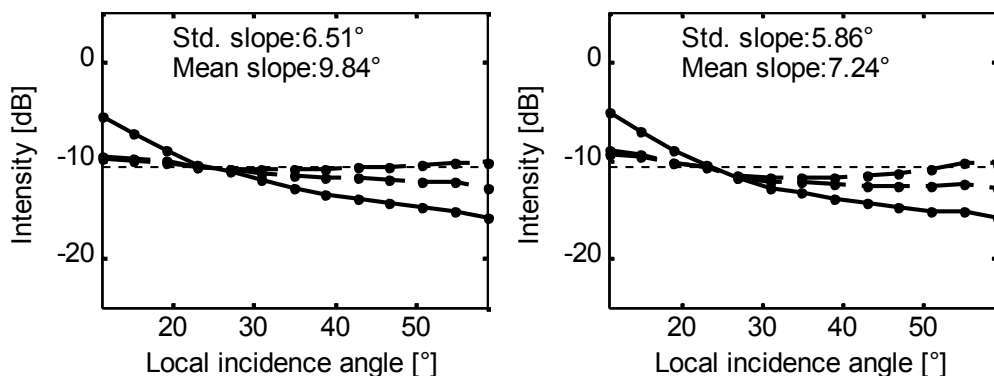


Figure 6.2. Dependence of ERS backscatter on local incidence angle 1) before topographic normalization (solid line) 2) after compensating for varying pixel area (dash-dotted line) and 3) after compensating for varying pixel area and scattering (dashed line) in areas with VCF > 60 % (left) and VCF < 10 % (right). The intensity image was acquired 22 January 1996 over the Changbai Mountains.

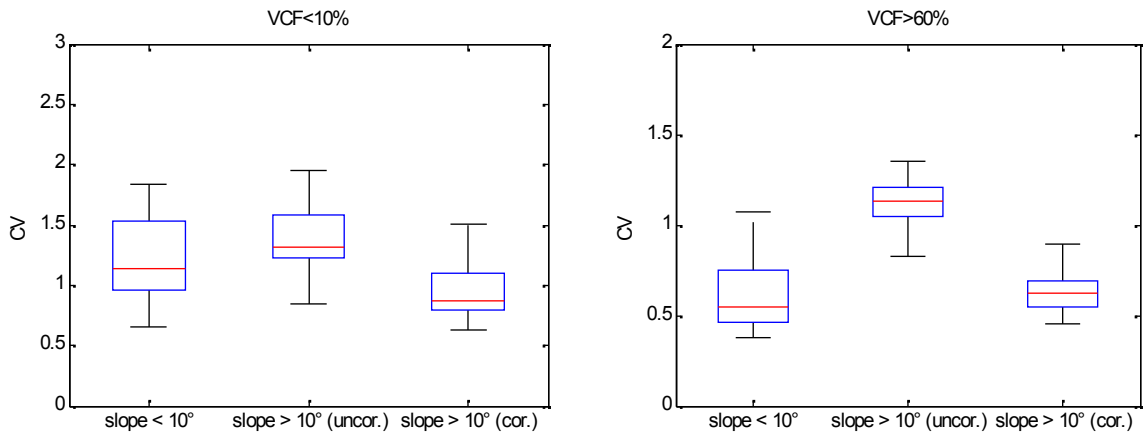


Figure 6.3. The boxplots show the quartiles of the CVs in areas with low (left plot) and high (right plot) VCF tree cover for 87 ERS-1 intensity images of Northeast China. The CVs refer to flat areas with slope $< 10^\circ$ (left), slopes $> 10^\circ$ when not normalizing (middle) and when normalizing (right) the intensity images according to Equation (6.1).

6.2 Topographic effects in ERS-1/2 tandem coherence

The reduced coherence over mountainous terrain is a consequence of spatial decorrelation. According to Askne et al. (1997), spatial decorrelation can be split into two components (under the assumption that the stable part of volume backscatter is solely a function of the height above the surface plane), the slant-range (or surface) decorrelation in case of surface scattering and volume decorrelation when the scatterers are distributed in height (see Chapter 2.2.2).

To illustrate the effect of surface decorrelation, some rather simplified but, for illustrational purposes, appropriate simulations have been carried out. Coherence is known to decrease with increasing fractions of non-common bandwidth, Δf , reaching total coherence loss when Δf equals the bandwidth W . Even though not entirely correct, a linear decrease of coherence with increasing fraction of non-common bandwidth can be presumed for the modeling of surface decorrelation (Bamler & Hartl, 1998; Lee & Liu, 2001). For a thorough description of surface decorrelation, the reader is referred to Hagberg et al. (1995). Range common-band filtering aims at removing the non-common fractions of the range spectra. Without information about the local topography, the filter has to assume a relative frequency shift corresponding to flat terrain, here denoted with Δf_0 (calculated from Equation (2.34) with $\alpha_s=0^\circ$), so that the fractions of non-common bandwidth $|\Delta f_0 - \Delta f|$ are not removed and the bandwidth is reduced to $W - \Delta f_0$ (Ferretti et al., 2007).

Figure 6.4 shows the fraction of non-common bandwidth for baselines of 100, 200 and 400 m before and after range common-band filtering. It can be seen that the filter completely recovers the coherence over flat areas as the fraction of non-common bandwidth is reduced to zero. It also increases the coherence for slopes facing the radar but decreases it for steep slopes tilted away from the sensor (negative slopes). With increasing length of the baseline, coherence decreases at each slope.

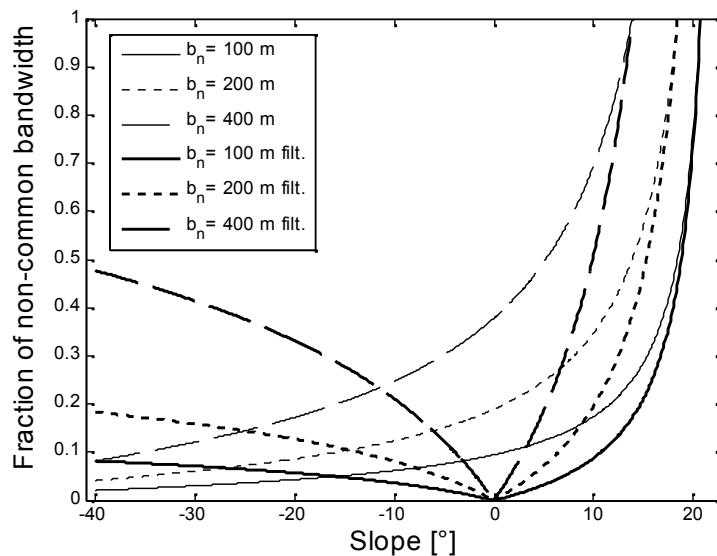


Figure 6.4. Fraction of non-common bandwidth before and after range common band filtering for slopes (in the line of sight) between -40 and 23° and perpendicular baselines of 100, 200 and 400 m.

In order to identify the effect of topography-induced decorrelation in the coherence images, two mostly unforested areas in Northeast China were considered for which two or more tandem pairs, acquired with different perpendicular baselines, were available. One area was located in Jilin province at the margins of the Changbai Mountain range (43.6° N, 124.7° E). The second area was located in Liaoning province (40.1° N, 122.3° E). In both regions, the flat areas were predominantly under agricultural use and a large fraction of the mountains was unforested. The area considered in Liaoning was characterized by an average slope of 6.4° (SD 5.8°). The average slope at the Jilin site was 3.37° (SD 3.8°). The Liaoning site was covered three times in winter 1996 by ERS-1 and ERS-2: 1) 18-19 January 1996 ($B_n = 148$ m), 2) 22-23 February 1996 ($B_n = 40$ m), 3) 28-29 March 1996 ($B_n = 101$ m). The Jilin site was covered by two tandem pairs: 1) 15-16 January 1996 ($B_n = 395$ m), 2) 19-20 February 1996 ($B_n = 84$ m). Figure 6.5 shows small subsets of the coherence images. In both areas, a decrease of coherence with increasing length of the perpendicular baseline could be noticed over sloped terrain. While layover areas were completely decorrelated in all images (right-hand side of the mountains in Figure 6.5), differences in the decorrelation strength were clearly visible for the slopes tilted away from the radar (left-hand side of the mountains).

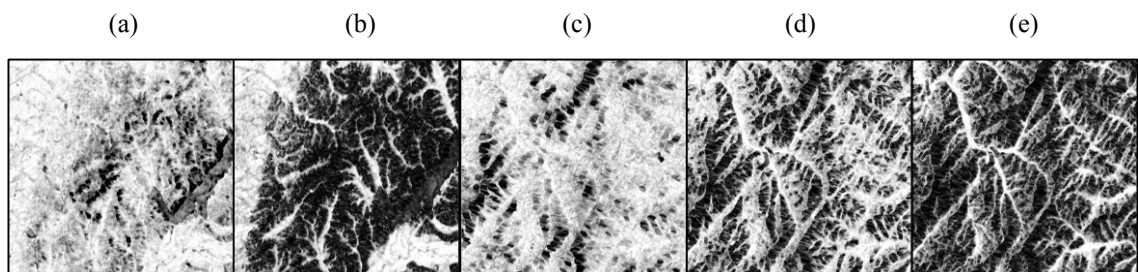


Figure 6.5. Subsets of five ERS-1/2 tandem coherence images acquired in winter over mountainous terrain in the Jilin (a & b) and Liaoning provinces (c - e). The perpendicular baselines were: (a) 84 m, (b) 395 m, (c) 40 m, (d) 101 m, (e) 146 m.

To get a more detailed view on topography-induced decorrelation, the pixel-wise coherence measurements were averaged for slope ranges of: 0-1°, 5-6°, 10-11°, 15-16° and >20°. In addition, the measurements were differentiated with respect to the aspect angle. Aspect angles range from 0 to 360° with 0° denoting slopes facing North and ~100° denoting slopes facing the radar (in case of descending ERS orbits). First, only areas where VCF indicated less than 2 % tree cover were considered in order to isolate the surface scattering case. Figure 6.6 shows that an increasing slope at the mountainsides facing the sensor was accompanied by a decrease in coherence. The decorrelation was strongest for those slopes directly facing the sensor, i.e. those with an aspect angle of ~100°. It has to be mentioned that only in case of aspect angles of ~100° and ~280°, total slope (in the SRTM slope map) and the slope in range direction, i.e. the slope that determines the wavenumber shift, are identical. For all other aspect angles, the slope in range direction is lower than the slope given in the SRTM slope map. In case of a baseline of 40 m, topography-induced decorrelation could be noticed first for slopes steeper than 15°. With increasing baseline, topographic decorrelation successively affected less steep slopes and for the steeper slopes the decorrelation became stronger. For a baseline of 150 m even slopes of 5° showed considerable decorrelation. In case of slopes tilted away from the sensor, decorrelation was less severe compared to the mountain fronts, which was in good agreement with what could be seen in Figure 6.4. As long as the baseline was shorter than ~100 m, decorrelation remained moderate. For slopes steeper than 10°, a slightly lower coherence could be noticed. Like for the mountain fronts, topographic decorrelation successively affected less steep slopes with increasing baseline. For a baseline of 395 m even slopes of 5° showed a somewhat lower coherence than flat terrain.

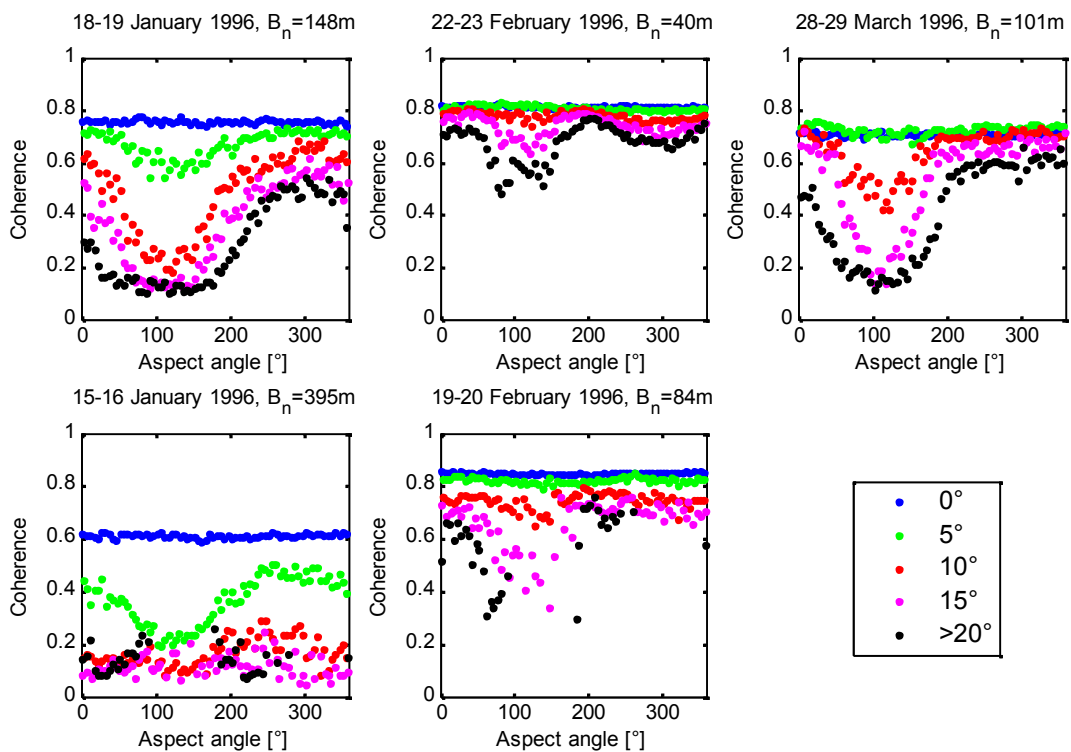


Figure 6.6. Average ERS-1/2 tandem coherence as function of aspect angle for slopes of 0, 5, 10, 15 and >20° in areas with low tree cover.

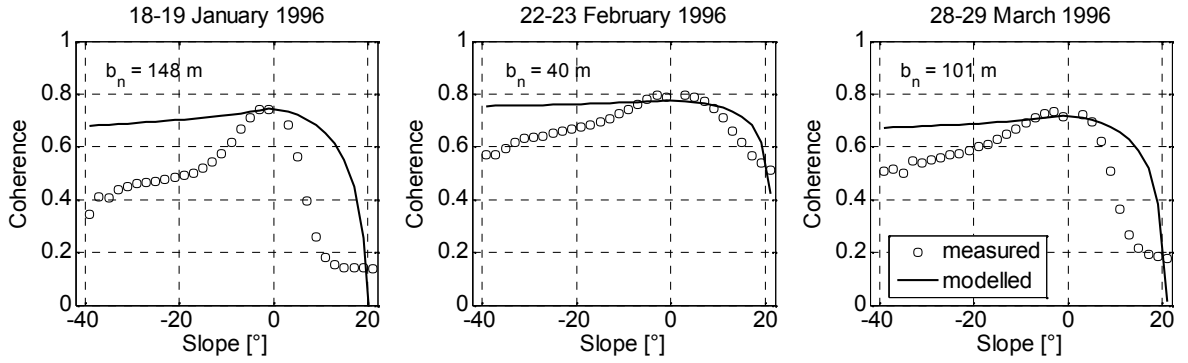


Figure 6.7. Measured (o) and modeled (line) coherence versus local slope in range for the images acquired over Liaoning province with baselines between 40 and 148 m.

Coherence was modeled as function of local slope and baseline according to the approximations for surface decorrelation after range common-band filtering outlined earlier in this section. Temporal decorrelation was accounted for by multiplying the spatial decorrelation term with the average coherence measured over flat and unforested terrain ($VCF < 2\%$).

$$|\gamma| = |\gamma_{slant-range}| |\gamma_{temporal}| = \left(1 - \frac{|\Delta f_0 - \Delta f|}{W - \Delta f_0}\right) \cdot \bar{\gamma}(\alpha_s = 0^\circ, VCF < 2\%) \quad (6.3)$$

Modeled and measured coherence as function of local slope have been illustrated for the coherence images covering the site in Liaoning province in Figure 6.7. For the sake of a better interpretability, only slopes in the radar look direction have been illustrated. When comparing model and measurements, an increasing difference between modeled and measured coherence had to be stated, the steeper the terrain was. The differences between model and observations could have been due to:

- uncompensated topography in the coherence estimation window
- co-registration offsets
- the simplifications in the model

A variation of interferometric phase within the coherence estimation window because of uncompensated topographic phase in the interferogram reduces coherence (cf. Equation (2.28)). For the compensation of the topographic phase before computing coherence with the Siberian and Chinese ERS-1/2 tandem datasets, the local phase slope was estimated from the interferogram itself. This phase slope estimate, however, suffered from uncertain phase estimates on steep slopes because of surface decorrelation so that an additional decorrelation term added up to the wavenumber shift effects over sloped terrain. In order to assess the impact of uncompensated topography on coherence, the slope estimates from the SRTM DEM were used to calculate the local standard deviation of slope for each pixel in a window of 9x9 pixels centered at the particular pixel. The average coherence for pixels has been plotted as function of slope for those 5 % of the pixels with the highest and lowest standard deviation of slope, respectively. As can be seen in Figure 6.8, the coherence pixels with the lowest standard deviation of slope resembled the modeled relationship much better, in particular in case of the slopes facing the sensor. The observation indicated that the accuracy of the phase slope estimates from the interferogram, used to eliminate the topographic phase in the

coherence estimation window, decreased the more rugged the terrain was. As also the 90 m pixel size of the SRTM DEM could be expected to resemble only a part of the ‘true’ topographic variation that affected the ERS-1/2 interferometric measurements, it can be assumed that the non-perfectly compensated topographic phase was the most important reason why the modeled and the observed relationship differed in Figure 6.7. Still, co-registration errors over rugged terrain, in particular when the baseline was long, may have further increased the difference between model and measurements. In addition, the rather simplified model for surface decorrelation may not have fully reflected the true topographic effect in the coherence measurements.

Figure 6.8 shows that the effect of residual topographic phase in coherence varies within the images and cannot solely be modeled as function of slope. The spatial estimation principle of coherence may even cause a coherence loss for pixels on flat ground when they are located close to steep slopes, i.e. up to 4 pixels distance when the coherence estimation window reaches the defined maximum size of 9x9 pixels.

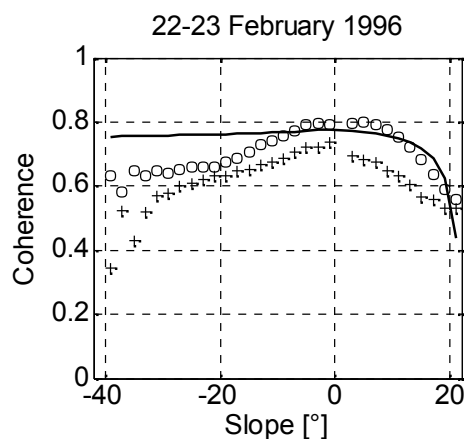


Figure 6.8. Modeled (line) and measured coherence versus local slope for pixels with the lowest (o) and the highest (+) standard deviation of slope in a window of 9x9 pixels.

The coherence measurements over mountainous densely forested terrain revealed a similar behavior as unforested terrain (Figure 6.9), i.e. stronger decorrelation on slopes tilted towards the sensor and increasing decorrelation with increasing baseline for a given slope on both mountainsides. This observation suggested that topography mainly affected dense forest coherence through varying fractions of non-common range spectra after common band filtering. However, further topography related effects may alter the stem volume-coherence relation: 1) different weights of ground and canopy backscatter contributions dependent on the local incidence angle, 2) alterations in volume decorrelation as the signal path length through the canopy increases from slopes facing the sensor to those tilted away from the sensor, 3) dependence of the area-fill factor, and thus the forest transmissivity, on topography as the fraction of gaps in the canopy should decrease with increasing local incidence angle (Nilson, 1999). No studies are known to the author that addressed these issues yet.

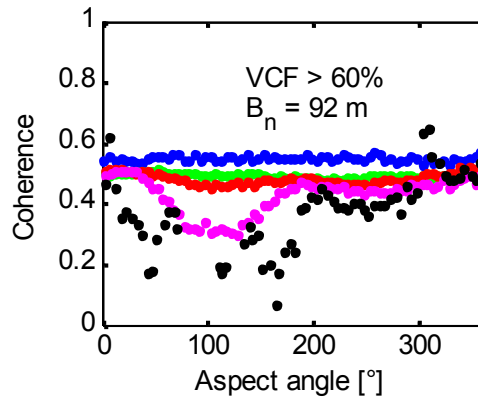


Figure 6.9. Average ERS-1/2 tandem coherence for aspect angles between 0 and 360° and different slopes of 0, 5, 10, 15 and >20° (legend as in Figure 6.6) in areas with high tree cover.

6.3 Implications with respect to a VCF-based model training

Concerning the identification of pixels that were affected by topography-induced decorrelation, it had to be stated that there were a number of uncertainties. The investigations showed that the topography-induced decorrelation depended on slope, aspect angle, perpendicular baseline as well as the spatial context, i.e. the relief in the coherence estimation window. In addition, co-registration offsets between the tandem images may have caused additional decorrelation over rugged terrain. In case of coherence over forest, several other effects could, in addition, have affected the relationship between coherence and stem volume. The modeling of these effects would require a thorough investigation, accompanied by ground measurements (e.g. the area-fill factor at different incidence angles), which was beyond the scope of this thesis.

Because of the uncertainties in the identification of topographic effects in coherence, a rather coarse topographic masking procedure had to be applied for the automated VCF- and histogram-based model training approaches in order to guarantee that no coherence pixels that were affected by topography-induced decorrelation were considered for model training. All pixels located on slopes steeper than 10° were masked as well as the surrounding four pixels in order to account for the effects of the spatial coherence estimation principle. With this approach, even in case of the longest baselines, no residual low coherence pixels in the histograms for dense forest and open areas (according to VCF) were noticed. As this masking procedure was rather coarse and the likelihood of excluding pixels that would have allowed reasonable stem volume estimates was high, a different topographic masking procedure was applied for the creation of the forest stem volume map of Northeast China (see Chapter 8.3).

With respect to the topographic distortions in the intensity images, only layover areas had to be masked. It was observed that, when further masking steep slopes (besides layover affected areas), the VCF-based estimates for the IWCM parameters σ_{gr}^0 and σ_{veg}^0 did not change.

Chapter 7 - Model training results

In this chapter, the automated model training approaches that were described in Chapter 5 are tested. First, the validity of the underlying assumptions of the histogram-based model training approach are checked. Then the VCF-based model training is applied. The reasonability of the training results is assessed by comparing the obtained model parameters with those obtained when fitting the models to the measurements at the test sites by means of regression. Due to the lack of reliable ground data for Northeast China, the VCF-based training results could only be crosschecked with the weather data in order to evaluate the general reasonability of the determined model parameters with respect to the prevailing weather conditions.

7.1 SIBERIA model training approach

The coherence histogram-based model training approach comprised several assumptions that needed to be checked in order to evaluate if the approach is applicable for stem volume retrieval with multi-seasonal ERS-1/2 tandem coherence data. The main assumptions were:

- Close relationship between the coherence histogram parameter, γ_{75} , in Equation (5.13) and the ‘saturated’ forest coherence, γ_{∞} , in Equation (5.1).
- Linear relationship between forest floor coherence, γ_0 , and the coherence histogram parameter γ_{75} .

In order to verify these assumptions, the model in Equation (5.1) was fitted to the measurements at the Siberian test sites. The parameter estimates were compared to those obtained with the histogram-based training of the model in Equation (5.13). In Equation (5.13), the parameter for forest floor coherence does not appear per se as the forest floor coherence is expressed as function of γ_{75} . That is why, the modeled coherence at 0 m³/ha stem volume was computed and denoted $\gamma_{0(\text{SIB})}$.

The correlation between γ_{75} and γ_{∞} was high (Pearson correlation of 0.92) when computing γ_{∞} by means of non-linear regression and γ_{75} from the coherence histograms for all images acquired over the Siberian test sites. The estimates closely followed the 1:1 line in Figure 7.1 (left). Thus, a good characterization of the saturation level of coherence seemed to be given with γ_{75} , even for the winter images acquired with different baselines between 65 and 171 m, respectively. This indicated that, when further compensating γ_{75} for residual volume decorrelation effects as described in Section 5.2.3.5, it might as well be used to derive the IWCM parameter γ_{veg} .

The correlation between γ_0 and γ_{75} was about the same as reported in Wagner et al. (2003). Even though an increase of forest floor coherence with increasing coherence of dense canopies could be observed (Figure 7.1, right), this increase showed considerable spread along the assumed linear relationship. In case of the acquisition from 14-15 January 1996 covering Chunksy N & E, the inventory data-based model training resulted in a forest floor coherence of ~0.8 whereas the histogram training predicted a forest floor coherence of 1.05, i.e. an unphysical value. Considering the different mechanisms of decorrelation (see Chapter 2.2.3), the coherence at the forest floor and

the canopy should be considered as independent variables. Wind, for instance, can be considered the main agent of temporal decorrelation over dense forest canopies but not over bare soil. In addition, the baseline dependent volume decorrelation affects coherence measured over dense forest but not the coherence over open ground. Consequently, an automated training of the model in Equation (5.1), relying upon a linear relationship between forest floor and canopy coherence properties, cannot be considered a physically justified approach.

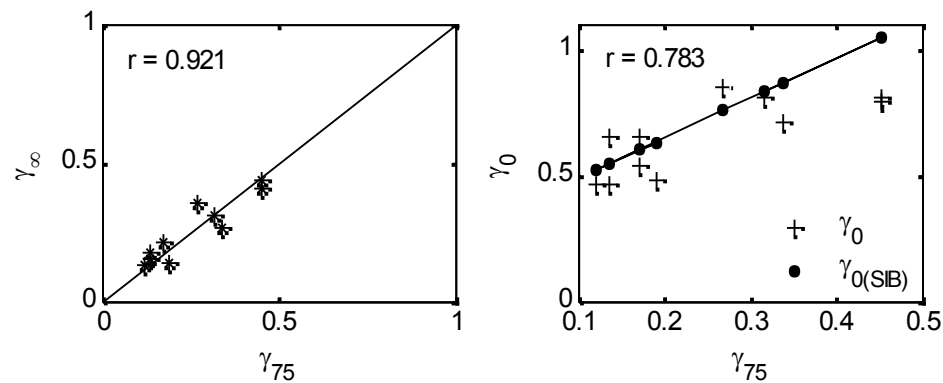


Figure 7.1. Left – Histogram coefficient γ_{75} versus dense forest coherence γ_{∞} . Right – γ_{75} versus γ_0 from inventory data-based training of the model in Equation 5.1 and the predicted forest floor coherence from the histogram-based training of the model in Equation (5.13), $\gamma_{0(SIB)}$.

Furthermore, the histogram-based model training approach relies upon the dominance of dense forest in the area covered by the coherence image as only then the typical dense forest peak appears in the coherence histogram. This was given for the test areas in Central Siberia but not for Northeast China where for many of the available ERS-1/2 tandem coherence images only a small part of the area covered was forest.

In addition, large forest areas in Northeast China are structurally degraded with only a small fraction of forests being in the mature or over-mature development stages. The test of the histogram-based model training approach for the three ERS-1/2 tandem coherence images covering the Northeast Chinese test sites resulted in values for γ_{75} clearly too high, in particular in case of the images that covered the Daxinganling and Xiaoxinganling test sites (Figure 7.2). This showed that, although the largest fraction of the areas covered by the tandem pairs was forest, the histogram-based training approach could not be considered feasible when the forests are not predominantly in the mature and overmature forest development stages.

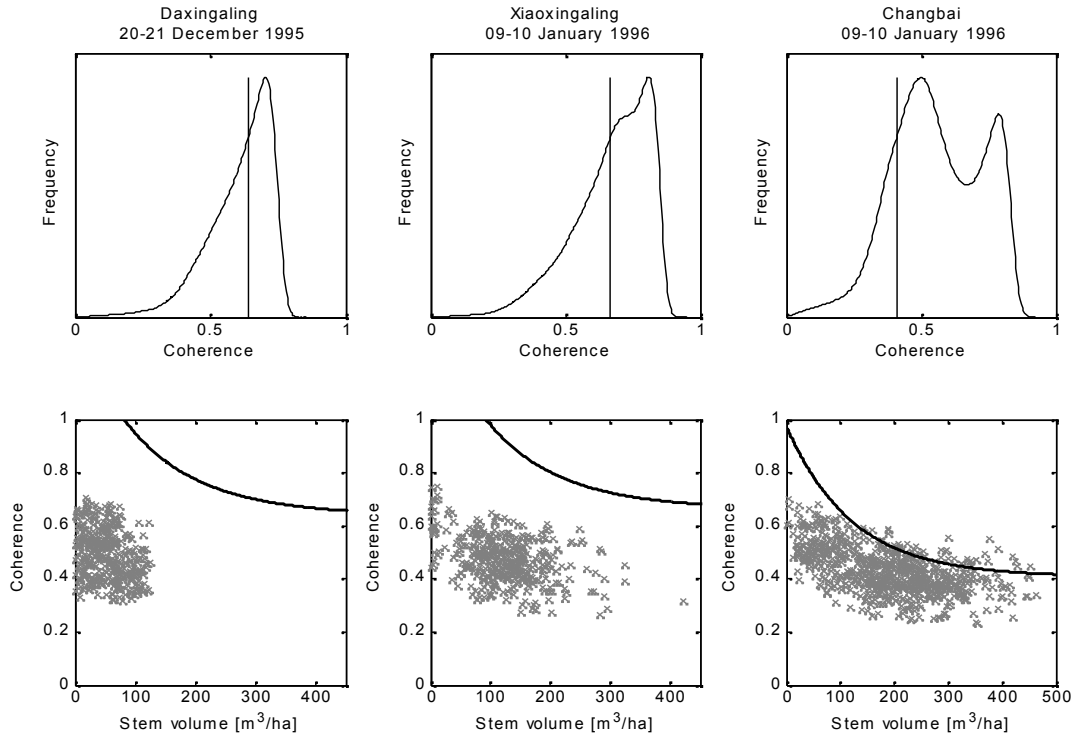


Figure 7.2. Histograms for the three ERS-1/2 tandem coherence images covering the Chinese test sites (top row). The vertical lines denote the model parameter γ_{75} . The bottom row shows the model lines (Equation (5.13)) that were obtained with the histogram-based model training, and the measurements at the test sites.

7.2 VCF-based model training for the ERS-1/2 tandem data of Siberia

7.2.1 VCF-based model training on a frame-by-frame-basis

The VCF-based model training was carried out for each ERS-1/2 tandem coherence image covering the Siberian test sites as follows:

- The peaks of the coherence and intensity histograms for areas with low VCF tree cover ($\leq 2^{\text{nd}}$ percentile of tree cover in the corresponding subset of the VCF map) were interpreted as γ_{gr} and σ_{gr}^0 , respectively (see Figure 7.3).
- The peaks of the coherence and intensity histograms for areas with maximum VCF tree cover ($\geq 98^{\text{th}}$ percentile of tree cover in the corresponding subset of the VCF map - always close to 80 % tree cover for the area covered by the Siberian ERS-1/2 tandem data) were interpreted as coherence and intensity of dense forest, γ_{VCF} and σ_{VCF}^0 (see Figure 7.3).
- γ_{veg} and σ_{veg}^0 were determined by compensating γ_{VCF} and σ_{VCF}^0 for residual ground contributions - and volume decorrelation in case of γ_{VCF} (see Chapter 5.2.3.5). A stem volume of 400 m³/ha was assumed to represent the stem volume of forests with high tree cover according to VCF.
- The IWCM was fully parameterized with a fixed value for β of 0.006 ha/m³ and a two-way signal attenuation α of 1 dB/m in case of frozen and 2 dB/m in case of unfrozen conditions.

- In case of the images that were acquired under unstable imaging conditions (see Chapter 5.2.3.4), the simple empirical model in Equation (5.1) was calculated instead of the IWCM using a fixed value for V_γ of 0.015 ha/m^3 .

The model curves that were obtained with the aid of VCF for each coherence image and the standwise measurements at the Siberian test sites have been illustrated in Figures 7.4 and 7.5. The figures also show the models obtained when fitting the models to the measurements at the particular test site by means of least-squares regression (see Chapter 5.2.1). Figure 7.4 shows the measurements and models for the images acquired under unstable conditions in fall and spring. For these images, the empirical model was used. For the sake of completeness, also the model training results for the ERS-1 intensity images have been included although they were not considered in the empirical model (Equation 5.1). The model curves represent the results of the inventory data- and VCF-based training (β set to 0.012 ha/m^3) of the model in Equation (5.3). Figure 7.5 shows the IWCM model training results for the images that were acquired under stable conditions. The obtained model parameters have been summarized in Table 7.1. It has to be stressed that the VCF-based model training was carried out on a frame-by-frame basis. That is why, the model curves in Figures 7.4 and 7.5, obtained with the VCF-based training, are identical for different test sites when the test sites were covered by the same ERS-1/2 tandem pair. This was the case for the tandem pairs from 25-26 September 1997 and 28-29 May 1998, which both covered Bolshe NE and Bolshe NW, and from 14-15 January 1996, which covered Chunksy N and Chunksy E.

At first sight, the results of the VCF-based model training drew a heterogeneous picture. The model curves, obtained with the aid of VCF, closely followed the trend of the coherence measurements as function of stem volume at the test sites in case of the ERS-1/2 tandem coherence images from 29-30 December 1996 at Chunksy N, 14-15 January 1996 at Chunksy E and 25-26 September 1997 at Bolshe NW. In case of the ERS-1 intensity images, a good agreement of the model curves, derived with the aid of VCF, and the trend of the measurements at the test sites could be observed for the images from 25 September 1997 at Bolshe NE and NW, 29 December 1996 at Chunksy N and 1 January 1996 at Bolshe NE. In all other cases, more or less significant deviations from the trend, as indicated by the standwise measurements at the test sites, had to be stated.

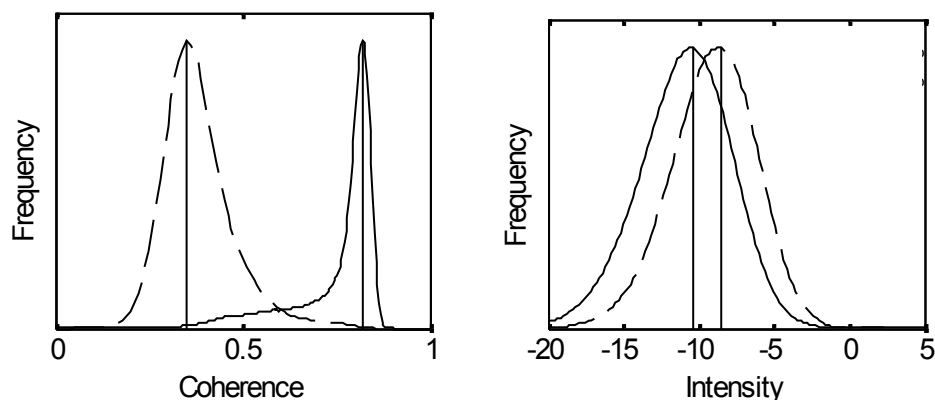


Figure 7.3. Example for the VCF-based model parameter estimation with the coherence and intensity histograms for areas with high (dashed lines) and low (solid lines) VCF tree cover. The vertical lines denote the peaks of the histograms.

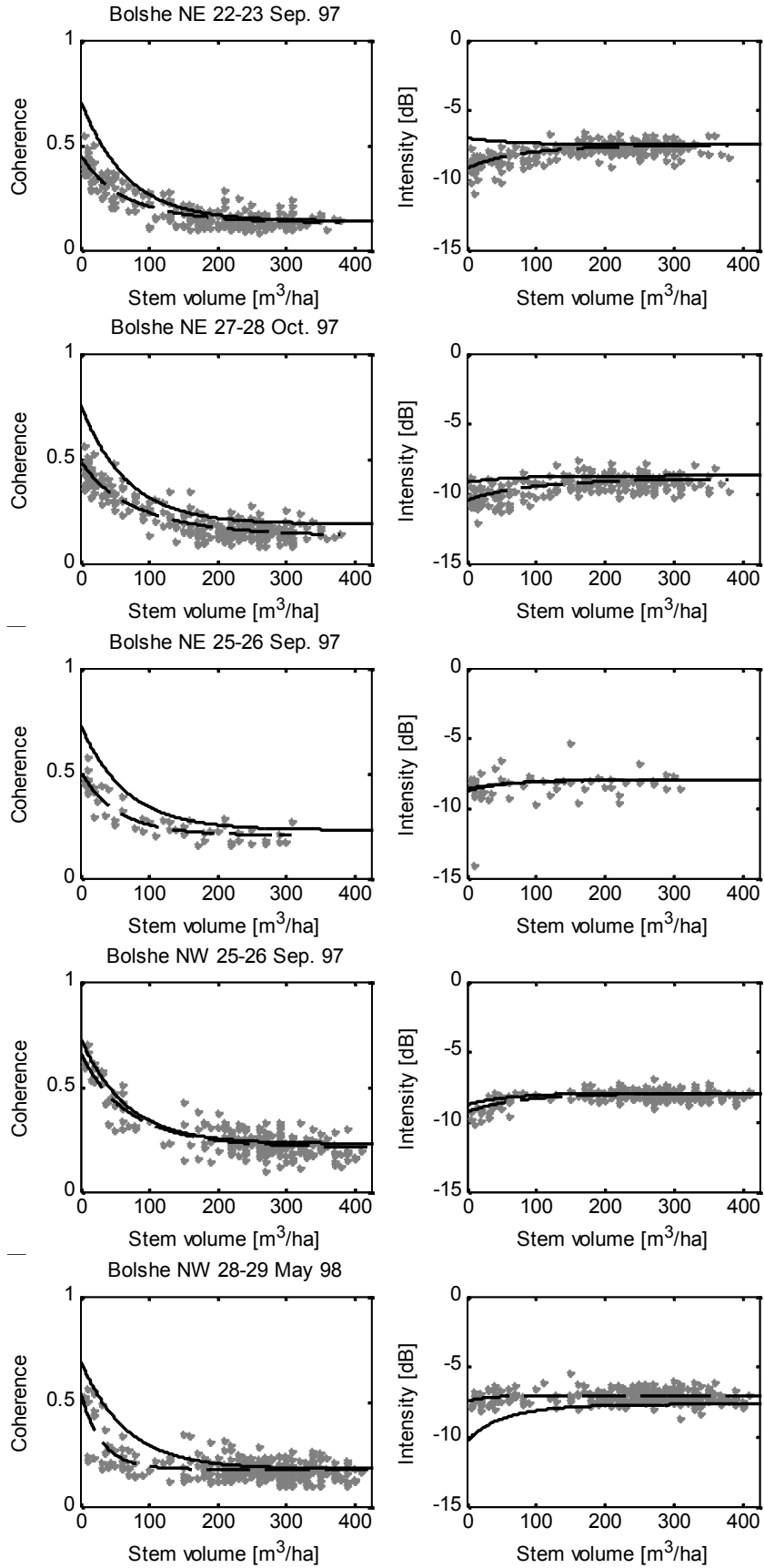


Figure 7.4. Measured and modeled coherence/intensity (models in Equation (5.1) for coherence and (5.3) for intensity) as function of stem volume. The solid lines show the VCF training results and the dashed lines refer to the regression-based model fits.

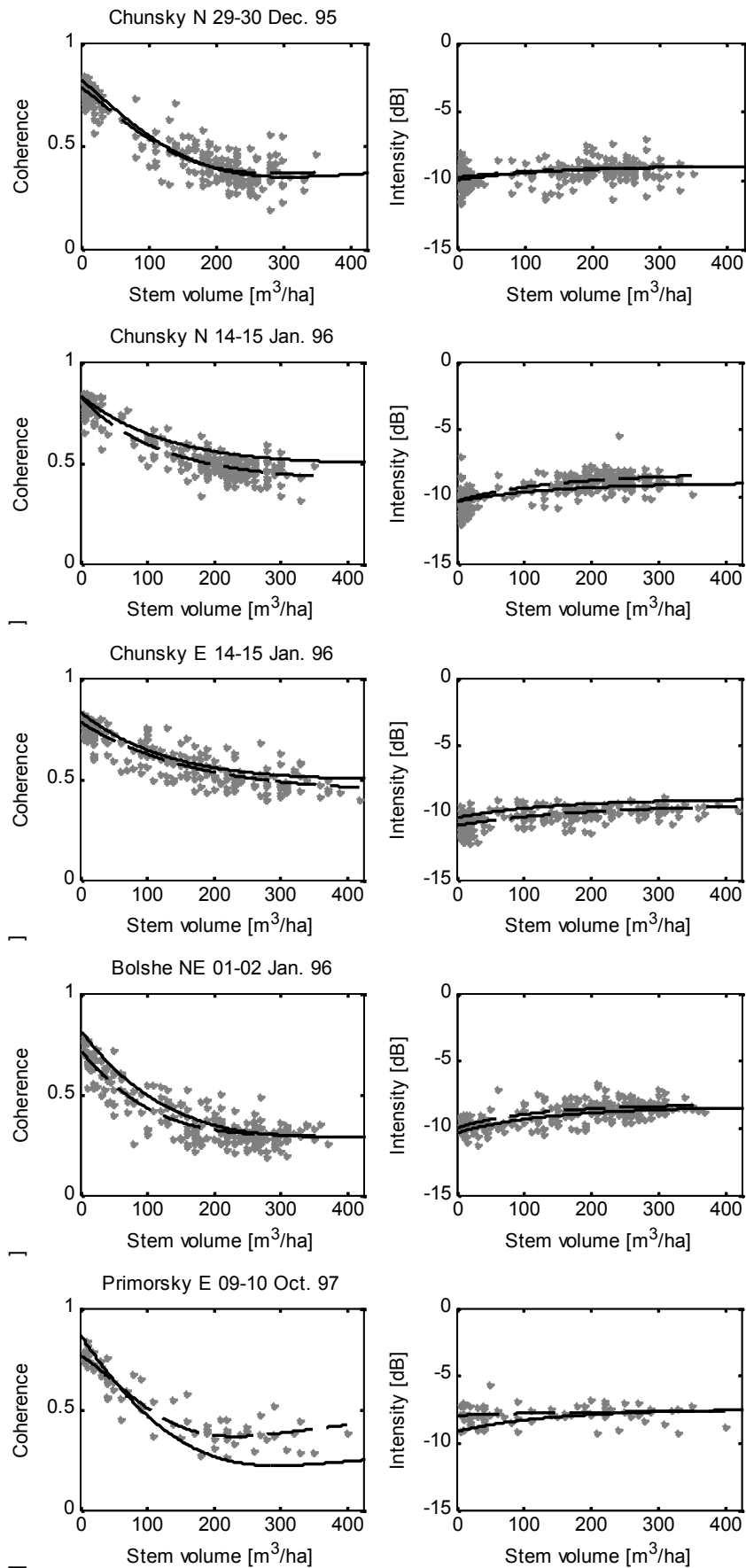


Figure 7.5. Measured and modeled coherence/intensity (IWCM) as function of stem volume. The solid lines show the VCF training results and the dashed lines refer to the model fits to the measurements at the test sites.

Table 7.1. Model parameters of the IWCM, respectively the empirical model in Equation (5.1), determined with the VCF- and inventory data-based model training (FID). For the latter, the 95% confidence bounds, CI, are provided.

Test site	Training	Acquisition date	Baseline [m]	γ_{gr} +/-CI	γ_{veg} +/-CI	σ_{gr}^0 +/-CI [dB]	σ_{veg}^0 +/-CI [dB]
Chunsky N	FID	29-30 Dec. 95	171	0.780	0.540	-10.07	-8.80
Chunsky N	VCF			+/-0.016	+/-0.026	+/-0.17	+/-0.15
Chunsky N	FID	14-15 Jan. 96	65	0.824	0.423	-10.59	-8.21
Chunsky E	FID			+/-0.013	+/-0.030	+/-0.19	+/-0.14
Chunsky N & E	VCF			0.799	0.470	-10.92	-9.62
Chunsky N & E	VCF			+/-0.015	+/-0.030	+/-0.14	+/-0.13
Primorsky E	FID	9-10 Oct. 97	183	0.836	0.514	-10.40	-8.97
Primorsky E	VCF			+/-0.044	+/-0.044	+/-0.33	+/-0.27
Primorsky E	VCF	1-2 Jan. 96	144	0.872	0.315	-9.20	-7.47
Bolshe NE	FID			0.704	0.336	-10.58	-7.99
Bolshe NE	VCF			+/-0.027	+/-0.013	+/-0.26	+/-0.11
Bolshe NE	VCF			0.820	0.345	-10.40	-8.39
For the following acquisitions the empirical model in Equation (5.1) was used. For the sake of completeness, also σ_{gr}^0 and σ_{veg}^0 have been estimated by fitting the model in Equation (5.3) to the intensity measurements.				γ_0	γ_∞	σ_{gr}^0 [dB]	σ_{veg}^0 [dB]
Bolshe NE	FID	22-23 Sep. 97	260	0.466	0.134	-9.17	-7.71
Bolshe NE	VCF			+/-0.021	+/- 0.001	+/-0.21	+/-0.09
Bolshe NE	FID	25-26 Sep. 97	233	0.716	0.139	-7.00	-7.49
Bolshe NE	FID			0.534	0.216	-8.64	-8.18
Bolshe NE	FID			+/-0.054	+/-0.020	+/-0.64	+/-0.28
Bolshe NW	FID			0.633	0.228	-9.48	-7.98
Bolshe NE & NW	VCF	27-28 Oct. 97	158	+/-0.062	+/-0.018	+/-0.27	+/-0.055
Bolshe NE	FID			0.732	0.229	-8.80	-7.94
Bolshe NE	FID			0.483	0.138	-10.45	-8.84
Bolshe NE	VCF			+/-0.021	+/-0.01	+/-0.24	+/-0.10
Bolshe NE	VCF			0.764	0.189	-9.00	-8.72
Bolshe NE	FID			0.452	0.161	-7.45	-6.84
Bolshe NE	FID	28-29 May 98	313	+/-0.049	+/-0.034	+/-0.71	+/-0.45
Bolshe NW	FID			0.549	0.177	-7.61	-7.07
Bolshe NE & NW	VCF			+/-0.063	+/-0.006	+/-0.47	+/-0.05
Bolshe NE & NW	VCF			0.696	0.179	-10.40	-7.69

When considering the four parameters separately, a mostly good agreement could be stated for the model parameters γ_{veg} , γ_∞ and σ_{veg}^0 . The Pearson correlation between the inventory data- and VCF-based estimates was 0.84 (Figure 7.6) when not differentiating between γ_{veg} and γ_∞ . The largest difference of 0.2 occurred for the image from 9-10 October 1997 at the test site Primorsky E. Here the VCF-based estimate for γ_{veg} was lower than the inventory data-based estimate. In contrast, VCF predicted a higher value for γ_{veg} in case of the ERS-1/2 tandem coherence image from 14-15 January 1996 at both test sites covered. Even when the model, that was trained with the aid of VCF, closely followed the trend of the standwise coherence measurements as function of stem volume, there were differences between the inventory data and VCF-based estimates for γ_{veg} , for instance in case of the coherence image from 29-30 December 1995 at the test site Chunsky N. Here the difference in the estimates was 0.07.

In case of σ_{veg}^0 , the correlation was 0.8. Differences between the inventory data- and VCF-based estimates of more than 0.5 dB were only observed in case of the intensity images from 14 January 1996 and 28 May 1998. In case of the image from 14 January 1996, the VCF-based estimate for the whole frame was lower than the inventory data-based estimate at Chunksy N whereas at Chunksy E the inventory data-based estimate was lower, clearly indicating within-frame variations of dense forest intensity. For the ERS-1 intensity image from 28 May 1998, the VCF-based estimate for σ_{veg}^0 was lower than the inventory data-based estimates at both test sites covered.

For γ_{gr} – denoted γ_0 when the empirical model was used - the correlation between the inventory data and VCF-based estimates was 0.76. A clear deviation from the 1:1 line could be observed for the coherence images that were acquired over Bolshe NE under unstable conditions in fall and spring. The VCF-based estimates were up to 0.3 higher than the estimates derived with the aid of the inventory data. In case of the images that covered Bolshe NE and NW (25-26 September 1997 and 28-29 May 1998), the VCF-based estimates (for the whole frame) agreed better with the inventory data-based estimates at the test site Bolshe NW. For two of the tandem pairs that were acquired under stable conditions over Bolshe NE (1-2 January 1996) and Primorsky E (9-10 October 1997), the VCF-based estimate for γ_{gr} was about 0.1 higher than the inventory data-based estimate.

A very low correlation of ~ 0.1 between the inventory data- and VCF-based estimates had to be stated in case of σ_{gr}^0 . The largest deviations occurred, as in case of γ_{gr} , for the images that were acquired under unfrozen conditions. When only considering σ_{gr}^0 for the three images acquired under stable frozen conditions, the Pearson correlation was very high (0.96) and the differences between the inventory data- and VCF-based estimates were less than 0.5 dB. The largest difference was observed for the intensity image from 28 May 1998. Here, the VCF-based estimate was 3 dB lower than the values obtained when fitting the model in Equation (5.3) to the measurements at the test sites Bolshe NE and NW, indicating much drier soil conditions outside of the forest areas. In contrast, the VCF-based estimate for σ_{gr}^0 was 2.2 dB higher than the inventory data-based estimate for the intensity image from 22 September 1997 at the test site Bolshe NE.

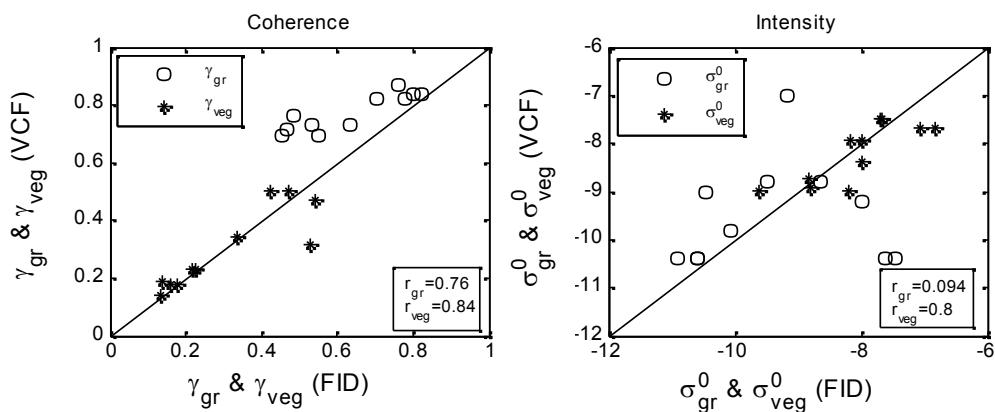


Figure 7.6. IWCM and SIBERIA model parameter estimates from the VCF and inventory data-based model training; note that γ_{veg} and γ_{∞} as well as γ_{gr} and γ_0 are not differentiated.

7.2.2 Regionalized VCF-based model training

In Chapter 5.2.3.2, two preconditions for a successful model training with VCF were formulated. Accordingly, the observed differences between the inventory data- and frame-by-frame VCF-based parameter estimates, exceeding clearly the confidence bounds of the regressed parameters in several cases (see Table 7.1), could mean that:

1. Coherence and intensity in areas with low VCF tree cover did not reflect the conditions at the forest floor.
2. The coherence and intensity measurements in areas with high VCF tree cover did not allow to infer reliably on the properties of ideally opaque canopies.

Before, however, discussing these fundamental questions, it had to be considered that the environmental and meteorological imaging conditions might have varied within the area covered by an ERS-1/2 tandem pair. Variations in coherence and intensity because of differing environmental and meteorological imaging conditions can occur in very different spatial scales. For instance, variations related to soil moisture can occur at the stand level but there may also be variations related to larger scale drainage patterns or soil type specific effects (e.g. Pulliainen et al., 1994, 1996; Fella et al., 1997; Hallikainen et al., 1998). The model training with the inventory data was restricted to the area of the particular test site (200 – 400 km²) so that the training was only affected by any kind of variations in the imaging conditions that occurred within the area of the test site. The VCF-based training, instead, was carried out on an ERS frame (~10000 km²) so that it may have reflected variations in the environmental or meteorological imaging conditions that did not occur in the area of the test sites. In order to minimize the effect of spatial variations, before addressing the fundamental questions raised under bullet points 1 and 2, the model training was carried out again but this time only the VCF map and the ERS-1/2 coherence and intensity measurements in the area of the test sites were considered so that inventory data- and VCF-based model training referred to the same area. When restricting the model training to the area of the test sites, the problem arised that the number of pixels with low or high VCF tree cover was much reduced as the area of the test sites was much smaller than an ERS frame. Still, non-noisy coherence and intensity histograms were achieved at the test sites Chunksy N, Chunksy E, Bolshe NW and Primorsky E when delineating open areas with an upper VCF tree cover threshold of 15 % and dense forests with a lower tree cover threshold of 75 %. In case of the test site Bolshe NE, however, very few VCF pixels indicated low tree cover. The coherence and intensity histograms for areas with low tree cover were very noisy and a derivation of γ_{gr} and σ_{gr}^0 was not possible.

In case of the ERS-1/2 tandem pairs that were acquired under unfrozen conditions over the Bolshe test sites, it was observed that the forest floor coherence differed considerably between the test sites Bolshe NE and Bolshe NW (see Chapter 4.1). It was assumed that the differences were related to the differing soil types in the area, i.e. the peatland at Bolshe NE and the sandy soils at Bolshe NW. To make clear how this may have affected the VCF-based parameter estimates, the VCF tree cover map in the Bolshe-Murtinsky area is shown in Figure 7.7 (left). The map shows the area covered by the ERS-1/2 tandem pairs from 1-2 January 1996, 22-23 September 1997 and 27-28 October 1997. The pixels with low and high tree cover have been marked in red (VCF≤10%) and green (VCF≥78%). The VCF tree cover map shows a strip with mostly dense forest in the center of the image. This strip corresponds to the peatland

area in which also the test site Bolshe NE can be found. Most of the areas with low tree cover are located west and east of the peatland where soil types are different (mostly sandy). It is obvious that, if there were differences in coherence or intensity measured over the sand and the peat soils, the VCF-based estimates for γ_{gr} and σ_{gr}^0 would only have reflected the conditions in the sandy areas. For comparison, the VCF pixels that were used for the model parameter estimation in case of the tandem pairs that covered the test sites at Chunsky (Figure 7.7, right) and Primorsky were distributed all over the area of the corresponding ERS frames so that the VCF-based parameter estimates would most likely have represented some sort of average conditions if the environmental or weather conditions had varied within the area covered.

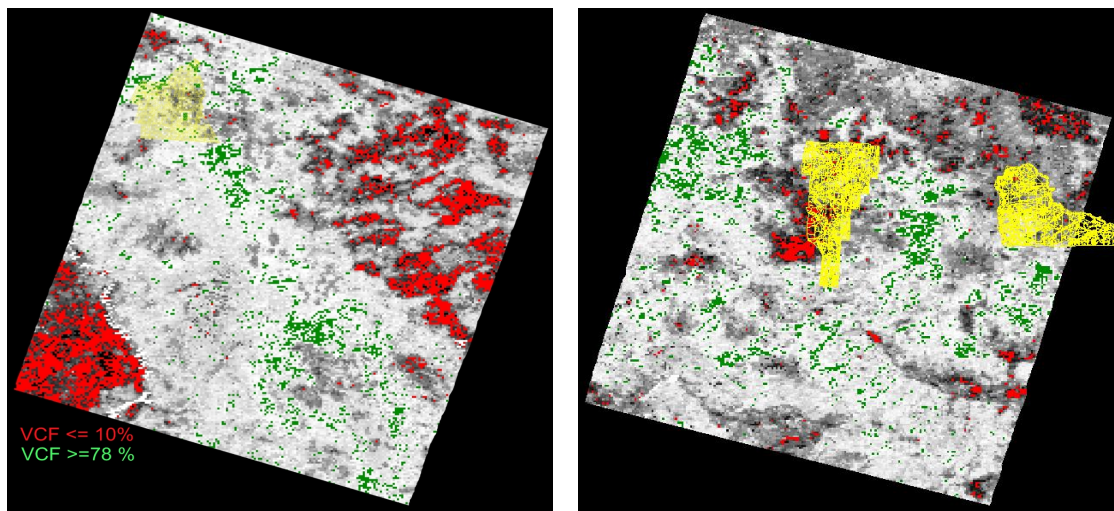


Figure 7.7. Subsets of the VCF tree cover map showing the area of two ERS frames ($100 \times 100 \text{ km}^2$). The red areas highlight VCF pixels with a tree cover $\leq 10\%$. The green areas highlight those pixels with a tree cover $\geq 78\%$. In the left image, the yellow polygons show the forest stands at Bolshe NE. In the right image, the polygons show the stands at Chunsky N & E.

As a VCF-based model training was not possible when restricting it to the area of the test site Bolshe NE, the area considered for the estimation of γ_{gr} and σ_{gr}^0 had to be extended. The most plausible larger area for training was the area of the peatland. The peatland could be delineated by means of a soil map that was available at a scale of 1:2.5 Million (Stolbovoi & McCallum, 2002; downloaded from 'http://www.iiasa.ac.at/Research/FOR/russia_cd/download.htm'). In this way, non-noisy histograms and reasonable parameter estimates could be achieved for the acquisitions from 1-2 January 1996, 22-23 September 1997 and 27-28 October 1997; the acquisitions from 25-26 September 1997 and 28-29 May 1997 covered only a small fraction of the peatland area east of the Yenissei which is why no model training was possible.

The agreement of the inventory data- and VCF-based model parameter estimates improved when carrying out the VCF-based training for the area of the particular test site, respectively the peatland in case of the Bolshe NE test site. The Pearson correlation coefficients between the VCF- and inventory data-based parameter estimates increased for all parameters (see Figure 7.8).

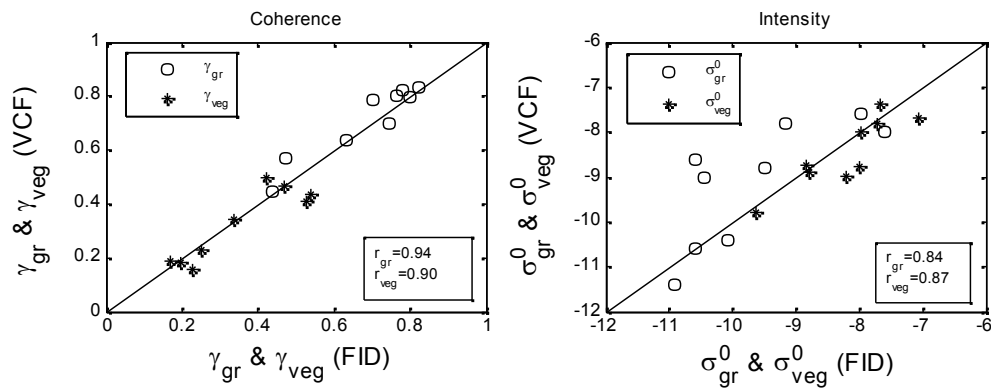


Figure 7.8. IWCM and SIBERIA model parameter estimates from the VCF and inventory data-based model training. The VCF-based parameter estimation was restricted to the area of the test sites.

A better agreement of the inventory data- and VCF-based estimates for γ_{gr} was achieved for the images from fall that covered the test sites Bolshe NE and Primorsky E; the corresponding coherence histograms have been illustrated for two of these images in Figure 7.9. In case of the images from fall 1997 that covered the test site Bolshe NE, the improved parameter estimates seemed to confirm the assumption that the differences in ground coherence within the images were related to the different soil types respectively their response to rain or snow melt induced wetting in terms of heterogeneous (at the sub-pixel scale) soil moisture variations. The standwise coherence and intensity measurements as well as the model lines are shown in Figure 7.10 for one of the tandem pairs from fall 1997. It can be seen that with the VCF-based training, restricted to the area of the peatland, the empirical model well followed the trend of the measurements at the test site. The largest differences between the inventory data and VCF-based estimates for γ_{gr} of 0.07 and 0.08 had to be stated for the images from 1-2 January 1996 and 28-29 May 1998 at the test sites Bolshe NE and Bolshe NW, respectively. In case of the image from 1-2 January 1996, the training, when restricted to the area of the peatland, hardly changed the estimate. This suggested that the differences between the estimates for γ_{gr} from VCF and inventory data were not related to the soil types in the Bolshe area. As the ground was covered with snow, the differences in the estimates were most likely related to spatial variations in the snow properties.

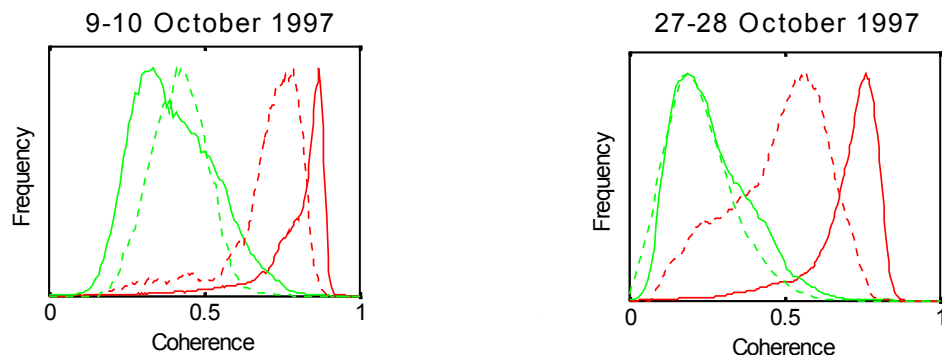


Figure 7.9. Coherence histograms for VCF < 15 % (red line) and VCF > 75 % (green line) in the area of the test site Primorsky E (left plot, dashed lines) and the peatland area (right plot, dashed lines). The solid lines show the histograms for low and high VCF tree cover when considering the whole ERS frames. For a better comparability, the histograms have been rescaled to a common height.

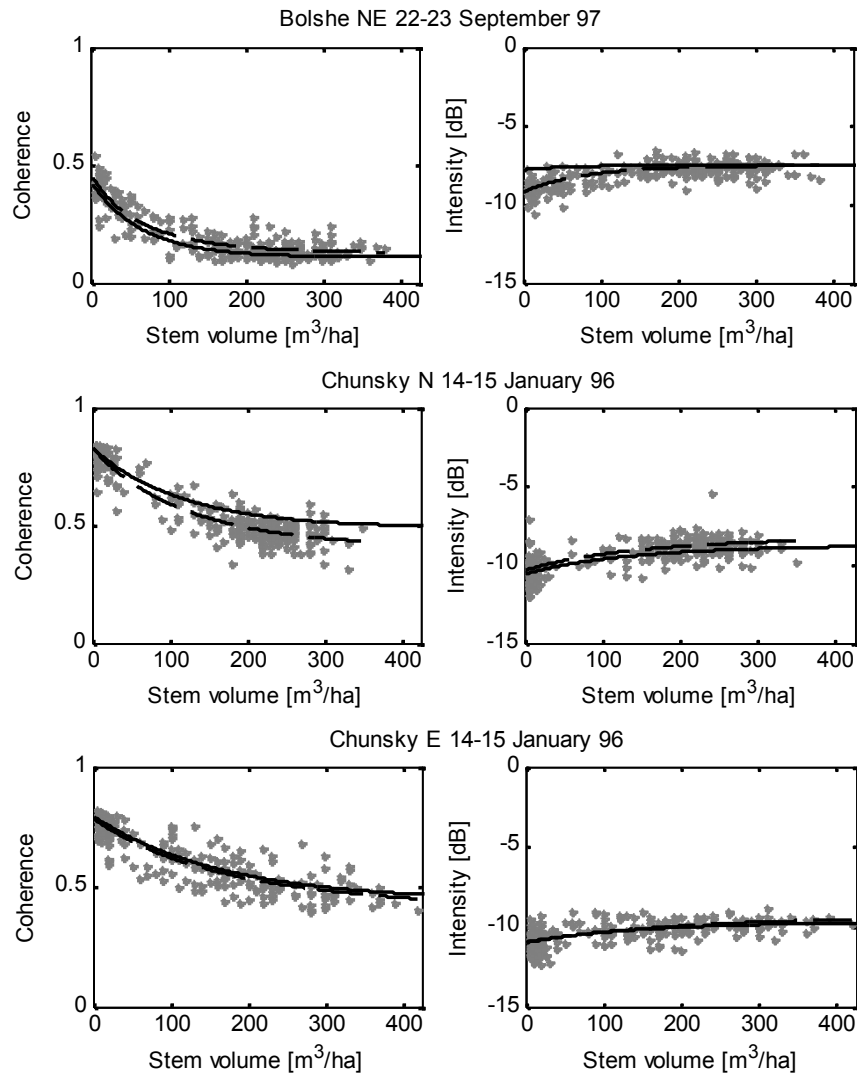


Figure 7.10. Measured and modeled ERS-1/2 tandem coherence and ERS-1 intensity (IWCM) as function of stem volume. The solid lines denote the results of the VCF-based model training, restricted to the area of the particular test site, and the dashed lines show the inventory data-based model fits.

In Figure 7.8 (right) it can be seen that in four cases (all correspond to the intensity images from fall that covered the Bolshe NE and NW test sites) the estimates for σ_{gr}^0 with VCF were 1 to 2 dB higher than the estimates with the inventory data whereas for the images acquired under frozen conditions, the VCF-based σ_{gr}^0 estimates were always close to the values obtained with the aid of the inventory data. The inventory data and VCF-based estimates were also similar for the images from 9 October 1997 and 28 May 1998 at the test sites Primorsky E and Bolshe NW. Figure 7.10 shows the standwise intensity measurements at the test site Bolshe NE and the model line that was obtained with the VCF-based training, restricted to the area of the peatland, for the intensity image from 22 September 1997, i.e. one of those for which the VCF-based estimate for σ_{gr}^0 was clearly too high.

This brings us back to the fundamental question if it is possible to infer from the ERS measurements over open ground (i.e. VCF < 10 %) on the forest floor conditions. As has been mentioned before, areas with low tree cover comprise a wide range of land cover types like barren ground, wetland, grassland, shrubland, burnt areas or cropland

which do not necessarily - or only temporally - exhibit the backscatter properties of forest floor (e.g. Dobson et al., 1995b; Kasischke et al., 1997; 2007; Brisco & Brown, 1998; Proisy et al., 2000; Quegan et al., 2000; Moran et al., 2000; Henderson & Lewis, 2008). Concerning soil moisture, the soil moisture levels at the forest floor and open unforested ground can differ because of the effects of evapotranspiration and rainfall interception over forest (Geiger et al., 2003). This could explain why the VCF-based model training tended to overestimate σ_{gr}^0 in case of unfrozen and rainy weather conditions. Accordingly, the observation that the VCF-based estimates for σ_{gr}^0 were consistently better for the winter images may be explained with the frozen snow covered ground that diminishes a lot of the potential differences between forest floor and areas without tree cover. As in case of intensity, one may expect that it could be critical to infer from the coherence observed over non-forest land on the coherence at the forest floor. However, the comparison of the inventory data- and VCF-based estimates for γ_{gr} (when restricting the VCF-based training to the area of the particular test site) revealed less pronounced differences than in case of σ_{gr}^0 . A reason for this could have been that coherence, in contrast to intensity, is not sensitive to soil moisture differences that may arise between forest and open land because of, for instance, evapotranspiration or rainfall interception. Only heterogeneous variations of soil moisture between the tandem acquisitions lower the coherence (Luo et al., 2001). Not much knowledge has been gathered yet concerning the question when soil moisture fluctuations are heterogeneous or homogeneous at the sub-pixel scale though. This may be related to the root concentration, soil type/porosity or ground water depth. In addition, the impact of understorey vegetation on coherence has not been analyzed yet. It is thus difficult to appraise under which conditions it may be critical to infer from the coherence that was measured in areas without tree cover on the forest floor coherence. As in case of intensity, it can be assumed that potential differences should be minimized in case of frozen ground surfaces. Nevertheless, the ERS-1/2 tandem pairs that were acquired over Bolshe-Murtinsky showed that, in particular under unfrozen and wet conditions, the ground coherence level can vary considerably within the area of an ERS frame but the variations were obviously a consequence of soil type specific effects and did not reflect systematic differences in coherence between forest floor and unforested terrain.

A better agreement of the inventory data- and VCF-based estimates for γ_{veg} was achieved for the image from 9-10 October 1997 when restricting the VCF-based model training to the area of the test site Primorsky E. The new estimate was only 0.06 lower than the estimate from the inventory data. In Figure 7.9, it can be seen that the coherence histogram for areas with high VCF tree cover showed a wide, almost bimodal, distribution when computing it for the whole coherence frame, indicating different levels of dense forest coherence within the image. The reasons for these variations were not clear. For all other images, the VCF-based γ_{veg} (or γ_{∞}) estimates hardly changed when restricting the training to the area of the test sites. Similar observations could be made in case of σ_{veg}^0 . Slightly improved estimates for σ_{veg}^0 were only observed in case of the intensity image from 14 January 1996 at the test sites Chunksy N and Chunksy E. With the VCF-based parameter estimation, restricted to the area of the test sites, the different intensities measured over dense forest at both test sites were now well captured (compare with the VCF-based model fits shown in Figure 7.5). The maximum difference between the VCF- and inventory data-based estimates for γ_{veg} was 0.06 and the differences in case of σ_{veg}^0 were always in a sub-dB range (<0.7 dB). In Chapter 5.2.3.5, it was described that the derivation of γ_{veg} from γ_{VCF} required the VCF-based estimates for the model parameters γ_{gr} , σ_{gr}^0 and σ_{veg}^0 and the predefined

value for β . Thus, differences between the inventory data- and VCF-based estimates for γ_{gr} , σ_{gr}^0 and σ_{veg}^0 (as well as β) result in different estimates for γ_{veg} even when γ_{VCF} and the modeled coherence at V_{eq} (according to the model fit to the measurements at the test sites) were identical. That is why, the comparison of the γ_{veg} estimates from VCF and inventory data was somewhat misleading when trying to answer the question how reliable γ_{VCF} and σ_{VCF}^0 could be related to γ_{veg} and σ_{veg}^0 , respectively. More meaningful was the relationship between γ_{VCF} and the modeled coherence (i.e. the model curve fitted to the measurements at the test sites). In most cases, γ_{VCF} well agreed with the modeled coherence at stem volumes above $\sim 250 \text{ m}^3/\text{ha}$. Only in case of the coherence image from 14-15 January 1996 and the test site Chunsy N, the IWCM trained with the aid of VCF rather represented the upper margin of the trend of the coherence measurements at the test site (see Figure 7.10). Here, γ_{VCF} was similar to the coherence modeled with the IWCM (trained with the aid of the inventory data at Chunsy N) at a stem volume of $170 \text{ m}^3/\text{ha}$ (see Figure 7.11). An equivalent stem volume of $170 \text{ m}^3/\text{ha}$ appeared to be too low when considering that, according to Figure 5.15, forests with maximum VCF tree cover should mostly exceed a stem volume of $200 \text{ m}^3/\text{ha}$. The reason for the ‘overestimation’ of dense forest coherence in this case remained unclear. All in all, however, it can be stated that, when presuming that the coherence measurements over forest with maximum VCF tree cover reflect a stem volume of 250 to $400 \text{ m}^3/\text{ha}$, reasonable estimates for γ_{veg} can be achieved with the aid of VCF.

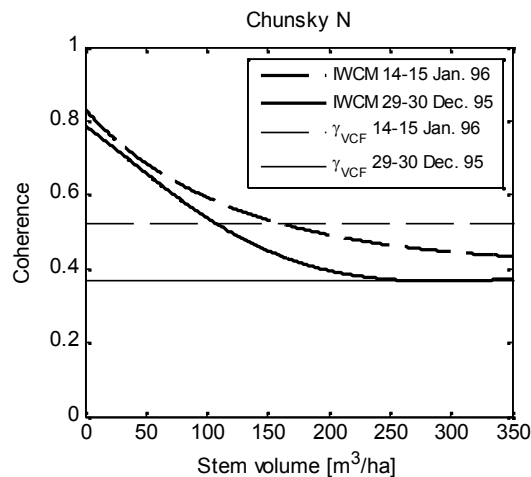


Figure 7.11. IWCM model lines as obtained when fitting the model to the ERS-1/2 tandem coherence and intensity measurements from 14-15 January 1996 and 29-30 December 1995 at Chunsy N. The horizontal lines show the estimate for γ_{VCF} when restricting the VCF-based parameter estimation to the area of Chunsy N.

7.3 VCF-based model training for the ERS-1/2 tandem data of Northeast China

The correlation between ERS-1/2 tandem coherence and the *in situ* stem volumes at the test sites in Northeast China was low (see Chapter 4.2). It was assumed that the low correlation was a consequence of a low quality/timeliness of the inventory data. Still, a larger forest structural diversity of the forests in Northeast China may have contributed to the low correlation. When fitting the IWCM to the standwise ERS-1/2 tandem coherence and intensity measurements at the test sites by means of least-squares regression, the large spread of the coherence and intensity measurements along the hardly noticeable main trend resulted in highly uncertain model parameter estimates. A

comparison of these model parameters with the VCF-based parameter estimates could not be considered meaningful.

Hence, the VCF-based training was applied to all ERS-1/2 tandem pairs available for Northeast China and the estimates for the IWCM parameters were compared to the measurements of temperature, precipitation and wind speed available from 43 weather stations (see Chapter 3.5). The analysis aimed at identifying the general properties of the coherence measurements with respect to the weather conditions. In Chapter 4.1, it was observed that the weather conditions had a major impact on the overall level of coherence observed over dense forest canopies and the forest floor as well as on the saturation behavior of coherence. Coherence showed no saturation up to stem volumes of at least 200 m³/ha in case of the tandem pairs acquired with baselines between 65 and 183 m when the ground coherence was above 0.7 and when the coherence over dense forest did not fall below 0.25. Thus, it was of interest if the VCF-based parameter estimates for the Chinese ERS-1/2 tandem dataset revealed similar patterns. This would allow an, at least rough, appraisal of the reasonability of the VCF-based parameter estimates.

For the VCF-based training of the IWCM, the two-way signal attenuation coefficient α was set to 1 and 2 dB/m when the temperatures, measured at the nearest weather stations, indicated frozen or unfrozen conditions, respectively. The forest transmissivity parameter β was set to 0.006 ha/m³ and V_{eq} to 400 m³/ha for all images. In the last chapter, only ERS-1/2 tandem pairs were considered for the VCF-based model training for which the corresponding subsets of the VCF tree cover map comprised a sufficient number of pixels with very low or high tree cover close to the maximum of 80 %, respectively. In the ERS-1/2 tandem dataset for Northeast China, however, there were many images for which the 98th percentile of VCF tree cover was much lower than 80 %. The model sensitivity analysis indicated that the estimates for γ_{VCF} and σ_{VCF}^0 should hardly be affected by differing ground contributions in the range of stem volumes characterized by maximum tree cover in the VCF map. This, however, may change when including lower tree cover levels in the estimation of γ_{VCF} and σ_{VCF}^0 . In Figures 5.4 and 5.7, it could be seen that the average coherence almost linearly decreased with increasing VCF tree cover up to the maximum tree cover levels, indicating that when integrating VCF tree cover levels much lower than 80 % into the estimation of γ_{VCF} and σ_{VCF}^0 , the relevance of ground contributions in the measurements may increase (in particular in case of Scenario 1-kind of VCF-stem volume relations, see Chapter 5.2.3). Thus, tandem pairs for which the 98th percentile of VCF was lower than 70 % were not considered in order to avoid that coherence pixels with strong ground contributions in the measurements affected the determination of γ_{VCF} and σ_{VCF}^0 . With this constraint, the VCF-based training of the IWCM could be considered successful for 87 out of 223 tandem pairs; note that there was always a sufficient number of VCF pixels that indicated low tree cover. For 30 out of these 87 images, weather stations were located close to, i.e. less than 50 km away, or within the area covered by the particular ERS-1/2 tandem pair. These 30 tandem pairs were distributed all over the major forest areas in Northeast China and were acquired in all seasons (except the summer months between June and August).

Figure 7.12 illustrates the relationship between the obtained model parameters and the weather conditions in terms of temperature and the amount of rain in the 10 days prior to the ERS-2 acquisition for each of the 30 ERS-1/2 tandem pairs. When relating the IWCM parameter estimates to the temperature at the time of the ERS-1 overpass (note

that the differences in temperature between the ERS-1 and ERS-2 acquisitions were generally negligible), high Pearson correlation coefficients of at least ± 0.78 were obtained for all four IWCM parameters. γ_{gr} and γ_{veg} decreased and σ_{gr}^0 and σ_{veg}^0 increased with increasing temperature (Figure 7.12, a-d). The high correlations were somewhat surprising as the main temperature effects in coherence and intensity measurements over forested terrain were expected to arise between the images acquired under frozen and unfrozen conditions (for which the dielectric properties of the soil and the canopy constituents differ strongly). Beyond the freeze-thaw transition, other factors like the wind speed, rainfall, snow properties or moisture content in the trees, all not or not directly related to temperature, should determine the coherence and intensity measurements. When, however, computing the correlation of temperature and the model parameters for the images acquired under frozen and unfrozen conditions separately, the predictive power of temperature reduced considerably for all four parameters. This showed that the high correlations between temperature and the model parameters mostly reflected the good separability of the parameter estimates for images that were acquired under frozen and unfrozen conditions, respectively, and that temperature itself, besides the strong dielectric effects related to the differences between frozen and unfrozen conditions, did not explain the variations in the estimated parameters. In the following, the parameters will thus be regarded for frozen and unfrozen conditions separately.

γ_{gr} was between 0.5 and 0.75 when the temperatures were above 0° C. This range was similar to that observed for the ERS-1/2 tandem pairs from spring and fall that covered the Siberian test sites (see Table 7.1). In contrast to the observations in Drezet & Quegan (2006) or Askne & Santoro (2005), γ_{gr} revealed no dependence on the amount of rain, the maximum daily rain rate or the mean rain rate in different periods prior to the ERS tandem acquisitions. In Figure 7.10 (e), γ_{gr} has been plotted as function of the amount of rain in the 10 days prior to the ERS-2 overpasses. The plot shows that γ_{gr} was mostly between 0.5 and 0.6, regardless of the amount of rain that fell in the days before the acquisitions. Even when the weather stations reported rainfall between the tandem acquisitions, which was the case for two tandem pairs from 3-4 October 1997 (the nearest as well as several other weather stations in the area reported about 5 mm rain between the acquisitions), γ_{gr} did not fall below 0.5. In literature, examples can be found where ERS-1/2 tandem coherence dropped to 0.2 to 0.3 when rainfall between the acquisitions occurred (Koskinen et al., 2001; Santoro et al., 2002; Pulliainen et al., 2003). In case of the images from 3-4 October 1997, the decorrelating effect of rain was obviously not as strong. Only in case of one tandem pair from 3-4 October 1997 (the same orbit as the images for which rain occurred between the acquisitions), γ_{gr} was above 0.7 although the nearest weather station (20 km west of the imaged area) reported 4 mm of rain the day before the ERS-1 overpass. Thus, the occurrence or the amount of rain did not explain the differences in the estimates for γ_{gr} .

The estimates for σ_{gr}^0 for the intensity images that were acquired under unfrozen conditions were between -9 and -6.5 dB. The highest values for σ_{gr}^0 of -7 to -6.5 dB were observed for an ERS-1 intensity image from 24 September 1997 and two images from 3 October 1997, all acquired over the Changbai Mountain range. For the two acquisitions from 3 October 1997, the nearest weather stations registered about 6 mm of rain at the last four measurements before the ERS-1 overpass (between 12 and 24 o'clock UTC). Hence, this high backscatter from open ground may be interpreted as short-term response to rain induced wetting of the soils. For the image from 24 September 1997, however, the last rain event occurred on 21st, i.e. 3 days prior to the

tandem acquisitions, which means that the high value for σ_{gr}^0 was not a short-term response to rain.

In case of constant subzero temperatures, the estimates for γ_{gr} varied between 0.7 and 0.85. This range of values was similar to that observed for the coherence images in the Siberian ERS-1/2 tandem dataset that were acquired under frozen conditions and with snow cover on the ground (Table 7.1). The corresponding estimates for σ_{gr}^0 confirmed the expectation of stable frozen ground conditions as they were very low with -14 to -11 dB. For all images, except one, the NSIDC maps (see Chapter 3.5) indicated that snow covered the ground. Hence, the differences in the estimates for γ_{gr} and σ_{gr}^0 were most likely related to differences in the snow properties. As detailed information about the snow cover was not available, these differences could not be further explored.

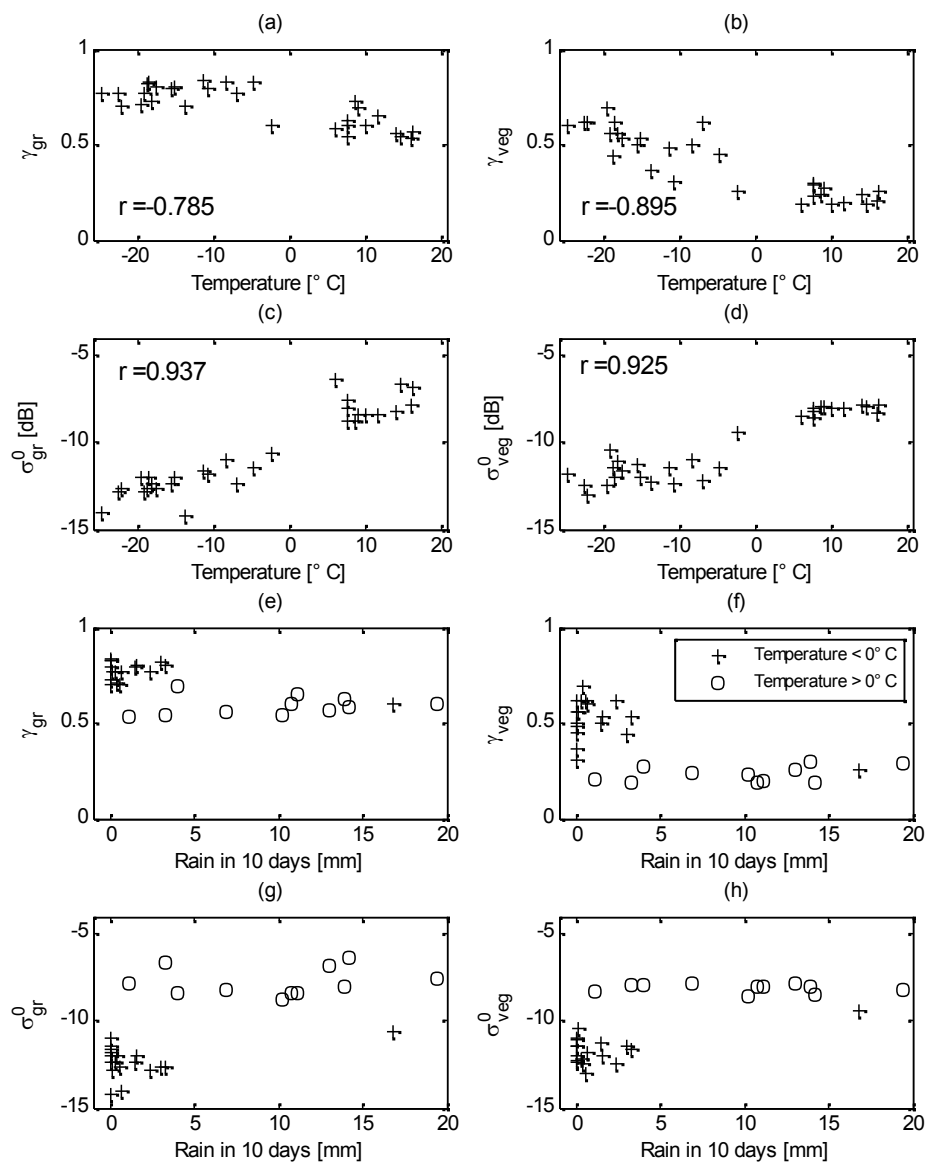


Figure 7.12. IWCM parameters obtained with the aid of VCF versus the temperature at the ERS-1 overpass (plots a-d) and the amount of rain [mm] in the ten days preceding the ERS-2 acquisition (plots e-h). In plots (e-h) '+' denotes the parameters obtained for images that were acquired at temperatures below 0°C and 'o' denotes those acquired at temperatures above the freezing point.

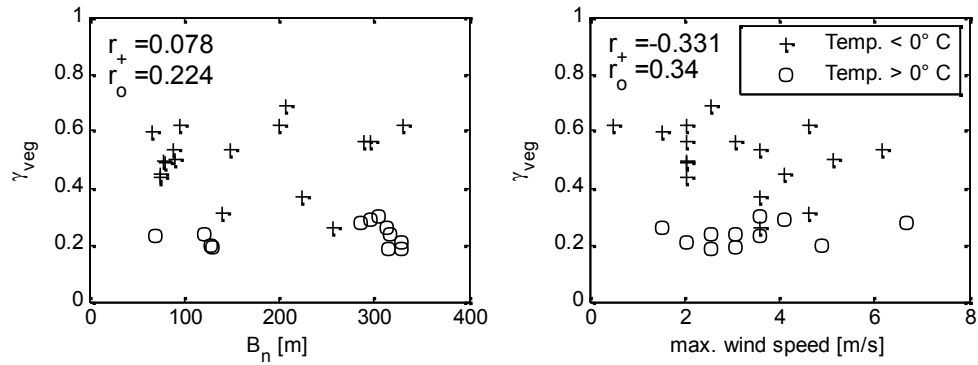


Figure 7.13. γ_{veg} versus baseline (left) and maximum wind speed (right). Tandem pairs that were acquired under frozen and unfrozen conditions are distinguished.

Only in case of one ERS-1/2 tandem pair from 18-19 October 1997, acquired over the northern Daxinganling, some sort of transitional conditions were observed. Here, γ_{gr} was lower than 0.7 although the temperatures at the ERS-1 and ERS-2 overpasses were below 0° C. This tandem pair was acquired during a period with diurnal oscillations of temperature around the freezing point. In addition, the nearest weather station registered 17 mm precipitation (or snowfall) in the ten days prior to the ERS-2 overpass. The temperatures oscillating around the freezing point and the rainfalls indicated overall unstable conditions with a non- or only partially frozen soil surface. This assumption was confirmed when looking at the estimate for σ_{gr}^0 , which was between those observed for the intensity images that were acquired under constantly frozen and unfrozen conditions, respectively.

γ_{veg} was always below 0.3 in case of temperatures above or oscillating around the freezing point, regardless of the baseline length (Figure 7.13, left), the amount of rain in between or prior to the tandem acquisitions (Figure 7.12f) or the wind speeds (Figure 7.13, right). This again resembled the observations that were made for the coherence images from fall and spring that covered the Siberian test sites. Compared to σ_{gr}^0 , the estimates for σ_{veg}^0 varied only in a narrow range between -8 and -9 dB, indicating constantly moist tree canopies throughout the observation period (May 1996, September - October 1997); note that rain was registered for all images in the days prior to the acquisitions. Even in case of 3 images that were acquired in early May over Daxinganling and Xiaoxinganling, σ_{veg}^0 did not exceed a level of -8 dB although, according to the NSIDC snow cover maps, the snow finally melted only one or two weeks before. This may have been a consequence of a mostly low snow cover in the overall dry winter so that the melt of the snow cover did not increase the water availability in the soils as strong as in Central Siberia where backscatter from forest reached a maximum of -7 dB in the period after snowmelt (see Chapter 4.1).

In case of the tandem pairs that were acquired during the winter period between December and March 1996, when temperatures were constantly below the freezing point, the estimates for γ_{veg} varied between 0.3 and 0.65. The corresponding estimates for σ_{veg}^0 were low (-10 to -13 dB), indicating frozen forest canopies. The wind speed should have been one of the main factors, determining the coherence over dense forest canopies (Zebker & Villasenor, 1992; Askne et al., 2003). When comparing the maximum wind speeds in the period of the sensor overpasses (see Chapter 3.5) with the values for γ_{veg} obtained for the winter images, only a weak relationship was found. The correlation was -0.33 and lower than that reported in Askne et al. (2003) who found that

γ_{veg} decreased with increasing wind speed up to ~ 4 m/s for ERS-1/2 tandem coherence images acquired over Swedish boreal forest at temperatures between -5 and 20° C, i.e. with mostly unfrozen tree canopies. As in case of the Chinese dataset the wind speed measurements at the weather stations were made approximately 3 hours before and after the sensor overpasses, it was likely that, due to the high spatial and temporal variability of wind, the wind speeds measured at the weather stations did not represent the wind conditions at the time of the sensor overpasses. Another reason for the low correlation could have been related to the frozen state of the canopies. Frozen canopies allow a deeper penetration of the signals into the canopy so that the backscatter arises from larger and stiffer branches. Furthermore, snow cover on the branches may have dampened the response of the branches to wind induced motions. However, no information about the existence of a snow cover on the branches was available.

No correlation was observed between the length of the perpendicular baseline and γ_{veg} , neither in case of the winter images (Pearson correlation of 0.08) nor in case of the images from spring and fall (Pearson correlation of 0.22). At first sight, this finding gave some confidence in the estimates for γ_{veg} , which is supposed to describe solely the temporal coherence of ideally opaque canopies. A correlation with the baseline length would have indicated problems in the derivation of the parameter, i.e. the compensation of γ_{VCF} for volume decorrelation effects. For the Siberian tandem coherence images from winter, acquired with baselines < 200 m, the IWCM predicted only minor differences in volume decorrelation in the range of stem volumes between 200 and 500 m^3/ha (see Chapter 5.2.3.5). For longer baselines, the IWCM predicted a higher relevance of volume decorrelation related coherence differences in this range of stem volumes. Figure 7.14 illustrates the VCF-based training results (histograms and obtained model line) for one of the long baseline tandem pairs acquired in winter over Northeast China. The model predicts an oscillation of coherence at a stem volume of ~ 200 m^3/ha and an increase for higher stem volumes of ~ 0.2 up to the maximum stem volumes of 400 to 500 m^3/ha that can be found in Northeast China. It is not clear what γ_{VCF} means when volume decorrelation introduces considerable responses in coherence to increasing stem volume (strictly speaking to increasing tree height). γ_{VCF} may strongly depend on the stem volume distribution of the forests that show high tree cover in the VCF maps so that the compensation of γ_{VCF} for the effect of volume decorrelation may require detailed information about the stem volume distribution in the area covered. In fact, in literature there is no example where this oscillation of C-band coherence could clearly be identified. The coherence histogram for high VCF tree cover in Figure 7.14 (middle) appeared to be similar to those histograms obtained for short baseline tandem pairs, e.g. in terms of standard deviation, which indicated no increased variability of coherence for forest with mostly closed canopies. It was, however, striking that the VCF-based estimates for γ_{veg} were always high with about 0.6 for the tandem pairs that were acquired in winter with baselines in the range of 300 to 330 m (Figure 7.13, left), regardless of the wind speeds measured at the nearest weather stations. Hence, without any long baseline tandem pair available that was acquired under stable conditions over one of the test sites, a systematic bias in the VCF-based estimates for γ_{veg} could not be ruled out.

In summary, it can be established that the Northeast Chinese ERS-1/2 tandem dataset can be divided into two main parts:

- 1) In case of constantly frozen conditions in the period between December 1995 and March 1996, γ_{gr} was always above 0.7 and γ_{veg} above 0.3. For the Siberian ERS-1/2

tandem dataset it was observed that under comparable conditions, the modeling of coherence as function of stem volume with the IWCM produced reasonable results and coherence did not saturate up to a stem volume of at least 200 m³/ha. It has, however, to be reminded that high uncertainty is connected to the VCF-based estimates for the IWCM parameter γ_{veg} in case of baselines > 200 m.

2) In case of the tandem pairs from spring and fall, acquired at temperatures above or oscillating around the freezing point, γ_{gr} was mostly below 0.7 and γ_{veg} below 0.3. The weather conditions were constantly rather wet with rainfall occurring prior to most of the tandem acquisitions. Due to the overall wet conditions, the backscatter from ground and dense forest was constantly high. The rain amount hardly explained the differences in coherence, which as well pointed to overall rather wet and unstable conditions independent of singularly rain events. Considering the observations that were made for the Siberian test sites, it could be expected that coherence from fall and spring saturated early and clumped at low levels for stem volumes above ~100 m³/ha. No tandem pair, however, showed a complete loss of ground coherence which means that it should be possible to map at least a few low stem volume classes, e.g. the four stem volume classes (0-20, 20-50, 50-80 and > 80 m³/ha) that were mapped with the first ERS-1/2 tandem data-based forest map of Central Siberia. This map was produced with tandem data that was acquired exclusively in fall 1997 (Schmullius et al., 2001; Balzter et al., 2002; Wagner et al., 2003); some of the tandem pairs that were used in this study belonged to this dataset.

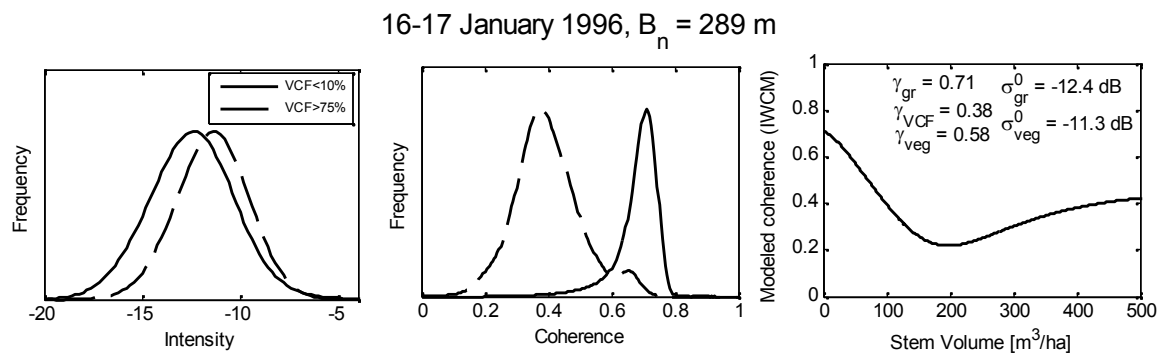


Figure 7.14. Intensity (left) and coherence histograms (middle) for areas with high and low VCF tree cover. Right - IWCM model line with the parameters derived from the histograms.

7.4 Summary

In this chapter, the histogram- and VCF-based model training approaches have been applied to the multi-seasonal ERS-1/2 tandem dataset available for Central Siberia. The automated model parameter estimates were compared to the parameters obtained when fitting the models to the measurements at the test sites for which *in situ* stem volume measurements were available.

The histogram-based approach was not found suited for large-area stem volume mapping with a multi-seasonal ERS-1/2 tandem dataset. First of all, the identification of dense forest coherence properties relied upon the dominance of dense forest in the area covered by the ERS-1/2 tandem images. This was given for Central Siberia, where the

histogram-based estimation of dense forest coherence performed well, but not for Northeast China. Secondly, the approach relied upon a linear relationship between dense forest and forest floor coherence. This assumption cannot be considered physically meaningful as different mechanisms determine the coherence over open ground and forest.

With the aid of VCF, both constraints in the histogram-based model training were obviated as 1) the ground contributions in the coherence and intensity measurements were determined independently and 2) the model parameters related to the dense forest coherence and backscatter properties were only determined if dense forest existed in the area covered by the particular ERS-1/2 tandem pairs. The model training was first tested for the ERS-1/2 tandem pairs that covered the Siberian test sites. The IWCM was only used for coherence modeling in case of the tandem pairs that were acquired under stable conditions with high(er) ground and dense forest coherence (see Chapter 5.2.3.4). In all other cases, the empirical model in Equation (5.1) was used. Although not required for the empirical model, the model in Equation (5.3), relating intensity to stem volume, was trained for the intensity images that were acquired under unstable imaging conditions.

When testing the VCF-based model training for each ERS-1/2 tandem pair that covered the Siberian test sites, the results drew a heterogeneous picture. The overall agreement between the inventory data- and VCF-based parameter estimates was generally better for the tandem pairs that were acquired in winter under frozen conditions. Still, differences between the inventory data- and VCF-based parameter estimates could be observed for coherence and intensity images from all seasons. As the VCF-based model training was done on an ERS frame basis, it was assumed that spatial variations of the environmental and meteorological imaging conditions within the area covered by an ERS-1/2 tandem pair were responsible for, or at least contributed to, the differences between the inventory data- and VCF-based parameter estimates as the former reflected only the much smaller areas of the test sites. When accounting for the possibility of variations in the environmental and meteorological imaging conditions by carrying out the VCF-based training restricted to the area of the test sites, the agreement between the VCF- and inventory data-based model parameter estimates improved. After having minimized the effect of spatial variations in the imaging conditions, a mostly good estimation of the parameters γ_{veg} , γ_{∞} and σ_{veg}^0 could be stated. An overall good agreement between the models trained with the inventory data and VCF was achieved when assuming that the forests with maximum tree cover in the VCF maps represented a stem volume of $> 250 \text{ m}^3/\text{ha}$. When considering the results of the model sensitivity analysis in Chapter 5.2.3.5, the overall low sensitivity to V_{eq} should have been due to the fact that the coherence measurements over forests with maximum VCF tree cover were mostly saturated (i.e. low ground contributions and minor differences in volume decorrelation in the corresponding range of stem volumes).

The estimates for γ_{gr} from inventory data and VCF did not show any systematic differences when restricting the VCF-based model training to the area of the particular test site. The estimation of σ_{gr}^0 appeared to be more critical. With VCF, the forest floor backscatter level was overestimated for about 1 to 2 dB in case of several images that were acquired under unfrozen and wet conditions over the Bolshe NE and Bolshe NW test sites. As C-band intensity strongly depends on soil moisture, an explanation could have been that systematic differences in soil moisture between forest floor and open areas (i.e. all areas with VCF $< 10 \%$), e.g. due to evapotranspiration and rainfall interception, were responsible for the failed parameter estimation with VCF. Also

differing surface roughness and herbaceous or shrub cover may have contributed to the different σ_{gr}^0 estimates from inventory data and VCF as areas with low tree cover comprise a wide range of land cover types. In case of the ERS-1 intensity images that were acquired under frozen conditions in winter, the VCF-based estimates for σ_{gr}^0 were better, probably because the frozen snow covered ground diminished a lot of the potential differences in backscatter that may arise between typical forest floor (which is not necessarily uniform as well) and all areas with low tree cover cover like grassland, cropland, wetland, etc. Anyway, in Chapter 5.2.3.4 it was shown that there was no advantage in using the IWCM instead of the simple empirical model in Equation (5.1) in case of the tandem pairs that were acquired under unfrozen wet conditions. Thus, estimates for the backscatter contributions from forest floor and canopy were not required for the ‘rough’ modeling of the trend of coherence as function of stem volume.

The effect of spatial variations of the environmental and meteorological imaging conditions on the model parameter estimates showed that a model training should be carried out as local as possible, e.g. with a moving window running over the image. This, however, is limited by the requirement for a sufficient number of VCF pixels indicating low and maximum tree cover, i.e. the parameters always have to be estimated over somewhat larger ‘landscape-scale’ areas. Furthermore, when the spatial variations are tied to landscape features (as for instance the peatland in case of the ERS-1/2 tandem pairs from fall that covered the Bolshe NE test site) detailed knowledge about the local landscape would be required, contradicting the intended full automation of the model training. The adaptivity of the VCF-based model training approach to sub-frame variations of the imaging conditions represents one of the points where the algorithm, as outlined in this thesis, can be improved in the future.

Due to the lack of reliable ground data, the VCF-based IWCM parameter estimates for the ERS-1/2 tandem dataset of Northeast China could only be interpreted with respect to the prevailing weather conditions. Although the comparison of the VCF-based IWCM parameter estimates with the temperature, precipitation and wind speed measurements at the weather stations was itself no proof for the accuracy of the estimates, it could be stated that the main patterns with respect to the prevailing weather conditions agreed with those observed for the Siberian ERS-1/2 tandem dataset. None of the coherence images showed a complete loss of ground coherence due to rainfall or snow melt between the tandem acquisitions, indicating that for all tandem pairs the classification of at least a few low stem volume classes, like those mapped in the SIBERIA project (Schmullius et al., 2001; Balzter et al., 2002; Wagner et al., 2003), should be possible with reasonable accuracy.

Chapter 8 - Large-area forest stem volume mapping

In the last chapters, a VCF-based model training procedure was developed and tested. In this chapter, it is discussed how the trained models can be used to map forest stem volume over large areas. At the end of this chapter, a scheme for large-area mapping of forest stem volume with ERS-1/2 tandem coherence is set up, merging the outcomes of the investigations in this thesis, and applied to the ERS-1/2 tandem data available for Northeast China.

8.1 Stem volume retrieval

Once the unknown coefficients of the IWCM, respectively the empirical model, have been determined, the models can be inverted to estimate stem volume from coherence. A widely applied measure for the retrieval accuracy is the root mean square error RMSE, which can be calculated as follows:

$$RMSE = \sqrt{\frac{1}{N_{test}} \sum_{i=1}^{N_{test}} (V_i - V_i^{gt})^2} \quad (8.1)$$

with N_{test} being the number of stands in the *in situ* test dataset, V_i the estimated stem volume at stand i and V_i^{gt} the corresponding stem volume in the inventory data. The RMSE depends on the forest properties, i.e. the total stem volume range and distribution, and is only of limited use when comparing the retrieval results for different forest sites. That is why, the relative RMSE is often given as well. The relative RMSE is defined as the ratio of the RMSE to the average stem volume in the test dataset (multiplied with 100 to get percent values).

Santoro et al. (2007) already discussed the retrieval accuracy possible with the Siberian ERS-1/2 tandem coherence images that were used in this study. They reported relative RMSEs in the 20 to 25 % range for large homogenous forest stands with high relative stocking for the images that were acquired under stable frozen conditions. The tandem pairs that were acquired with baselines > 100 m and under windy conditions generally allowed the most accurate retrieval but also the image from 14-15 January 1996, acquired with short baseline and low wind speeds, reached a retrieval accuracy in the 25 % range at the test site Chunksy N. When considering all stands regardless of their relative stocking or size, the relative RMSEs were lower for all images (> 30 %). The retrieval accuracies achieved with the images that were acquired under unstable conditions in spring and fall at Bolshe-Murtinsky and Chunksy were low (Santoro et al., 2004; Eriksson, 2004) and in a range no longer of interest for forestry applications. A weighted multitemporal combination of the single image retrieval results, after fitting the simple empirical model in Equation (5.1) to the measurements at the test sites Bolshe NE (six ERS-1/2 tandem coherence images including one from winter) and Bolshe NW (4 coherence images, no winter image), resulted in relative RMSEs of 43 % and 36 % for stands larger 2 ha (Santoro et al., 2004).

Similar to what has been observed at the Siberian test sites, several publications reported a limited potential of single ERS-1/2 tandem coherence images for stem volume retrieval. For instance, in Pulliainen et al. (2003) a relative RMSE better than 50

% was only achieved for stands >1.5 ha with a multitemporal retrieval approach using two winter coherence images for the test site Tuusula in southern Finland. A relative RMSE of 26 % was achieved for the 37 largest out of 210 stands when the retrieval results, based on the inversion of the IWCM, for eight coherence images were combined in a weighted manner (Askne & Santoro, 2005). In Askne & Santoro (2007b), the retrieval accuracy for Tuusula was found to further improve to 20 % when a higher number of optimal winter images was available. The improvement of the retrieval accuracy with a multitemporal combination generally depended on the number of coherence images acquired under optimal conditions. The integration of images that were acquired under non-optimal conditions would not improve the retrieval accuracy. The best results were yet reported for a highly managed boreal forest site in Sweden (Fransson et al., 2001; Santoro et al., 2002; Askne et al., 2003) where for 21 forest stands (2-14 ha large) with a maximum stem volume of 335 m³/ha (average of 135 m³/ha) a RMSE of 10 m³/ha was achieved when combining the retrieval results from four optimal ERS-1/2 tandem coherence images in a weighted manner (Santoro et al., 2002). The best retrieval result for a single ERS-1/2 tandem coherence image was achieved with a coherence image that was acquired under stable frozen conditions with a baseline of 218 m and wind speeds of ~5 m/s. For this image the RMSE was 21 m³/ha.

The mentioned studies showed that stem volume retrieval with an accuracy of interest for forestry applications (relative RMSE < 20 %) requires a multitemporal stack of ERS-1/2 tandem pairs acquired under optimal weather conditions; preferably with baselines in the 100 to 250 m range. As with the ERS-1/2 tandem dataset available for Northeast China most areas were only covered once and about one third of the tandem pairs were acquired under unstable imaging conditions in spring and fall, large-area stem volume retrieval could not be expected to reach acceptable accuracies.

8.2 Forest stem volume mapping

With the requirements for a successful large-area stem volume retrieval lacking, it was tested if the discrimination of the stem volume classes that were used for the SIBERIA-1 map (Schmullius et al., 2001; Wagner et al., 2003) was possible with sufficient accuracy. These classes would at least allow the identification of the succession stages of young regrowing stands, i.e. forests growing after stand-replacing fires or clear-cutting. For this, the models that were trained with the aid of VCF on a frame-by-frame basis were inverted for stem volume. In case the empirical model in Equation (5.1) was used, the calculation of stem volume for each coherence pixel was straightforward:

$$V = -\frac{1}{V_\gamma} \ln \left(\frac{\gamma_\infty - \gamma_{for}}{\gamma_\infty - \gamma_0} \right) \quad (8.2)$$

As the volume decorrelation term in the IWCM is a complex number, the inversion of the IWCM requires numerical methods. An iterative procedure was utilized. The stem volume was estimated from the coherence images by modeling coherence for stem volumes between 0 m³/ha and a defined maximum stem volume and selecting for each pixel the stem volume for which the difference between modeled and measured coherence was minimized. In case of coherence measurements higher than γ_{gr} , the model could not be used to estimate the stem volume. As a coherence higher than γ_{gr} indicates unforested terrain, a stem volume of 0 m³/ha was assigned to these

measurements (see Figure 8.1). Likewise, no direct estimation of stem volume was possible for coherence measurements lower than the lowest modeled coherence in the range of stem volumes considered. In this case, a fixed stem volume has to be assigned; typically the maximum stem volume that can be found in the area. As only stem volume classes up to 80 m³/ha were considered, any stem volume above 80 m³/ha could be assigned without any effect on the classification accuracy. The IWCM may predict an oscillation of coherence for longer baselines (see example in Figure 8.1). An oscillation in the range of existing stem volumes means that the inversion becomes ambiguous. In this case the lower possible stem volume was selected; note that this could be critical in case of the longest baselines when the IWCM predicts an oscillation of coherence at stem volumes of about 200 m³/ha (see Figure 7.14). After inversion, the retrieved stem volumes were grouped into the four stem volume classes 0-20, 20-50, 50-80 and > 80 m³/ha.

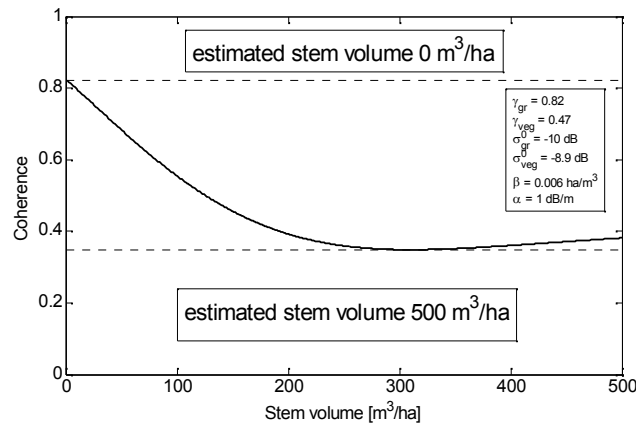


Figure 8.1. Coherence modeled as function of stem volume with the IWCM (example). The horizontal lines indicate the maximum and minimum modeled coherence.

Due to the lack of reliable ground data for Northeast China, no accuracy assessment could be carried out here. Accuracy statistics could only be generated for the coherence images covering the Central Siberian test sites. Following accuracy measures were computed: the overall accuracy and the κ coefficient, which also accounts for pure chance agreement between the classified image and the reference map. Both accuracy measures can be derived from the confusion matrix, i.e. the cross-tabulation of the classes in the produced and the reference map (Foody et al., 2002). In a confusion matrix, the main diagonal numbers denote the class agreement whereas the off-diagonal elements contain the disagreeing class assignments. From the confusion matrix, the per-class Producer and User accuracies can be derived. The Producer accuracy specifies which fraction of a class, as given in the reference map, was assigned to the same class by the classifier. The User accuracy denotes which fraction of a class in the classification result actually falls into the corresponding class in the reference map. The kappa coefficient κ can be calculated from the confusion matrix with elements p_{jk} (k denotes the column and j the row) as follows (Cohen et al., 1960 as quoted in Balzter et al., 2002):

$$\kappa = \frac{p_0 - p_e}{1 - p_e} \quad p_0 = \frac{1}{N} \sum_{j=1}^n p_{jj} \quad p_e = \frac{1}{N^2} \sum_{j=1}^n \sum_{k=1}^n p_{j \cdot} \cdot p_{\cdot k} \quad (8.3)$$

where p_0 denotes the overall accuracy, i.e. the fraction of correctly classified pixels representing the main diagonal p_{jj} in the confusion matrix, and p_e the expected chance agreement with p_j . and $p_{\cdot k}$ being the column and row sums in the confusion matrix. N is the total number of pixels and n the number of classes. κ can take values between 0 and 1 with 0 indicating pure chance and 1 perfect agreement. κ does not account for the seriousness of a misclassification. The seriousness of a misclassification can be accounted for with the weighted kappa coefficient κ_w (Cohen, 1968 as quoted in Balzter et al., 2002):

$$\kappa_w = \frac{\sum_{j=1}^n \sum_{k=1}^n w_{jk} p_{jk} - \sum_{j=1}^n \sum_{k=1}^n w_{jk} p_{j\cdot} p_{\cdot k}}{1 - \sum_{j=1}^n \sum_{k=1}^n w_{jk} p_{j\cdot} p_{\cdot k}} \quad w_{jk} = 1 - \frac{(j-k)^2}{(n-1)^2} \quad (8.4)$$

where w_{jk} represents the weight for each element in the confusion matrix. The weighting factor accounts for the severeness of the misclassification. For instance, when a pixel that represents a forest with 30 m³/ha stem volume has been classified into the classes ‘50-80 m³/ha’ or ‘>80 m³/ha’, the error connected to the latter class assignment is given more weight.

Table 8.1. Overall classification accuracy, Producer / User Accuracies [%] and kappa statistics obtained with the VCF-based training for the ERS-1/2 tandem coherence images covering the Siberian test sites.

Test site & ERS-1/2 tandem pair	Producer / User Accuracy [%] of the stem volume classes [m ³ /ha]				Overall. Accuracy	κ & κ_w
	0-20	20-50	50-80	>80		
CH N 29-30 Dec. 95	76.19/ 93.20	38.48/ 24.28	18.25/ 1.20	93.76/ 93.92	81.30	.69/.88
CH N 14-15 Jan. 96	77.27/ 88.23	17.29/ 22.13	10.49/ 1.29	90.43/ 80.15	77.57	.61/.75
CH E 14-15 Jan. 96	59.49/ 89.67	42.44/ 20.07	24.15/ 4.30	89.26/ 87.70	68.13	.52/.80
BM NE 01-02 Jan. 96	31.72/ 72.63	29.59/ 34.22	37.68/ 23.69	96.42/ 80.28	64.73	.44/.70
PM E 09-10 Oct. 97	18.76/ 83.67	40.56/ 20.72	61.75/ 35.31	91.99/ 79.78	56.67	.42/.65
BM NE 22-23 Sep. 97	1.69/ 97.72	14.98/ 25.38	34.88/ 11.52	95.20/ 75.57	55.50	.28/.46
BM NE 27-28 Oct. 97	0.62/ 53.33	28.33/ 28.80	34.02/ 12.72	90.42/ 77.31	54.31	.29/.51
BM NE 25-26 Sep. 97	14.54/ 97.84	22.76/ 13.41	52.89/ 9.10	81.58/ 69.12	39.73	.23/.53
BM NW 25-26 Sep. 97	79.85/ 94.94	69.00/ 32.44	37.21/ 14.84	79.99/ 96.79	79.80	.61/.86
BM NE 28-29 May 98	17.87/ 99.72	34.43/ 16.89	50.00/ 7.39	45.78/ 68.67	31.83	.21/.50
BM NW 28-29 May 98	77.35/ 91.91	46.48/ 23.10	27.83/ 6.67	57.19/ 92.87	71.08	.53/.84

Table 8.2. Confusion matrix for the classification with the ERS-1/2 tandem acquisition from 29-30 December 1995 at Chunsky N (number of pixels).

Classified	Forest Inventory data				
	0-20 m ³ /ha	20-50 m ³ /ha	50-80 m ³ /ha	>80 m ³ /ha	Total
0-20 m ³ /ha	14654	996	10	63	15723
20-50 m ³ /ha	3012	1049	50	210	4321
50-80 m ³ /ha	777	434	25	847	2083
>80 m ³ /ha	791	247	52	16834	17924
Total	19234	2726	137	17954	40051

For the accuracy assessment of the produced forest stem volume maps, the rasterized and edge-eroded inventory stem volume maps were used as reference. Slopes steeper than 10° plus all pixels less than four pixels away from steep slopes were masked (cf. Chapter 6.2). Erroneous polygons, either in terms of a clear misregistration between the stand borders in the GIS data and the borders visible in the coherence images or in terms of a failed inventory update (see Chapter 4.1), were excluded.

Table 8.1 lists the Producer, User and overall accuracies plus the κ and κ_w coefficients for the produced stem volume maps. For the sake of clarity, the full confusion matrix has only been attached for one example (Table 8.2). The overall accuracies varied between 31 and 81 %, κ between 0.21 and 0.69 and κ_w between 0.46 and 0.88. κ_w was always higher than κ . The Producer accuracies for the class ‘0-20 m³/ha’ varied in a wide range between 0.6 and 80 %. The User accuracies were always higher and between 53 and 100 %. The Producer accuracies of the class ‘>80 m³/ha’ were between 46 and 96 % and the User accuracies between 68 and 98 %. The Producer and User accuracies of the intermediate classes ‘20-50 m³/ha’ and ‘50-80 m³/ha’ were mostly below 50 %. The highest overall accuracies of ~80 % ($\kappa > 0.6$; $\kappa_w > 0.85$) were achieved for the coherence images from 29-30 December 1995 at Chunsky N and 25-26 September 1997 at Bolshe NW. This showed that similar accuracies could be achieved with images that were acquired under frozen and unfrozen conditions. With 77.6 % the overall accuracy was slightly lower in case of the image from 14-15 January 1996 at Chunsky N (κ 0.61, κ_w 0.75). The lowest accuracies were achieved for the images from fall and spring that covered the test site Bolshe NE. The overall accuracy was between 31 and 56 %, κ between 0.2 and 0.3 and κ_w between 0.46 and 0.53. Also for the tandem pair from 9-10 October 1997, an overall accuracy of only 57 % was achieved.

The accuracies in Table 8.1 could not be considered sufficient for practical applications. In particular, the very low accuracies of the intermediate stem volume classes suggested a very limited potential of ERS-1/2 tandem coherence for the mapping of the selected stem volume classes. When considering that by far the most stands at the test sites fell into the ‘0-20 m³/ha’ and ‘>80 m³/ha’ stem volume classes, the achieved classification accuracies appeared to reflect mainly the good forest/non-forest contrast in the coherence images. The misclassifications in case of the intermediate classes hardly affected the overall accuracy simply because very few stands had stem volumes between 20 and 80 m³/ha according to the inventory data (see Table 8.2). However, in all cases κ_w was clearly higher than κ , which means that the main confusion occurred between neighboring classes. Thus, the uncertainty in the inventory data may have strongly affected the achieved accuracies.

Following issues may have affected the accuracy (respectively the agreement of the classified maps and the inventory data):

- 1) Non-optimal parameter estimates of the VCF-based model training
- 2) Errors in the inventory data
- 3) Forest structural diversity

In Chapter 7.2, it was shown that in several cases the models that were trained with the aid of VCF on a frame basis did not optimally reflect the trend of the coherence measurements as function of stem volume at the test sites, mostly because of spatial variations of the environmental and meteorological imaging conditions within the area covered by the ERS-1/2 tandem pairs. In order to assess the impact of a non-optimal model fit, the models that were trained with the aid of the inventory data were inverted and the estimated stem volumes were grouped into the four stem volume classes. Table 8.3 shows the agreement of these stem volume maps and the inventory data for a number of images and test sites. Clear improvements of the overall accuracy were observed in case of the images that covered the Bolshe NE test site. In particular, the Producer accuracies of the lowest stem volume class improved and reached now at least 60 %. The accuracies of the other classes showed only minor changes; only in case of the image from 28-29 May 1998 a clearly higher Producer accuracy was achieved for the class '>80 m³/ha'. The improved accuracy of the lowest stem volume class was related to the fact that with the VCF-based model training, γ_{gr} (respectively γ_0 when the empirical model was used) overestimated the forest floor coherence at the Bolshe NE test site respectively reflected the ground coherence in other regions of the imaged area (see Chapter 7.2). This showed that the classification of the lowest stem volume class strongly depended on the uniformity of the ground conditions within the area covered by an ERS-1/2 tandem pair. The modeled coherence difference between 0 and 20 m³/ha stem volume was always between 0.05 and 0.15. Within-frame variations of the coherence at the ground of the same order caused the Producer accuracy of this class to drop to very low levels, at least in parts of the classified area; note that the User accuracy was always higher as VCF tended to overestimate γ_{gr}/γ_0 .

Table 8.3. Overall classification accuracy, Producer / User Accuracies [%] and kappa statistics obtained when inverting the models that were fitted to the measurements at the Siberian test sites and summarizing the estimated stem volumes to the four stem volume classes 0-20, 20-50, 50-80 and > 80 m³/ha.

Test site & ERS-1/2 tandem pair	Producer / User Accuracy [%] of the stem volume classes [m ³ /ha]				Overall Accuracy	κ & κ_w
	0-20	20-50	50-80	>80		
CH N 29-30 Dec. 95	80.9 94.1	26.6 23.6	12.1 1.3	96.3 85.3	82.3	.68 / .84
BM NE 01-02 Jan. 96	75.2 87.6	28.1 36.6	29.9 18.3	88.2 71.5	71.5	.55 / .71
BM NE 22-23 Sep. 97	72.4 85.9	34.8 28.7	23.8 14.2	84.1 77.7	69.3	.52 / .74
BM NE 25-26 Sep. 97	60.9 87.5	27.8 27.0	21.9 8.2	81.1 68.7	60.3	.43 / .67
BM NW 25-26 Sep. 97	86.0 92.5	49.7 35.1	28.0 28.4	93.3 94.1	84.0	.73 / .92
Bolshe NW 28-29 May 98	89.8 87.3	32.0 19.8	14.8 7.5	74.6 93.1	72.8	.57 / .87

Even when inverting the models that were ‘optimally’ fitted to the conditions at the test sites, the accuracy of the intermediate stem volume classes was low. This observation was in line with what has been reported in Balzter et al. (2002), Gaveau et al. (2003), Eriksson (2004) and Tansey et al. (2004). They all tested the classification of the same stem volume classes with ERS-1/2 tandem coherence for several of the SIBERIA project test sites, i.e. they all used the same inventory database for the accuracy assessment. In contrast, an independent ground survey, carried out for the SIBERIA stem volume map, resulted in class accuracies above 80 %, even for the intermediate stem volume classes, and a κ and κ_w of 0.88 and 0.94, respectively (Balzter et al., 2002). These high accuracies pointed out the importance of using an up-to-date reference dataset for a meaningful accuracy assessment. Motivated by the obvious discrepancies between the accuracy statistics obtained with the inventory data and the ground survey, Balzter et al. (2002) further explored the relevance of the uncertainty in the inventory data. An uncertainty model was set up that described the stem volume in the inventory data, V^{gt} , as center of a fuzzy interval (Balzter et al., 2002). The true stem volume was assumed to lie in a Gaussian distributed interval between $V^{gt}-2SD$ and $V^{gt}+2SD$ with 95 % certainty. SD denoted the presumed standard error of the inventory stem volume measurements. Based on this uncertainty model, a pixel was considered correctly classified when the fuzzy interval overlapped with the stem volume interval of the class the pixel was assigned to. When applying this uncertainty model to a pooled confusion matrix, comprising the classification results for seven forest compartments (Bolshe, Chunsky and Primorsky were not included), a non-linear increase of the overall accuracy, κ and κ_w was observed. For an uncertainty, SD, of 20 m³/ha, which was considered a realistic description of the inventory data accuracy, a κ of 0.72 and a κ_w of 0.86 was obtained. When not accounting for the uncertainty in the inventory data, i.e. SD was set to 0 m³/ha, κ and κ_w were 0.43 and 0.72, respectively.

When applying the uncertainty model to account for the uncertainty in the inventory data to the stem volume maps obtained with the VCF-based approach, a non-linear increase of the overall accuracy and κ could be observed as well. κ_w showed only minor improvements, basically because it already accounted for the fuzziness in the inventory data. For the ERS-1/2 tandem coherence images from winter, κ improved for about 0.2 to 0.3 when allowing for an uncertainty of 20 m³/ha. For this level of uncertainty, all three winter acquisitions reached a κ of at least 0.7 (Figure 8.2, right). In case of the ERS-1/2 tandem coherence images from fall and spring, comparable accuracies with a κ of at least 0.7 were only reached for the acquisitions from 25-26 September 1997 at Bolshe NW and from 9-10 October 1997 at Primorsky E (Figure 8.2, left). In case of the coherence images acquired over Bolshe NE, the accuracy was lower with a κ of about 0.5. This was clearly a consequence of the overestimation of γ_{gr}/γ_0 with the VCF-based training approach (see Chapter 7.2). Thus, besides the images that were acquired in fall over the Bolshe NE test site, the accuracies achieved with the VCF-based approach were comparable to that observed for the accuracy assessment of the SIBERIA stem volume map; note that no pooled confusion matrix was created as all test sites were covered by more than one ERS-1/2 tandem pair so that any selection of images/test sites for a pooled confusion matrix (e.g. those with the best results) would have tampered the accuracy statistics.

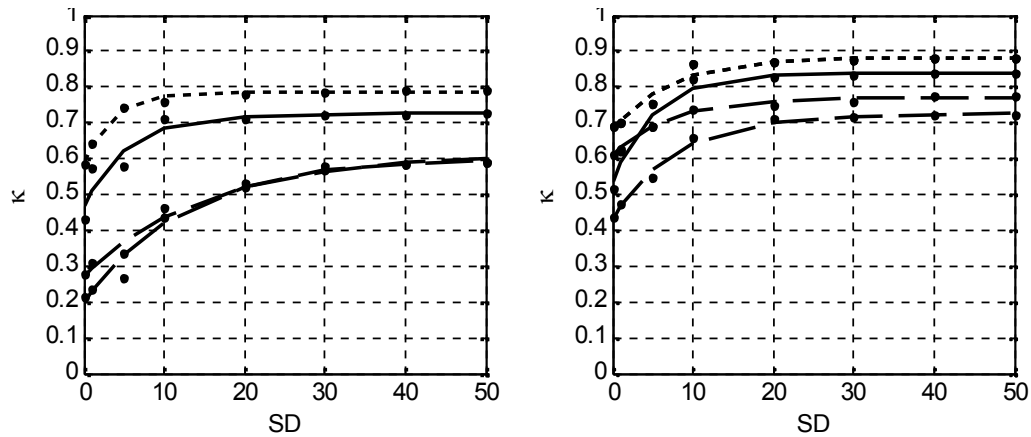


Figure 8.2. Kappa coefficient as function of the uncertainty SD in the inventory data for the tandem pairs from fall 1997 covering Bolshe NE, Bolshe NW and Primorsky E (left) and the tandem pairs from winter 1995/96 covering Bolshe NE, Chunsky N and Chunsky E (right).

In Santoro et al. (2007), a higher stem volume retrieval accuracy has been reported for stands with high relative stocking when inverting the IWCM, trained with the inventory data at the test sites in Bolshe and Chunsky, for the coherence images from 29-30 December 1995, 14-15 January 1996 and 1-2 January 1996. Similarly, the accuracy of the produced stem volume maps was found to depend on relative stocking. In Figure 8.3, it can be seen for the classified coherence images from 1-2 January 1996 (Bolshe NE) and 29-30 December 1995 (Chunsky N) that κ was about 0.2 when only considering stands with less than 50 % relative stocking. Even when allowing for 20 m³/ha uncertainty in the inventory data, κ only reached a level of 0.5 to 0.6.

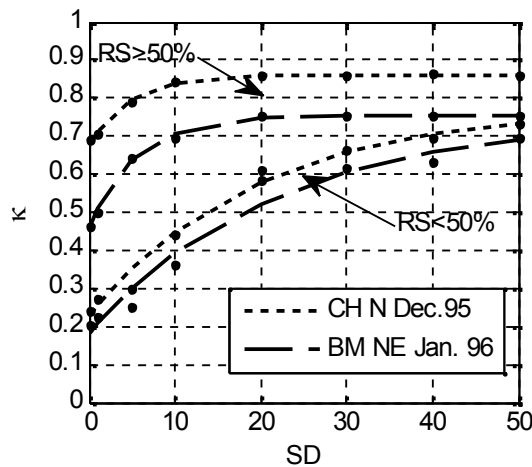


Figure 8.3. Kappa coefficient as function of the uncertainty SD in the inventory data for stands with RS > 50 % and RS < 50 %.

The lower map accuracy for stands with low relative stocking may have been due to 1) a less pronounced link between area-fill factor and stem volume as forests with low relative stocking are assumed to have a more heterogeneous canopy structure and 2) a higher impact of coherence variations at the forest floor as at a given stem volume, stands with low relative stocking are less dense than stands with high relative stocking

(see Chapter 3.3). The lower density may coincide with an overall more open canopy structure, resulting in higher (spatially more variable) ground contributions in the measurements. These assumptions, however, need to be confirmed with ground measurements of the area-fill factor for forests with different relative stocking. As a higher proportion of forests in Northeast China should grow in an understocked state (see Chapter 3.3), it can be expected that the mapping of the four low stem volume classes does not reach accuracies in the range of those achieved for Siberia.

8.3 Creation of a forest stem volume map for Northeast China

For the creation of a forest stem volume map of Northeast China, following scheme was applied:

1) VCF-based model training:

The VCF-based model training was carried out on a frame-by-frame basis. Areas where topography was likely to affect the training were excluded according to Chapter 6.2. The estimation of γ_{gr} and σ_{gr}^0 was done by calculating the mode of coherence and intensity in areas with low VCF tree cover, i.e. for the lowest two percent of the VCF pixels (always < 10 %). The parameters γ_{VCF} and σ_{VCF}^0 were calculated with the mode of the coherence and intensity measurements in areas with high tree cover; only when the 98th percentile of VCF tree cover was at least 70 % (the case for 87 tandem pairs). If this precondition was not fulfilled, a neighbor frame was integrated into the training. When even in this case no estimation of γ_{VCF} and σ_{VCF}^0 was possible, the parameters obtained for the closest frame in the same orbit, for which model training was possible, were used. Five of the orbits almost exclusively covered unforested areas in Inner Mongolia and the Northeast China Plain so that for none of the frames a determination γ_{VCF} and σ_{VCF}^0 was possible. In these cases, some rough estimates for γ_{veg} and σ_{veg}^0 were made based on the relationship with temperature observed in Figure 7.12 (b) & (d). The model parameters γ_{veg} and σ_{veg}^0 were derived from γ_{VCF} and σ_{VCF}^0 by compensating for residual ground and, only in case of γ_{veg} , volume decorrelation contributions according to Chapter 5.2.3.5. The forest transmissivity parameter β was set to 0.006 ha/m³. V_{eq} was set to 400 m³/ha. The decision for the usage of the IWCM respectively the empirical model was straightforward (see Chapter 7.3). When the initial estimates for γ_{gr} and γ_{veg} were lower than 0.7 and 0.3, respectively, the IWCM model training results were rejected and the empirical model was trained instead, using a fixed value for the coefficient V_γ of 0.015 ha/m³.

2) Model inversion and class assignment:

The model inversion was done as described in Chapter 8.2. The retrieved stem volumes were aggregated to the four stem volume classes: 0-20, 20-50, 50-80 and > 80 m³/ha. Water surfaces could not be classified by means of coherence or intensity as the signatures varied unpredictably between the tandem pairs. That is why the SRTM Water Body product was used.

3) Masking of topography:

With the topographic masking procedure applied for the VCF-based model training (see Chapter 6.3), large forest areas were not considered for model training as large fractions of the forests in Northeast China grow on mountainous terrain. However, different levels of uncertainty in the measurements due to topographic effects could be expected. For instance, in case of tandem pairs that were acquired with baselines shorter than 200

m it was observed for slopes tilted away from the sensor with $>10^\circ$ that there was forest related information like visible clear-cuts. This observation motivated the application of a different masking procedure for the production of the forest stem volume map. In the map, only those pixels located in areas where the layover map indicated layover or those on slopes steeper than 10° and facing the sensor were masked. The masked areas were widened for four pixels to account for the spatial coherence estimation principle. For all other areas in the produced stem volume map of Northeast China, a quality flag map was produced, which indicated the risk for low class accuracy because of topographic distortions in the coherence images. The quality flag map distinguished three levels of map quality. Level 1 was assigned to all areas when the perpendicular baseline was shorter than 100 m. Level 2 was assigned to all areas located on slopes steeper than 10° and tilted away from the sensor, plus the 4 surrounding pixels, when the baseline was between 100 and 200 m. For these areas, the forest/non-forest information in the stem volume map could be useful but the observed influence of spatial decorrelation (Chapter 6.2) questioned the stem volume classes. In case of baselines above 200 m, Level 3 was assigned to each pixel located on a slope steeper than 10° , or up to four pixels away from a slope steeper than 10° , as with these baselines topography-induced decorrelation reaches magnitudes comparable to the forest/non-forest contrast in coherence.

4) Mosaicking of the classified images:

For the production of the forest stem volume map, 223 coherence images were classified and mosaicked. Some areas were covered by more than one tandem pair. In such a case, a multitemporal combination of the stem volume estimates from each image may have increased the accuracy of the class assignment. For the Siberian test sites it was tested if the combination of the single image retrieval results according to the procedure described in Santoro et al. (2002), before aggregating the volume estimates into the four desired classes, improved the classification. However, no improvements were achieved regardless of the combination of images, e.g. two winter images or one from fall and one from winter. The accuracies were always between those achieved for the better and the worse of the images combined. That is why, the stem volume maps created with coherence images that were acquired under frozen conditions and/or with a shorter baseline were selected when more than one coherence image was available as in case of frozen conditions spatial variations of the imaging conditions and in case of short baselines the effects of topography could be expected to be less severe.

Figure 8.4 shows the final forest stem volume map. The outstanding characteristic of the map is that there are almost no border effects visible between adjacent orbits that were acquired under different environmental and meteorological conditions, being a good indicator for the spatial consistence of the stem volume classes. The accuracy of the map will be assessed in the frame of the ESA-MOST (Ministry of Science and Technology, China) DRAGON-II project. Right now, it represents an unvalidated product.

In Table 8.4, the proportions of each assigned quality level in the stem volume map have been listed. Almost 10 % of the area in the map had to be masked because of the strong topographic effects on steep slopes $>10^\circ$ facing the sensor. Approximately 23 % of the map were assigned to the quality levels 2 and 3 where the stem volume classes could be expected to be distorted. This relatively high proportion of pixels that were assigned to quality levels 2 and 3 points out the high importance of the orbit planning as the fraction of pixels with a coherence affected by topography could be reduced when

the baselines were kept short (< 100 m); note that this contradicts the recommendations for an optimal retrieval for which baselines in the 150 to 250 m range are preferable.

Table 8.4. Statistics of the Quality Flag Map for the forest stem volume map of Northeast China.

Class	Count	Area [km ²]	% of total map area
Quality Level 1	377413392	943533	66.85
Quality Level 2	10107306	25268	1.79
Quality Level 3	121036118	302590	21.44
Masked	56046161	140115	9.92

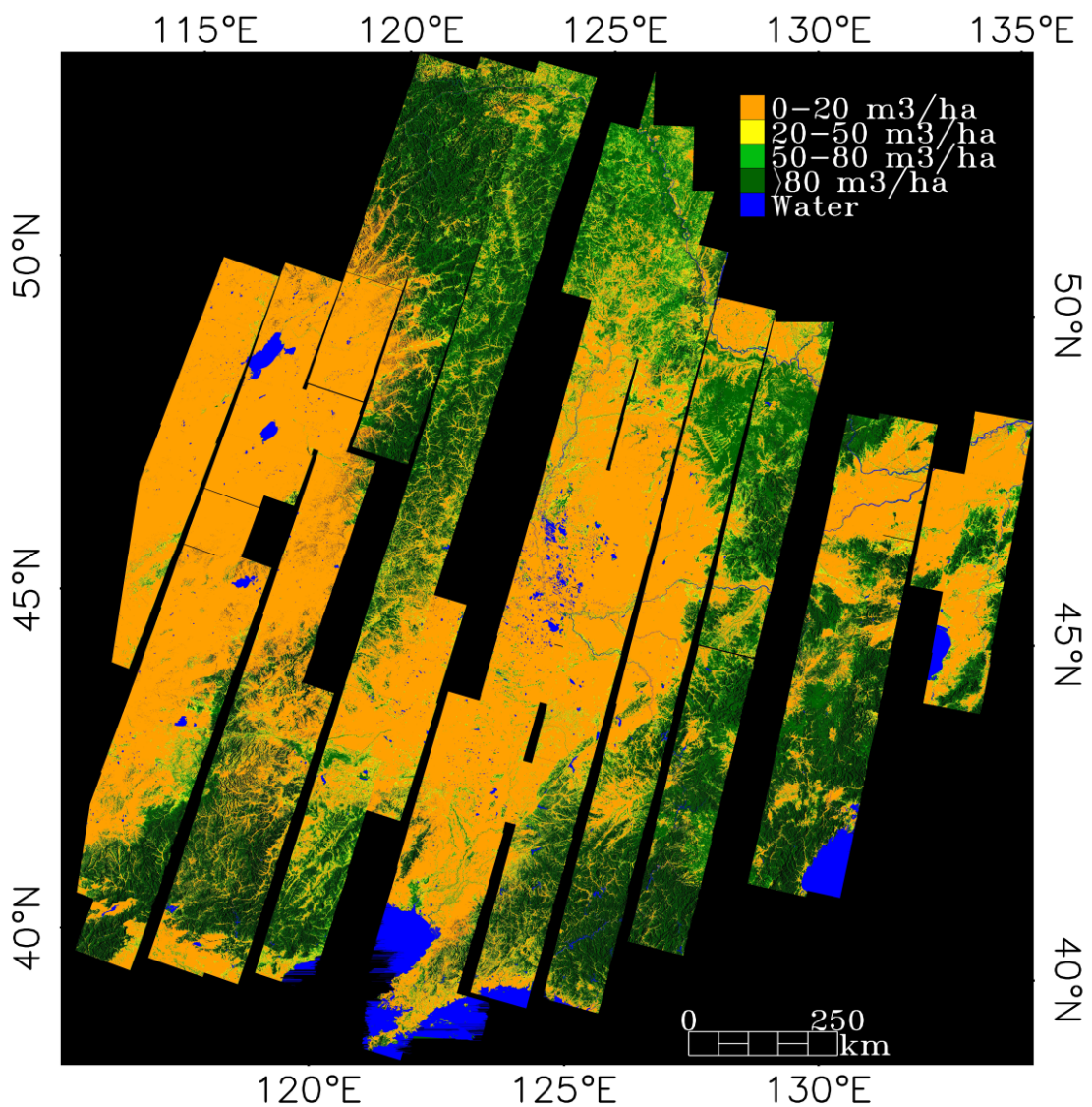


Figure 8.4. Mosaic of the classified ERS-1/2 tandem dataset comprising 223 frames. Projection: Albers Conical Equal Area, standard parallels at 25° & 47° latitude and projection centre at 0° latitude and 115° longitude, Ellipsoid: Krassovsky, Pixel size: 50x50 m².

Chapter 9 - Conclusions

9.1 Summary and discussion

In this thesis, the feasibility of large area forest stem volume mapping with multi-seasonal and multi-baseline ERS-1/2 tandem data was investigated. The primary goal was to develop, for the showcase scenario of Northeast China, a method that allows the exploitation of the existing archives of the ERS-1/2 tandem mission. Along with this overall goal, the effects of forest structural diversity and topography on the ERS-1/2 tandem coherence measurements were addressed.

The analysis of the variability of coherence at the Siberian and Chinese test sites in Chapter 4 traced the observations reported in many predecessor studies. A considerable response of coherence to varying environmental and meteorological imaging conditions could be observed. Although there were some seasonal patterns, e.g. high forest floor coherence in winter, coherence revealed considerable responses to short-term effects related to rain or changes in the snow properties. Hence, approaches aiming at the exploitation of the ERS-1/2 tandem archive have to be adaptive to the local weather and environmental conditions at the time of the sensor overpasses. Despite the strong effects of the environmental and meteorological imaging conditions on the overall coherence level, the forest stem volume information in coherence was found to be robust as the multitemporal consistency of the measurements was high.

The only yet existing algorithm for a fully-automated training of a simple empirical model, relating ERS-1/2 tandem coherence to boreal forest stem volume, has been checked for its transferability to a multi-seasonal ERS-1/2 tandem dataset. This training approach, which relied solely on the coherence histogram statistics to determine the unknown model parameters, did not allow reliable model parameter estimates when applied to the multi-seasonal ERS-1/2 tandem datasets available. A severe limitation of the training approach, which was initially developed and tested for ERS-1/2 tandem coherence data that was acquired solely in fall, was connected to the requirement for dense forest being the dominant land cover type in the imaged area and the assumed linear relationship between the coherence measured over dense forest canopies and the forest floor.

A new approach was developed that aimed at the fully-automated determination of the unknown parameters of the semi-empirical Interferometric Water Cloud Model with the aid of the MODIS Vegetation Continuous Field tree cover product. The IWCM, models the coherence over forest as the sum of a ground and a canopy contribution, both weighted by the forest transmissivity, which can be expressed as function of stem volume. The VCF-based model training based on two main assumptions: 1) the coherence/intensity in areas with low VCF tree cover reflects the coherence/intensity at the forest floor and 2) it is possible to infer from the coherence/intensity measured over forest with maximum VCF tree cover on the IWCM parameters related to the coherence and intensity that would be measured over ideally opaque canopies. A third prerequisite for a VCF-based training of the IWCM was that the relationship between forest transmissivity and stem volume could be predicted.

The IWCM forest transmissivity concept considers the forest transmissivity in C-band to be mainly a function of the gap fraction in the canopy, i.e. the canopy cover. The

transmissivity is assumed to be exponentially related to stem volume. The empirical forest transmissivity parameter β in the IWCM, which is needed to relate the forest transmissivity to forest stem volume, could not be estimated by means of VCF. The comparison of VCF tree cover and the stem volume measurements in the Central Siberian inventory data confirmed the forest transmissivity concept of the IWCM though. When fitting the IWCM to the ERS-1/2 tandem coherence measurements at the Central Siberian test sites, the estimates for the forest transmissivity parameter β varied only in a narrow range in case of the images that were acquired under stable weather conditions with high ground coherence, i.e. all tandem pairs from winter but also one tandem pair from fall. This indicated a rather similar relationship between forest transmissivity and stem volume for the different test sites and acquisition dates. For the rest of the tandem pairs, all acquired in spring and fall, the pronounced spread of the coherence measurements along the main trend with respect to stem volume caused the estimates for β to vary in a wide range, exceeding by far the range that could be considered a realistic description of forest transmissivity-stem volume relation. It was found that a simple exponential model could be fitted to the trend of the coherence measurements as function of stem volume even better than the IWCM. The general trend of coherence as function of stem volume in case of the images acquired under unstable conditions could roughly be described when parametrizing the empirical model with a fixed value for the parameter V_γ , which corresponds to the IWCM parameter β (but without physical meaning). Thus, for the set up of a fully-automated VCF-based model training, it was decided to use the IWCM with a fixed value for β in case of tandem pairs that were acquired under stable conditions with high ground coherence (and also high(er) dense forest coherence) whereas under unstable conditions, the simple empirical model was preferred.

For the VCF-based model training, the mode values of the coherence and intensity measurements in areas where VCF indicated minimum and maximum tree cover were used to determine the unknown IWCM model parameters (besides β). The mode values of coherence and intensity in areas with maximum VCF tree cover had to be compensated for residual ground contributions and, in case of coherence, volume decorrelation effects to derive the IWCM parameters describing the properties of ideally opaque canopies. The comparison of VCF tree cover and the inventory stem volume measurements showed that forests with maximum VCF tree cover should mostly exceed a stem volume of 200 m³/ha. A model sensitivity analysis with the IWCM indicated for stem volumes > 200 m³/ha only minor differences in the ground contributions and volume decorrelation effects as long as the baselines did not exceed ~ 200 m. In this case, the derivation of the model parameters appeared uncritical. For baselines of ~300 m length, however, the expected effect of volume decorrelation in the range of stem volumes above 200 m³/ha caused a higher uncertainty in the parameter estimates.

When applying the VCF-based model training to the ERS-1/2 tandem coherence images that covered the Siberian test sites on a frame-by-frame basis, the results drew a heterogeneous picture. When comparing the parameter estimates with those obtained when fitting the models to the measurements at the test sites with the aid of the inventory data, clear differences in the parameter estimates were, in particular, observed for the images acquired under unfrozen conditions in spring and fall but also in case of the images that were acquired under winter frozen conditions there were some differences. The differences between the inventory data- and VCF-based parameter estimates could be reduced when restricting the VCF-based model training to the area of the particular test site so that both training approaches reflected the same area. The

better agreement of the parameter estimates showed that spatial variations in the environmental and meteorological imaging conditions were one of the main reasons for the differences in the parameter estimates. This clearly showed that the model training should account for sub-frame variations in the imaging conditions. The adaptivity of the model training algorithm represents one of the issues where the algorithm has potential to be improved.

While the coherence in areas with low tree cover well reflected the coherence at the forest floor, it was more critical to infer from the intensity measured over open ground on the forest floor conditions. In particular under unfrozen rainy conditions, the VCF-based estimates for the forest floor backscatter tended to be too high. As intensity, in contrast to coherence, is highly sensitive to soil moisture, systematic differences in soil moisture between open ground, i.e. with low tree cover, and forest floor (due to for instance evapotranspiration and rainfall interception in forest) would not allow to infer from the intensity measurements in areas with low VCF tree cover on the IWCM model parameter related to forest floor intensity. Thus, the VCF-based estimates for the forest floor intensity have to be interpreted with care, at least in case of wet conditions.

In case of the ERS-1/2 tandem coherence images that covered the Siberian test sites, it was possible to infer from the coherence and intensity measured over forest with maximum VCF tree cover on the IWCM model parameters related to dense forest properties when assuming that the observed coherence/intensity over forest with maximum VCF tree cover reflected a stem volume of at least 250 m³/ha. This was due to the fact that for the range of stem volumes delineated by means of VCF both, coherence and intensity, had mostly reached saturation with respect to increasing stem volume. This finding actually represents a critical point in the concept of the VCF-based model training. When solely considering the parameter estimation, it can be stated that the IWCM parameters, related to the temporal coherence and backscatter properties of ideally opaque forest, are best estimated when the coherence/intensity measured over forest with maximum VCF tree cover represent what can be considered the saturation level of the measurements, i.e. when there are no differences in the ground contributions and in volume decorrelation in the range of stem volumes corresponding to maximum VCF tree cover. When the SAR or InSAR measurements show a pronounced sensitivity above stem volumes of 200 - 250 m³/ha, as for instance observed in Santoro et al. (2002) or Pulliainen et al. (2003), it could be more difficult to infer from the coherence/intensity in areas with high VCF tree cover on the model parameters related to ideally opaque canopies as then the model parameter estimation may require information about the stem volume distribution in forests with maximum VCF tree cover. A pronounced sensitivity in this case means that the response in the measurements to increasing stem volume clearly exceeds the noise in the coherence estimates.

When carrying out the VCF-based model training for the ERS-1/2 tandem dataset of Northeast China, the estimates for the IWCM parameters showed similar patterns with respect to the meteorological imaging conditions as in case of the ERS-1/2 tandem coherence images covering the Siberian test sites. The estimates for γ_{veg} , i.e. the IWCM parameter describing the temporal coherence of opaque canopies, were suspicious in case of very long baselines around 300 m. The IWCM predicted an oscillation, i.e. an increase of coherence with increasing stem volume, at stem volumes around 200 m³/ha. The expected sensitivity of coherence, i.e. the increase, to increasing stem volume for stem volumes above 200 m³/ha may have affected the IWCM parameter estimates in

that sense that it was not clear which stem volume level was represented by the estimate of dense forest coherence from VCF.

The influence of topography-induced decorrelation was analyzed with the aid of the SRTM-3 DEM. Topography was found to introduce decorrelation over sloped terrain when the range common band filtering could not entirely compensate for uncommon range band spectra. The topography-induced coherence loss after range common band filtering increased with increasing length of the perpendicular baseline and from slopes tilted away from the sensor to slopes facing the sensor. The filtering could recover the coherence over flat terrain and for baselines < 100 m on slopes tilted away from the sensor. The longer the baseline, the more the forest biophysical information in coherence was distorted by topographic effects on both, slopes tilted towards as well as away from the sensor. Uncompensated topographic phase in the coherence estimation window and co-registration offsets further contributed to the loss of coherence over mountainous terrain. The topography-induced decorrelation over dense forest resembled the observations over open ground. In addition, the coherence to stem volume relation may have been altered by differences in volume decorrelation, ground to canopy backscatter weighting and canopy gap fractions dependent on the topographic position of the forest. These effects were not analyzed in this thesis. For Northeast China, the coherence in about one third of the area covered could be expected to be affected by topography. For future missions, the recommendation with respect to the orbit planning would be to keep the baselines as short as possible, i.e. < 100 m. This, however, contradicts the requirements for an optimal stem volume retrieval for which somewhat longer baselines in the range of 150 to 250 m are preferable. Recent advances in the processing of InSAR data allow reducing the topographic effect in coherence over mountainous areas (Santoro et al., 2007c). When doing slope adaptive common band filtering using, for instance, the almost globally available SRTM-3 DEM for the simulation of the topographic phase, the effect of spatial decorrelation can be somewhat reduced.

Accurate stem volume retrieval with ERS-1/2 tandem coherence is known to require a multitemporal stack of images that were acquired under optimal conditions. As this precondition was not fulfilled with the ERS-1/2 tandem dataset available for Northeast China, the accuracy of a classification of the four stem volume classes 0-20, 20-50, 50-80 and >80 m³/ha was assessed. These classes were also mapped in the SIBERIA project for Central Siberia. The classes were considered useful for Russian foresters for the identification of the development stages of young stands growing after disturbance; from the Chinese side there were no demurs against the use of the same classes for Northeast China. Due to the lack of reliable ground data for Northeast China, the agreement between the forest inventory data and the stem volume maps produced with ERS-1/2 tandem coherence could only be checked for the ERS-1/2 tandem dataset that covered the Central Siberian test sites.

When inverting the models, i.e. the IWCM or the simple empirical model, that were trained with the aid of VCF on a frame-by-frame basis and aggregating the obtained volume estimates into the four desired stem volume classes, a non-sufficient accuracy (respectively agreement with the inventory data) had to be stated. Only the extreme classes 0-20 and > 80 m³/ha reached accuracies of 80 % whereas the intermediate classes hardly exceeded Producer and User accuracies of 50 %. As the VCF-based model training was carried out on a frame-by-frame basis, within frame variations of ground coherence conditions caused the classification accuracy of the lowest stem

volume class to drop to low levels, at least in certain parts of the image where the VCF-based ground coherence estimate did not reflect the local conditions. Spatial variations of the ground coherence mainly affected ERS-1/2 tandem pairs from spring and fall but were also observed for a coherence image from winter. A low agreement of the intermediate stem volume classes with the inventory data was also reported for the SIBERIA stem volume map (Balzter et al., 2002). Instead, an independent ground survey reported even for these classes accuracies above 80 %. Thus, the uncertainty in the inventory data should have been a major reason for the low agreement of the coherence-based stem volume maps and the inventory data, in particular in case of the intermediate stem volume classes.

The real value of the produced stem volume map of Northeast China is yet unclear as no accuracy assessment could be carried out. The map itself revealed a promising characteristic in the sense that, with the VCF-based model training approach, the differences in the imaging conditions appeared to be adequately accounted for in the stem volume map as no border effects between adjacent tracks were visible. On the other side, the structural deficits of the forests in Northeast China questioned the reliability of the classified stem volume classes. At the Siberian test sites it was observed that for stands with low relative stocking, the classification accuracy was lower than for fully or close-to-fully stocked stands. Hence, at this point the map should rather be interpreted as an indicator for sparse and dense forest.

9.2 Outlook

Although developed for a particular data type, the interferometric data of the ERS-1/2 tandem mission, the concept of the VCF-based model training approach goes beyond a sensor-specific implementation. Principally, VCF may aid the identification of the backscatter and coherence properties of open ground and dense forest canopies for various radar data types.

Since the end of the ERS-1/2 tandem mission in the year 2000, when ERS-1 ceased operation, C-band repeat-pass coherence could be obtained with the cross-interferometric processing of the C-band SAR data from ERS-2 and ENVISAT ASAR. ERS-2 and ENVISAT ASAR provide interferometric image pairs with a short temporal baseline of 28 minutes. ERS-ENVISAT coherence was found to contain land cover and forest related information (Santoro et al., 2007a) but the complications with respect to the 31 MHz shift in carrier frequency between both sensors put narrow constraints to the application of ERS-ENVISAT coherence as a long perpendicular baseline (~2 km) is needed to compensate for the slight difference in carrier frequency between both sensors so that the coherence over flat surfaces is optimally recovered (Santoro et al., 2007a). In addition, ERS-2 works since 2001 in a so-called Zero-Gyro mode, which does not provide a sufficient stability of the satellites attitude so that many image pairs cannot be used for interferometry because of non-overlapping Doppler spectra. Canada's recent Radarsat-2 C-band mission provides interferometric capabilities as well but the 24-days repeat-cycle represents a severe limitation concerning the exploitation of Radarsat-2 repeat-pass coherence for forestry applications (Van Der Sanden, 2004). The same constraint applies for the data of the Japanese ALOS PALSAR mission, which provides interferometric image pairs in L-band with 46 days temporal baseline, or to ENVISAT ASAR repeat-pass interferometry, which acquires in C-band with 35-days temporal baseline. For such long temporal baselines, forestry applications of

coherence are, if possible at all, limited to interferometric image pairs acquired during constantly frozen conditions. Such conditions usually only occur during the long winters in the boreal zone (Eriksson et al., 2003). Somewhat more promising is ESAs upcoming SENTINEL-1 C-band mission, which will provide interferometric capabilities and repeat cycles of 12 days when the first satellite will be in space and a 6-day repeat cycle when SENTINEL-1b will be launched. A 6-day repeat cycle is still much longer than the one-day repeat cycle of the ERS-1/2 tandem mission, increasing the risk for strong decorrelation on the ground, but may still allow stem volume retrieval for a larger number of image pairs. As one of the main mission objectives is to acquire consistent multitemporal datasets (Attema et al., 2007), SENTINEL-1 may provide a sufficient number of image pairs, acquired under optimal conditions, for the application of multitemporal stem volume retrieval approaches, which have been shown to reach high accuracies. A transfer of the VCF-based training of the IWCM to the SENTINEL-1 case would be straightforward.

Another possible application of the VCF-based model training approach, which has recently been tested for medium resolution ENVISAT ASAR data (Santoro et al., 2007b), considers multitemporal stacks of C-band intensity measurements. A single C-band intensity image is not suited for stem volume retrieval. When, however, combining the retrieval results for a large number of images, high accuracies can be achieved, at least when aiming at stem volume statistics at regional, provincial or national level (Pulliainen et al., 1996; Kurvonen et al., 1999; Santoro et al., 2007b). This is particularly interesting with respect to the upcoming SENTINEL-1 mission, which will provide C-band measurements in two polarizations every three days (dependent on the latitude). A crucial issue in a multitemporal retrieval, however, is the preselection of suitable images. With respect to the VCF-based model training, for instance, we have seen in Chapter 7.2 that the intensity measured over open ground, i.e. with low tree cover according to VCF, did not necessarily reflect the forest floor conditions so that care has to be taken to exclude such cases.

Multitemporal and multipolarimetric L-band intensity, which is now available from the Japanese ALOS PALSAR mission (for which the follow-up mission has already been approved), appears to be even more promising than C-band intensity as it suffers less from saturation and shows a temporally more consistent relation to stem volume or biomass (Le Toan et al., 1992; Imhoff, 1995; Harrel et al., 1995; Kurvonen et al., 1999; Fransson & Israelsson, 1999; Mougouin et al., 1999; Askne et al., 2003; Santoro et al., 2006). Limitations concerning a transfer of the VCF-based model training approach to the L-band case are related to the Water-Cloud-type-of model. The semiempirical model that was utilized for the modeling of the relationship of intensity and stem volume in this thesis was developed for short-wavelength radar data, i.e. X- and C-band, and does not account for trunk-ground interactions. Existing studies about the contribution of double bounce to L-band backscatter from forest give somewhat contradictory answers. On the one side, Sun et al. (1991) or Saatchi & McDonald (1997) indicate a significant double bounce contribution in L-band measurements over forest whereas in Israelsson & Askne (1994), Ranson & Sun (1994b) or Pulliainen et al. (1999) the results indicated negligible contributions; the different observations could be related to the forest floor which dampens double bounce backscatter if rough. Several studies for Scandinavian and Siberian boreal forest sites, however, indicated that it is possible to model L-band intensity as function of stem volume with simple Water-Cloud-based models (Pulliainen et al., 1999; Fransson & Israelsson, 1999; Kurvonen et al., 1999; Askne et al., 2003;

Santoro et al. 2006) so that the transfer of the VCF-based model training and retrieval approach should be possible.

The most promising spaceborne SAR mission with respect to biomass mapping in the next years is supposed to be ESAs P-band Earth Explorer BIOMASS, which, however, has not been approved yet (summer 2009). P-band is known to show high sensitivity to biomass without suffering from saturation as early as X-, C- or L-band (Le Toan et al., 1992; Lang et al., 1994; Rignot et al., 1995; Ranson et al. 1994, 1997; Mougin et al., 1999; Saatchi et al., 2007). The Water-Cloud-based modeling of the relationship between SAR intensity and stem volume, as used in this study, in combination with the fully automated VCF-based model parameter estimation, cannot simply be transferred to the P-band case as P-band measurements over forest contain considerable contributions from trunk-ground interactions. Anyhow, the identification of the backscatter intensity of open ground and dense forest (whatever 'dense' may mean in P-band) could be of use as well.

References

- Abdel-Messeh, M. and Quegan, S. (2000). Variability in ERS scatterometer measurements over land. *IEEE Transactions on Geoscience and Remote Sensing*, 38, 4, pp. 1767-1776.
- Achard, F., Mollicone, D., Stibig, H.J., Aksenov, D., Laestadius, L., Li, Z., Popativ, P. and Yaroshenko, A. (2006). Areas of rapid forest-cover change in boreal Eurasia. *Forest Ecology and Management*, 237, pp. 322-334.
- Ahern, F.J., Leckie, D.J. and Drieman, J.A. (1993). Seasonal changes in relative C-band backscatter of northern forest cover types. *IEEE Transactions on Geoscience and Remote Sensing*, 31, pp. 668-680.
- Anonymous (2003). SRTM Water Body Data Product specific guidance. Available at: 'ftp://e0srp01u.ecs.nasa.gov/srtm/version2/SWBD/SWBD_Documentation/', last date of access: May 1st 2009.
- Armstrong, R.L. and Brodzik, M.J. (2005). Northern Hemisphere EASE-Grid weekly snow cover and sea ice extent version 3. National Snow and Ice Data Center, Boulder, Digital media.
- Askne, J., Dammert, P.B.G., Fransson, J., Israelsson, H. and Ulander, L.M.H. (1995). Retrieval of forest parameters using intensity and repeat-pass interferometric SAR information. *Proceedings of Retrieval of Bio- and Geophysical Parameters from SAR Data for Land Applications*, 10 - 13 October, Toulouse, pp. 119-129.
- Askne, J. and Smith, G. (1996). Forest InSAR decorrelation and classification properties. *Proceedings of Fringe'96*, 30 September - 2 October, Zurich, ESA SP-406, pp. 95-103.
- Askne, J., Dammert, P. B. G., Ulander, L. M. H. and Smith, G. (1997). C-band repeat-pass interferometric SAR observations of the forest. *IEEE Transactions on Geoscience and Remote Sensing*, 35, pp. 25-35.
- Askne, J., Dammert, P.B.G. and Smith, G. (1999). Understanding ERS InSAR coherence of boreal forest. *Proceedings of IGARSS'99*, 28 June - 2 July, Hamburg, pp. 2111-2114.
- Askne, J., Santoro, M., Smith, G. and Fransson, J. E. S. (2003). Multitemporal repeat-pass SAR interferometry of boreal forests. *IEEE Transactions on Geoscience and Remote Sensing*, 41, pp. 1540-1550.
- Askne, J. and Santoro, M. (2005). Multitemporal repeat pass SAR interferometry of boreal forests. *IEEE Transactions on Geoscience and Remote Sensing*, 43, pp. 1219-1228.
- Askne, J. and Santoro, M. (2007a). Boreal forest stem volume estimation from multitemporal C-band InSAR observations. *Proceedings of Envisat Symposium*, 21-25 April, Montreux, ESA SP 635, CD-ROM.
- Askne, J. and Santoro, M. (2007b). Selection of forest stands for stem volume retrieval from stable ERS Tandem InSAR observations. *IEEE Transactions on Geoscience and Remote Sensing Letters*, 4, 1, pp. 46-50.
- Attema, E. and Ulaby, F.T. (1978). Vegetation modeled as a water cloud. *Radio Science*, 13, 2, pp. 357-364.
- Attema, E., Levrini, G. and Davidson, M. (2007). SENTINEL-1 ESA's new European Radar Observatory. *ESA Bulletin*, 131, Noordwijk.
- Baker, J.R. and Luckman, A.J. (1999). Microwave observations of boreal forests in the NOPEX area of Sweden and a comparison with observations of a temperate plantation in the United Kingdom. *Agricultural and Forest Meteorology*, 98-99, pp. 389-416.

-
- Bamler, R. and Just, D. (1993). Phase statistics and decorrelation in SAR interferograms. Proceedings of IGARSS'93, 18-21 August, Tokyo, pp. 980-984.
- Bamler, R. and Hartl, P. (1998). Synthetic aperture radar interferometry. *Inverse Problems*, 14, pp. 1-54.
- Balzter, H. (2001). Forest mapping and monitoring with interferometric synthetic aperture radar (InSAR). *Progress in Physical Geography* 25, 2, pp. 159-177.
- Balzter, H., Talmon, E., Wagner, W., Gaveau, D., Plummer, S., Yu, J. J., Quegan, S., Davidson, M., Le Toan, T., Gluck, M., Shvidenko, A., Nilsson, S., Tansey, K., Luckman, A. and Schmullius, C. (2002). Accuracy assessment of a large-scale forest cover map of central Siberia from synthetic aperture radar. *Canadian Journal of Remote Sensing*, 28, pp. 719-737.
- Balzter, H., Rowland, C.S. and Saich, P. (2007). Forest canopy height and carbon estimation at Monks Wood National Nature Reserve, UK, using dual-wavelength SAR interferometry. *Remote Sensing of Environment*, 108, pp. 224-239.
- Beaudoin, A., Troufleau, D., Desbois, N., Piet, L. and Deshayes, M. (1995). On the use of ERS-1 SAR data over hilly terrain. Proceedings of IGARSS'95, 10-14 July, Florence, pp. 2179-2182.
- Bensi, P., Berger, M., Davidson, M., Ingman, P., Langen, J., Rebhan, H. and Silvestrin, P. (2007). A new Earth Explorer – the third cycle of Core Earth Explorers. *ESA Bulletin*, 131, August 2007, Noordwijk.
- Bergen, K., Dobson, M.C., Pierce, L. and Ulaby, F.T. (1997). Effects of within-season dielectric variations on terrain classification using SIR-C/X-SAR. Proceedings of IGARSS'97, 3-8 August, Singapore, pp. 1072-1074.
- Bicheron, P., Defourny, P., Brockmann, C., Schouten, L., Vancutsem, C., Huc, M., Bontemps, S., Leroy, M., Achard, F., Herold, M., Ranera, F. and Arino, O. (2008). GLOBCOVER – Products Description and Validation Report. Media France, 2008.
- Blaes, X. and Defourny, P. (2003). Retrieving crop parameters based on tandem ERS 1/2 interferometric coherence images. *Remote Sensing of Environment*, 88, pp. 374-385.
- Borgeaud, M. and Wegmüller, U. (1996). On the Use of ERS SAR Interferometry for the Retrieval of Geo- and Bio-Physical Information. Proceedings of Fringe'96, 30 September - 2 October, Zurich, ESA SP-406, pp. 105-115.
- Born, M. and Wolf, E. (1980). *Principles of Optics*. Pergamon Press, Edition 6.
- Bosisio, A.V. and Dechambre, M. (2004). Predictions of microwave attenuation through vegetation: a comparison with measurements. *International Journal of Remote Sensing*, 28, 29, pp. 3973-3997.
- Box, E. and Choi, J. (2003). Climate of Northeast Asia. In: Kolbek, J., Srutek, M. and Box, E.O. [ed.], *Forest vegetation of Northeast Asia*, Kluwer, Dordrecht, pp. 93-180.
- Brisco, B. and Brown, R.J. (1998). Agricultural applications with radar. In: Henderson, F.M. & Lewis, A.J. [ed.], *Principles and Applications of Imaging Radar*, Vol. 2 of *Manual of Remote Sensing*, Third Edition, John Wiley & Sons, New York.
- Bruniquel, J. and Lopes, A. (1997). Multi-variate optimal speckle reduction in SAR imagery. *International Journal of Remote Sensing*, 18, 3, pp. 603-627.
- Bull, G.Q. and Nilsson, S. (2004). An assessment of China's forest resources. *International Forestry Review*, 6, 3, pp. 210-220.
- Castel, T., Martinez, J.M., Beaudoin, A., Wegmueller, U. and Strozzi, T. (2000). ERS INSAR Data for Remote Sensing Hilly Forested Areas. *Remote Sensing of Environment*, 73, pp. 73-86.

-
- Castel, T., Beaudoin, A., Stach, N., Stussi, N., LeToan, T., and Durand, P. (2001a). Sensitivity of space-borne SAR data to forest parameters over sloping terrain. Theory and experiment. *International Journal of Remote Sensing*, 22, 12, pp. 2351-2376.
- Castel, T., Beaudoin, A., Floury, N., Le Toan, T., Caraglio, Y. and Barczi, J.F. (2001b). Deriving forest canopy parameters for backscatter models using the AMAP architectural plant model. *IEEE Transactions on Geoscience and Remote Sensing*, 39, 3, pp. 571-583.
- Castel, T., Guerra, F., Caraglio, Y. and Houllier, F. (2002). Retrieval biomass of a large Venezuelan pine plantation using JERS-1 SAR data. Analysis of forest structure impact on radar signature. *Remote Sensing of Environment*, 79, pp. 30–41.
- Chang, Y., He, H.S., Hu, Y., Bu, R. and Li, X. (2008). Historic and current fire regimes in the Great Xing'an Mountains, northeastern China: Implications for long-term forest management. *Forest Ecology and Management*, 254, pp. 445–453.
- Chao, S. (1994). *Geography of China: environment, resources, population and development*. John Wiley & Sons, New York.
- Chauhan, N.S., Lang, R.H. and Ranson, K.J. (1991). Radar modelling of a boreal forest. *IEEE Transactions on Geoscience and Remote Sensing*, 29, 4, pp. 627-638.
- Chen, X.W. (2002). Modelling the effects of global climate change at the ecotone of boreal larch forests and temperate forest of Northeast China. *Climate Change*, 55, pp. 77-97.
- Chen, X. and Li, B.L. (2003). Effect of global climate change and human disturbances on tree diversity of the forest regenerating from clear-cuts of mixed broadleaved Korean pine forest in Northeast China. *Chemosphere*, 51, pp. 215–226.
- Chen, J.M., Thomas, S.C., Yin, Y, Maclaren, V., Liu, J., Pan, J., Liu, G., Tian, Q., Zhu, Q., Pan, J.J., Shi, X., Xue, J. and Kang, E. (2007). Enhancing forest carbon sequestration in China: Toward an integration of scientific and socio-economic perspectives. *Journal of Environmental Management*, 85, pp. 515–523.
- Curlander, J.C. and McDonough, R.N. (1991). *Synthetic Aperture Radar: Systems and signal Processing*. John Wiley & Sons, New York.
- Dammert, P.B.G. (1996). Accuracy of INSAR measurements in forested areas. *Proceedings of Fringe'96*, 20 September – 2 October, Zurich, ESA SP-406, pp. 37-49.
- Dammert, P.B.G. and Askne, J. (1998). Interferometric tree height observations in boreal forests with SAR interferometry. *Proceedings of IGARSS'98*, 6-10 July, Seattle, pp. 1363-1366.
- Dammert, P.B.G., Askne, J. and Kühlmann, S. (1999). Unsupervised segmentation of multitemporal interferometric SAR images. *IEEE Transactions on Geoscience and Remote Sensing*, 37, 5, pp. 2259–2271.
- DeFries, R.S., Hansen, M.C. and Townshend, J.R.G. (2000). Global continuous field of vegetation characteristics: a linear mixture model applied to multi-year 8 km AVHRR data. *International Journal of Remote Sensing*, 21, 6 & 7, pp. 1389-1414.
- Dobson, M.C., McDonald, K.C. and Pierce, L. (1991a). Diurnal variation in radar backscatter from a loblolly pine forest in late summer. *Proceedings of IGARSS'91*, 3 - 6 June, Espoo, pp. 1115-1116.
- Dobson, M.C., McDonald, K.C. and Pierce, L. (1991b). Seasonal change in radar backscatter from mixed conifer and hardwood forests in northern Michigan. *Proceedings of IGARSS'91*, 3 - 6 June, Espoo, pp. 1121-1124.

-
- Dobson, M.C., Ulaby, F.T., LeToan, T., Beaudoin, A., Kasischke, E.S. and Christensen, N. (1992). Dependence of radar backscatter on coniferous forest biomass. *IEEE Transactions on Geoscience and Remote Sensing*, 30, pp. 412-415.
- Dobson, M.C., Ulaby, F.T., Pierce, L.E., Sharik, T.L., Bergen, K.M., Kellendorfer, J., Kendra, J.R., Li, E., Lin, Y.C., Nashashibi, A., Sarabandi, K. and Siqueria, P. (1995a). Estimation of forest biophysical characteristics in northern Michigan. *IEEE Transactions on Geoscience and Remote Sensing*, 33, 4, pp. 877-895.
- Dobson, M.C., Ulaby, F.T. and Pierce, L.E. (1995b). Land-Cover classification and estimation of terrain attributes using synthetic aperture radar. *Remote Sensing of Environment*, 51, pp. 199-214.
- Drezet, P.M.L. & Quegan, S. (2006). Environmental effects on the interferometric repeat-pass coherence of forests. *IEEE Transactions on Geoscience and Remote Sensing*, 44, pp. 825-837.
- Drezet, P.M.L. & Quegan, S. (2007). Satellite-based radar mapping of British forest age and Net Ecosystem Exchange using ERS tandem coherence. *Forest Ecology and Management*, 238, pp. 65–80.
- Elachi, C., Bicknell, T., Jordan, R.L. & Wu, c. (1982). Spaceborne synthetic aperture imaging radars: application, techniques and technology. *Proceedings of IEEE*, 70, pp. 1174-1209.
- Elachi, C. (1988). *Spaceborne Radar Remote Sensing: Applications and Techniques*. IEEE Press, New York.
- Engdahl, M.E. and Hyypä, J.M. (2003). Land-cover classification using multitemporal ERS-1/2 InSAR data. *IEEE Transactions on Geoscience and Remote Sensing*, 41, 7, pp. 1620-1628.
- Engdahl, M. E., Pulliainen, J. T. and Hallikainen, M. T. (2004). Boreal forest coherence-based measures of interferometric pair suitability for operational stem volume retrieval. *IEEE Geoscience and Remote Sensing Letters*, 1, pp. 228–231.
- Enquist, B.J. and Niklas, K.J. (2001). Invariant scaling relations across tree-dominated communities. *Nature*, 410, pp. 655-741.
- Eriksson, L.E.B., Santoro, M., Wiesmann, A. and Schmullius, C. (2002). Multi-seasonal study of the SIBERIA classification procedure. *Proceedings of ForestSAT Symposium 2002, 5-9 August, Edinburgh, CD-ROM*.
- Eriksson, L.E.B., Santoro, M., Wiesmann, A. and Schmullius, C. (2003). Multitemporal JERS repeat-pass coherence for growing-stock volume estimation of Siberian forest. *IEEE Transactions on Geoscience and Remote Sensing*, 41, 7, pp. 1561-1570.
- Eriksson, L.E.B. (2004). *Satellite-borne L-band interferometric coherence for forestry applications in the boreal zone*. PhD thesis, Friedrich-Schiller-University, Jena.
- Food and Agriculture Organization of the United Nations FAO (2001). *Forest Resource Assessment – main report*. FAO Forestry Paper No. 140, Rome.
- Food and Agriculture Organization of the United Nations FAO (2006). *Global Forest Resource Assessment 2005. Progress towards sustainable forest management*. FAO Forestry Paper No. 147, Rome.
- Fang, J., Chen, A., Peng, C., Zhao, S. and Ci, L. (2001). Changes in Forest Biomass Carbon Storage in China Between 1949 and 1998. *Science*, 292, pp. 2320-2322.
- Fellah, K., Meyer, C., Laugier, O., Clandillon, S. and De Fraipont, P. (1997). Potential and limitations of multi-temporal SAR data in a quantitative approach for multi-scalar hydrological applications. *Synthesis of ERS Alsace/Camargue Pilot Project. Proceedings of the 3rd ERS Symposium, 18-21 March, Florence*, pp. 61-70.

-
- Ferrazzoli, P. and Guerriero, L. (1995). Radar sensitivity to tree geometry and woody volume: a model analysis. *IEEE Transactions on Geoscience and Remote Sensing*, 33, pp. 360–371.
- Ferretti, A., Monti-Guarnieri, A., Prati, C., Rocca, F. and Massonet, D. (2007). *InSAR principles: Guidelines for SAR interferometry processing and interpretation*. ESA Special Publication, TM-19, Noordwijk.
- Fleischman, J.G., Ayasli, S., Adams, E.M. and Gosselin, D.R. (1996). Part 1: Foliage attenuation and backscatter analysis of SAR imagery. *IEEE Transactions on Aerospace and Electronic Systems*, 32, 1, pp. 135-144.
- Floury, N., Le Toan, T., Souyris, J.-C., Singh, K., Stussi, N., Hsu, C. C. and Kong, J. A. (1996). Interferometry for forest studies. *Proceedings of Fringe'96*, 30 September- 2 October, Zurich, ESA SP-406, pp. 57-70.
- Floury, N., Le Toan, T., Souyris, J.C. and Bruniquel, J. (1997). A Study of SAR Interferometry over Forests: Theory and Experiment. *Proceedings of IGARSS'97*, 3-8 August, Singapore, pp. 1868 – 1870.
- Foody, G.M. (2002). Status of land cover classification accuracy assessment. *Remote Sensing of Environment*, 80, pp. 185 – 201.
- Foody, G.M., Boyd, D.S. and Cutler, M.E.J. (2003). Predictive relations of tropical forest biomass from Landsat TM data and their transferability between regions. *Remote Sensing of Environment*, 85, pp. 463-474.
- Franklin, J. (1986). Thematic Mapper analysis of coniferous forest structure and composition. *International Journal of Remote Sensing*, 7, pp. 1287-1301.
- Fransson, J. E. S. and Israelsson, H. (1999). Estimation of stem volume in boreal forests using ERS-1 C- and JERS-1 L-band SAR data. *International Journal of Remote Sensing*, 20, 1, pp. 123–137.
- Fransson, J. E. S., Smith, G., Askne, J. and Olsson, H. (2001). Stem volume estimation in boreal forests using ERS-1/2 coherence and SPOT XS optical data. *International Journal of Remote Sensing*, 22, pp. 2777-2791.
- Frost, V.S., Stiles, J.A., Shanmugan, K.S. and Hotzman, J.C. (1982). A model for radar images and its application to adaptive digital filtering of multiplicative noise. *IEEE Transactions on Pattern Analysis and Machine Intelligence*, 4, 2, pp. 157-166.
- Fung, A.K. (1994). *Microwave scattering and emission models and their applications*. Artech House, Norwood.
- Gao, J., Liu, Y. and Chen, Y. (2006). Land cover changes during agrarian restructuring in Northeast China. *Applied Geography*, 26, pp. 312-322.
- Gatelli, F., Monti Guarnieri, A., Parizzi, F., Pasquali, P. Prati, C., and F. Rocca (1994). The wavenumber shift in SAR interferometry. *IEEE Transactions on Geoscience and Remote Sensing*, 32, pp. 855-865.
- Gaveau, D.L.A. (2002). Modelling the dynamics of ERS-1/2 tandem coherence with increasing woody biomass over boreal forest. *International Journal of Remote Sensing*, 23, 18, pp. 3879-3885.
- Gaveau, D.L.A., Balzter, H. and Plummer, S. (2003). Forest woody biomass classification with satellite-based radar coherence over 900 000 km² in Central Siberia. *Forest Ecology and Management*, 174, pp. 65-75.
- Geiger, R., Aron, A.H. and Todhunter, P. (2003). *The climate near the ground*. Rowman & Littlefield, 6th Edition, Lanham, MD, USA.
- Goldstein, R.M. and Zebker, H.A. (1987). Interferometric radar measurement of ocean surface current. *Nature*, 328, pp. 707-709.
- Goldstein, L.C. (1995). Atmospheric limitations to repeat-track radar interferometry. *Geophysical Research Letters*, 22, 18, 2517-2520.

-
- Graham, L.C. (1974). Synthetic interferometer radar for topographic mapping. *Proceedings of the IEEE*, 62, 6, pp. 763-768.
- Guglielmetti, M., Schwank, M., Mätzler, C., Oberdörster, C., Vanderborcht, J. and Flüher, H. (2007). Measured microwave radiative transfer properties of a deciduous forest canopy. *Remote Sensing of Environment*, 109, pp. 523-532.
- Guneriussen, T. (1997). Backscattering properties of a wet snow cover derived from DEM corrected ERS-1 SAR data. *International Journal of Remote Sensing*, 18, 2, pp. 375-392.
- Guneriussen, T., Høgda, K.A., Johnsen, H. and Lauknes, I. (2001). InSAR for estimation of changes in snow water equivalent of dry snow. *IEEE Transactions on Geoscience and Remote Sensing*, 39, 10, pp. 2101-2108.
- Hagberg, J. O., Ulander, L. M. H. and Askne, J. (1995). Repeat-pass SAR interferometry over forested terrain. *IEEE Transactions on Geoscience and Remote Sensing*, 33, pp. 331-340.
- Hajnsek, I., Kugler, F., Lee, S.K. and Papathanassiou, K.P. (2008). Tropical-forest-parameter estimation by means of Pol-InSAR: The INDREX-II Campaign. *IEEE Transactions on Geoscience and Remote Sensing*, 47, 2, pp. 481-493.
- Hallikainen, M., Mäkynen, M., Laakso, S., Rantala, A., Tares, T., Uusitalo, J., Koskinen, J., Pulliainen, J., Hyyppä, J. and Hyyppä, H. (1998). Experimental results on radar response to boreal forest. *Proceedings of the 2nd International Workshop on Retrieval of Bio- & Geo-Physical Parameters from SAR Data for Land Applications*, 21–23 October, Noordwijk, ESA SP-441, 325–332.
- Hansen, M., DeFries, R.S., Townshend, J.R.G., Sohlberg, R., Dimiceli, C. and Carroll, M. (2002a). Towards an operational MODIS continuous field of percent tree cover algorithm: examples using AVHRR and MODIS data. *Remote Sensing of Environment*, 83, pp. 303–319.
- Hansen, M., DeFries, R.S., Townshend, J.R.G., Marufu, L. and Sohlberg, R. (2002b). Development of a MODIS tree cover validation data set for Western Province, Zambia. *Remote Sensing of Environment*, 83, pp. 320-335.
- Hansen, M., DeFries, R.S., Townshend, J.R.G., Carroll, M., Dimiceli, C. and Sohlberg, R. (2003). Global percent tree cover at a spatial resolution of 500 meters: first results of the MODIS vegetation continuous fields algorithm. *Earth Interactions*, 7, 10, pp. 1-15.
- Hansen, M., Townshend, J.R.G., DeFries, R.S. and Carroll, M. (2005). Estimation of tree cover using MODIS data at global, continental and regional/local scales. *International Journal of Remote Sensing*, 26, 10, pp. 4359-4380.
- Hanssen, R.F., Weckwerth, T.M., Zebker, H.A. and Klees, R. (1999). High resolution water vapor mapping from interferometric radar measurements. *Science*, 283, 5406, pp. 1297-1299.
- Henderson, F.M. & Lewis, A.J. [ed.] (1998): *Synthetic Aperture Radar, Manual of Remote Sensing*, Vol. 2, Third Edition. John Wiley & Sons, New York.
- Henderson, F.M. and Lewis, A.J. (2008). Radar detection of wetland ecosystems: a review. *International Journal of Remote Sensing*, 29, 20, pp. 5809-5835.
- Harrel, P.A., Bourgeau-Chavez, L.L., Kasischke, E.S., French, N.H.F. and Christensen, N.L. (1995). Sensitivity of ERS-1 and JERS-1 radar data to biomass and stand structure in Alaskan boreal forest. *Remote Sensing of Environment*, 54, pp. 247–260.
- Harrel, P.A., Kasischke, E.S., Bourgeau-Chavez, L.L. and Haney, E.M. (1997). Evaluation of approaches to estimating aboveground biomass in southern pine forest using SIR-C data. *Remote Sensing of Environment*, 59, pp. 223-233.

-
- Hirata, Y., Tsubota, Y. and Sakai, A. (2009). Allometric models of DBH and crown area derived from QuickBird panchromatic data in *Cryptomeria japonica* and *Chamaecyparis obtusa* stands. *International Journal of Remote Sensing*, 30, 19, pp. 5071 – 5088.
- Hoehn, E.W. and Zebker, H.A. (2000). Penetration depths inferred from interferometric volume decorrelation observed over the Greenland ice sheet. *IEEE Transactions on Geoscience and Remote Sensing*, 38, 6, pp. 2571-2583.
- Holecz, F. (1993). Postprocessing von SAR-Satellitenbilddaten. *Remote Sensing Series*, Vol. 23, University of Zurich, Department of Geography, Zurich.
- Houghton, R.A. (2005). Aboveground forest biomass and the global carbon balance. *Global Change Biology*, 11, pp. 945-958.
- Houghton, R.A., Butman, D., Bunn, A.G., Krankina, O.N., Schlesinger, P. and Stone, T.A. (2007). Mapping Russian forest biomass with data from satellites and forest inventories. *Environmental Research Letters*, 2, pp. 1-7.
- Hyypä, J., Hyypä, H., Inkinen, M., Engdahl, M., Linko, S. and Zhu, Y.-H. (2000). Accuracy comparison of various remote sensing data sources in the retrieval of forest stand attributes. *Forest Ecology and Management*, 128, pp. 109-120.
- Hyypä, J. and Hyypä, H. (2001). Effects of stand size on the accuracy of remote sensing-based forest inventory. *IEEE Transactions on Geoscience and Remote Sensing*, 39, 12, pp. 2613-2621.
- Imhoff, M.L. (1995). Radar backscatter and biomass saturation: ramifications for global biomass inventory. *IEEE Transactions on Geoscience and Remote Sensing*, 33, 2, pp. 511-518.
- Intergovernmental Panel on Climate Change (2006). *IPCC Guidelines for National Greenhouse Gas Inventories. Volume 4: Agriculture, Forestry and Other Land Use*. Published for the IPCC by the Institute for Global Environmental Strategies, Japan.
- Israelsson, H. and Askne, J. (1994). Importance of dihedral reflection in radar remote sensing of forests. *International Journal of Remote Sensing*, 15, pp. 1585–1593.
- Israelsson, H., Askne, J. and Sylvander, R. (1994). Potential of SAR for bole volume estimation. *International Journal of Remote Sensing*, 15, 14, pp. 2809-2825.
- Izzawati, Wallington, E.D. and Woodhouse, I.H. (2006). Forest height retrieval from commercial X-band SAR products. *IEEE Transactions on Geoscience and Remote Sensing*, 44, 4, pp. 863-869.
- Karam, M.A., Fung, A.K., Lang, R.H. and Chauchan, N. (1992). A microwave scattering model for layered vegetation. *IEEE Transactions on Geoscience and Remote Sensing*, 30, pp. 767-784.
- Karam, M.A., Amar, F. and Fung, A. (1995). A microwave polarimetric scattering model for forest canopies based on a vector radiative transfer theory. *Remote Sensing of Environment*, 53, pp. 16-30.
- Kasischke, E.S., Christensen, N.L., Haney, E. and Bourgeau-Chavez, L.L. (1994). Observations of the sensitivity of ERS-1 SAR image intensity to changes in aboveground biomass in young loblolly pine forests. *International Journal of Remote Sensing*, 15, pp. 3-16.
- Kasischke, E.S., Christensen, N.L. and Bourgeau-Chavez, L.L. (1995). Correlating radar backscatter with components of biomass in loblolly pine forests. *IEEE Transactions on Geoscience and Remote Sensing*, 33, pp. 643-659.
- Kasischke, E.S., Melack, J.M. and Dobson, M.C. (1997). The use of imaging radars for ecological applications – a review. *Remote Sensing of Environment*, 59, pp. 141-156.

-
- Kasischke, E.S., Bourgeau-Chavez, L.L. and Johnstone, J.F. (2007). Assessing spatial and temporal variations in surface soil moisture in fire-disturbed black spruce forests in interior Alaska using spaceborne synthetic aperture radar imagery – implications for post-fire tree recruitment. *Remote Sensing of Environment*, 108, pp. 42-58.
- Kellndorfer, J., Walker, W., Pierce, L., Dobson, C., Fites, J.A., Hunsaker, C., Vona, J. and Clutter, M. (2004). Vegetation height estimation from Shuttle Radar Topography Mission and national elevation datasets. *Remote Sensing of Environment*, 93, pp. 339-358.
- Koskinen, J.T., Pulliainen, J.T. and Hallikainen, M.T. (1997). The use of ERS-1 SAR data in snow melt monitoring. *IEEE Transactions on Geoscience and Remote Sensing*, 35, 3, pp. 601-610.
- Koskinen, J.T., Metsämäki, S., Grandell, J., Jänne, S., Matikainen, L. And Hallikainen, M. (1999). Snow monitoring using radar and optical satellite data. *Remote Sensing of Environment*, 69, pp. 16-29.
- Koskinen, J.T., Pulliainen, J. T., Hyypä, J. M., Engdahl, M. E. and Hallikainen, M. T. (2001). The seasonal behavior of interferometric coherence in boreal forest. *IEEE Transactions on Geoscience and Remote Sensing*, 39, pp. 820-829.
- Kramer, H.J. (2002). *Observation of the earth and its environment*. Springer, Berlin.
- Krieger, G., Moreira, A., Fiedler, H., Hajnsek, I., Werner, M., Younis, M. and Zink, M. (2007). TanDEM-X: a satellite formation for high resolution SAR interferometry. *IEEE Transactions on Geoscience and Remote Sensing*, 45, 11, pp. 3317-3341.
- Kostak, M., Krestov, P. and Okistu, S. (2003). Basic geomorphological and geological characteristics of Northeast Asia. In: Kolbek, J., Srutek, M. and Box, E.O. [ed.], *Forest vegetation of Northeast Asia*, Kluwer, Dordrecht, pp. 33-50.
- Krestov, P. (2003). Forest vegetation of easternmost Russia (Russian Far East). In: Kolbek, J., Srutek, M. and Box, E.O. [ed.], *Forest vegetation of Northeast Asia*, Kluwer, Dordrecht, pp. 93-180.
- Kurvonen, L., Pulliainen, J. and Hallikainen, M. (1999). Retrieval of biomass in boreal forests from multi-temporal ERS-1 and JERS-1 SAR images. *IEEE Transactions on Geoscience and Remote Sensing*, 37, 1, pp. 198-205.
- Lang, R.H., Chauhan, N.S., Ranson, K.J. and Kilic, O. (1994). Modeling P-Band SAR returns from a red pine stand. *Remote Sensing of Environment*, 47, pp. 132-141.
- Lang, M.W., Townsend, P.A. and Kasischke, E.S. (2008). Influence of incidence angle on detecting flooded forests using C-HH synthetic aperture radar data. *Remote Sensing of Environment*, 112, 3898-3907.
- Laur, H., Bally, P., Meadows, P., Sanchez, J., Schättler, B., Lopinto, E. and Esteban, D. (2004). Derivation of the Backscattering coefficient σ^0 in ESA ERS SAR PRI products. ESA Document No. ES-TN-RS-PM-HL09, Issue 2, Rev. 5f.
- Leckie, D.G. and Ranson, K.J. (1998). Forestry applications using imaging radar. In: Henderson, F.M. & Lewis, A.J. [ed.], *Principles and Applications of Imaging Radar*, Vol. 2 of *Manual of Remote Sensing*, 3rd Edition, John Wiley & Sons, New York.
- Leclerc, G., Beaulieu, N. and Bonn, F. (2001). A simple method to account for topography in the radiometric correction of radar imagery. *International Journal of Remote Sensing*, 22, 17, pp. 3553-3570.
- Lee, H. and Liu, J.G. (2001). Analysis of topographic decorrelation in SAR interferometry using ratio coherence imagery. *IEEE Transactions on Geoscience and Remote Sensing*, 39, 2, pp. 223-232.
- Lee, J.S. (1981). Speckle analysis and smoothing of synthetic aperture radar images. *Computer Graphics and Image Processing*, 35, 1, pp. 24-32.

-
- Lei, X., Lu, Y., Peng, C., Zhang, X., Chang, J. and Hong, L. (2007). Growth and structure development of semi-natural larch-spruce-fir (*Larix olgensis*–*Picea jezoensis*–*Abies nephrolepis*) forests in northeast China: 12-year results after thinning. *Forest Ecology and Management*, 240, pp. 165–177.
- Leng, W., He, H.S., Bu, R., Dai, L., Hu, Y. and Wang, X. (2008). Predicting the distributions of suitable habitat for three larch species under climate warming in Northeastern China. *Forest Ecology and Management*, 254, pp. 420–428.
- Le Toan, T., Beaudoin, A., Riom, J. and Guyon, D. (1992). Relating forest biomass to SAR data. *IEEE Transactions on Geoscience and Remote Sensing*, 30, 2, pp. 403-411.
- Li, S. and Sturm, M. (2002). Patterns of wind-drifted snow on Alaskan arctic slope detected with ERS-1 interferometry. *Journal of Glaciology*, 48, 163, pp. 495-504.
- Li, D., Fan, S., He, A. And Yin, F. (2004). Forest resources and environment in China. *Journal of Forest Resources*, 9, pp. 307-312.
- Liu, J.G., Black, A., Lee, H., Hanaizumi, H. (2001). Land surface change detection in a desert area in Algeria using multi-temporal ERS SAR coherence images. *International Journal of Remote Sensing*, 22, 13, pp. 2463-2477.
- Liu, J. (2005). Forestry development and forest policy in China. *Journal of Forest Economics*, 10, pp. 159–160.
- Loew, A. and Mauser, W. (2007). Generation of geometrically and radiometrically terrain corrected SAR image products. *Remote Sensing of Environment*, 106, pp. 337-349.
- Lopes, A., Nezry, E., Touzi, R. and Laur, H. (1993). Structure detection and statistical adaptive speckle filtering in SAR images. *International Journal of Remote Sensing*, 14, 9, pp. 1735-1758.
- Lu, W. (2004). China's growing role in world timber trade. *Unasylva*, 219, 27-31.
- Luckman, A.J. (1998). Correction of SAR imagery for variation in pixel scattering area caused by topography. *IEEE Transactions on Geoscience and Remote Sensing*, 36, 1, pp. 444-450.
- Luckman, A.J., Baker, J. and Wegmüller, U. (2000). Repeat-pass interferometric coherence measurements of disturbed tropical forest from JERS and ERS satellites. *Remote Sensing of Environment*, 73, pp. 350-360.
- Luo, X., Askne, J., Smith, G. and Dammert, P. (2001). Coherence characteristics of radar signals from rough soil. *Progress in Electromagnetic Research PIER*, 31, pp. 69-88.
- Magagi, R. and Bernier, M. (2003). Optimal conditions for wet snow detection using RADARSAT SAR data. *Remote Sensing of Environment*, 84, pp. 221-233.
- Magnusson, M. and Fransson, E.S. (2004). Combining CARABAS-II VCF SAR and Landsat TM satellite data for estimation of forest stem volume. *Proceedings of IGARSS'04*, 20-24 September, Anchorage, pp. 2318-2322.
- Mäkelä, H. and Pekkärinen, A. (2004). Estimation of forest stand volumes by Landsat TM imagery and stand-level field-inventory data. *Forest Ecology and Management*, 196, pp. 245–255.
- Manninen, T., Parmes, E., Häme, T., Septon, A., Bach, H. And Borgeaud, M. (2000). ERS coherence and SLC images in forest characterization. *Proceedings of ERS-ENVISAT Symposium 2000*, 16-20 October, Gothenburg, CD-ROM.
- Martinez, J.M., Floury, N., Le Toan, T., Beaudoin, A., Hallikainen, M.T. and Mäkynen (2000). Measurements and modelling of vertical backscatter distribution in forest canopy. *IEEE Transactions on Geoscience and Remote Sensing*, 38, 2, pp. 710-719.

-
- Mätzler, C. (1995). Microwave permittivity of dry snow. *IEEE Transactions on Geoscience and Remote Sensing*, 34, 2, pp. 573-581.
- Mayr, S., Wieser, G. and Bauer, H. (2006). Xylem temperatures during winter in conifers at the alpine timberline. *Agricultural and Forest Meteorology*, 137, pp. 81-88.
- McDonald, K.C., Dobson, M.C. and Ulaby, F.T. (1991). Modeling multifrequency diurnal backscatter from walnut orchard. *IEEE Transactions on Geoscience and Remote Sensing*, 29, pp. 852-863.
- McDonald, K.C., Zimmermann, R. and Kimball, J.S. (2002). Diurnal and spatial variation of xylem dielectric constant in Norway spruce (*Picea abies* [L.] karst.) as related to microclimate, xylem sap flow, and xylem chemistry. *IEEE Transactions on Geoscience and Remote Sensing*, 40, 9, pp. 2063-2082.
- Mette, T., Papathanassiou, K., Hajnsek, I., Pretzsch, H. and Biber, M. (2004). Applying a common allometric equation to convert forest height from Pol-InSAR data to forest biomass. *Proceedings of IGARSS'04*, 20-24 September, Anchorage, pp. 270-272.
- Moeremans, B. and Dautrebande, S. (2000). Soil moisture evaluation by means of multi-temporal ERS SAR PRI images and interferometric coherence. *Journal of Hydrology*, 234, pp. 162-169.
- Moghaddam, M. and Saatchi, S.S. (1999). Monitoring tree moisture using an estimation algorithm applied to SAR data from BOREAS. *IEEE Transactions on Geoscience and Remote Sensing*, 37, 2, pp. 901-916.
- Moran, M.S., Hymer, D.C., Qi, J. and Sano, E.E. (2000). Soil moisture evaluation using multi-temporal synthetic aperture radar (SAR) and optical remote sensing in semiarid rangeland. *Journal of Agriculture and Forest Meteorology*, 105, pp. 69-80.
- Moreira, A. (1991). Improved multi-look techniques applied to SAR and ScanSAR imagery. *IEEE Transactions on Geoscience and Remote Sensing*, 29, 529-534.
- Mougin, E., Proisy, C., Marty, G., Fromard, F., Puig, H., Betoulle, J.L. and Rudant, J.P. (1999). Multifrequency and multipolarization radar backscattering from mangrove forests. *IEEE Transactions on Geoscience and Remote Sensing*, 37, 1, pp. 94-102.
- Nagler, T., Rott, H., Hanssen, R., Moisseev, D., Adam, N., Eineder, M., Kampes, B., Hajnsek, I., Papathanassiou, K.P. and Cloude, S.R. (2004). The use of synthetic aperture radar (SAR) interferometry to retrieve bio- and geo-physical variables. Final Report, European Space Agency Study Contract Report, Contract No. 16366/02/NL/MM.
- Narayanan, R.M., Doerr, D.W. and Rundquist, D.C. (1992). Temporal decorrelation of X-band backscatter from wind-influenced vegetation. *IEEE Transactions on Aerospace and Electronic Systems*, 28, 2, pp. 404-411.
- Narayanan, R.M., Doerr, D.W. and Rundquist, D.C. (1994). Power spectrum of wind-influenced vegetation backscatter at X-band. *IEEE Proceedings of Radar and Sonar Navigation*, 141, 2, pp. 125-131.
- Nemilostiv, Y.P. and Reymer, V.V. (2007). Timber Resources of the Amur Region and the Problem of their Effective Utilization. *Eurasian Journal of Forest Research*, 10, 1, pp. 121-124.
- Ni, J. (2002). Effects of climate change on carbon storage in boreal forests of China: a local perspective. *Climate Change*, 55, pp. 61-75.
- Niklas, K.J. (1994). *Plant allometry: the scaling of form and process*. University of Chicago Press, Chicago.

-
- Nilson, T. (1999). Inversion of gap frequency data in forest stands. *Agricultural and Forest Meteorology*, 98-99, pp. 437-488.
- Oliver, C.J. and Quegan, S. (1998). *Understanding Synthetic Aperture Radar Images*. Artech House, Boston.
- Olmstedt, C. (1993). *Scientific SAR User's Guide*. Technical Document, ASF-SD-003.
- Pang, Y., Sun, G., Li, Z., Dong, Y. And Zhang, Z. (2003). Land cover change monitoring after forest fire in Northeast China. *Proceedings of IGARSS'03*, Toulouse, 21-25 July, pp. 3386-3388.
- Pang, Y., Li, Z., Tan, B. and Chen, E. (2005). *FOREST DRAGON Project - Ground Truth Data Workbook*. March 2005, Chinese Academy of Forestry, not published.
- Papathanassiou, K.P. and Cloude, S.R. (2001). Single-baseline polarimetric SAR interferometry. *IEEE Transactions on Geoscience and Remote Sensing*, 39, pp. 2352-2363.
- Pothier, D., Margolis, H.A. and Waring, R.H. (1989). Patterns of change of saturated sapwood permeability and sapwood conductance with stand development. *Canadian Journal of Forest Research*, 19, pp. 432-439.
- Pretzsch, H. (2002). *Grundlagen der Waldwachstumsforschung*. Parey Verlag, Berlin.
- Pretzsch, H. (2006). Species-specific allometric scaling under self-thinning: evidence from long-term plots in forest stands. *Ecosystem Ecology*, 146, pp. 572-583.
- Proisy, C., Sarti, F., Mougin, E., Lopes, A., Dufrene, E., LeDantec, V., Ruiz, C., Borderies, P. and Chenerie, I. (1999). Temporal variations of interferometric coherence over a deciduous forest. *Proceedings of CEOS SAR Workshop*, 26-29 October, Toulouse, pp. 25-30.
- Proisy, C., Mougin, E., Dufrene, E. and Le Dantec, V. (2000). Monitoring seasonal changes of a mixed temperate forest using ERS SAR observations. *IEEE Transactions on Geoscience and Remote Sensing*, 38, 1, pp. 540-552.
- Pulliainen, J. T., Heiska, K., Hyyppä, J. and Hallikainen, M. T. (1994). Backscattering properties of boreal forests at the C- and X-bands. *IEEE Transactions on Geoscience and Remote Sensing*, 32, pp. 1041-1050.
- Pulliainen, J.T., Mikkela, P.J., Hallikainen, M.T. and Ikonen, J.P. (1996). Seasonal Dynamics of C-Band Backscatter of Boreal Forests with Applications to Biomass and Soil Moisture Estimation. *IEEE Transactions on Geoscience and Remote Sensing*, 34, 3, pp. 758-770.
- Pulliainen, J.T., Kurvonen, L. and Hallikainen, M.T. (1999). Multitemporal behavior of L- and C-Band SAR observations of boreal forests. *IEEE Transactions on Geoscience and Remote Sensing*, 37, 2, pp. 927-937.
- Pulliainen, J., Engdahl, M. and Hallikainen, M. (2003). Feasibility of multi-temporal interferometric SAR data for stand-level estimation of boreal forest stem volume. *Remote Sensing of Environment*, 85, pp. 397-409.
- Quegan, S., Le Toan, T., Yu, J.J., Ribbes, F. and Floury, N. (2000). Multitemporal ERS SAR analysis applied to forest mapping. *IEEE Transactions on Geoscience and Remote Sensing*, 38, 2, pp. 741-735.
- Quegan, S. and Yu, J.J. (2001). Filtering of multi-channel SAR images. *IEEE Transactions on Geoscience and Remote Sensing*, 39, 12, pp. 2373-2379.
- Qian, H., Yuan, X.Y. and Chou, Y.L. (2003). Forest vegetation of Northeast China. In: Kolbek, J., Srutek, M. and Box, E.O. [ed.], *Forest vegetation of Northeast Asia*, Kluwer, Dordrecht, pp. 181-230.
- Rabus, B., Eineder, M., Roth, A. and Bamler, R. (2003). The shuttle radar topography mission - a new class of digital elevation models acquired by spaceborne radar. *ISPRS Journal of Photogrammetry and Remote Sensing*, 57, 4, pp. 241-262.

-
- Ranson, K.J. and Sun, G. (1994a). Northern forest classification using temporal multifrequency and multipolarimetric SAR images. *Remote Sensing of Environment*, 47, pp. 142–153.
- Ranson, K.J. and Sun, G. (1994b). Mapping biomass of a northern forest using multifrequency SAR data. *IEEE Transactions on Geoscience and Remote Sensing*, 32, pp. 388–396.
- Ranson, K.J. and Sun, G. (1997). An evaluation of AIRSAR and SIR-C/X-SAR images for mapping northern forest attributes in Maine, USA. *Remote Sensing of Environment*, 59, pp. 203-222.
- Ranson, K.J., Sun, G., Weishampel, J.F. and Knox, R.G. (1997). Forest Radar Biomass from combined ecosystem backscatter modelling. *Remote Sensing of Environment*, 59, pp. 118-133.
- Ranson, K.J. and Sun, G. (2000). Effects of environmental conditions on boreal forest classification and biomass estimates with SAR. *IEEE Transactions on Geoscience and Remote Sensing*, 38, 3, pp. 1242–1252.
- Ranson, K.J., Sun, G., Kharuk, V.I. and Kovacs, K. (2001a). Characterization of forests in western Sayani mountains, Siberia from SIR-C SAR data. *Remote Sensing of Environment*, 75, pp. 188-200.
- Ranson, K.J., Sun, G., Knox, R.G., Levine, E.R., Weishampel, J.F. and Fifer, S.T. (2001b). Northern forest ecosystem dynamics using coupled models and remote sensing. *Remote Sensing of Environment*, 75, pp. 291-302.
- Reineke, L.H. (1933). Perfecting a stand density index for even-aged forests. *Journal of Agricultural Research*, 46, pp. 627-638.
- Reese, H., Nilsson, M., Sandström, P. and Olsson, H. (2002). Applications using estimates of forest parameters derived from satellite and forest inventory data. *Computers and Electronics in Agriculture*, 37, pp. 37-55.
- Ribbes, F., Le Toan, T., Floury, N., and Wasrin, U. R. (1997). Deforestation monitoring in tropical regions using multitemporal ERS/JERS SAR and InSAR data. *Proceedings of IGARSS'97, 3-8 August, Singapore*, pp. 1560-1562.
- Rignot, E., Way, J.B., McDonald, K., Viereck, L., Williams, C., Adams, P., Payne, C., Wood, W. and Shi, J. (1994). Monitoring of environmental conditions in taiga forests using ERS-1 SAR. *Remote Sensing of Environment*, 49, pp. 145-154.
- Rignot, E. and Way, J.B. (1994). Monitoring freeze–thaw cycles along north–south Alaskan transects using ERS-1 SAR. *Remote Sensing of Environment*, 49, 2, pp. 131–137.
- Rignot, E., Zimmermann, R. and Van Zyl, J. (1995). Spaceborne applications of P band imaging radars for measuring forest biomass. *IEEE Transactions on Geoscience and Remote Sensing*, 33, 5, pp. 1162– 1169.
- Rignot, E. (1996). Dual-frequency interferometric SAR observations of a tropical rain-forest. *Geophysical Research Letters*, 23, pp. 993-996.
- Rodriguez, E. and Martin, J.M. (1992). Theory and design of interferometric synthetic-aperture radars. *Proceedings of IEE*, vol. 139, 2, pp. 147-159.
- Rosen, P.A., Hensley, S., Joughon, I.R., Li, F.K., Madsen, S.N., Rodriguez, E. and Goldstein, R.M. (2000). Synthetic Aperture Radar Interferometry. *Proceedings of the IEEE*, 88, 3, pp. 333-382.
- Rott, H., Nagler, T. and Scheiber, R. (2003). Snow mass retrieval by means of SAR interferometry. *Proceedings of FRINGE'03, Frascati, 1-5 December, ESA SP-550, CD-ROM*.
- Saatchi, S.S and McDonald, K.C. (1997). Coherent effects in microwave backscattering models for forest canopies. *IEEE Transactions on Geoscience and Remote Sensing*, 35, pp. 1032-1044.

-
- Saatchi, S.S. and Rignot, E. (1997). Classification of boreal forest cover types using SAR images. *Remote Sensing of Environment*, 60, 3, pp. 270-281.
- Saatchi, S.S. and Moghaddam, M. (2000). Estimation of crown and stem water content and biomass of boreal forest using polarimetric SAR imagery. *IEEE Transactions on Geoscience and Remote Sensing*, 38, 2, pp. 697-709.
- Saatchi, S.S., Halligan, K., Despain, D.G. and Crabtree, R.L. (2007). Estimation of forest fuel load from radar remote sensing. *IEEE Transactions on Geoscience and Remote Sensing*, 45, 6, pp. 1726-1740.
- Salas, W.A., Ranson, J.K., Rock, B.N. and Smith, K.T. (1994). Temporal and spatial variations in dielectric constant and water status of dominant forest species from New England. *Remote Sensing of Environment*, 47, pp. 109-119.
- Santoro, M., Askne, J., Dammert, P.B.G., Fransson, J.E.S. and Smith, G. (1999). Retrieval of biomass in boreal forest from multi-temporal ERS-1/2 interferometry. *Proceedings of Fringe'99*, 10-12 November, Liège, ESA SP-478, CD-ROM.
- Santoro, M., Askne, J., Smith, G. and Fransson, J. E. S. (2002). Stem volume retrieval in boreal forests with ERS-1/2 interferometry. *Remote Sensing of Environment*, 81, pp. 19-35.
- Santoro, M. (2003). Estimation of biophysical forest parameters in boreal forests from ERS and JERS SAR interferometry. Technical Report No. 188, PhD thesis, Gothenburg.
- Santoro, M., Askne, J., Eriksson, L.E.B. and Schmillius, C. (2004). Comparison of stem volume retrieval accuracy in boreal forest using multi-temporal ERS coherence images. *Proceedings of ENVISAT Symposium 2004*, 6-10 September, Salzburg, Austria, ESA SP-572, CD-ROM.
- Santoro, M., Askne, J. and Dammert, P. B. G. (2005a). Tree height influence on ERS interferometric phase in boreal forest. *IEEE Transactions on Geoscience and Remote Sensing*, 43, pp. 207-217.
- Santoro, M., Cartus, O., Schmillius, C., Wegmüller, U., Werner, C., Wiesmann, A., Pang, Y., and LI Z. (2005b). On the generation of a forest biomass map for Northeast China: SAR interferometric processing and development of classification algorithm. *Proceedings of Fringe'05*, Frascati, 28 November - 2 December, ESA SP-610, CD-ROM.
- Santoro, M., Eriksson, L., Askne, J. and Schmillius, C. (2006). Assessment of stand-wise stem volume retrieval in boreal forest from JERS-1 L-band SAR backscatter. *International Journal of Remote Sensing*, 27, 16, pp. 3425-3454.
- Santoro, M., Shvidenko, A., McCallum, I., Askne, J., Schmillius, C. (2007). Properties of ERS-1/2 coherence in the Siberian boreal forest and implications for stem volume retrieval. *Remote Sensing of Environment*, Vol. 106, pp. 154-172.
- Santoro, M., Askne, J., Wegmüller, U. and Werner, C. (2007a). Observations, modeling, and applications of ERS-ENVISAT coherence over land surfaces. *IEEE Transactions on Geoscience and Remote Sensing*, 45, 8, pp. 2600-2611.
- Santoro, M., Beer, C., Shvidenko, A., McCallum, I., Wegmüller, U., Wiesmann, A. and Schmillius, C. (2007b). Comparison of forest biomass estimates in Siberia using spaceborne SAR inventory-based information and the LPJ Dynamic Global Vegetation Model. *Proceedings of Envisat Symposium*, 21-25 April, Montreux, ESA SP 635, CD-ROM.
- Santoro, M., Werner, C., Wegmüller, U. and Cartus, O. (2007c). Improvement of interferometric SAR coherence estimates by slope adaptive range common band filtering. *Proceedings of IGARSS'07*, 23-27 July, Barcelona, pp. 129-132.

-
- Sarabandi, K. and Wilson, C.B. (2000). Temporal decorrelation of vegetation by environmental and seasonal effects. Proceedings of IGARSS'2000, 24-28 July, Honolulu, pp. 1399-1401.
- Schaber, G.G., McCanley, J.F., Breed, C.S. and Olhoeft, G.R. (1986). Shuttle imaging radar: physical controls on signal penetration and subsurface scattering in the eastern Sahara. IEEE Transactions on Geoscience and Remote Sensing, 24, pp. 603-623.
- Schmullius, C. E., Baker, J., Balzter, H., Davidson, M., Eriksson, L., Gaveau, D., Gluck, M., Holz, A., Le Toan, T., Luckman, A.J., Marschalk, U., McCallum, I., Nilsson, S., Öskog, A., Quegan, S., Rauste, Y., Roth, A., Rozhkov, V., Sokolov, V., Shvidenko, A., Skuding, V., Strozzi, T., Tansey, K., Vietmeier, J., Voloshuk, L., Wagner, W., Wegmüller, U., Wiesmann, A. and Yu, J. J. (2001). SIBERIA - SAR Imaging for Boreal Ecology and Radar Interferometry Applications. Final Report, EC- Center for Earth Observation, Project Reports, Contract No. ENV4-CT97-0743-SIBERIA.
- Schwäbisch, M. and Geudtner, D. (1995). Improvement of phase and coherence map using azimuth prefiltering: Examples from ERS-1 and X-SAR. Proceedings of IGARSS'95, 10-14 July, Florence, pp. 205-207.
- Shi, J. and Dozier, J. (1995). Inferring snow wetness using C-band data from SIR-C polarimetric synthetic aperture radar. IEEE Transactions on Geoscience and Remote Sensing, 33, pp. 905-914.
- Shi, J. and Dozier, J. (1997). Mapping seasonal snow with SIR-C/X-SAR in mountainous areas. Remote Sensing of Environment, 59, pp. 294-307.
- Shi, J., Kattlemann, R. and Dozier, J. (1997). Effects of large structure in wet snow cover on SAR measurements. Proceedings of IGARSS'97, 03-08 August, Singapore, pp. 1451-1453.
- Shi, J. and Dozier, J. (2000a). Estimation of snow water equivalence using SIR-C/X-SAR, part 1: inferring snow density and subsurface properties. IEEE Transactions on Geoscience and Remote Sensing, 38, 6, pp. 2465-2474.
- Shi, J. and Dozier, J. (2000b). Estimation of snow water equivalence using SIR-C/X-SAR, part 2: inferring snow depth and particle size. IEEE Transactions on Geoscience and Remote Sensing, 38, 6, pp. 2475-2488.
- Shvidenko, A., McCallum, I., Nilsson, S. and Vaschuk, L. (2007). IRIS – Irkutsk Regional Information System for Environmental Protection: Integrating and strengthening the European Research Area. Deliverable D4.1, International Institute for Applied Systems Analysis, Project No. INCO-CT2006-015110.
- Smith, G., Dammert, P.B.G. and Askne, J. (1996). Decorrelation mechanisms in C-band SAR interferometry over boreal forest. Proceedings of SPIE, 2958, pp. 300-310.
- Smith, G. and Askne, J. (2001). Clear-cut detection using ERS interferometry. International Journal of Remote Sensing, 22, 18, pp. 3651-3664.
- Spanner, M.A., Pierce, L.L., Peterson, D.L. and Running, S.W. (1990). Remote sensing of temperate coniferous forest leaf area index: the influence of canopy closure, understorey vegetation and background reflectance. International Journal of Remote Sensing, 11, pp. 95-111.
- Srivastava, S.K. and Jayaraman, V. (2001). Relating interferometric signature of repeat-pass ERS-1 SAR signals to dynamic land cover changes. Acta Astronautica, 48, 1, pp. 37-44.
- Srivastava, H.S., Patel, P. and Navalgund, R.R. (2006). Applications potentials of synthetic aperture radar interferometry for land-cover mapping and crop-height estimation. Current Science, Research Communication, 91, 6, pp. 783-788.

-
- Stolbovoi, V. and McCallum, I. (2002). Land Resources of Russia. International Institute for Applied Systems Analysis and the Russian Academy of Science, Laxenburg, Austria. Available at: 'www.iiasa.ac.at/Research/FOR/', last date of access: May 1st 2009.
- Stebler, O., Pasquali, P., Small, D., Holezz, F. and Nüesch, D. (1996). Analysis of ERS-SAR tandem time-series using coherence and backscattering coefficient. Proceedings of Fringe'96, 30 September - 2 October, Zurich, ESA SP-406, pp. 105-115.
- Strozzi, T., Wegmüller, U., Mätzler, C. (1999). Mapping wet snow covers with SAR interferometry. *International Journal of Remote Sensing*, 20, 12, pp. 2395-2403.
- Strozzi, T., Dammert, P.B.G., Wegmüller, U., Martinez, J.M., Askne, J., Beaudoin, A. and Hallikainen, M.T. (2000). Landuse Mapping with ERS SAR interferometry. *IEEE Transactions on Geoscience and Remote Sensing*, 38, 2, pp. 766-774.
- Sun, G., Simonett, D. and Strahler, A. (1991). A radar backscatter model for discontinuous coniferous forest. *IEEE Transactions on Geoscience and Remote Sensing*, 29, pp. 639-650.
- Sun, G., Ranson, K.J. and Kharuk, V.I. (2002). Radiometric slope correction for forest biomass estimation from SAR data in the Western Sayani Mountains, Siberia. *Remote Sensing of Environment*, 79, pp. 279-287.
- Tan, K., Piao, S., Peng, C. and Fang, J. (2007). Satellite-based estimation of biomass carbon stocks for northeast China's forests between 1982 and 1999. *Forest Ecology and Management*, 240, pp. 114-121.
- Tang, S., Meng, C.H., Meng, F.R. and Wang, Y.H. (1994). A growth and self-thinning model for pure even-age stands: theory and applications. *Forest Ecology and Management*, 70, pp. 67-73.
- Tang, S., Meng, F.R. and Meng, C.H. (1995). The impact of initial stand density and site index on maximum stand density index and self thinning index in a stand self-thinning model. *Forest Ecology and Management*, 75, pp. 61-68.
- Tansey, K. J., Luckman, A. J., Skinner, L., Balzter, H., Strozzi, T. and Wagner, W. (2004). Classification of forest volume resources using ERS tandem coherence and JERS backscatter data. *International Journal of Remote Sensing*, 25, pp. 751-768.
- Teillet, P.M., Guindon, B., Meunier, J.F. and Goodenough, D.G. (1985). Slope-aspect effects in synthetic aperture radar imagery. *Canadian Journal of Remote Sensing*, 11, pp. 39-49.
- Thomas, S.C., Malczewski, G. and Saprunoff, M. (2007). Assessing the potential of native tree species for carbon sequestration forestry in Northeast China. *Journal of Environmental Management*, 85, pp. 663-671.
- Törmä, M. (1999). Classification of tree species using ERS intensity and coherence images. Proceedings of Fringe'99, Liege, 10-12 November, CD-Rom.
- Touzi, R., Lopes, A., Bruniquel, J. and Vachon, P.W. (1999). Coherence estimation for SAR imagery. *IEEE Transactions on Geoscience and Remote Sensing*, 37, 1, pp. 135-149.
- Treuhaft, R. N., Madsen, S. N., Moghaddam, M. and van Zyl, J. J. (1996). Vegetation characteristics and underlying topography from interferometric radar. *Radio Science*, 31, pp. 1449-1485.
- Treuhaft, R.N. and Siqueira, P.R. (2004). The calculated performance of forest structure and biomass estimates from interferometric radar. *Waves in Random Media*, 14, 2, pp. 345-358.

-
- Trotter, C.M., Dymond, J.R. and Goulding, C.J. (1997). Estimation of timber volume in a coniferous plantation forest using Landsat TM. *International Journal of Remote Sensing*, 18, 10, pp. 2209-2223.
- Ulaby, F.T., Moore, R.K. and Fung, A.K. (1986). *Microwave Remote Sensing, Active and Passive*, vol. II, Artech House, Dedham.
- Ulaby, F.T., Sarabandi, K., McDonald, K., Witt, M. and Dobsom, M.C. (1990). Michigan microwave canopy scattering model. *International Journal of Remote Sensing*, 11, pp. 1223-1253.
- Ulander, L.M.H. (1996). Radiometric slope correction of Synthetic Aperture Radar images. *IEEE Transactions on Geoscience and Remote Sensing*, 34, 5, pp. 1115-1122.
- Usai, S. and Klees, R. (1999). SAR interferometry on a very long time scale: a study of the interferometric characteristics of man-made features. *IEEE Transactions on Geoscience and Remote Sensing*, 37, 4, pp. 2118-2123.
- Van Der Sanden, J.J. (2004). Anticipated applications potential of RADARSAT-2 data. *Canadian Journal of Remote Sensing*, 30, 3, pp. 369-379.
- Van Laar, A. and Akca, A. (2007). *Forest mensuration*. Springer, Dordrecht.
- Van Zyl, J.J. (1993). The effect of topography on radar scattering from vegetated areas. *IEEE Transactions on Geoscience and Remote Sensing*, 31, 1, pp. 153-160.
- Van Zyl, J.J., Chapman, B.D., Dubois, P. and Shi, J. (1993). The effect of topography on SAR calibration. *IEEE Transactions on Geoscience and Remote Sensing*, 31, pp. 1036-1043.
- Wagner, W., Luckman, A., Vietmeier, J., Tansey, K., Balzter, H., Schmulius, C., Davidson, M., Gaveau, D., Gluck, M., Le Toan, T., Quegan, S., Shvidenko, A., Wiesmann, A. and Yu, J. J. (2003). Large-scale mapping of boreal forest in SIBERIA using ERS tandem coherence and JERS backscatter data. *Remote Sensing of Environment*, 85, pp. 125-144.
- Wang, Y., Kasischke, E., Melack, J., Davis, F., and Christensen, N. (1994). The effects of changes in loblolly pine biomass and soil moisture on ERS-1 SAR backscatter. *Remote Sensing of Environment*, 49, pp. 25-31.
- Wang, Y., Day, J.L. and Davis, F.W. (1995). Sensitivity of modeled C- and L-band radar backscatter to ground surface parameters in loblolly pine forest. *Remote Sensing of Environment*, 66, pp. 331-342.
- Wang, Y., Kasischke, E.S., Davis, F.W., Melack, J.M. and Christensen, N.L. (1995a). The effects of changes in forest biomass on radar backscatter from tree canopies. *International Journal of Remote Sensing*, 16, pp. 503-513.
- Wang, Y., Hess, L.L., Filoso, S. and Melack, J.M. (1995b). Understanding the radar backscatter from flooded and non-flooded Amazonian forests: results from canopy backscatter modeling. *Remote Sensing of Environment*, 54, pp. 324-332.
- Wang, X., Fang, J., Tang, Z. and Zhu, B. (2006a). Climatic control of primary forest structure and dbh-height allometry in Northeast China *Forest Ecology and Management*, 234, pp. 264-274.
- Wang, X., Tang, Z. and Fang, J. (2006b). Climatic control on forests and tree species distribution in the forest region of Northeast China. *Journal of Integrative Plant Biology*, 48, 7, pp. 778-789.
- Way, J. (1991). Diurnal change in trees. *IEEE Transactions on Geoscience and Remote Sensing*, 29, 6, pp. 807-821.
- Wegmüller, U. (1990). The effect of freezing and thawing on the microwave signatures of bare soil. *Remote Sensing of Environment*, 33, pp. 123-135.
- Wegmüller, U. & Werner, C. (1995). SAR interferometric signatures of forest. *IEEE Transactions on Geoscience and Remote Sensing*, 33, 5, pp. 1153-1161.

-
- Wegmüller, U., Werner, C. and Strozzi, T. (1998). SAR interferometric and differential interferometric processing. Proceedings of IGARSS'98, 6-10 July, Seattle, pp. 1106-1108.
- Wegmüller, U. (1999). Automated terrain corrected SAR geocoding. Proceedings of IGARSS'99, 28 June – 2 July, Hamburg, pp. 1712-1714.
- Wegmüller, U., Werner, C., Strozzi, T. and Wiesmann, A. (2001). Automated and precise image registration procedures. Proceedings of 1st International Workshop on the Analysis of Multitemporal Remote Sensing Images, 13-14 September, Trento.
- Werner, C., Wegmüller, U., Strozzi, T. and Wiesmann, A. (2000). GAMMA SAR and interferometric processing software. Proceedings of ERS-Envisat Symposium 2000, 16-20 October, Gothenburg, ESA SP-461, CD-ROM.
- West, P.W. (2004). Tree and Forest Measurement. Springer, Berlin.
- Weydahl, D.J. (2001). Analysis of ERS SAR coherence images acquired over vegetated areas and urban features. International Journal of Remote Sensing, 22, 14, pp. 2811-2830.
- White, M.A., Shaw, J.D. and Ramsey, R.D. (2005). Accuracy assessment of the Vegetation Continuous Field tree cover product using 3954 ground plots in the south-western USA. International Journal of Remote Sensing, 26, 12, pp. 2699-2704.
- Woodall, C.W., Fiedler, C.E. and Milner, K.S. (2003). Stand density in uneven-aged ponderosa pine stands. Canadian Journal of Forest Research, 33, pp. 96-100.
- Wulder, M., White, J.C., Fournier, R.A., Luther, J.E. and Magnussen, S. (2008). Spatially explicit large area biomass estimation: three approaches using forest inventory and remotely sensed imagery in a GIS. Sensors, 8, pp. 529-560.
- Xiao, X., Boles, S., Liu, J., Zhuang, D. and Liu, M. (2002). Characterization of forest types in Northeastern China, using multi-temporal SPOT-4 VEGETATION sensor data. Remote Sensing of Environment, 82, pp. 335–348.
- Xiaodong, Y. and Shugart, H.H. (2005). FAREAST: a forest gap model to simulate dynamics and patterns of eastern Eurasian forests. Journal of Biogeography, 32, pp. 1641–1658.
- Yang, X., Ding, Z., Fan, X., Zhou, Z. and Ma, N. (2007). Processes and mechanisms of desertification in northern China during the last 30 years, with a special reference to the Hunshandake Sandy Land, eastern Inner Mongolia. Catena, 71, pp. 2–12.
- Yin, R. (1998). Forestry and the environment in China: the current situation and strategic choices. World Development, 26, 12, pp. 2153-2167.
- Zebker, H.A. and Villasenor, J. (1992). Decorrelation in interferometric radar echoes. IEEE Transactions on Geoscience and Remote Sensing, 30, 5, pp. 950-959.
- Zeide, B. (1985). Tolerance and self-tolerance of trees. Forest Ecology and Management, 13, pp. 149-166.
- Zhao, M. and Zhou, G.S. (2005). Estimation of biomass and net primary productivity of major planted forests in China based on forest inventory data. Forest Ecology and Management, 207, pp. 295-313.

Appendix A

Perpendicular baselines of the ERS-1/2 tandem dataset used for the creation of the forest stem volume map of Northeast China. The values for the northern- and southernmost frames in an orbit are given.

Track	ERS-1 Acquisition Date	ERS-2 Acquisition Date	perp. baseline of northernmost frame	perp. baseline of southernmost frame	No. of Frames
0304	01 Jan. 96	02. Jan. 96	-179	-203	7
0046	02 May 98	03 May 98	-66	-70	4
0418	09 Jan. 96	10 Jan. 96	-67	-43	11
0447	11 Jan. 96	12 Jan. 96	-66	-99	12
0289	14 Apr. 96	15 Apr. 96	-94	-95	2
0218	14 May 96	15 May 96	-120	-130	7
0003	15 Jan. 96	16 Jan. 96	-315	-395	10
0017	16 Jan. 96	17 Jan. 96	-273	-304	5
0261	17 May 96	18 May 96	-90	-90	1
0046	18 Jan. 96	19 Jan. 96	-82	-155	12
0003	19 Feb. 96	20 Feb. 96	93	74.5	7
0132	20 Dec. 95	21 Dec. 95	-191	-267	16
0046	22 Feb. 96	23 Feb. 96	64	37	9
0103	22 Jan. 96	23 Jan. 96	154	138	8
0046	28 Mar. 96	29 Mar. 96	-98	-103	8
0261	29 Dec. 95	30 Dec. 95	-211	-252	11
0275	30 Dec. 96	31 Dec. 95	-195	-254	13
0289	31 Dec. 95	01 Jan. 96	-209	-217	3
0447	02 Oct. 97	03 Oct. 97	311	325	4
0461	03 Oct. 97	04 Oct. 97	285	328	12
0490	05 Oct. 97	06 Oct. 97	288	323	10
0103	13 Oct. 97	14 Oct. 97	210	241	8
0175	18 Oct. 97	19 Sep. 97	248	301	15
0304	22 Sep. 97	23 Sep. 97	313	348	7
0318	23 Sep. 97	24 Sep. 97	337	361	6
0332	24 Sep. 97	25 Sep. 97	296	334	8
0361	26 Sep. 97	27 Sep. 97	295	308	4
0318	30 Jun. 98	01 Jul. 98	-376	-389	3

Tabellarischer Lebenslauf

Persönliche Angaben:

Name: Oliver Cartus
Geburtsdatum: 27. Juli 1976
Geburtsort: Trier
Nationalität: Deutsch
Familienstand: Verheiratet, 1 Kind

Schulische Ausbildung:

1983-1987 Grundschule Sasbachried
1987-1996 Gymnasium Achern
Leistungskurse: Mathematik und Geschichte
06/1996 Abitur, Note: 1,5

Wehrersatzdienst:

08/1996-09/1997 „Spastikerverein Offenburg“ – Tätigkeit im Pflegedienst

Studium:

10/1997-09/1998 Diplomstudium der Meteorologie an der Universität Karlsruhe
10/1998-02/2005 Diplomstudium der Geographie an der Friedrich-Schiller-Universität Jena, Abschlussnote: 1,3
Hauptfächer: Fernerkundung und Physische Geographie
Nebenfächer: Physik (4 Semester), Ökologie, Sozialgeographie
Spezialisierung auf angewandte Radarfernerkundung und SAR-Interferometrie
Studienprojekt: „Landoberflächenanalyse mittels InSAR-Methoden für ein Testgebiet in der Mongolei“
Diplomarbeit: „Analyse der Anwendbarkeit von SAR- und InSAR-Methoden zur Bestimmung biophysikalischer Forstparameter im Thüringer Wald“
04/2005-04/2008 Doktorand im Rahmen des ESA/MOST DRAGON Projekts

Tätigkeiten neben dem Studium, Praktika und Auslandsaufenthalte:

2001 Studentische Hilfskraft am Lehrstuhl für Geoinformatik und Fernerkundung im Rahmen des BMBF Projekts TERRADEW
2002-2004 Studentische Hilfskraft am Lehrstuhl für Geoinformatik und Fernerkundung im Rahmen des EU Projekts SIBERIA-II. Schwerpunkt der Arbeit: Interferometrische Prozessierung von ERS-1/2 Tandem- sowie JERS-Repeat-Pass-Daten
2002 Praktikum: Institut für Methodik der Fernerkundung, DLR (6 Wochen)

2003	Praktikum: Deutsches Fernerkundungsdatenzentrum, DLR (8 Wochen)
2003	Bodenkundlich-ökologische Exkursion durch Westrussland
2005	Einmonatiger Aufenthalt im Rahmen des DRAGON Projekts an der Chinese Academy of Forestry, Institute of Forest Resources Information Techniques, Peking, China

Projektarbeit für:

04/2005-11/2007	ESA/MOST DRAGON
12/2007-05/2008	ESA AMOC
11/2008-11/2009	ESA BIOMASAR

Sprachkenntnisse:

Gute Englischkenntnisse in Wort und Schrift
 Grundkenntnisse in Französisch

EDV-Kenntnisse:

Programmierung: Matlab, IDL (Grundkenntnisse), Shell-Script
 Betriebssysteme: Windows, Linux/Unix, Mac OSX
 Office: Word, Excel, Powerpoint
 Digitale Bildverarbeitung & GIS: ENVI, Erdas Imagine, ESRI ArcView (Grundkenntnisse), Photoshop
 SAR- und InSAR-Prozessierung: Gamma, Sarscape

Publikationen:

- Santoro, M., Cartus, O., Schullius, C., Wegmüller, U., Werner, C., Wiesmann, A., Pang, Y. and LI, Z., (2005). On the generation of a forest biomass map for Northeast China: SAR interferometric processing and development of classification algorithm. Proceedings of Fringe 2005 Workshop, 28 November - 2 December, Frascati, CD-Rom.
- Schullius, C., Li, Z., Bouvet, A., Cartus, O., Chen, E., Jeannin, N., Le Toan, T., L'Hermitte, J., Pang, Y., Santoro, M., Tian, X., Wegmüller, U., Wiesmann, A., Werner, C. and Zhu, H. (2005). Mid-term status of the Forest Dragon Project. Proceedings of Dragon Symposium, 27 June– 01 July 2005, Santorini, ESA SP-611, CD-Rom.
- Cartus, O., Santoro, M. and Schullius, C. (2005). Feasibility of forest parameter retrieval in mountainous areas using ERS and JERS SAR Interferometry. Proceedings of the 9th International Symposium on Physical Measurements and Signatures in Remote Sensing, 17-19 October, Beijing, pp. 530-532.
- Pang, Y., Li, Z., Chen, E., Santoro, M., Schullius, C., Cartus, O. and Le Toan, T. (2006). Forest mapping and change detection using ERS SAR and ENVISAT ASAR data. Proceedings of FIEOS 2006, 3rd International Symposium on Future Intelligent Earth Observation Satellites, 24-26 May, Beijing.

-
- Cartus, O., Santoro, M., Schmullius, C., Pang, Y. and Li, Z. (2007). Creation of Large Area Forest Biomass Maps for NE China Using ERS-1/2 tandem coherence. Proceedings of Envisat Symposium 2007, 23-27 April, Montreux, ESA SP-636, CD-Rom.
- Tian, X., Li, Z., Chen, E., Pang, Y., Schmullius, C., Cartus, O., Santoro, M. and Le Toan, T. (2007). Assessment and update of forest classification using multi-parameter satellite SAR data for NE China. Proceedings of Envisat Symposium 2007, 23-27 April, Montreux, ESA SP-636, CD-Rom.
- Santoro, M., Schmullius, C., Cartus, O., Thiel, C. and Wegmüller, U. (2007). Observations of forest cover and forest growing stock volume in Siberia from PALSAR backscatter and coherence data. ALOS PI Symposium, November 2007, Kyoto.
- Cartus, O., Santoro, M., Schmullius, C., Pang, Y., Chen, E. and Li, Z. (2008). Creation of large area forest biomass maps for Northeast China using ERS-1/2 tandem coherence. Proceedings of Dragon 1 Programme Final Results 2004–2007, 21–25 April, Beijing, ESA SP-655, CD-Rom.
- Santoro, M., Werner, C., Wegüller, U. and Cartus, O. (2007). Improvement of interferometric SAR coherence estimates by slope adaptive range common band filtering. Proceedings of IGARSS'07, 23-27 July, Barcelona, CD-ROM.
- Santoro, M., Askne, J., Beer, C., Cartus, O., Schmullius, C., Wegmüller, U. and Wiesmann, A. (2008). Automatic model inversion of multi-temporal C-band coherence and backscatter measurements for forest stem volume retrieval. Proceedings of IGARSS'08, 6-11 July, Boston, CD-ROM.
- Cartus, O., Santoro, M., Schmullius, C. and Li, Z. (2008). Creation of large area forest stem volume maps for China using ERS tandem coherence. Eos Transactions AGU, 89,53, Fall Meeting Suppl., B41C-0389.
- Groisman, P.Y., Clark, E.A., Kattsov, V.M., Lettenmaier, D.P., Sokolik, I.N., Aizen, V.B., Cartus, O., Chen, J., Conard, S., Katzenberger, J., Krankina, O., Kukkonen, J., Machida, T., Maksyutov, S., Ojima, D., Qi, J., Romanovsky, V.E., Santoro, M., Schmullius, C., Shiklomanov, A.I., Shimoyama, K., Shugart, H.H., Shuman, J.K., Sofiev, M., Sukhinin, A.I., Vörösmarty, C., Walker, D. and Wood, E.F. (2009). The Northern Eurasia Earth Science Partnership: An example of science applied to societal needs. Bulletin of American Meteorological Society, May 2009, pp. 671-688.
- Thiel, C., Cartus, O., Eckardt, R., Richter, N., Thiel, C. and Schmullius, C. (2009). Analysis of multi-temporal land observation at C-band. Proceedings of IGARSS'09, 12-17 July, Capetown, CD-Rom.
- Cartus, O., Reiche, J., Leiterer, R., Santoro, M., Schmullius, C. and Li, Z. (2009). Generation and cross-validation of large-area forest stem volume maps for Northeast and Southeast China using ERS-1/2 tandem coherence. Proceedings of the 6th International Symposium on Digital Earth (ISDE), 9-12 September, Beijing, CD-Rom.

Selbständigkeitserklärung

Hiermit erkläre ich, dass ich die vorgelegte Arbeit selbständig und unter Verwendung der angegebenen Hilfsmittel und Quellen angefertigt habe.

Jena, den 28.09.2009

Oliver Cartus